

ABSTRACT

Title of Document: FLEXIBLE MULTI-BODY DYNAMICS
MODEL OF A BIO-INSPIRED
ORNITHOPTER WITH EXPERIMENTAL
VALIDATION.

Cornelia Altenbuchner, Ph.D., 2014

Directed By: NASA Langley Distinguished Professor, Dr.
James E. Hubbard, Jr., Department of Aerospace
Engineering

There is currently a large effort underway to understand the physics of avian-based flapping wing vehicles, known as ornithopters. There is a need for small aerial robots to conduct a variety of civilian and military missions. Efforts to model the flight physics of these vehicles have been complicated by a number of factors, including nonlinear elastic effects, multi-body characteristics, unsteady aerodynamics, and the strong coupling between fluid and structural dynamics. Experimental verification is crucial in order to achieve accurate simulation capabilities. A multi-disciplinary approach to modeling requires the use of tools representing individual disciplines, which must be combined to form a comprehensive model. In the framework of this research a five body flexible vehicle dynamics model and a novel experimental verification methodology is presented. For the model development and verification of the modeling assumptions, a data set providing refined wing kinematics of a test

ornithopter research platform in free flight was used. Wing kinematics for the verification was obtained using a Vicon motion capture system. Lagrange equations of motion in terms of a generalized coordinate vector of the rigid and flexible bodies are formulated in order to model the flexible multi-body system. Model development and verification results are presented. The ‘luff region’ and ‘thrust flap region’ of the wing are modeled as flexible bodies. A floating reference frame formulation is used for the ornithopter. Flexible body constraints and modes are implemented using the Craig-Bampton method, which incorporates a semi-physical subspace method. A quasi-steady aerodynamic model using Blade Element Theory was correlated and verified for the problem using the experimental wing kinematics. The aerodynamic model was then formulated in terms of generalized coordinates of the five-body flexible multi-body system and is used in the resulting model in order to account for aero-elasticity. Modeling assumptions were verified and simulation results were compared with experimental free flight test data.

FLEXIBLE-MULTI-BODY DYNAMICS MODEL OF A BIO-INSPIRED
ORNITHOPTER WITH EXPERIMENTAL VALIDATION.

By

Cornelia Altenbuchner

Dissertation submitted to the Faculty of the Graduate School of the
University of Maryland, College Park, in partial fulfillment
of the requirements for the degree of
Doctor of Philosophy
2014

Advisory Committee:

Professor Dr. James E. Hubbard Jr., Chair

Dr. Amr Baz

Dr. Alison Flatau

Dr. Sung Lee

Dr. Norman Wereley

© Copyright by
Cornelia Altenbuchner
2014

Preface

The author wishes to mention NASA Langley Research Center, the University of Maryland and the National Institute of Aerospace for their continuing support in this research. Funding was supplied by NASA Langley Research Center.

Foreword

Before this journey I was very good with situations that are well thought out, achievable, and were therefore in my comfort zone. I liked to have a plan, follow it, make sure things work out, and have a backup. Taking on this challenging problem for my PhD, I had to let go of that in order to really learn, make strides, make new findings, and bring it all together at the end. Keep pushing out of your comfort zone, be fearless, work hard, never give up, live with integrity, and trust in God. During this journey I learned what it means to live this, which ultimately allowed me to succeed, and to grow professionally and personally. This became my new expanded comfort zone and I can't wait for future growth.

My PhD work looked like a three dimensional map of interconnected information in my mind. I am hoping to convey this information in a two dimensional and streamlined way in this document. God bless you and hope you enjoy reading my dissertation.

Dedication

“Always remember God loves you and helps you”

This work is dedicated to my lovely family and friends.

Acknowledgements

I would like to thank first and foremost my advisor and mentor Dr. James E. Hubbard Jr., and his unwavering support he offered me during this journey. I feel extremely blessed to have had such an incredible person become my mentor, advisor, role model, and inspiration.

Furthermore I would like to thank my family, especially my siblings Marlene, Christine, Barbara, and Josef who are my rocks. Their amazing and supportive presence in my life allowed me the freedom to pursue adventures such as this, and going to live in another continent in pursuit of my PhD in Aerospace engineering. Thank you for always being there for me and I feel very blessed to have you.

Thanks to all of my friends, some of who became my family during the past four years at NASA Langley and the National Institute of Aerospace and made my experience here a great one. I also like to especially thank my friends Rania, Christy, Paul, Jared, Max, Justin, Shane, Steven, and Ryan who helped me break through language challenges.

My team members and friends at the Morpheus Lab; Alex, Aimy, Ben, Goeff, Michael, Nelson, Jose, Jared and Zohaib, for your teamwork and support. Aimy, who was involved to save my live at one point. I am forever grateful to you.

My friends whom I have lost during this journey. Noah who taught me how to fly and Alex and Tyler who showed me how to love live every day. You are an inspiration.

I additionally wish to acknowledge University of Maryland, NASA Langley Research Center, and the National Institute of Aerospace for their continuing support in this research.

Last but not least I also would like to thank my Committee; Dr. James E. Hubbard Jr, Dr. Amr Baz, Dr. Alison Flatau, Dr. Sung Lee, and Dr. Norman Wereley for continuing advice and for supporting my professional growth.

I learned so incredibly much in the pursuit of excellence while working on my PhD and I am very grateful for all the people and opportunities who have come into my live during this journey.

Table of Contents

Chapter 1: Introduction	1
1.1 Motivation	1
1.2 Background Flapping Wing	1
1.2.1 Background Aerial Vehicles and Flapping Wing	1
1.3 Model of Ornithopter for Performance Optimization	6
1.3.1 Desired Improvements in Flight Platforms	7
1.3.2 Flapping Wing Flight Aerodynamics	10
1.4 Review Bio- Inspired Flapping Wing Flight and Robotics	20
1.5 Problem Introduction.....	27
1.5.1 Research Objectives	27
1.5.2 Classification of Flexible Multi-Body Systems	29
1.5.3 Flexible Multi-Body Dynamics Modeling	34
1.5.4 Suitable code and Software Background	36
1.5.5 Vehicle Dynamics Modeling of Ornithopter.....	42
1.5.6 Aeroelastic Analysis of Flapping Wing Vehicles	47
1.5.7 Related Avian Scale Aerodynamics and Models	50
Chapter 2: Modeling Methodology	62
Chapter 3: Bio- Inspired Research Platform	66
3.1 Research Platform Details	66
3.2 Experimental Data.....	73
3.2.1 Clamped Test Experiment - E1	74
3.2.2 System-ID Experiment - E1-I	80
3.2.3 Free Flight Experiment – E2	82
3.2.4 Vacuum Camber Experiment – E3.....	92
Chapter 4: Flexible Multi-Body Dynamics Model	94
4.1 Linear- Elastic Multibody Systems	96
4.1.1 Floating Frame of Reference Formulation (FFR)	103
4.2 Five Body Multi Body Dynamics Model.....	104
4.3 Coordinate Systems.....	106
4.4 Underlying Articulated Rigid Body Model.....	107
4.4.1 Kinematic Relations	110
4.5 Lagrange Formulation of Equations of Motion.....	113
4.5.1 Kinetic Energy.....	114
4.5.2 Potential Energy	115
4.5.3 Position Vector – Rigid Body Equations of Motion	118
4.5.4 Position Vector – Flexible Body Equations of Motion	120
4.5.5 Modal Superposition	122
4.6 Formulation of Five Body Flexible Multi Body Dynamics Model.....	123
4.6.1 Model Generalized Coordinate Vector	123
4.6.2 Position Vector.....	126
4.6.3 Velocity	129
4.6.4 Orientation.....	129
4.6.5 Angular Velocity	131

4.6.6	Inertia Invariants in Mass Matrix	133
4.6.7	Craig-Brampton Method	135
4.6.8	Modal Synthesis Method – Mode Shape Orthonormalization	139
4.7	Structural Dynamics Model of the Wings	141
4.7.1	Implementation - Mode Neutral File	145
	Chapter 5: Aerodynamics	146
5.1	Aerodynamic Model Versions	146
5.2	Aero- Model A	149
5.3	Aero- Model B/C	151
5.4	Aerodynamic Model Implementation	159
5.4.1	Distributed Aerodynamic Loads	165
5.5	Global Resulting Forces and Moments	167
5.5.1	Generalized Forces	168
5.5.2	Generalized Moments	171
5.5.3	Generalized Modal Force	172
	Chapter 6: Results	173
6.1	Modeling Assumptions Verification and Wing Flexibility	173
6.1.1	Coordinate Varriation	173
6.1.2	Large Global Deformations	178
6.1.3	Wing Fixed Reference Frames	179
6.1.4	Leading Edge Spar Flexibility	190
6.2	Model Results	194
6.3	Constraint Model Verification	196
6.3.1	Integrated Forces	196
6.3.2	Wing Tip Kinematics	198
6.4	Unconstraint Model Verification	201
6.4.1	Integrated Forces	201
6.4.2	Wing Inertia Forces	202
6.4.3	Inertia Invarriants	205
6.4.4	Aerodynamic Forces	207
	Chapter 7: Concluding Remarks	210
7.1	Summary of Work	210
7.2	Scope and Contributions	211
7.2.1	Vehicle Dynamics Model of Ornithopter	212
7.2.2	Aerodyamics Model and Aeroelasticity	214
7.2.3	Modeling Methodology	215
7.2.4	Understanding of flight Physics and Dynamics	216
7.3	Summary of Novel Contributions	217
7.4	Summary of Conclusions	218
7.5	Recommendations	220
	References	222

List of Tables

Table 1: <i>Properties of Natural Flyers in comparison to well-known aircraft</i>	21
Table 2: <i>FEM and MBD university codes and commercial packages</i>	37
Table 3: <i>Material and Dimensions of Ornithopter Structures</i>	70
Table 4: <i>Aircraft Specifications</i>	71
Table 5 <i>Material properties and dimensions of ornithopter structures used for the model [82]</i>	143
Table 6: <i>Aerodynamic Model Versions Overview</i>	147
Table 7: <i>Blade Element Selection ML101 Orntihopter Configuration</i>	158

List of Figures

Figure 1: <i>Flight Capability of Flapping Wing Flyers</i>	3
Figure 2: <i>Mission Applications for UAV vehicles, a) Military [11] b) Civilian [10]</i> ...	4
Figure 3: <i>Natural flyers demonstrate, glide, hover dive and perch</i>	5
Figure 4: <i>Bats exhibit adjustable stiffness across the wing [1]</i>	7
Figure 5: <i>Fuselage Body Accelerations in state of art flapping wing robotic</i>	9
Figure 6: <i>Position State Fuselage of Ornithopter Research Platform.</i>	10
Figure 7: <i>Lift and Thrust Generating Mechanisms of flapping wing flight a) down stroke b) upstroke [9]</i>	13
Figure 8: <i>Wing tip path as indicator or dominant wing motion shown on natural flyers a) albatross in fast forward flight mode, b) pigeon in slow flight mode, c) horseshoe bat in fast forward flight mode and d) horseshoe bat in slow flight mode [21]</i>	15
Figure 9: <i>Passive Wing Morphing a) Bio-inspired Research Platform Wing Morphing though thrust flap region b) Radical Shape Morphing wing [14]</i>	23
Figure 10: <i>Active Wing Morphing Bio- inspired Research Platform a) Ornithopter Platform b) Extended Half Wingspan vs. Retracted Half Wingspan [39]</i>	24
Figure 11: <i>First Ornithopter Vehicle designs a) DaVincis 1490 b) Lilienthal 1894 [19].</i>	25
Figure 12: <i>Com-Bat intended robotic spy plane 3 D image -University of Michigan 2008 [46]</i>	26
Figure 13: <i>Ornithopter Research Platform "Phoenix" - Massachusetts Institute of Technology 2010 [47]</i>	26
Figure 14: <i>MAV -University of Arizona's Ornithopter [48]</i>	26
Figure 15: <i>Brown University Robotic Bat Wing a) ABS 3 D Print b) Schematic [49]</i>	26
Figure 16: <i>"Robo Bat"s the skeleton of the robotic bat uses shape-memory metal alloy that is superelastic for joints [50]</i>	27
Figure 17: <i>Ornithopter Schematic: Rigid Multi-Body system</i>	30
Figure 18: <i>Ornithopter Schematic: Linear Elastic Multi-Body Systems</i>	31
Figure 19: <i>Ornithopter Schematic: Nonlinear Elastic Multi-Body Systems</i>	32
Figure 20: <i>SimXpert: Flexible -Multi Body Dynamics Model Implementation</i>	41
Figure 21: <i>SimXpert: Image of Fully Integrate Flexible Multi-Body Dynamics Model of Ornithopter</i>	42
Figure 22: <i>Ornithopter Vehicle Dynamics Models a) Single Rigid Body b) Rigid - Multi Body Dynamics and c) Flexible Multi-Body Dynamics Model</i>	43
Figure 23: <i>Quasi-Steady Blade Element Model [49]</i>	51
Figure 24: <i>CFD analysis showing a) Vorticity contours on the flexible deformed wing b) Deformed Grid at 50% span location during upstroke of the wing at start of upstroke [81]</i>	57
Figure 25: <i>Rigid-body ornithopter fit in flight test data for aerodynamic model structure determination [16].</i>	59
Figure 26: <i>Modeling Methodology: Workflow Stage 1</i>	62
Figure 27: <i>Modeling Methodology: Workflow Step 2</i>	63
Figure 28: <i>Modeling Methodology: Workflow Step 3</i>	64
Figure 29: <i>Modeling Methodology: Workflow Stage 4</i>	64

Figure 30: Modeling Methodology: <i>Workflow Stage 5</i>	64
Figure 31: Modeling Methodology: <i>Workflow Stage 6</i>	65
Figure 32: Modeling Methodology: <i>Workflow Stage 7</i>	65
Figure 33: <i>Primary Research Platform Morpheus Lab Custom-Build test Ornithopter (ML101)</i>	66
Figure 34: <i>Secondary Research Platform Modified Ornithopter Shawn Kinkade (MSK004)</i>	67
Figure 35: <i>Wing Structure Bio – inspired Ornithopter Research Platform (ML101)</i>	67
Figure 36: <i>Design Feature Wing Spars (ML101) a) Leading Edge Spar, b) Diagonal Spar c) Finger Spar (ML101)</i>	68
Figure 37: <i>Schematic and Nomenclature Stiffening Carbon Fiber Spar Configuration</i>	68
Figure 38: <i>A bat (Cynopterus brachyotis) in flight Photo from Kampang et. all 2007 (Wei Shyy, 2008)</i>	69
Figure 39: <i>Upper Wing surface of a Natural Avian Flyer Skua. Photo from Becert et al. 1997 indicating flap region in bird flight</i>	69
Figure 40: <i>Design Feature Tail (ML101)</i>	70
Figure 41: <i>Design Feature Fuselage (ML101)</i>	70
Figure 42: <i>Definition Flapping Angle (FA) and Upstroke and Downstroke on shoulder joint/ bar linkage (ML101)</i>	72
Figure 43: <i>Upstroke and Down stroke Sequence Orntihopter (ML101) scale; Image credit Harmon [19]</i>	73
Figure 44 <i>MSK004 wings with tracking markers [19]</i>	74
Figure 45: <i>MSK004 and Vicon camera system for the measurement of</i>	75
Figure 46: <i>Harmon Aerodynamic Model Results and Bench Test Results Measured Integrated forces ML 101 at 5 Hz Flapping frequency, over a flapping cycle t/T a) Vertical Propulsive Force VPF b) Horizontal Propulsive Force (HPF) c) Normalized Flapping angle FA</i>	76
Figure 47: <i>Harmon Bench Test Results Measured Integrated forces ML 101 at 5 Hz Flapping frequency, over a flapping cycle t/T a) Vertical Propulsive Force VPF b) Horizontal Propulsive Force vs. normalized flapping angle (FA)</i>	77
Figure 48: <i>Harmon Aerodynamic Model Results and Bench Test Results Measured Integrated forces ML 101 at 6.17Hz Flapping frequency, over a flapping cycle t/T a) Vertical Propulsive Force VPF b) Horizontal Propulsive Force (HPF) c) Normalized Flapping angle (FA)</i>	77
Figure 49: <i>Harmon Bench Test Results Measured Integrated forces ML 101 at 6.17 Hz Flapping frequency, over a flapping cycle t/T a) Vertical Propulsive Force VPF b) Horizontal Propulsive Force vs. normalized flapping angle (FA)</i>	78
Figure 50: <i>Results and Bench Test Results Measured Integrated forces ML 101 vs. flapping frequency, over a flapping cycle t/T a) Mean Absolute Value Vertical Propulsive Force VPF b) Horizontal Propulsive Force vs. Flapping angle [19]</i>	79
Figure 51: <i>Vicon Vision ® wing Kinematic sequence – 3 Position State Tracking Markers i=1 to 110 a) isometric view b) side view in a fuselage fixed Reference Frame CB0</i>	80
Figure 52: <i>Vicon ® camera system for the measurement</i>	81

Figure 53: <i>Aerodynamic forces on the wings –Results System ID Model by Grauer [9]</i>	82
Figure 54: <i>Asymmetric retro reflective markers on the wing (seen as white dots) and Wing tip Location (Marked in Red)</i>	84
Figure 55: <i>Retro reflective Marker position on the wing measured with Vicon Vision System Marers $i=1$ to 53. Markers $i=1$ to 5 were mounted on the fuselage.</i>	85
Figure 56: <i>Image SUAS Flight test facility - Vicon ®Vision System Cameras [14]</i> ...	85
Figure 57: <i>Test Set up Schematic – [Wissa et al., 2012] Test Chamber Dimensions: 70'(W) x 35'(D) x 35'(H) [14]</i>	85
Figure 58: <i>Schematic Ornithopter and Reference Frames used for the processing of free flight test data.</i>	87
Figure 59: <i>Data Set Marker Position during Free Flight in the inertia reference frame CI 0.</i>	88
Figure 60: <i>Data Set Marker Position $i=1$ to 53 during Free Flight in the inertia reference frame CI 0 – View ZI 0/ZI 0</i>	88
Figure 61: <i>Data Set Marker Position $i=1$ to 53 during Free Flight in the inertia reference frame CI 0 – View YI 0/XI 0</i>	89
Figure 62: <i>Position States all tracking markers on the wing/ Volume shows test data used for model development- 3.5 Flappingcycles.</i>	89
Figure 63: <i>Single position state on Ornithopter shows all tracking markers $i=1$ to 53 in the fuselage fixed reference frame CB0</i>	90
Figure 64: <i>Vertical Propulsive forces acting on the fuselage center of mass – Obtained from Experiment</i>	91
Figure 65: <i>Vacuum Chamber at NASA Langley Research Center. Left) Research Platform Mounted on 6-degrees of freedom Load Cell, Right) Vacuum Chamber</i>	92
Figure 66: <i>Results Vacuum Chamber test ML 101 Research Platform vs. flapping frequency a) Inertial Horizontal Propulsive Force IHPF b) Inertial Horizontal Propulsive Force c) Inertial Pitching Moment vs. Magnitude.</i>	93
Figure 67: <i>Schematic Five- Body Dynamics System</i>	105
Figure 68: <i>Schematic inertial and Fuselage Body fixed Reference Frames</i>	106
Figure 69: <i>Schematic Wing Fixed Reference Frames</i>	107
Figure 70: <i>Articulated Multi- Body System representation of the Ornithopter</i>	108
Figure 71: <i>Position Vector of Rigid Multi-Body Model of Ornithopter</i>	119
Figure 72: <i>Position Vector of Flexible Multi-Body Model of Ornithopter</i>	121
Figure 73: <i>Schematic notation Definition for generalized coordinates of the flexible multi-body system</i>	124
Figure 74: <i>Position Vector of Flexible Multi-Body Model of Ornithopter, luff region (blue and red), thrust flap region (orange and red)</i>	127
Figure 75: <i>Schematic FEM Wing Structure Carbon Fiber Spars and Wing</i>	143
Figure 76: <i>Thrust Flap Region Mesh Nodes=352, Elements=860</i>	144
Figure 77: <i>Thrust Flap Region Mode Shapes Couture Plot</i>	144
Figure 78: <i>Model Image Flexible Wing Component Connections</i>	145
Figure 79: <i>BE Grid Schematic Aero-Model A</i>	147
Figure 80: <i>BE Grid Schematic Aero-Model B</i>	147
Figure 81: <i>BE Grid Schematic Aero-Model C</i>	147

Figure 82: Variables for calculation of aerodynamic forces [73].	153
Figure 83: <i>ML101 Ornthopter Configuration Blade Element Selection</i>	157
Figure 84: <i>Blade Element Selection Trust Flap Region ML101 Ornthopter Configuration</i>	159
Figure 85: <i>Aerodynamic Loads Model – Workflow</i>	160
Figure 86: <i>Aerodynamic Loads Model – Workflow AEROIEC</i>	164
Figure 87: <i>Isometric View Position States Path all Vicon Markers over one Flapping Cycle at 6.06 Hz</i>	174
Figure 88: <i>Side View Position States Path all Vicon Markers over one Flapping Cycle at 6.06 Hz</i>	175
Figure 89: <i>Top View Position States Path all Vicon Markers over one Flapping Cycle at 6.06 Hz</i>	175
Figure 90: <i>Top View Ornithopter Markers Position State 0 Deflection Plane</i>	176
Figure 91: <i>Top View Y Coordinate Flexibility in the Wing Fixed Reference Plane CW</i>	177
Figure 92: <i>Top View X Coordinate Flexibility in the Wing Fixed Reference Plane CW</i>	178
Figure 93: <i>Bio-inspired ornithopter research platform in free flight: Three Experimental Orientations During a Wing Beat: Viewed in the fuselage Body Fixed Reference Frame CB0</i>	179
Figure 94: <i>Wing Fixed Reference Frame CW</i>	181
Figure 95: <i>Bio-inspired ornithopter research platform wing in free flight: Maximal elastic deflections of the wing in the wing fixed reference frame during a wing beat; Viewed in the fuselage fixed reference frame CB0.</i>	182
Figure 96: <i>Bio-inspired ornithopter research platform wing in free flight: Maximal occurring elastic deformation in the thrust flap region of the wing in the wing fixed reference frame CW</i>	182
Figure 97: <i>Bio-inspired ornithopter research platform ML 101 wing in free flight: Maximal occurring elastic deflections luff region in the wing fixed reference frame CW</i>	183
Figure 98: <i>Bio-inspired ornithopter research platform wing in free flight: Maximal occurring elastic deflections of the wing fixed reference frame during a wing beat; Vied in the fuselage reference frame CB0</i>	184
Figure 99: <i>Schematic location Trust flap region Reference frame</i>	185
Figure 100: <i>Bio-inspired ornithopter research platform wing in free flight: X- axis of modeled thrust flap region reference frame in 34 position states viewed in the fuselage fixed reference frame CB0.</i>	185
Figure 101: <i>Bio-inspired ornithopter research platform wing in free flight marker location: XBT- axis location on experimental research platform resulting in minimal deformation off a reference YBT/ZBT reference plane using a 1 degree of freedom flapping motion.</i>	186
Figure 102: <i>Flapping Angle Zeta and Beta location on shown in experimental wing test data (maximal deformation of CW, 0 reference plane and XBT Position states)</i>	187
Figure 103: <i>Modeled Flapping Angle Time History based on Flight test data vs. Flapping angle in flight test data E-2</i>	188

Figure 104: <i>Experimental Thrust Flap Reference motion in 34 position states in the fuselage fixed reference plane CB0 vs. wing at zero deformation (PS0)</i>	189
Figure 105: <i>Modeled thrust flap reference motion in 34 position states in the fuselage fixed reference plane CB0 vs. wing at zero deformation (PS0)</i>	190
Figure 106: <i>Experimental elastic deflections in the fuselage fixed reference frame CB0</i>	192
Figure 107: <i>Experimental elastic deformation in the wing fixed reference frame CW</i>	193
Figure 108: <i>Model Image SimXpert - ML101 5 body Flexible Multi Body Dynamics Model (Fuselage reference frame CB is highlighted)</i>	194
Figure 109: <i>Verification Bench Test – Model 3 A– Scale ML101 (6.17Hz)</i>	197
Figure 110: <i>Wing Tip Location – Viewed at one Experimental Position state</i>	199
Figure 111: <i>Results Wing Kinematics Model 5 - Experiment: Flight Test: a) Back View b) Side View</i>	200
Figure 112: <i>Vertical Propulsive forces acting on the fuselage center of mass – Obtained from Experiment (E-2)</i>	201
Figure 113: <i>Simulated Inertia forces on Fuselage Center of Mass CB in free flight (IVPF) – Upstroke – Down stroke transition</i>	203
Figure 114: <i>Results Inertia forces (E3) with error bars vs. simulation results with STD a) Inertial Horizontal Propulsive Force IHPF b) Inertial Horizontal Propulsive Force c) Inertial Pitching Moment vs. Magnitude</i>	204
Figure 115: <i>Results: Body force magnitude System ID Model (MSK 004 E1-I -.) [9] – Body force magnitude - Aero model C</i>	208

List of Nomenclature

Roman Symbols

a	Location of Airfoil Pitching Access form 0.5 cord Point
b	Blade Element
c	Reference Cord
dc	Blade Element Cord Length
dr	Blade Element with (span- direction)
f_n	Force Vector
f_g	Generalized gravitational force
f_e	Externally applied forces
f_v	Corriolis and centrifugal forces
f_c	Constraint forces
i	Number of bodies
u_B	Interface DOF
u_I	Interior DOF
k	Denotes Rigid Link
m	Number of Rigid Links
n	Number of Blade Elements
nm	Number of nodes a force is applied on Bodies III (L/R)
nl	Number of nodes a force is applied on Bodies II (L/R)

m_{pp}	Node's mass
\vec{p}_{BOA^n}	Position vector from the origin of the local body reference frame CBW (B0) of Bodies II (L/R) to the nodal point nl of force application.
$\vec{p}_{TA^{nm}}$	Position vector from the origin of the local body reference frames CBT (T) to the nodal point's nm of force application on Bodies III (L/R).
\mathbf{q}	Vector of modal coordinates
q^*	Orthogonalized Craig- Bampton modes
q_c	Modal coordinates of the constraint modes
q_N	Modal coordinates of the flexible-boundary modes
\mathbf{q}_i	Modal coordinates
q_f	Elastic coordinates can be introduced using component mode methods
\vec{r}_{B0P}	Position vector of the unreformed position of point P with respect to the local fuselage body reference frame of Body B0.
\vec{r}_{BB0}	Position vector from the fuselage fixed reference frame to CB to the fuselage fixed reference frame CB0.
\vec{r}_{IP}	Position vector origin of the inertial (ground) reference frame CI to the unreformed location of marker P on the rigid wing body.
\vec{r}_{IB}	Position vector from the origin of the inertial (ground) reference frame to the origin of the local fuselage body fixed reference frame CB.
$\vec{r}_{PP'}$	Translational deformation vector of Point P, the position vector from its undeformed to its deformed position P'.

\vec{r}_{B0TR}	Position vector from the fuselage fixed reference frame to B0 to the wing fixed reference frame TR
\vec{r}_{TRP}	Position vector, undeformed position of point P with respect to the wing fixed reference frame of the wing Body II
$s(t)$	Shape function
u_B	Interface DOF
u_I	Interior DOF
v_k	Linear velocity of center of mass of link k
$v(\xi_{IB(E)})$	Experimental free flight velocity of the vehicle fuselage fixed reference frame B in the inertia reference frame I
v_p	Undeformed location
x	Physical nodal DOF
x,y,z	Cartesian coordinates
x_k	Position coordinates of link k

Capital Roman Symbols

A	Transformation matrix form the local body reference frame of B0 (Fuselage Body Fixed) to the inertial reference frame.
C	Energy dissipation function
C_d	Drag coefficient

$C(\xi\dot{\xi})$	Coriolis and centrifugal forces in terms of the generalized coordinates
D_{camber}	Cord- wise force due to camber
D_{camber}	Cord- friction drag
F_L	Force vector
F_{horiz_nc}	Non-circulatory force horizontal component
F_{vert_nc}	Non-circulatory force vertical component
I	Inertia invariants
J	Jacobien matrix
K	Stiffness matrix
$K(\xi)$	The stiffness matrix in terms of the generalized coordinate
K_{tt}	Translational slice of the time varying stiffness matrix
K_{oo}	Rotational slice of the time varying stiffness matrix
K_{mm}	Modal Slice of the time varying stiffness matrix
K_{mt}	Modal and translational cross terms in the time varying stiffness matrix
K_{ot}	Rotational and translational cross terms in the time varying stiffness matrix
K_{mo}	Modal and rotational cross terms in the time varying stiffness matrix
\hat{K}	Generalized stiffness matrix
\hat{K}_{NN}	Diagonal stiffness associated with eigenvectors.
K_{ff}	Stiffness matrix due to elasticity

L	Marker L
L	Lagrange
M	Mass matrix
M_{ff}	Flexible slice of the time varying mass matrix
M_{rr}	Flexible slice of the time varying mass matrix
M_{fr}	Elastic and rigid cross terms in the time varying mass matrix
M_{rf}	Elastic and rigid cross terms in the time varying mass matrix
$M(\xi)$	Mass matrix of the generalized coordinate
M_{tt}	Translational slice of the time varying mass matrix
M_{oo}	Rotational slice of the time varying mass matrix
M_{mm}	Modal slice of the time varying mass matrix
M_{mt}	Modal and translational cross terms in the time varying mass matrix
M_{ot}	Rotational and translational cross terms in the time varying mass matrix
M_{mo}	Modal and rotational cross terms in the time varying mass matrix
\hat{M}_{NN}	Diagonal mass matrices associated with eigenvectors.
\hat{M}	Generalized mass matrix
ME_L	Moment vector
N	Number of modes
N	Normal Force dN

N_a	Non-circulatory force
$N(\xi)$	Constraint forces
N_{nc}	Non-circulatory force
N_c	Circulatory normal force
Q	Generalized forces
$Q(\xi)$	Generalized applied force projected to the generalized coordinate
Q_F	Generalized translational force
Q_{ME}	Generalized moments
Q_M	Generalized modal force
Q^I_F	For the total integrated forces in the inertia reference frame due to applied aerodynamics loads
Q^{CB}_{FIII}	Individual generalized translational force on bodies III a marker L/node nm
Q^{CB}_{FII}	Individual generalized translational force on bodies II on a marker L/node nl
Q^{CB}_{FI}	Generalized translational force on body I
R_k	Orientation coordinates of Link k
T	Kinetic Energy
T_s	Leading edge suction force
V	Potential Energy
$V_{0.25c}$	Velocity at the quarter cord location

V_x Is the flow speed tangential to the section.

Greek Symbols

α' Flow's relative angle of attack at the 0.75 chord location

α_0 Zero- lift angle of attack

β Flapping angle beta

$\ddot{\beta}$ Angular acceleration of the flapping wing

γ Flight path angle of flight velocity with respect to the ground

δ Angel between flapping axis and flight velocity

ε Vector of small angles

ζ Thrust flap angle zeta

ξ Generalized coordinates

ξ_I Generalized coordinated of the fuselage body I

$\xi_{II(L/R)}$ Generalized coordinated of the flexible luff region wing bodies II (R/L)

$\xi_{III(L/R)}$ Generalized coordinated of the flexible luff region wing bodies III (R/L)

$\xi_{IB(E)}$ Experimental generalized coordinates of the fuselage in the inertia reference frame

$\xi_{BBW(E)}$ Experimental generalized coordinates of the wing bodies in the inertia reference frame in the wing region

$\xi_{BWTW(E)}$ Experimental generalized coordinates of the wing bodies in the inertia

	reference frame in the Thrust flap region
ξ^i	Generalized coordinate of the flexible body i
ξ_r	Generalized coordinate of a rigid body
η_s	Leading-edge suction efficiency
θ	Pitch angle of blade element with respect to flapping axis
$\dot{\theta}$	Pitching velocity of wing section
$\bar{\theta}$	Total mean pitch angle
λ	Lagrange multipliers
ϕ	Shape vectors (or mode shapes)
$\psi, \theta, \phi.$	Euler angles
$\omega_k,$	Angular velocity of center of mass of the rigid link k
$\omega_{p(k)}$	Angular velocity of the parent link
Φ_p	is the slice from the modal matrix that corresponds to the translational DOF of node P
Φ_p^*	Size of the modal matrix that corresponds to the rotational degrees of freedom (DOF) of the node
Φ_p	Participation in the component modes
Φ_{IC}	Physical displacements of the interior DOF
Φ_{IN}	Physical displacements of the interior DOF in the normal modes
Ψ	Algebraic constraint Equation

Superscripts and Subscripts

B	Boundary DOF
C	Constraint DOF
I	Internal DOF
N	Normal DOF
f	Elastic coordinates
m	Modal degrees of freedom
nc	Circulatory force
r	Reference coordinates
o	Rotational degrees of freedom
t	Translational degrees of freedom

Acronyms

AEOI	Aeroelastic Open Interface
AFRL	Air Force Research Lab's
ANCF	Absolute Nodal Coordinate Formulation
AOA	Angle of Attack
BE	Blade Element
BEM	Boundary Element Method

CAD	Computer Aided Design
CFD	Computational Fluid Dynamics
DAE	Differential and Algebraic Equations
DOF	Degrees of Freedom
E1	Experiment 1
E1-I	Experiment 1 – Inertial
E2	Experiment 2
E3	Experiment 3
EMBS	Elastic Multi Body System
FE	Finite Elements
FEM	Finite Element Method
FEIM	Finite Element Incremental Method
FFR	Floating Frame of Reference Formulation
FSI	Fluid Structure interaction
FMBD	Flexible Multi-Body Dynamics
FMBSDA	Flexible Multi-Body Structural-Dynamic Model considering Aero elasticity
FSM	Finite Segment Method
GUI	Graphical User Interface
HF	Horizontal Force
HIF	Horizontal Inertia Force
HPF	Horizontal Propulsive Force

LEV	Leading Edge Vortices
LMBS	Linear Multi Body System
LRVF	Large Rotation Vector Formulations
LTED	Linear Theory of Elastodynamics
LTI	Linear Time Invariant
NLTP	Non-linear time periodic
MAV	Micro- Aerial Vehicles
MBD	Multi- Body Dynamics
MP	Multi- Physics
ODE	Ordinary Differential Equations
PDE	Partial Differential Equations
RMBD	Rigid Multi-Body Dynamics
SUAV	Small Unmanned Aerial Vehicles
TVL	Time Variant Loads
TVSD	Time – Variant and Spatially Distributed
TiV	Tip Vortices
VF	Vertical Force
VLM	Vortex Lattice Methods
VIF	Vertical Inertia Force
VPF	Vertical Propulsive Force
WPAFB	Wright Patterson Air Force Base

Chapter 1: Introduction

1.1 Motivation

Flapping-wing aerial vehicles, have the potential to be utilized for search and rescue missions, environmental surveillance and to aid first responders. The research presented here leads to a flexible multi-body dynamic representation of a flapping wing ornithopter considering aeroelasticity. This effort aims to bring advances in the understanding of flapping wing flight physics and dynamics that ultimately leads to an improvement in the performance of such flight vehicles, and thus reaching their high performance potential. To accomplish this for the complex problem of improving ornithopter flight dynamics, a novel approach to flexible multi-body dynamics and aero-elasticity modeling is developed in conjunction with experimental data. Principles of flapping wing flight strategies, and the simulation method developed here may also be employed in the future to enhance the performance of other aircraft to lower energy consumption and lead to more eco-friendly flight.

1.2 Background Flapping Wing

1.2.1 Background Aerial Vehicles and Flapping Wing

Small insect scale flyers, or micro-aerial vehicles (MAVs), as well as small unmanned aerial vehicles (SUAVs) avian scale flyers have generated a large interest in the recent years due to their variety of potential applications in the civilian and military sector. [1][2]. Research and development efforts of flapping wing flight has

mainly focused on the MAVs scale due to the advantageous aerodynamic efficiency associated with flapping wing vehicles operating in this flight regime [3] [4] [5]. Simple wing gates as well as the dual flight configurations of hover and straight and level flight, dominate the regime for flapping wing MAVs. Flapping wing flight on the avian scale is not entirely understood and has great performance potential due to its multi-flight configuration capability. MAV's wing gates, and associated kinematics are complicated and occur in a transition Reynolds number flight regime. Here the aerodynamic advantages associated with flapping wings can be utilized as well as to allow for also for efficient gliding flight. The associated wing gates (wing motion profiles), aerodynamics and dynamics are not entirely understood yet [6].

Small un-manned aerial vehicles (SUAVs) lie on the opposite end of the flight spectrum from the conventional systems currently in use today. Flapping-wing aerial vehicles fall in the category of SUAVs. These vehicles combine the ability to hover like rotary-wing aircraft as demonstrated by AeroVironment's hummingbird, while also allowing for gliding flight, much like fixed-wing aircraft [7].

Within the domain of SUAVs, the aerodynamics associated with flapping wing platforms show optimal properties, which can be characterized by: small vehicle size and low Reynolds number flight [8] [6]. Flapping wing flight vehicles have the capability to combine the three sides of the performance triangle: 1) ideal aerodynamic performance at a low Reynolds Number flight regime, 2) agility, and maneuverability and 3) mission adaptability in one vehicle, as illustrated in **Figure 1** below. Therefore they fill a niche in the design space of SUAV's [9].

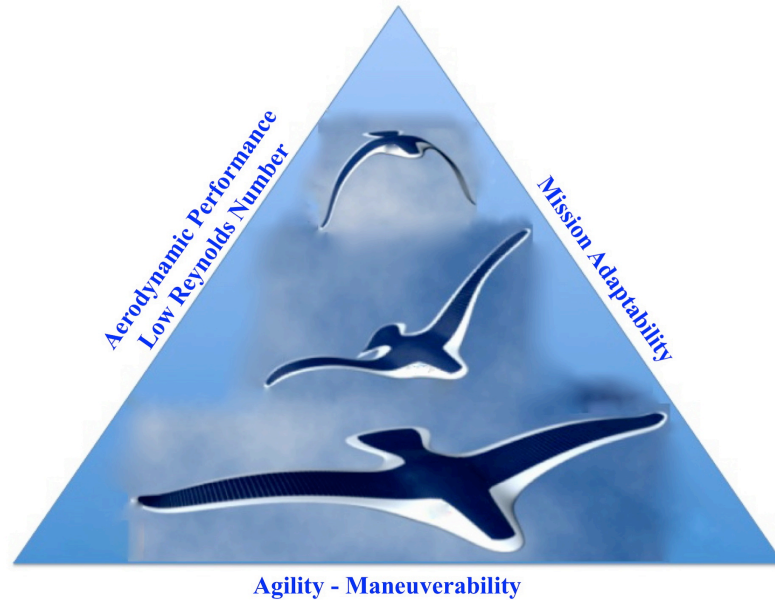


Figure 1: *Flight Capability of Flapping Wing Flyers*

Flapping wing vehicles have the ability to dive and perch, are highly maneuverable and agile, and have improved safety and reduced noise emissions when compared to rotary-wing vehicles. Flapping wing vehicles additionally have visual properties, which make them also ideal for contextual camouflage. These qualities and flight dynamics make them suitable, sustainable and ideal for a variety of civilian and military mission profiles. These vehicles also have the capability of performing specialized tasks like gathering environmental information, atmospheric data collection, aerial surveillance, homeland security, and supply, search, and rescue missions. In addition they can aid policemen and firefighters in the future in order to perform dull, dirty and dangerous jobs and act as supporting team members for surveillance tasks.



Figure 2: *Mission Applications for UAV vehicles, a) Military [11] b) Civilian [10]*

The flapping-wing flight strategy for lift and thrust generation is the key enabling technology in the varied multi-mission capability of SUAV ornithopters. In fact, at relatively light wing loadings, research shows that flapping wing SUAVs are more aerodynamically efficient than conventional fixed-wing or rotary-wing vehicles [4] [5]. As the vehicle size decreases, viscous effects become more pronounced and fixed-wing vehicles suffer from decreased lift to drag ratios and decreased flight performance [4] [3]. For rotary-wing aircraft, viscous effects reduce the aerodynamic efficiency of the vehicle [3]. Research by Wang et al. shows that when optimal wing motions are applied in low Reynolds number flight, flapping wing technologies can save up to 27% of the aerodynamic power required by fixed and rotary wing vehicles. This means that the aerodynamic power needed to support a specified weight is lower when using optimal flapping wing motions [8]. In the design space of SUAVs, simple one flight mode mission profiles can be in the satisfied with either rotary-wing or fixed-wing vehicles, but novel vehicle designs are needed that can fly in an agile manner in obstacle-filled and complex environments as well as efficient in straight and level flight [9].

Mechanical flapping wing aerial flyers show varying degrees of abilities in terms of accomplished flight performance [12] [13] [2]. The University of Maryland's Morpheus Lab ornithopters are among the most successful flapping-wing research flight platforms [14] [15] [16]. However, mimicking the flight of natural flyers is still a significant challenge for flapping-wing researchers due to the lack of a full understanding of the complex, non-linear and time varying dynamics involved [9]. The maneuverability agility, and duration of flight, when exploiting atmospheric thermals and natural wing gate dynamics are still not achieved in mechanical flyers. Desired capabilities are glide, hover, dive and perch capabilities such as those exhibited by birds. Figure 3 shows maneuverability performance.

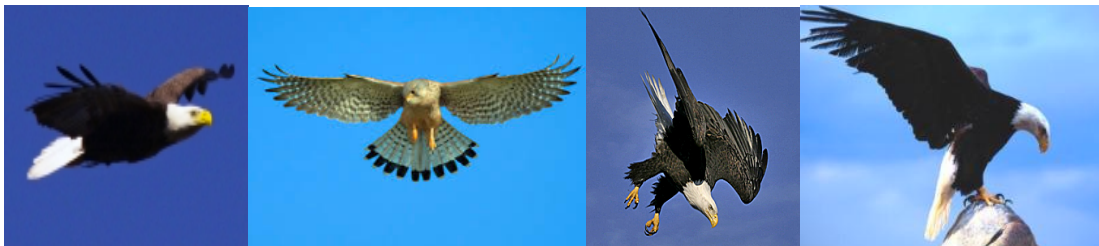


Figure 3 a): *Natural flyers demonstrate, glide, hover, dive and perch*



Figure 3 b): *Example maneuverability performance natural flyers*

1.3 Model of Ornithopter for Performance Optimization

In order to reach the performance capabilities of natural flyers a flexible- multi body dynamics model of an ornithopter considering aero-elasticity is developed in this research. The focus in the modeling effort is on the capability of improvement of flight characteristics in straight and level flight. Using this model it is desirable to reduce body accelerations and forces of an ornithopter vehicle, as well as to improve the aerodynamic performance, and enhance flight kinematics and forces which are the design optimization objectives. Achieving these objectives will result in the establishment of new requirements and model capabilities.

The primary influence factors identified in the open literature and empirical observations that influence these performance objectives and their improvements, as according to defined later in this chapter, are the wing geometry, wing configuration, the wing motion profile and the wing flexibility [2] [6] [8][17] [18].

Flapping wings with suitable wing kinematics, wing shapes, and flexible structures can enhance lift as well as thrust by exploiting large-scale vortical flow structures under various conditions [6].

The relevant model input variables are illustrated in **Figure 4** below on the anatomy of a bat, which accentuates mentioned influence parameters in natural flapping wing flyer.

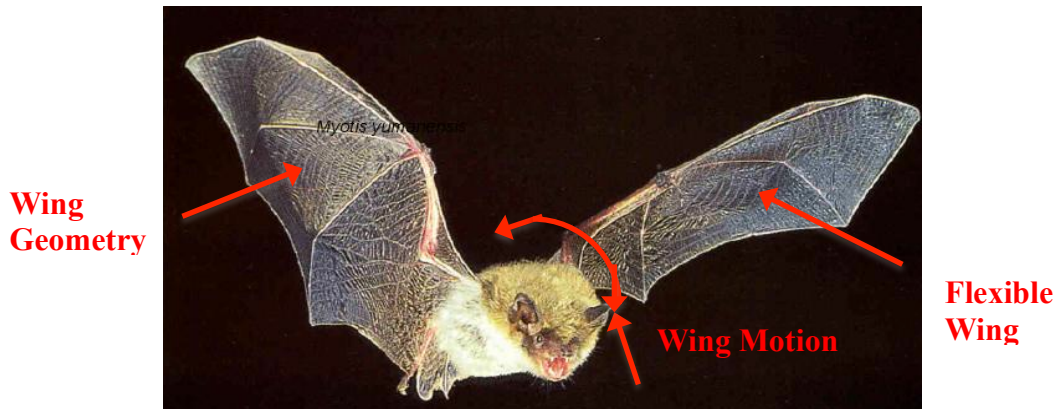


Figure 4: *Bats exhibit adjustable stiffness across the wing [1]*

In summary, wing geometry, wing motion profile and wing flexibility are variable and become input parameters in the model in order to be used to optimize performance of these vehicles in straight and level flight. These parameters are discussed in the context of aerodynamics of flapping wing and Bio-inspired flapping wing flight in this section. Desired improvements in dynamic characteristics of flapping wing flight vehicles are evaluated first followed by a brief explanation of aerodynamic mechanisms of flapping wing flight.

1.3.1 Desired Improvements in Flight Platforms

It is of interest to smooth the vehicle body dynamics, i.e. reduce the pitch and heave motions, reduce associated forces in vehicle platforms and improve the aerodynamic efficiency.

It is also desired to reduce body forces and accelerations in ornithopters, in order to build lighter vehicle platforms and improve imaging capabilities. In current state of the art ornithopter platforms, body accelerations up to 4 g's are found during straight

and level flight. **Figure 5** shows body accelerations on a state of art experimental ornithopter. Most desired mission scenarios for ornithopter platforms include aerial surveillance. An enhanced imaging capability can be achieved by reducing the body accelerations and forces. Here lighter, less robust camera systems will be feasible, lesser post processing, and reduced on board imaging post-processing equipment is required. Currently this is achieved through robust and highly specialized systems. With an improvement of body forces and accelerations payload can also be more fragile. State of art ornithopter flight platforms require customized and robust onboard avionics [16]. With the improvement of body dynamics, lighter and less robust and customized onboard avionics can be used, and can lead to a desired reduction in vehicle weight. This in turn leads to an improvement of range and endurance or an increase in payload capabilities. In summary, this will allow less customized on board cameras, processing, vehicle control and avionics packages can be used for vehicle designs. These factors ultimately drive the cost down and makes flapping wing feasible for commercialization.

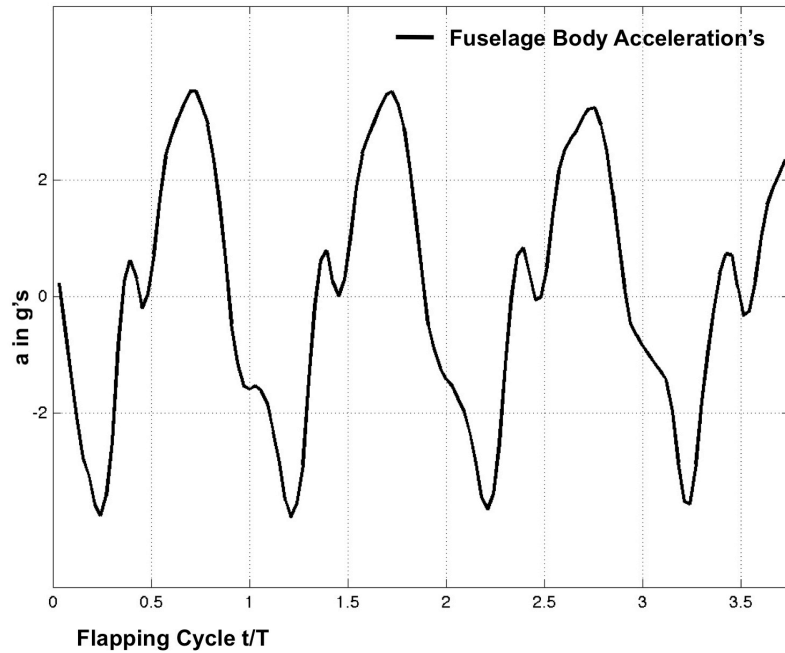


Figure 5: *Fuselage Body Accelerations in state of art flapping wing robotic*

It is also desired to reduce the oscillations on the fuselage kinematics i.e one can observe an oscillation in position state of the fuselage of a state of art ornithopter platform in **Figure 6**. This is associated with the reduction of variations in the lift and thrust profile which is consequently desired.

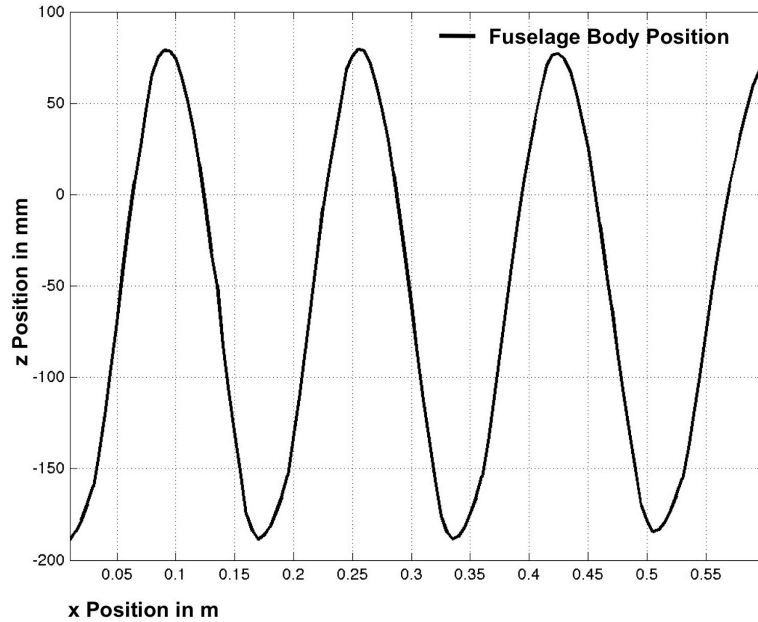


Figure 6: *Position State Fuselage of Ornithopter Research Platform.*

Natural flyers exhibit reduced variations in their lift and thrust profile as compared to vehicle platforms. A reduction in such variations lead to better contextual camouflage as well as to improved dynamics and consequently simplified flight control algorithms. It is also of interest to increase the aerodynamic efficiency of the flight vehicles and therefore improve the specific power required to generate lift and thrust. Significant characteristics that influence aerodynamic performance and basic aerodynamics in straight and level flight are discussed next.

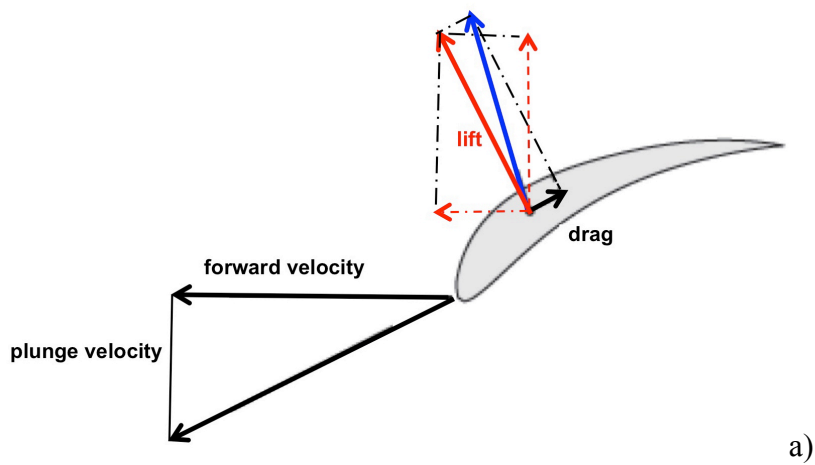
1.3.2 Flapping Wing Flight Aerodynamics

The aerodynamics of flapping wing flight is governed by steady and unsteady lift and thrust generating mechanisms [19]. The unsteady effects and circulatory forces that influence the flow structure for flapping wing flight are largely responsible

for aerodynamic force generation. Unsteady flow mechanisms and their contribution in the flapping wing flight performance is not entirely understood [18] [19] [20]. Basic effects to form advantageous flow structures, their interactions, and related open issues on a 2 dimensional and 3 Dimensional wing as well as a membrane wing structure are discussed. Basic effects like apparent mass effects, induced flows, wake capture and dynamics stall contribute to the flight dynamics of avian scale flapping wing flyers. Flow structures like the leading edge vortices (LEV) and Tip Vortices (TiV) behaviour influence these effects. Vortex behaviour is largely guided by wing kinematics, and wing design which are variable in ornithopter model for its design optimization. In order to categorize influence magnitude of mechanisms forming the aerodynamic flow structure in flapping wing flight the Reynolds number is suited to be used as similarity parameter. Reynolds number dimension for example changes the LEV formation and among other characteristics accounts indirectly for wing size and flapping frequency which is significant for this work. In flapping flight tip vortices (TiVs) can interact with the leading edge vortex (LEV) to enhance lift without increasing the power requirements [6] [21]. It is established that a change in Reynolds number for example caused by wing sizing, and flapping frequency leads to a change in the leading edge vortex (LEV). Spanwise flow structure is also influenced by the change of the Reynolds number. LEV, TiVs and the spanwise flow structure impact the aerodynamic force generation [6] [21]. In flapping wing flight unsteady effects such as the TiVs and LEV interaction can be exploited to improve the specific lift, while in a classical steady aerodynamics TiVs take away from the energy required for lift production [6]. More details about flapping wing flight effects can

also be found in References [18][19] [22] [23] which provide a comprehensive review.

The general aerodynamic force generation of flapping wing flight through wing beating is illustrated on a airfoil in **Figure 7** below and described next. In principle a horizontal propulsive force is achieved through a forward pointing force vector during a negative angle of attack while in the downstroke (**Figure 7 a**)). During the upstroke of the wing the generated force vector points backwards in the opposite direction of the desired flight velocity (**Figure 1b**)) and produces a negative thrust component at the positive angle of attack. It is apparent that the time history of the wing motion, and hence kinematics, play an important role to achieve a positive average horizontal propulsive force during a wing beat for forward flight.



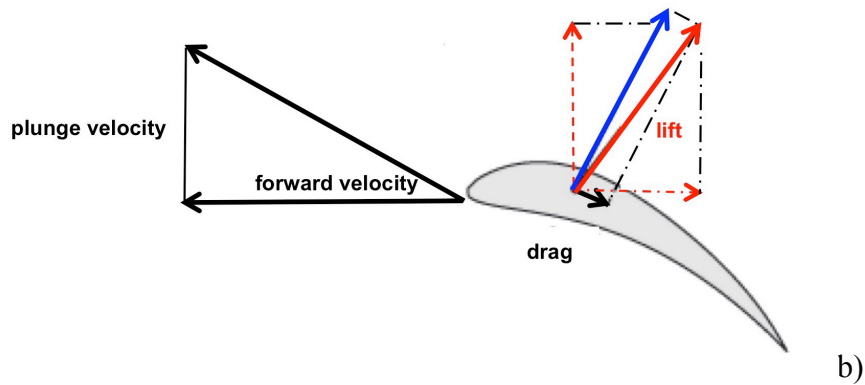


Figure 7: *Lift and Thrust Generating Mechanisms of flapping wing flight a) down stroke b) upstroke [9]*

For a fixed airfoil shape (2 dimensional flapping and plunging) according to Figure 7 the aerodynamic force generation depends on time history of angle of attack (AOA) during a wing beat, and on the shape of the airfoil similar to classical stationary wing theories. For a membrane like wing structure the magnitude and orientation of the lift, thrust force and drag component at an instance of time depend on the form of the camber and the angle of attack. During a flapping cycle camber forming as well as the time history of AOA during a wing beat, play an important role for the resulting flow structure and therefore aerodynamic force generation. The two time variant geometrical properties (camber form, AOA) indicate the many possible performance combinations employed in a flexible wing structure.

The possibilities of combinations for aerodynamic force generating effects are further increased when extending to a three dimensional wing. Here the shape can also differ in the span wise direction and generates new time variant lifting and control surfaces. Span-wise flexibility in forward flight creates a varied shape along the wingspan resulting in varied phase shift and effective angle of attack distribution from the wing

root to the wing tip [6]. Such a flapping wing design can also include passive or active joint motions in its 3 D wing topology, hence the aerodynamic performance possibilities are even further extended.

In summary, the basic aerodynamics mechanisms of flapping wing flight have been discussed in this section considering bio-inspired flapping wing flight.

1.3.2.1 Motion Profile and Wing Gates

Inherent lift and thrust depend on the geometrical properties and kinematics of the flapping wing. These are primarily governed by wing flexibility and therefore elastic structural properties of the wing as well as wing motion profiles and the wing shape. Flexibility and motion profiles determine the camber forming occurring during a wing stroke and the cord and span wise geometrical properties of the lifting surface during a wing stroke. Wing motions are the primary driver of the resulting unsteady aerodynamics associated with flapping wing flight [6].

Flapping wing kinematics fall into the category of Bio kinetics of flying and swimming. [18]. For example certain fish also operate in a comparable Reynolds number regime and similarly exhibits unsteady motion. A constant or a small variation in thrust profile is accomplished with the unsteady motion i.e. one doesn't see the fish speed up and slow down due to its body motion but rather swim at constant speed. This same effect is desired in flapping wing vehicles and reduces oscillations in the lift and thrust profile as well as pitch and heave motion.

Successful flyers exhibit wing motion profiles or so-called wing gates. During such gaits, the wing tip path serves as an indicator of the dominant wing displacements and determines wing gates in the field of flapping wing research. Different kinds of wing motions are found in different species as well as during different flight modes such as hover, straight and level flight, take off and landing [19]. Wing tip paths exhibited by natural flyers during one wing beat in straight and level flight can be observed in **Figure 8** below and are highlighted in red.

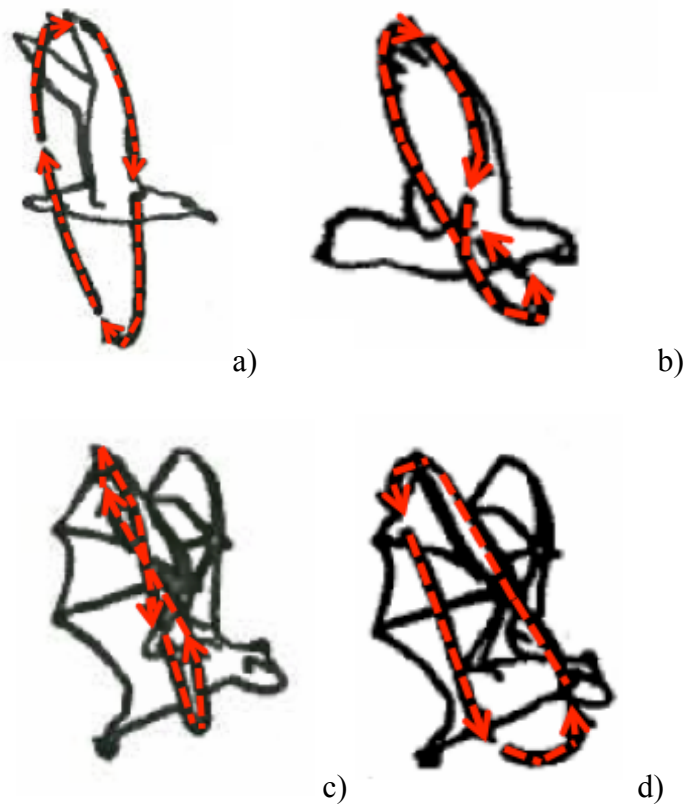


Figure 8: *Wing tip path as indicator or dominant wing motion shown on natural flyers a) albatross in fast forward flight mode, b) pigeon in slow flight mode, c) horseshoe bat in fast forward flight mode and d) horseshoe bat in slow flight mode [21]*

The velocity and accelerations needed to follow these trajectories as well as the wing path it self, are crucial parameters in the aerodynamic performance of flapping wing flyers. Knowledge of such optimal velocities and accelerations are desired for flapping wing vehicle platforms in order to improve aerodynamic efficiency for the flight mode. Further details about wing gates can be found in reference [18] and [19].

Based on Wang's research on two dimensional flapping motion, it is expected that performing various non-sinusoidal wing motion profiles will lead to an enhanced duration of flight through a lower power requirement for lift and thrust production [8].

A variable wing motion capability needs to be included in the modeling and simulation of such platforms in order to enhance their performance in straight and level flight. From this research, the resulting design model is capable of varying flapping motion profiles and within its assumptions can predict the resulting aerodynamic force generation on the wing. In return the model developed herein can be employed for an optimization of aerodynamic efficiency of the overall three dimensional wing by varying the actuating wing kinematics.

1.3.2.2 Wing Flexibility

It is widely understood that natural flyers like insect's birds and bats have flexible wings to adapt to the surrounding flow environment [21]. Natural flyers, like bats for example, have deforming bones and anisotropic wing membranes, which

have substantial variations of (adjustable) stiffness across the wings **Figure 4** [2] [17] [24]. Also it has been shown that the flexible wing has a higher thrust-to power ratio than its rigid counterpart [6]. Previously, Gopalakrishanan has analyzed the effects of elastic cambering of a rectangular membrane wing on the aerodynamics of flapping wing vehicles in forward flight [25]. Different membrane pre-stresses were investigated to give a desired camber in response to the aerodynamic loading. Results showed that the camber introduced by the wing flexibility increased the thrust and lift production considerably. The results show that the membrane wing outperforms the rigid wing in terms of lift, thrust and propulsive efficiency for various wing stiffnesses [25]. The primary reason for the increase in force production is attributed to the gliding of the LEV along the camber, which results in a high-pressure difference across the wing surface. Analysis of the flow structures revealed that, for flexible wings, the LEV stayed attached on the top wing surface and covered a major area of the wing, which resulted in high force production. On the other hand, the LEV lifted off from the surface of the rigid wing resulting in low force production. In addition, high stiffness in the span wise direction and low stiffness in the chord wise direction resulted in a uniform camber and high lift and thrust production. A flexible wing membrane also stalls at significantly higher angles of attack compared to a rigid configuration. This has been established for MAV's at very low Reynolds number and was conclusive for a non-flapping wing configuration [26]. Results are thought of to translate to flapping wing where a need of research is identified. Low aspect ratio rigid wings have lower lift curve slopes when achieving the same stall angle of the flexible wing [27]. Flexible properties of the wing can be used for flight quality

improvement and can effectively maintain desirable lift characteristics while having improved stall margins [21] [28]. Wing flexing due to flexibility is significant for its shape manipulation and reconfiguration, and therefore aid maneuvering and improve agility. Flexible wings form out control surfaces and can be used to enhance stability and control [26]. Garzia et al. developed a flapping wing MAV which improved agility performance due to its wing flexibility [29]. In regards to aero elasticity, chord wise flexibility in the forward flight can substantially adjust the projected area normal to the flight trajectory via shape deformation, and therefore redistributes lift and thrust [6]. In summary the wing flexibility is a significant property that influences the aerodynamic force generation and therefore the performance of ornithopter, and hence has to be included in the model capability. The model developed herein enables an enhancement of the understanding of the influence of variable wing stiffness on the performance.

1.3.2.3 Wing Geometry

The following section reviews the influence and implications of wing geometry in the straight- and level-flight aerodynamic performance of an ornithopter. A numerical investigation by Lentink and Gerritsma concluded that the thin airfoil with aft camber outperformed other airfoils including the more conventional airfoil shapes with thick and blunt leading edges [6] [30]. Flow was computed around plunging airfoils at Re of order 10^2 [6] [30]. Research by Usherwood and Ellington concluded a minor influence of aspect ratio at angles of attack below 50. They performed an experimental investigation using an experimental Hawkmoth. Research

platform had adjusted aspect ratios ranging from 4.53 to 15.84, with corresponding Re of 1.1×10^3 – 2.6×10^4 [6][31]. Green and Smith investigated 3-D effects using PIV measurements and unsteady pressure distributions on a pitching flat plate in forward flight, at a Reynolds number between 3.5×10^3 and 4.3×10^4 and aspect ratios of 0.54 and 2.25. They showed that 3-D effects increased with decreasing aspect ratio, or with increasing pitching amplitude [32]. An in-viscid model by Athshuler showed that the aspect ratio for hovering flapping wing vehicles is more significant. An increased aspect ratio, hence increased wing length and wing area, enhances the lift. [33] [34]. Altshuler et al. also showed for straight and level performance that lift tends to increase, and lift to drag ratios improve, as wing models approach natural configurations in terms of leading edge sharpness and having a substantial camber. The effect of wing shape was experimentally tested at Reynolds numbers revolving between 5×10^3 - 2×10^4 [6] [33]. The airfoil shape effect at comparing the flow field around a pitching and plunging airfoil (SD7003) to a flat plate was investigated by Kang et al. in forward flight. They used CFD and PIV measurements in order to investigate the formation of the flow structure around the wing shapes. It was shown that the sharp leading edge of the flat plate lead to a flow separation at all phases of motion because the flow was not able to turn around as on the airfoil structure with the blunter leading edge. The flow separation induces larger vertical flow structures on the suction side of the flat plate, leading to coverage of an increased area of lower pressure distribution there. The vertical flow structures are responsible for an increased lift generation on the flat plate compared to the SD7003 airfoil shape [6] [35]. The implications of this research include the capability of using a variation in

wing geometry in order to enhance forward flight aerodynamic performance, and the possibility that advantageous aerodynamic effects could be developed using a variety of wing shapes. Baseline models include an aft camber, and a thin airfoil structure and sharp leading edge spar, with both being viewed as advantageous for rigid flapping wings. A camber forming flexibility on the wing was used, which could be varied in order to obtain a rigid wing configuration, is used in the model developed here.

This concludes a review of the influence factors in achieving desired straight and level flight performance optimization of ornithopters. Aerodynamic mechanisms of flapping wing flight have been discussed in terms of input variables in the model. In the next section the state of art and scaling variance of Bio-inspired flapping wing robotics is discussed.

1.4 Review Bio- Inspired Flapping Wing Flight and Robotics

In principle it can be observed that smaller natural flapping wing flyers fly with a high flapping frequency at very low Reynolds numbers as compared to larger scale natural flapping wing flyers, which fly by gliding, and with a low flapping frequency at a higher Reynolds Number [18]. Larger scale avian flyers like albatrosses achieve range through soaring, where the wings are locked in place, which is interrupted by flapping motions. Biological studies of phylogenetically similar species suggest, based on weight and lower and higher flapping frequencies, a body mass of 41 kg and a 5.1 m wingspan is the largest scale for efficient flapping wing flight. Larger scale

dinosaurs, for instance, giant pterosaurs such as Pteranodon (16.6 kg, 6.95-m wingspan), Quetzalcoatlus (70 kg, 10.4-m wingspan) and Quetzalcoatlus (with a mass estimate from 85 to 250 kg) are believed to have conducted soaring flight [36]. Avian flyers encompass a transition region in the Reynolds number flight regime, where modeling efforts are challenging and results are often inaccurate. The role of the unsteady motion in the flow and its contribution to the aerodynamics is not fully answered by previous research studies and depends heavily on the scale of the flapping wing flyer [20]. Aerodynamic research efforts on flapping wings, which have been focused on insect flyers, are not necessarily able to be translated to avian scale flyers. Shyy states that a variation of the Reynolds number (wing sizing, flapping frequency, etc.) leads to a change in the leading edge vortex (LEV) and span wise flow structures, which impacts the aerodynamic force generation. The scaling invariance of both fluid dynamics and structural dynamics as the size changes is fundamentally difficult [6]. **Table 1** shows that the difference in the Reynolds number flight regime i.e between a fruit fly, a pigeon, and results in a comparable scaling invariance. The table provides an overview of flapping frequencies and Reynolds numbers of natural flyers.

Table 1: Properties of Natural Flyers in comparison to well-known aircraft

Species / Vehicle	Mass, m in kg	Wingspan b_w , m	Beating Frequency f, Hz	Reynolds Number flight Regime Re
Chalcid wasp (Encarsia Formosa)	2.5×10^{-8}		370	2×10^1

[18]

Fruit fly (<i>Drosophila virillis</i>) [18]	2×10^{-6}		240	2×10^2
Hummingbird (<i>Patagona gigasis</i>) [18]	2×10^{-2}	0.09	15	1.5×10^4
European Starling [20]	0.078	38.2	13.2	4.8×10^4
Bat (<i>Cynopterus brachyotis</i>)				
Pigeon [18]	3.5×10^{-1}		6	2×10^5
Soaring Seabirds i.e. Albatross [36]	12	3	3.7-7	
Avian Scale Research Platform	0.42-0.45	1.2 -1.2	4 – 7	1.9×10^4 - 2.3×10^5 [37]
Stork	3.5		2	4×10^5

Next features of bio- inspired avian scale vehicle platform are compared to natural flyers to further the understanding of inherent mechanisms in flapping wing aerodynamics. Aerodynamic features on birds and bats offer shape adaption to adjust the aerodynamic control surfaces [22]. Birds have feathers, which are flexible, layered, and often connected to each other [22]. Bats have more than 24 independently-controlled joints in the wing that enable them to fly in both positive or negative Angle of Attack AoA [22] [38]. This creates a complex 3-D wing topology.

birds and bats morph their wing-spans and change their spans to decrease and increase the wing area [22]. This speeds up the forward velocity, or reduces the drag during an upstroke [22]. In both bats and birds, a slight decrease of the surface area during the upstroke occurs in fast forward flight, while in intermediate flight speed, the surface area reduction during the upstroke becomes more pronounced. This effect is also desired in mechanical flapping wing platforms and can be achieved due to passive or active wing morphing, according to University of Maryland “Morpheus Lab” Flight Platforms (Figure 10 and Figure 9). These Figures shows a passive morphing flapping wing. Passive morphing is achieved though a flexible wrist joint and a thrust flap for radical shape morphing, or through a rigid leading edge spar with a thrust flap for a less radical shape change during flapping.

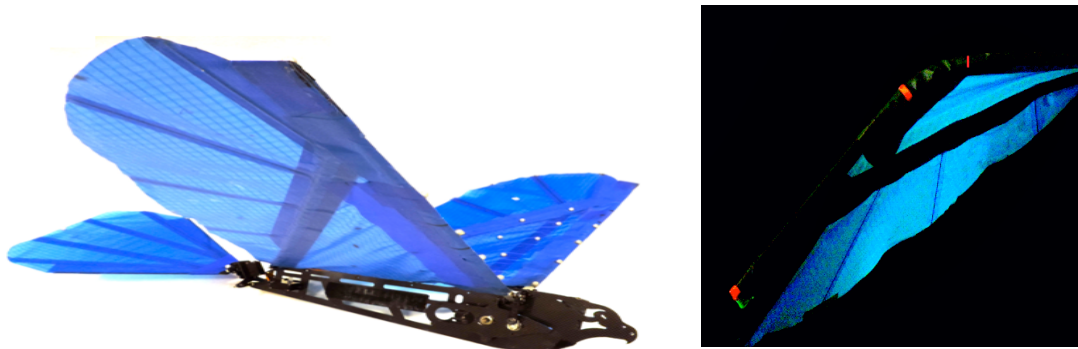


Figure 9: *Passive Wing Morphing a) Bio-inspired Research Platform Wing Morphing through thrust flap region b) Radical Shape Morphing wing [14]*



Figure 10: *Active Wing Morphing Bio- inspired Research Platform a) Ornithopter Platform
b) Extended Half Wingspan vs. Retracted Half Wingspan [39]*

Birds achieve wing morphing due to feathers, which slide on top of each other, thus maintaining a smooth surface. Bat wing architecture differs and consists of a thin membrane supported by stiffening bones. This enables the bats to reduce their wingspan by about 20% without generating considerable slack. The membrane is elastic and can be stretched [24]. Slack in the membrane induces drag, and the trailing edge is more prone to flutter [40]. In current state of art research platforms, according to **Figure 10**, a wing span reduction up to 25%. Fatigue and slack of the Spandex membrane used in this case is an issue, and could possibly be solved using smart material membranes. This would also lead to adjustable stiffness of the membrane and a tightening of the membrane during flight in order to avoid slack.

Bio- inspired flapping wing flight platforms date back to DaVinci's era in 1490. This was a human powered ornithopter, having membrane like wings. Lilienthal also developed the first a successful gliding human powered ornithopter in 1894 [19].

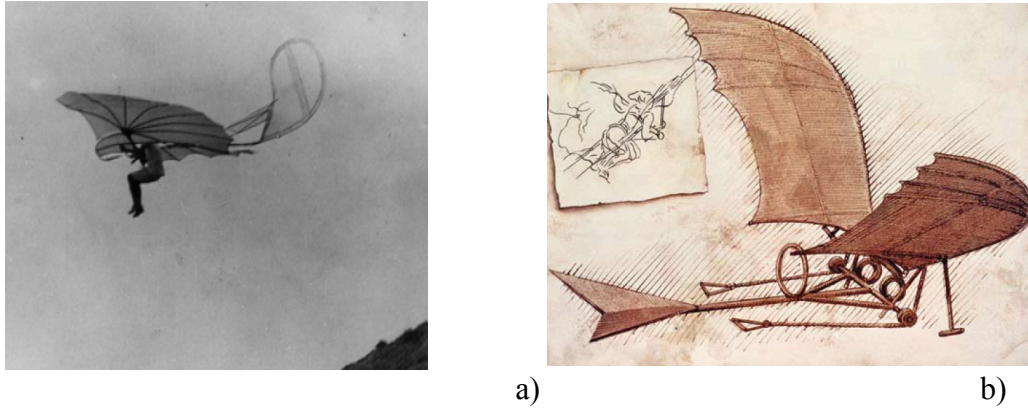


Figure 11: *First Ornithopter Vehicle designs a) DaVincis 1490 b) Lilienthal 1894 [19].*

In the 1870 designs of unmanned ornithopter designs started to appear by Jobert, Penaud, and Villeneuve [9]. First electric powered ones in 1961 by Spence's. More recent designs include DeLauriers ornithopter design 1991 from an ornithopter series started in 1975. Currently ornithopters designs have a wide spectrum of performance abilities and range from commercially available and University research platforms. Academic platforms include "Microbat" California Institute of Technology, the "Phoenix" at Massachusetts Institute of Technology Figure 13, University of Arizona Ornithopter as well as the University of Michigan's research collaborative research effort "COM-Bat" which mainly involves the University of California at Berkeley and the University of New Mexico [9] [41] [42]. Its conceptual design can be found in Figure 12. Recent successful smart material bat platform "Robo Bats" of North Carolina State University [1], and a multi-actuated Robotic bat wing of Brown University [43]. The most successful ornithopter research platforms in terms of aerodynamic performance, range and endurance are University of Arizona's Ornithopter Research Platforms and the University of Maryland Ornithopter research platforms Figure 10 to Figure 33 [44] [45].

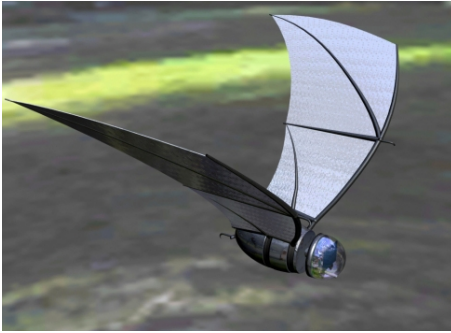


Figure 12: *Com-Bat intended robotic spy plane 3 D image -University of Michigan 2008 [46]*

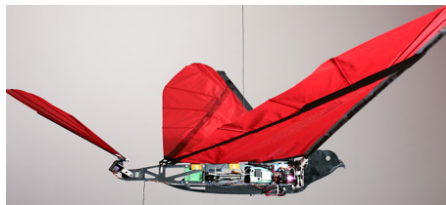


Figure 13: *Ornithopter Research Platform "Phoenix" - Massachusetts Institute of Technology 2010 [47]*

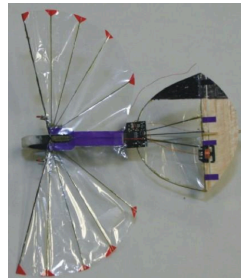


Figure 14: *MAV -University of Arizona's Ornithopter [48]*

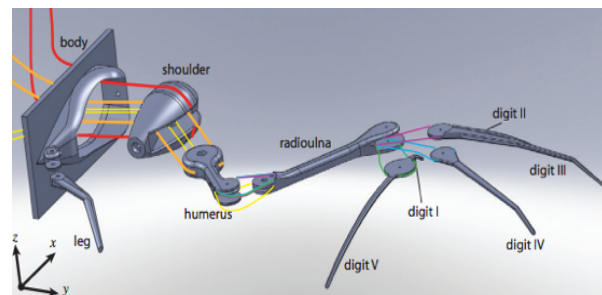


Figure 15: *Brown University Robotic Bat Wing a) ABS 3 D Print b) Schematic [49]*



Figure 16: “Robo Bat”s the skeleton of the robotic bat uses shape-memory metal alloy that is superelastic for joints [50]

1.5 Problem Introduction

In foregoing sections the background in flapping wing flight, flapping wing aerodynamics, flapping wing robotics, and desired capabilities of model developed has been provided. The following discusses the objective of this research and provides a background on the model.

1.5.1 Research Objectives

The objective of this research is to develop a flexible multi-body structural-dynamic model considering aero elasticity (FMBSDA) in conjunction with experimental data to identify and enhance the understanding of efficient flapping wing flight dynamics in biologically inspired ornithopters. This necessitates a novel flexible multi-body dynamics modeling methodology incorporating aero elasticity.

The scope of this work includes A) creating a (FMBSDA) of an ornithopter by supplementing existing rigid multi-body dynamics models, and the inclusion of flexibility in the membrane kinematics; B) designing the experiment and analyzing

kinematics of an experimental ornithopter membrane wing in free flight captured through a Vicon ® Vision system, which provides the kinematics of the membrane wing suitable and used for verification of the FMBSDA model; C) developing FMBSDA model enhancements in order to obtain accurate representation of the ornithopter that is coherent with experimental data; and D) developing a model capable of investigation of the flight dynamics and physics of flapping wing flyers, to quantify and identify the influence of varying flexibility i.e. camber stiffness, wing design and wing motion profiles, on the flight dynamics and performance and can hence be used for design optimization purposes.

Modeling of flapping-wing vehicles is challenging because of the complex nature of the problem, which is characterized by a strong coupling between fluid and structural dynamics, a nonlinear elastic multi body-system, and an associated unsteady aerodynamics. Geometric non-linearity's put the flapping wing problem into the category of non-linear elastic multi-body systems. Including flexibility in the wing membrane model is necessary for an accurate representation of ornithopter flapping wing flight dynamics. The addressed multi-disciplinary analysis methodology requires the evaluation of tools representing individual disciplines before they are interfaced together in a high fidelity comprehensive model.

Disciplines involved like flexible multi-body dynamics modeling, vehicle dynamics modeling, relevant existing models of ornithopter, and flapping wing aerodynamics models are discussed in the remainder of this chapter, and in addition, a

comprehensive review of aforementioned topics is provided. It provides the necessary background for the model development in individual modeling disciplines involved.

1.5.2 Classification of Flexible Multi-Body Systems

First a background on flexible- multi body systems is given. Originally, simple tree- like topologies were handled using multi-body dynamics. The field has considerably advanced to the point where it can handle linearly and nonlinearly elastic multi-body systems as well as arbitrary topologies. A multi-body system is typically comprised of bodies, joints, force elements, and components of control.

Multi-body dynamics modeling is now used as a fundamental design tool in many areas of engineering [51]. Multi- body dynamics is used to predict forces, moments, and kinematics of multiple objects moving relative to each other, and is used as well to calculate stresses and strains if the system is elastic. The field of flexible multi-body dynamics is concerned with the kinematic and dynamic analysis of flexible mechanical systems. Those are constrained deformable bodies that undergo large displacements, including large rotations. These large displacements are comprised by rigid-body motion as well as elastic deformations [52].

Multi body systems can be classified as 1) rigid multi-body systems 2) linearly elastic multi- body systems and 3) nonlinearly elastic multi- body systems. Linearly elastic and nonlinear elastic multi-body systems fall in the category of flexible multi- body dynamics models. Rigid multi- body models having flexible joints also fall within the

category. Within the definition, linear and nonlinear refers to material constitutive laws and strain displacement relationships of the flexible body. Multi-body systems are inherently nonlinear due to the large overall motions of the bodies and coriolis and centrifugal forces [51] [44].

Rigid multi body systems are comprised of tree like topology of rigid bodies. Rigid bodies are connected though mechanical joints and move relative to each other [51]. In this category the bodies of the systems are rigid, which means that two tracking points on the rigid body have no relative motion to each other and remain fixed in their distance. However within the category lumped elastic components may exist connecting rigid bodies, i.e. flexible joints, bushing or force elements [51]. Flexible joints represent localised elasticity and may exhibit arbitrary constitutive behaviour [51]. A rigid-multi body system schematic is presented for the ornithopter used in this research Figure 17.

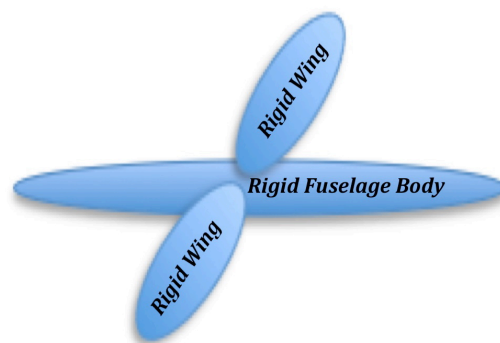


Figure 17: *Ornithopter Schematic: Rigid Multi-Body system*

Within the category of *linear elastic multi body models* the systems consist of an assembly of both rigid, and elastic bodies and elastic bodies only. Material

constitutive laws and strain-displacement relationship of the flexible bodies remain within the linear regime. Figure 18 shows an ornithopter system schematic modeled within this category. Here the flexible wings have linear elastic deformations, plane sections remain plane, strain-displacement relationships remain linear and local deformations of the wing are small [51].

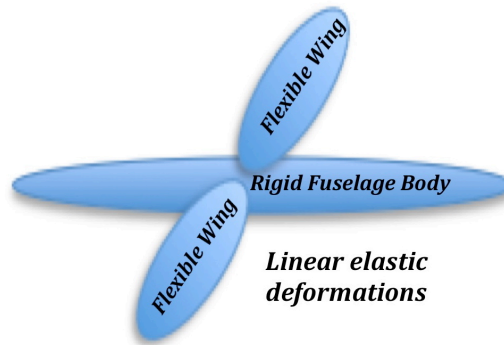


Figure 18: *Ornithopter Schematic: Linear Elastic Multi-Body Systems*

In the category of *nonlinear elastic multi-body models* the system consists of flexible and rigid bodies or flexible bodies only. The strain-displacement relationships of the elastic bodies lie within the nonlinear regime. Modeling of nonlinear elastic multi-body systems leads to a large order of the model [53]. A mechanical system may have to be handled as a nonlinear elastic multi-body system in case of geometrically nonlinear problems even if linear material constitutive laws describe the material behavior adequately. For example nonlinear elastic multi-body systems are modeled if large displacements, rotations are involved and or if strain components become large, hence in case of a materially nonlinear problem, and or a geometrically nonlinear problem.

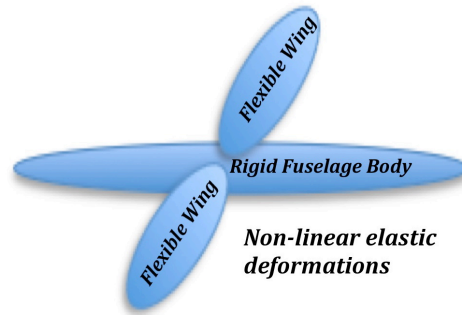


Figure 19: *Ornithopter Schematic: Nonlinear Elastic Multi-Body Systems*

The nature and physics of the elastic problem need to be well understood in order to categorize a system with flexible bodies in the linear elastic multi body systems or nonlinear elastic multi body system. It is advantageous to categorize a problem within the regime of linear elastic multi body system vs. nonlinear elastic multi body systems in terms of system order and modeling capabilities further discussed below in Section 1.5.3 Flexible Multi-Body Dynamics Modeling. The lines between linear and nonlinear elastic multi-body systems are sometimes blurry [51].

The categorizing of these systems presents a challenge when one considers the example of an helicopter rotor blade and wind turbine blade. As the blade rotate elastic displacements and rotations remain small and linear material constitutive laws are adequate. In the case of a wind turbin or a slow rotating helicopter rotor blade linear strain- displacement relationships can be used. Using proper linear elastic multi- body system assumptions can predict the dynamic response accurately [51]. As the helicopter rotor blade speeds up and significant centrifugal forces occur, which leads to centrifugal stiffening and nonlinear coupling between bending and torsional deformations. Nonlinear strain displacement relationships must be used to capture

effects adequately. Even in this case linear material constitutive laws still adequately predict the material behaviour. Nonlinear elastic bodies may be present for components which operate at high speed or high force loads, and the nature of the problem needs to be accurately understood. Due to this aforementioned geometric nonlinearities the problem of the helicopter rotor blade now quantifies as nonlinear elastic multi-body system [51]. Distinction of between category 2) and 3) is further complicated because nonlinear elastic and linear elastic components can appear simultaneously in a system such as the ornithopter problem at hand. The dynamic characteristics of an ornithopter must be examined and understood in order to lead to accurate dynamic modeling. Assumptions on geometric nonlinearities and dynamic properties used in the model development presented here were checked using its experimental in flight kinematics and detailed in Chapter: 6.

As one considers the problem of an ornithopter, as the wing flaps elastic displacements and rotations of the wing material viewed in a wing fixed reference frame may remain very small. Therefore linear material constitutive laws describe the elastic behaviour of the wing structure adequately. Now the wing was built to undergoes small strains so that the structural integrity of the wing is preserved over its live time. Due to the angular speed of the flapping motion of the wing its assumed that small centrifugal forces are induced. Considerable wing stiffening of the wing due to the forces as well nonlinear coupling between its two bending and torsional deformations may also remain small given the slow rotation rates. This is assumed due to the considerably low angular speed of the flapping motion and occurrent

motions on the wings. Therefore strain – displacement relationships remain also small and stay in the linear regime. Deformation assumption is also checked in wing kinematics data and presented in Chapter: 7 Concluding discussion, it's assumed that effects here can be captured adequately using a linear multi-body system (LMBS) model. The dynamics of the ornithopter need to be well know in order to use adequate modeling techniques. Assumptions are verified in order to use the category of (LMBS) and are discussed in Chapter 4 for the ornithopter problem.

1.5.3 Flexible Multi-Body Dynamics Modeling

A overview of the categorization of flexible- multi body systems was given in the last section. The following section discusses and reviews the adequate and existing modeling techniques of such systems. In elastic multi-body dynamics, the dynamic behavior can be calculated by a set of Partial Differential Equations (PDEs), however the solution of for example the bodies stress state is analytically possible in rare cases [53]. In rigid-body systems where a body is assumed to undergo no deformation compared to the overall motion, the equations of motion can be derived from a set of second order differential and algebraic equations (DAE's) [53] [54]. In the case of kinematic constraints, an additional set of second order ordinary differential equations (ODE's) or generalized coordinates have to be used. Rigid- body dynamics is typically computationally fast as it has a low order of the system and a low number of degrees of freedom (DOF's). There are six degrees of freedom per rigid body, three translational coordinates and three rotational coordinates. The degrees

of freedom of a multi-body system can be calculated using the Gruebler Equation [55]. According to previous discussions, elastic multi-body systems are modeled by a set of Partial Differential Equations (PDE's) and a solution has to be approximated using for example the Ritz-Galerkin method, the Ritz method, the Finite Element Method (FEM), or the Boundary Element Method (BEM) [53] [54]. Depending on the nature of the problem a combination of these methods may also be used to advantage. Under certain assumption the a discretization procedure leads to the definition of second order ODE's [53]. The finite element method is most popular for handling elastic multi-body dynamics. The Finite Element Method is most easily applicable, independent of geometric complexity, and a sparse pattern is achieved through the derivation of ODE's. In order to satisfy geometric and kinetic boundary conditions within the domain, modeling occurs using geometrical elements (Finite Elements (FE)) and shape functions (Ritz shape functions) for these elements [53]. The FEM method provides high accuracy for nonlinear and linear elastic structures. However to sufficiently describe an elastic multi-body system dynamics system a large number of elastic coordinates have to be considered, which leads to a large number of FE and nodes. This is computationally expensive and in cases of large mechanical systems unfeasible. A reduction of the Degrees of freedom is desired. This can be achieved through for example handling underlying rigid-body motions and a superimposed elastic deformation. Significant inertia changes due to elastic deformations may also occur, which leads to a coupling of the underlying rigid-body equations of motion (EOM) and the structural dynamics EOM's. Hence these EOM's cannot be solved independently. Nonlinear structural bodies within the

system as well as aeroelasticity, also lead to coupled EOMs. Coupled and uncoupled methods to integrate rigid and elastic dynamics exist for such hybrid systems. The basic approaches used in simulation and computer aided calculations for flexible multi-body dynamics and kinematics are the floating frame of reference formulation, the finite element incremental method, large rotation vector formulations, the finite segment method, and the linear theory of elasto-dynamics. In general modal expansion methods are reliable within the regime of linear elastic multi-body system [51]. Multi-body dynamics analysis is not yet widely applicable when dealing with nonlinear elastic systems and a deep understanding of the system modeled is required [56]. A more detailed review development in the field of flexible multi-body dynamics and related methods can be found in reference, [51] [52] [53] and is further discussed in Chapter 4.

1.5.4 Suitable code and Software Background

A brief overview of the theoretical background of modeling of flexible multi-body systems was given in proceeding section. The state of art of, the choice and integration of solvers for the EOM's used in this research are discussed in the following. Serial available codes and software packages exist in order to handle flexible-multi body dynamics problem. Both commercially available and University research codes. Codes and software packages incorporated in this research were chosen based on its ability to incorporate multi-physics, and change the solution procedure by adjusting code as well as to couple aerodynamics though both code and computer aided fluid dynamics (CFD). Due to the complexity of the ornithopter

problem and the experimental verification methodology described in Chapter 2: Modeling Methodology the solution procedure is required to be versatile and customizable through code. Requirements on the model capabilities are the following: 1) Ability to appropriately model geometry through Computer Aided Design (CAD), functional building blocks or coding 2) Handle rigid and Flexible multi-body dynamics linear and nonlinear adjustable solution procedures 3) Ability to use interface for aero elasticity. Flexible- Multi-body dynamics modeling generated huge interest due to its versatility and applicability, and is a growing field. Its modeling capabilities are desired in many areas of engineering like energy, automotive and aerospace. i.e. wind turbines, helicopter rotor blades, space manipulators, solar sails and lead to a wide array of existing codes and model assumptions and simplifications. Fidelity problems for nonlinear elastic multi-body dynamics applications lead to constant advancements and evolving of codes and software packages. In the recent years fast advancing and quick turnarounds in software packages been made in order to handle and categorize elastic multi-body dynamics problems. A comprehensive list of evolving software and codes available is found in **Table 2**.

Table 2: *FEM and MBD university codes and commercial packages*

Code/ Software	Primary TYPE	Geomet ry	RMBD	FMBD	FE Linear	FE Linear and Nonlinear	AEOI	Developer
ADAMS solver	MBD	Yes CAD	Yes	Yes Linear	Yes	NO	No	MacNeal- Schwendler Corporation
MARC Solver	FEM	Yes CAD	No	No	Yes	Yes	No	MacNeal- Schwendler Corporation

DYMORE	MBD	Programmable toolbox	Yes	Yes	Yes	Yes	Yes	Georgia Tech University
PATRAN/NASTRAN	FEM	CAD	No	No	Yes	Yes	No	Originally NASA marketed by MSC
ABAQUS	FEM	CAD	No	No	Yes	Yes	Limited	Dassault Systems
ANSYS	FEM	CAD	No	No	Yes	Yes	Limited	ANSYS
CAMRAD	MBD	Helicopter Geometry	Yes	Yes	Yes	Yes	Yes	Johnson Aeronautics
COMSOL	MP	CAD	Yes	Yes	Yes	Yes	Limited	COMSOL
SIMPACK	MBD	CAD	Yes	Yes	Yes	Yes	Limited	Originally DLR marked by SIMPACK AG and MathWorks Livermore
LS-Dyna	MBD	Programmable toolbox	Yes	Yes	Yes	Yes	Yes	Software Technology Corporation
MBDyne	MBD	Programmable toolbox	Yes	Yes	Yes	Yes	Limited	Polytechnic di Milano

For aerospace application an academic code CAMRAD was developed for helicopter and rotorcraft dynamics and aerodynamics and is commercially marked by Analytical Methods. It includes multi-body dynamics, nonlinear finite elements, structural dynamics, and rotorcraft aerodynamics. CAMRAD provides excellent performance abilities for rotorcraft applications but is not well suited for the ornithopter problem due to its limited versatility [57]. Multi-body dynamics codes for aerospace applications like MBDyne and developed by the Polytechnic di Milano and DYMORE by Georgia Tech University, which were also considered for this research.

MBDyn features the integrated multidisciplinary simulation of multi-body, multi-physics systems, including nonlinear mechanics of rigid and flexible bodies and can be coupled with aerodynamic codes and CFD. DYMORE is a Finite Element Based Tool for the Analysis of Nonlinear Flexible Multi-body Systems [56]. COMSOL a multipurpose software platform, which provides a multi-disciplinary solution capability but is ill suited for the multi-body dynamics simulation [58]. Furthermore individual discipline software packages were considered for an integration in a multi-physics simulation through an interface for high modeling fidelity. PATRAN/NASTRAN, ANSYS or ABAQUS was considered to handle the Structural Dynamics. PATRAN is a pre/post-processing software for Finite Element Analysis (FEA) by the MacNeal-Schwendler Corporation (MSC). Nastran is a multidisciplinary structural analysis (FEA) application for PATRAN. PATRAN/NASTRAN marketed by MSC was originally developed for NASA in the late 1960s. ANSYS and ABAQUS are other established and most widely used commercially available FEA software tools. ABAQUS is known for its high fidelity nonlinear structural modeling capabilities. MARC is a nonlinear finite element solver by MSC and also suitable to handle multi-body dynamics of the problem. LS-DYNA a general-purpose finite element program capable of simulating nonlinear dynamics and rigid-body dynamics, mostly used for rotor-blade applications. SIMPACK is another possible simulation software for general purpose Multi-Body Simulation (MBS). It is especially well-suited to high frequency transient analyses. SIMPACK is a commercially available package and was primarily developed to handle complex non-linear models with flexible bodies and harsh shock contact originally by the

German Aerospace Center (DLR). Limitations in aerodynamic interface are given with SIMPACK. MSC ADAMS is world's most widely used multi-body dynamics (MBD) software and ADAMS solver along with the MARC solver used for modeling the multi-body dynamics component of the problem. Solvers are facilitated in Multi-disciplinary SimXpert Graphical user interface (GUI). Interface of ADAMS Solver with aforementioned FEA tools is possible through a Mode Neutral Files (MNF). PYTHON, MATLAB and FLUENT to was considered to handle to the latter analytical aerodynamics or CFD for the fluid structure interaction. Choice of programming language or Software for the aerodynamics is based on the related flapping wing aerodynamics models discussed in section 1.5.7 of which proven theories are utilized and extended in this research. PYTHON and MATLAB are widely used programming languages ANSYS FLUENT a commercially available CFD software package in which preceding flapping wing aerodynamic modeling research was carried out. Due to the incorporation of experimental kinematics aerodynamics here was modeled and computed using MATLAB, and also interfaced through SimXpert.

SimXpert released in 2010 by MSC was chosen as the graphical user interface (GUI) for the multi-disciplinary simulation methodology. In the frame of this research it allows interfacing with MATLAB for an aero elastic consideration of the problem and opens up the ability to be interfaced with CFD for a higher fidelity but more costly simulation in the future. A versatile use of ADAMS solver for Multi-Body Dynamics or an explicit nonlinear solver utilizing LS-Dyna opens up the research space for the flexible multi-body simulation. Linear and nonlinear structural

dynamics of bodies in the Multi-Body System can be calculated by using MD Nastran solver integrated in the GUI. Geometry of ornithopter research platform is modeled using PTC Creo Computer Aided Designed (CAD) Software and is imported into the SimXpert Graphical User Interface (GUI). For all simulation computations, a multidisciplinary Software SimXpert GUI was employed. The solution procedure used here is according to following Figure 20 and fully integrated model image is shown in Figure 19.

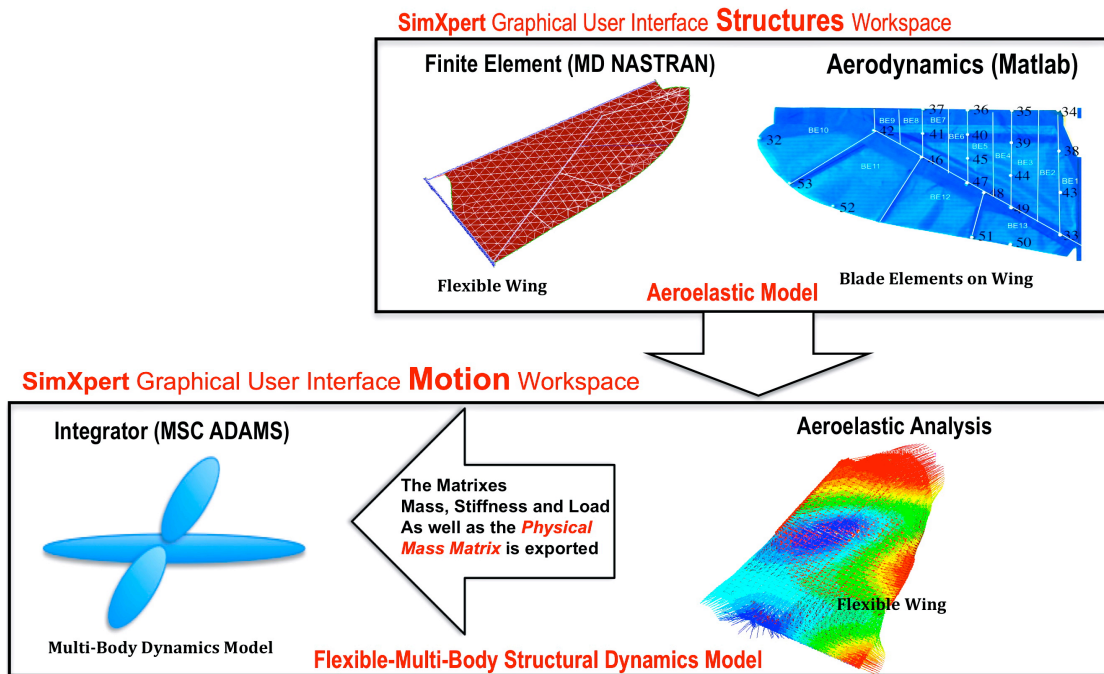


Figure 20: SimXpert: *Flexible -Multi Body Dynamics Model Implementation*

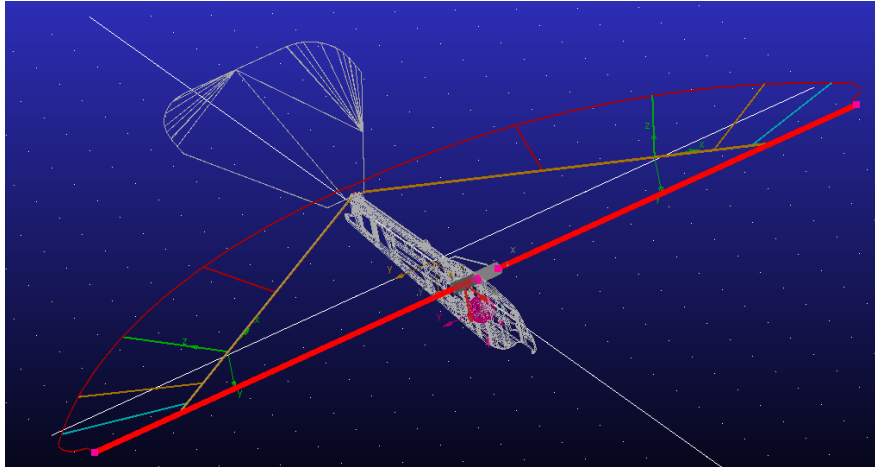


Figure 21: SimXpert: *Image of Fully Integrate Flexible Multi-Body Dynamics Model of Ornithopter*

Aeroelasticity was incorporated by a finite element (FE) computation of time variant aerodynamic loads as applied to the structure. Time variant loads (TVL) result from kinematics data described in the following chapters. For the determination of the time histories and magnitudes of TVL MATLAB was used. Finite Element (FE) and multi body dynamics calculations were performed using MD NASTRAN solver and Advanced Dynamic Analysis of Mechanical Systems (MD-ADAMS) Motion Solver accordingly [59]. The aeroelastic analysis provides mass, stiffness and load matrixes as well as the physical mass matrix and is exported into the Multi-body dynamics integration. A semi-physical modeling methodology is used which is further exploited in Chapter 4.

1.5.5 Vehicle Dynamics Modeling of Ornithopter

The level of complexity of vehicle dynamics models vary from simple single rigid-body models, to more complex rigid multi body dynamics models and finally the most complex kind flexible multi-body dynamics models. These elastic effects

can also couple with the aerodynamics associated with the system which makes it an aero elastic problem. This section discusses vehicle dynamics modeling in the context of ornithopter modeling, and provides a review and shortcomings of related models. Figure 22 shows the complexity of models on an example of ornithopter.

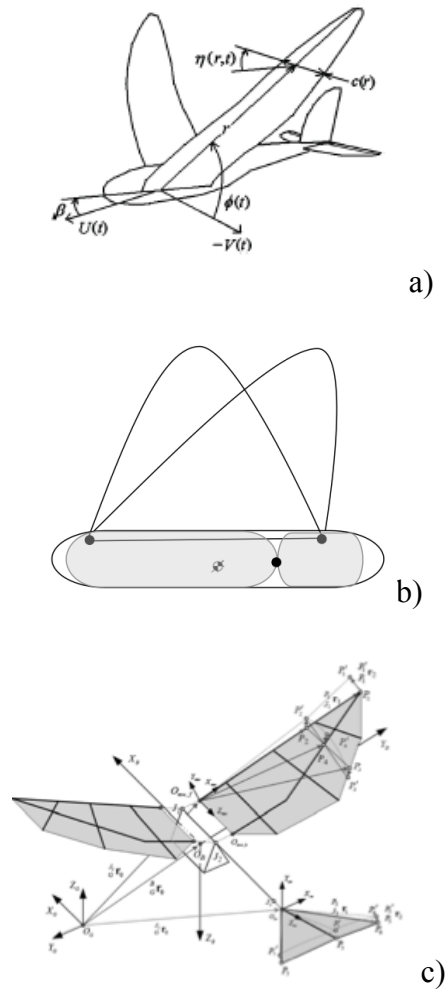


Figure 22: Ornithopter Vehicle Dynamics Models a) *Single Rigid Body* b) *Rigid - Multi Body Dynamics* and c) *Flexible Multi-Body Dynamics Model*

A variety of models that describe the flight dynamics of flapping wing flyers have been developed previously. Several rigid multi-body dynamics models for flapping

wing vehicles have been derived previously using an array of methods [44] [60] [61] [62] [63]. A single body rigid body dynamics model according to standard vehicle dynamics is shown in Figure a). These standard aircraft equations of motions can be mathematically described by evolving position and velocity states of the single rigid body, here the inertial effects of wings are negligible and flapping frequencies are significantly separated from dynamic frequencies [44] [64].

A single body representation is a commonly used modeling methodology for small-scale ornithopter problems but in limited cases valid for avian scale ornithopter [6] [44] [65]. Conventionally single body dynamics models for aircraft are nonlinear models in a body dynamics sense [9] [64]. Mass distribution variations due to flapping wings are significant here for the ornithopter research platform and the moments of inertia of the wing can vary up to 53.6% [9]. Dynamic frequencies are also in close proximity to flapping frequency, and require a multi-body dynamic representation of vehicle dynamics models for ornithopter. These models are more complex, and they contain position and velocity states for the individual rigid bodies, but of necessity as they can capture the inertial effects of the flapping wings [9]. An investigation by Orlowki employed a multi-body model and empirical scaling laws observed in nature. Their research concluded that linear momentum effects from flapping wings are always significant. Angular momentum effects are also significant for flapping frequencies below 40 Hz, and magnitude decreases below with rising flapping frequency up to 40 Hz [9] [66].

Figure 22 b) shows a multi-body model of an ornithopter where wing bodies and

fuselage bodies are treated as rigid bodies. A version of the rigid multi-body dynamics model of an insect has been previously developed by Dyhr, [60] and a sketch of it is highlighted in grey **Figure 22 b**). Fuselage (abdominal) body dynamics are of interest and aerodynamic forces are introduced, which are linear time invariant (LTI) into the models constraint term. Equations of motion for a model inspired by the Hawkmoth are linearized about a hovering equilibrium.

Several other models have been employed using time averaging theory to simplify the periodic forcing of the wings in a similar manner [67] [68] [66]. A common objective for the utilization of flapping wing modeling is for stability analysis and control of these vehicles. A number of models have been developed for these purposes. In order most continently employ classical and modern control, linear perturbation models are often desired for the stability analysis and controls synthesis. As linear time-invariant (LTI) models result in equilibrium points with Eigenvalues and Eigenvectors [9]. Faruque and Humbert also developed (LTI) models of insects using system identification techniques. They developed a reduced-order model of longitudinal hovering flight dynamics for dipteran insects. Here a quasi-steady wing aerodynamics model is extended by including perturbation states from equilibrium and paired with rigid-body equations of motion to create a nonlinear simulation of a *Drosophila*-like insect [61] [69]. The fidelity of LTI models for most control purposes and design optimization purposes like of interest in this work are questionable even by authors who have developed them [62] [70]. As a consequence Grauer, J. Lee and Taylor have developed more complex models [16] [63] [62]. Taylor developed a semi-empirical models of the longitudinal fight dynamics of

desert locusts *shistocerca gregaria* by representing approximately periodic instantaneous forces using Fourier series embedded in the equations of motion, and resulting in a nonlinear time-periodic (NLTP) model [62]. Grauer developed a rigid-multi body dynamics model that uses energy methods to determine equations of motion and cast them into a canonical form [44]. The model uses a time variant (TV) aerodynamics model identified through system identification techniques. It was primarily developed for control purposes and also recommends including wing flexibility to result in a higher fidelity for dynamic investigations. Figure 22 b) highlighted in white shows the schematic of a 3 body rigid- multi-body model by Grauer developed through system identification techniques in order to capture dynamics of experimental research ornithopter [9]. According to previous discussed vehicle dynamics models of category a) and b) mainly serve stability and control purposes.

Flexibility in the wings is a significant design metric in order to improve the performance of flapping wing vehicles. Flexibility also influences the stability and control characteristics of aircraft [26] [71]. Including wing flexibility significantly increases the level of complexity of a ornithopter model, its degree of freedom and entails an aeroelastic response. A kinematics model for a platform that features bat-inspired wings with a number of flexible joints was done by Bunget et. al. [2]. Sparse literature exists regarding the flight dynamics of ornithopters and considering flexibility and Fluid Structure Interaction (FSI) and multi- body dynamics [63]. Kim et al. states that generally, for the analysis of flight dynamics of ornithopters,

complex nonlinear flexible multi-body configuration of an ornithopter is simplified to linear rigid-body dynamics. Some relevant ornithopter dynamic models are by Dietl and Garcia, and use a single rigid-body model [72] [73]. Further relevant rigid-body dynamics models are developed by Rashid and Bolder. Rashid developed a rigid body flight dynamics model of a full scale ornithopter and Bolder et al. a rigid multi-body dynamics model for flapping wing MAV's using Kane's equations [74]. In particular, the passive deformation of a flexible wing structure is oftentimes not considered or at best assumed to have a prescribed form to guarantee enough lift and thrust to propel the vehicle aloft [16] [60] [63] [72]. Limited related research considering aeroelastic vehicle dynamics of flapping wing vehicles are further reviewed in discussed in the next section followed by a review of related aerodynamic models of avian scale flapping wing.

1.5.6 Aeroelastic Analysis of Flapping Wing Vehicles

J.Lee et al. developed a version of a flexible-multi body dynamics model of an ornithopter considering aeroelasticity and represents the only preceding model developed in open literature addressing multi-body dynamics, flexibility and aeroelasticity for avian scale ornithopter (Figure 22 c)) [63] [75]. Here the wings are treated as flexible bodies. The wing structure is modeled using a finite element method and a superimposed flapping motion. This model has shortcomings in verification and is based on the assumption that an entire wing body stays within a linear regime. Analysis of free flight test data presented in this research confirms this as not being the case for state of art research platforms and a multi-body

representation of an individual wing has to be used in order to accurately use these assumptions. Verification of geometric non-linearity's, wing deformation and coupling between torsion and bending deformation is necessary in order to verify modeling assumptions here. Flexible multi-body model by J. Lee provides limited experimental validation and uses a loosely coupled aerodynamic model [63]. Due to the complex nature of the problem in order to successfully develop the proper analysis tools, it is imperative that the model be validated and developed in conjunction with experimental flight data exposing wing motion profiles and actual dynamic performance. Furthermore coupling between elastic coordinates and underlying rigid multi-body motion is solved independently and not in a coupled fashion, this limits model fidelity and utilization for design parameter optimization.

A comprehensive paper addressing modeling of aero elastic vehicles in general can be found by Waszak and Brutrill [71]. All aero elastic vehicles can be described within two categories. In the first category the coupling term between the elastic body and the aerodynamics is due to the aerodynamics only. In the second category, the inertial coupling also occurs due to elastic deformation of a flexible body [71]. Inertial effects due to the elastic displacements are uncoupled in Lee's model [63] [75]. The coupling of elastic and rigid-body modes is advantageous in order to provide ornithopter configuration versatility by keeping modeling fidelity [63]. The model developed here considers inertial coupling due to elastic displacements besides the underlying rigid body displacements. Elastic displacements are also considered for the calculation of aerodynamic forces, hence results in an enhanced aero elastic

calculation.

Shortcomings in discussed related vehicle dynamics model of flapping wing can be summarized by having one or more of the following issues:

- 1) Flexibility in the wings are neglected [9] [72] [76] [72] [77] [78] .
- 2) Vehicle dynamics model valid for one configuration only [9] [16] .
- 3) Fluid structure interaction (FSI) is neglected or not included in model fidelity [9] [72] [74] [78].
- 4) Only existing vehicle dynamics model addressing wing flexibility, multi-bodys and FSI by J. Lee [63] is limited though
 - a. Limited experimental verification.
 - b. Simplified wing kinematics and flexibility: Flexibility assumptions are not in tune with flexibility and wing deformation kinematics found in working ornithopter platforms
 - c. Inertial coupling through elasticity is neglected
 - d. Limitations in accuracy of FSI a) coupling methodology: loosely coupled aerodynamics model b) aerodynamic model assumptions itself c) input in aerodynamic model: resulting aerodynamic loads are based on simplified deformation assumptions of a flapping wing in free flight and not on experimental wing kinematics

These shortcomings are adressed in the model deveped in this research. This completes the review of ornithopter vehicle dynamics models and related models and

relevant flapping wing dynamics for the aerodynamic component in the multi-physics problem is reviewed next.

1.5.7 Related Avian Scale Aerodynamics and Models

A variety of analytical, experimental and numerical models have been developed in order to calculate aerodynamic forces on the flapping wing. For a flapping wing in addition to forward motion that fixed wing experiences, a flapping wing also flaps up and down, and can deform a wing membrane in order to adjust its camber. In addition, a bird for example can sweep forward and back, twist along the span, and folds to adjust the wing platform area [21] [25] [24]. Due to the resulting unsteady low Reynolds number flow and circulatory effects due to any or a combination of those capabilities, the accurate prediction of the flow field is challenging. The Reynolds number of the modeled test ornithopter presented here varies between 19,000 and 232, 000 for steady level flight, which encompasses the transition region where flapping wing vehicles are more aerodynamically efficient than fixed wing vehicles [9].

The most popular analytical model for avian flyers is the model developed by DeLaurier is a quasi-steady blade element model to capture wake/vortex interactions, post-stall phenomenon, and partial leading edge suction [49]. DeLaurier used modified strip theory approach shown in Figure 23 to develop a quasi-steady blade element model.

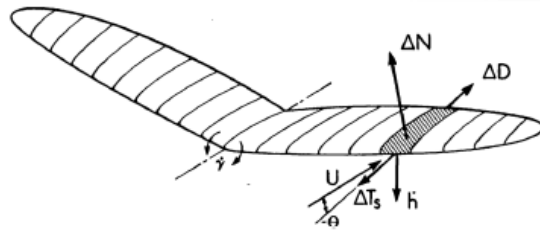


Figure 23: *Quasi-Steady Blade Element Model* [49]

DeLaurier's model is based on the modified Theodorsen function, or three-dimensional Theodorsen function, that takes into account a three-dimensional wake correction factor in terms of the wing aspect ratio and the reduced frequency [63] [49]. Contributions of the section mean angle of attack, camber, partial leading edge suction, and friction drag are taken to account here, which allows the model to be used for the calculation of the average lift, thrust, power required, and propulsive efficiency of a flapping wing in equilibrium flight [73]. The wing's aspect ratio is assumed large enough that the flow over each section is essentially chord wise and therefore in the mean-stream direction according to observed in avian scale flyers [4]. Variants of this model are widely used in the literature Jun-Soung Lee, tested the design-oriented aerodynamic model for unsteady aerodynamics proposed by DeLaurier using flight tests of avian scale ornithopter [73]. He concluded that the model this model failed to predict the amplitude of the time-varying aerodynamic forces and moment according to the continuous flapping-wing motion. The model is limited so as to classify the attached flow range and the post stall flow range [63] [49].

A modified version of DeLauriers Blade Element Theory (BET), namely MST stall has been developed by Kim et al.. The improved version of the modified strip theory (MST) includes a dynamic stall model for large plunging wing motion. Here the dynamic stall cut off angle is adjusted to a flapping and plunging plate. DeLaurier's analytical models dynamic stall cut off assumption rely on data for a fixed wing. Here the inclusion of dynamic stall in the model shows significant improvement in correlation of the root mean square values of aerodynamic coefficients to experimental data of a flapping plunging plate by Okamoto [79] [75].

Jea-Huns assumptions in showed improvements compared to DeLauriers original model and are adopted in current research. The classification of the flow in is more refined in terms of attached flow range, dynamic stall range, and post-stall flow range.

However the model fails to take into consideration the 3-D wing topologies of flexible wings. Namely flexibility adjustments in the cord wise direction taking fore and aft camber into consideration. More refined flight kinematics obtained from experiments shows the necessity of this adjustment [19].

Walker studied the unsteady aerodynamics of deformable airfoils and used a series of Chebychev polynomials to represent the deformation of the airfoil. The aerodynamics model was developed using potential flow aerodynamics and the Joukowski conformal mapping technique was used to map the flow. He concluded that Theodorsen's function reduces the magnitude of the lift due to circulation as reduced

frequency increases and shifts the phase of the circulatory lift with respect to the motion for all airfoil deformation. The magnitude of the phase shift is dependent on the reduced frequency [80].

An analytical model using blade element theory has been previously developed in the framework of a research effort of the University of Maryland Morpheus Lab [19]. The analytical model has been developed in conjunction with experimental data in parallel with a Computational Fluid Dynamics (CFD) model [81].

An analytical Blade Element theory developed by Harmon uses refined wing kinematics of experimental ornithopter platform and was defined by quasi-steady motions, including flapping or plunging, pitching, and forward motion [19]. However the effects of unsteady flow mechanisms, such as leading edge suction, wake capture, dynamic stall, or spanwise-flow, were neglected. The momentum theory, with an actuator disk that is the swept area of the wing was used to adequately capture induced velocity magnitudes on the wing. The core value of this model is defined by its development with experimental wing kinematics, which serves as input variable and allows a time variant aerodynamic force generation on the blade elements and is therefore specially distributed over the wing. The model is developed for the membrane behavior of a flexible experimental wing ML101 and MSK004 Research platform (

Chapter 3: Bio- Inspired Research Platform), which was measured in clamped

conditions. Here the membrane behavior is computed and divided in a fore and aft approach for two cord wise regions of the wing. The upstream region is modeled using first order modeling assumptions that has a pitching axis located at the chord point with a time- varying length of the blade element. The blade element length of the cord wise downstream region is fixed and takes no flexibility into account. Attached flow is assumed regardless of the relative angle of attack. Kinematic fluctuations of the camber during stroke transition are neglected which is positive during down stroke and negative during upstroke. In the downstream cord wise region the inflow angle for blade elements is adjusted by the pitch angle of the blade elements that are in the upstream region. When compared with CFD, the blade element model was determined to provide a good approximation of the complex problem of flapping wing aerodynamics and at a reduced computational cost [14] [81] [19] [82]. Work concludes that the quasi-steady circulation model by Harmon can capture the aerodynamic behavior when adjusted to account for unsteady motion and membrane aerodynamics [19].

With a rising reduced frequency the unsteady effects become more pronounced as the influence of the wake is increased. The wake couples aerodynamic forces from one time step to another. Therefore the wake is a significant factor in aerodynamic force generation and increasingly depends on the wing shape of the previous time step as the reduced frequency increases. Wake structure has to be included in modeling in order to archive the desired fidelity. Vortex Lattice Methods (VLM) provide means to do so, and is a simple numerical method to compute lift and drag. The VLM neglects

the viscosity of the flow field and has been used to analyze flapping wings by several authors but provides moderate fidelity [4] [83].

For example Stanford et al. developed an unsteady model by the means of the vortex lattice method. The model results in the derivative of time-averaged vertical force, propulsive force, power and propulsive efficiency of the flapping wing at the time step. Model was employed for a gradient-based design optimization but showed limited fidelity [4] [83].

In order to obtain viscous solution Computational fluid Dynamic (CFD) simulations have been carried out by numerous authors. Mainly flapping and plunging structures without consideration of flexibility is addressed in literature, consideration of 3D effects is also limited. Unsteady aerodynamics of Micro air vehicles were investigated using a RANS solver in order to compute a pitching and plunging and compared to a experiments. Results were correlated well. (RTO, 2010) [84]. Studies agree that 3 D effects have to be considered for a flapping wing platforms with low aspect ratios for design optimization purposes. A study by Visbal concluded comparing a 3-D and a 2-D computation of the instantaneous spanwise vorticity component at a given phase of a pure plunging airfoil that 2-D and 3-D effects are in close agreement over a significant portion of the airfoil. Study was carried out for a SD7003 airfoil section using large-eddy simulation (4° angle of attack, Reynolds number in the order of 10^4 and a reduced frequency of $k=3.93$) [85].

One can note that the significance of 3-D effects, depends on the aspect ratio,

Reynolds number regime and reduced frequency while the leading-edge vortex formation exhibits a well defined two-dimensional character. The study by Visbal concludes that as the Reynolds number increases above 4×10^4 differences between 2-D and 3-D results become significant because coherent vortices observed in the 2-D simulations break down in spanwise direction [4] [85]. The Reynolds number of interest in this modeling effort varies between 1.9×10^4 and 23×10^4 , and a consideration of 3-D effects becomes beneficial. Below a Re of 4×10^4 the flow is essentially laminar given the case study of Visbal et. al.. Minor differences are observed near the trailing edge aft portion and in the near wake due to translational effects and the 2-D approach predicts the flow well in this regime. In this dissertation developed cases represent a transition region in the Reynolds number flow regime where 3-D effects become significant.

Aforementioned study by Yuan et al. overpredicts force generation using a 3-Dimensional approach overpredicts force generation when compared to a 2 dimensional approach [86]. Here a highly 3 dimensional flow was observed for the root flapping case. In summary authors note that 3-D effects of low aspect ratio wings have to be considered for aerodynamic force prediction [86].

Like aforementioned most studies considering viscous flow have been carried out using 2D CFD analysis on pitching and plunging rigid airfoils by the means of non-linear flow equations or the Navier-Stokes Equations [87] [88]. A variety of further CFD codes have been developed for flapping wing [81] [86] [89] [85]. Short

comings here include limited experimental verification and validity for avian scale ornithopter. The inclusion of flexibility in CFD studies is rare as a CFD prediction of avian flight with flexible wings presents many difficult challenges such as large elastic grid deformations and the aforementioned possibility of laminar to turbulent transition [81]. Generally CFD is computationally expensive for fluid structure interaction. A summary of most applicable and successful studies for the problem at hand is discussed in the following.

Roget et al. computed aerodynamic forces produced by a flexible flapping wing and are simulated using a Computational Fluid Dynamics (CFD) based methodology and compared with integrated forces obtained from experiment. The CFD model is based on the compressible Reynolds Averaged form of the Navier- Stokes equations and uses a structured curvilinear grid. Refined experimental wing kinematics from experiment were used as input variable and an efficient grid deformation algorithm is devised which deforms the body-conforming volume grid at each time step consistent with the

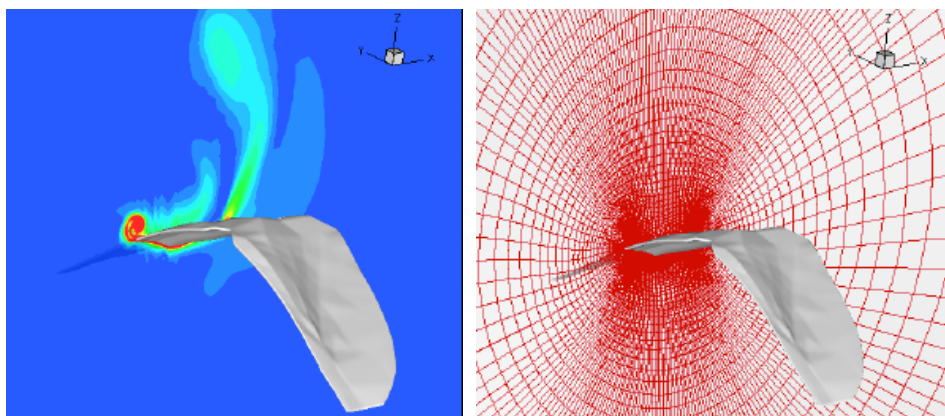


Figure 24: CFD analysis showing a) Vorticity contours on the flexible deformed wing b) Deformed Grid at 50% span location during upstroke of the wing at start of upstroke [81]

The study was previously conducted using MSK 004 an ML001 Ornthopter Research platform at a Reynolds number regime of 10.5×10^4 - 21.3×10^4 using a modified version of University of Maryland unsteady Navier-Stokes solver (UMTURNS). The deforming grid methodology was adjusted to the flexible wing with large deformations. The UMTURNS codes is a compressible Reynolds Averaged Navier-Stokes (RANS) solver which uses body fitted curvilinear structured grids here grid deforming methodology was adjusted to accommodate the flexible wing with large deformations. In the model the 2-D planes along the wing-span (Figure 24) extend in the normal direction and a cosine interpolation is applied in order to form a 3-Dimensional grid that is valid in deformed and unreformed positions of the flexible wing [81]. Figure 24 shows a plane of 2 Dimensional deformed grid and Vorticity contour results of the computation on a deformed flexible wing.

The Data correlation of simulation results and experiment showed good agreement with measured vertical force and satisfactory agreement with measured horizontal force at low flapping frequency. Research concludes a higher fidelity of model prediction with decreasing flapping frequency and suggests inertial effects from the vehicle body and support mounts may be one of the contributors to disagreement between data and analysis [81]. Fluid structure interaction coupling of solver developed by Roget et. al. to the Flexible-Multi-Body Dynamics Solver is computationally expensive.

Grauer et al. developed a aerodynamic model of a avian scale ornthopter MSK004 Research platform (Chapter 0) using system identification and flight test [9]. Model

adequately predicts aerodynamic force generation of orhopter wings by means of aerodynamic coefficients. Here the model structure determination was performed in the time domain with equation error and step-wise regression [16]. The model structue consists of aerodynamic coefficients in nonlinear expansion in terms of the state variables. **Figure 25** shows the rigid body kinematics fit in flight test data used for the model structure determination through system identification.

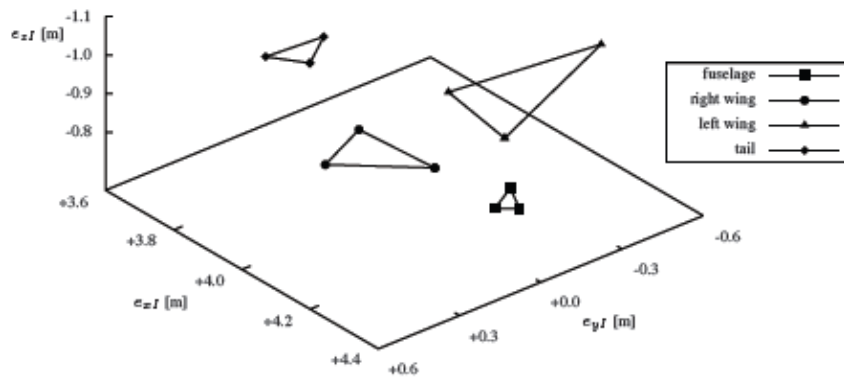


Figure 25: *Rigid-body ornithopter fit in flight test data for aerodynamic model structure determination [16].*

Validity of model is limited to flight test configuration and not suited for fluid structure interaction. It adequately takes into consideration the in the flight test occurent flow physics due to the development though flight test data and can be used as the configuration specific verification point for the aerodynamic model development adressed in this research.

Aforementioned efficient aerodynamic model was suggested by Kim et al., was based on DeLauriers modified strip theory and further improved to take into account a high relative angle of attack for dynamic stall effects induced by the pitching and plunging

motions. Limited experimental validation was provided with experimental data of a rigid rectangular wing but showed improvements compared to the modified strip theory and are therefore adopted in this research [90].

Although these studies are very insightful, further considerations are required to gain a complete understanding of the complex aerodynamic phenomena during actual flight, an approach of combining previous insights and modeling approaches, integrating them in a high fidelity and low computational cost model for fluid structure interaction is taken in addition to considering experimental in flight kinematics.

In summary previously developed analytical, experimental or numerical (CFD) aerodynamic analyses mentioned above suffered from one or more of the following shortcomings or limitations:

- 1) Simulation and modeling of flapping plunging plates without the inclusion of flexibility [85] [86] [87] [88] [89].
- 2) Most studies were carried out in a very low Reynolds Number flow field regime which can be contributed to MAV scale and not avian scale orntihopter, which is of focus here [6]. This has implications according to mentioned in previous sections.
- 3) Limited Experimental validation,
 - a. if experimentally validated mainly through PIV of rigid flapping and plunging plates without the consideration of flexibility which

considerably alters the flow structure, Reynolds number flight regime in the scale of MAV's [6] [80] [86] [89] .

- b. limited experimental in flight verification , one study exists by J.Lee at al. but doesn't consider wing kinematics and is merely justified by flight trajectory force integration [63].
 - c. If experimental wing kinematics are considered wake effects which are significant for the unsteady flow field and aerodynamic force production are neglected and provide limited fidelity [19].
 - d. Verification is limited to constraint data measurements through PIV or Vicon which significantly influences circulatory effects and pressure distribution on the wing (the aerodynamic force generation) [81].
- 4) Computationally expensive CFD simulation without the consideration of fluid structure interaction or inertia effects occurrent in avian scale ornithopter [81].
 - 5) Aerodynamic model through System ID is verified through flight test but tailored to one specific ornithopter configuration and therefore not suitable for design optimization purposes [76].
 - 6) 3 D effects or spanwise lift distribution are neglected [8] [19].

Research effort combines and improves successful models previously developed in order to negate their individual shortcomings. Refined experimental wing kinematics is used for model development, the inclusion of wing flexibility, wake effects, dynamic stall and span wise lift distribution is considered in a computationally

efficient manner by using blade element theory. The model is tailored to the avian scale Reynolds number flight regime. Model is experimentally verified through flight test and inertia effects and fluid structure interaction is considered through coupling with flexible- multi- body dynamics model.

Chapter 2: Modeling Methodology

In following the workflow overview of the model development is presented. This results in the novel flexible multi-body dynamics modeling methodology.

In the following Figure 26 to Figure 32 the experimental input is marked in blue, red represents the model and yellow the experimental validation.

In the first stage of the development methodology according to (Figure 26) the wing kinematics obtained in the free flight experiment serve as input for the aerodynamic model. The output of aerodynamic model within its modeling assumptions results in time-variant and spatially distributed forces (TVSD) on the wing.

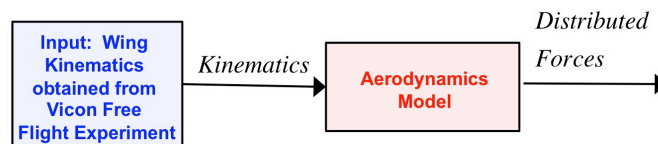


Figure 26: Modeling Methodology: *Workflow Stage 1*

Integrated forces are compared to integrated forces obtained through free flight test data in the second stage of the model development. Aerodynamic modeling

assumptions are adjusted in order to correlate system ID model and aerodynamic model results. Aerodynamic model and Flexible multi-body dynamics model are verified independently before they get interfaced into a comprehensive model.

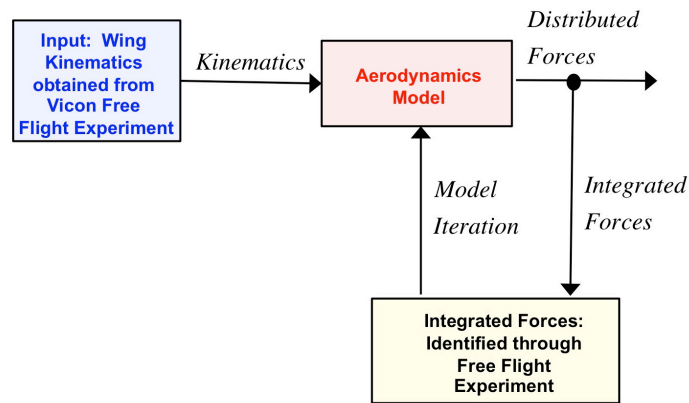


Figure 27: Modeling Methodology: *Workflow Step 2*

Thus, in the third step of the model development Flexible multi-body dynamics model output is verified employing inertial forces and wing kinematics obtained though the vacuum chamber experiment. Leading edge spar kinematics serves as input variable (Figure 28).

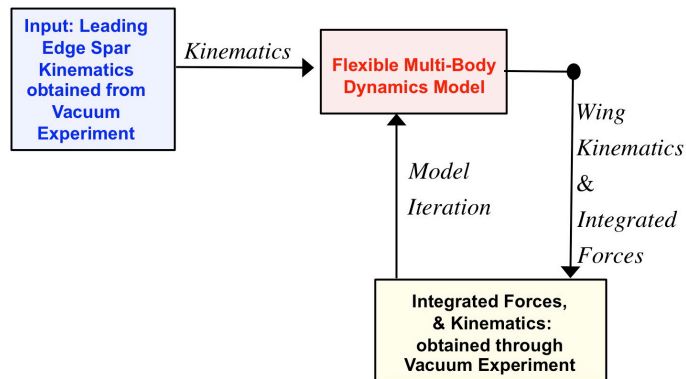


Figure 28: Modeling Methodology: *Workflow Step 3*

In the next step of the model development Aerodynamic and Flexible Multi –Body dynamics model are combined, the distributed forces resulting from the aerodynamics model are applied on the structural representation of the wing in the flexible multi-body dynamics model. (Figure 29)

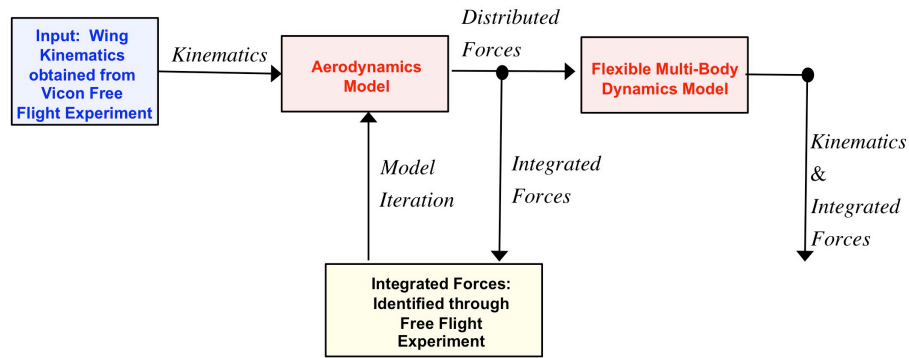


Figure 29: Modeling Methodology: *Workflow Stage 4*

Output kinematics and integrated forces are verified against experiment in the following stage. Model is iterated to archive correlation to Experiments in workflow Stage 5. (Figure 30)

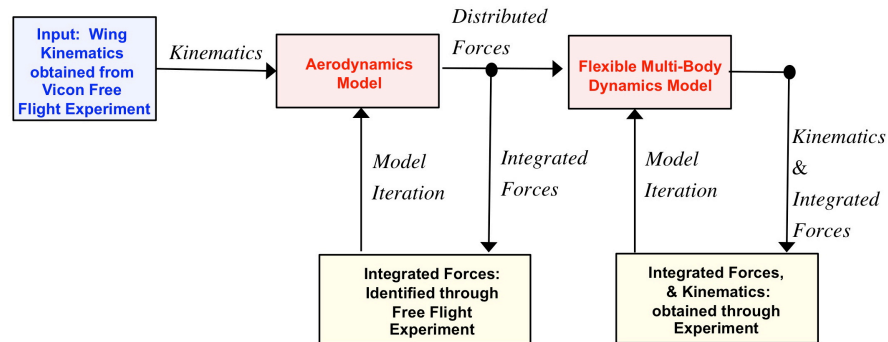


Figure 30: Modeling Methodology: *Workflow Stage 5*

Output of the iterated Flexible Multi-Body Dynamics model considering aero elasticity are wing kinematics body forces and wing stress and strain. (Figure 31)

Overall Model operates with wing kinematics obtained from Vicon Free Flight experiment at the Stage.

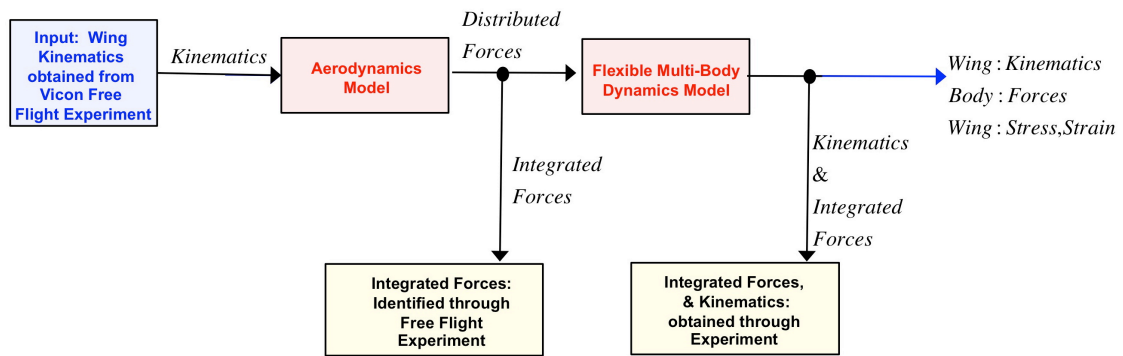


Figure 31: Modeling Methodology: *Workflow Stage 6*

At the final stage of the model development the Input kinematics are removed and the model is coupled. Output wing kinematics serves as input kinematics. The model is initialized by experimental kinematics (Figure 32).

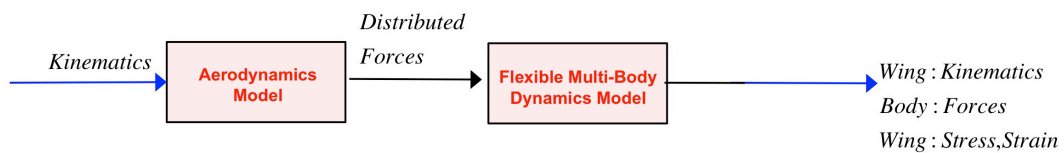


Figure 32: Modeling Methodology: *Workflow Stage 7*

The configuration of the ornithopter model can now be changed and coupled model can now serve for design optimization purposes.

In summary, Wing kinematics obtained from experiment serves as input variable for model development. Individual models are correlated against experiment, integrated

into a comprehensive model and further correlated. Experimental kinematics are removed and resulting model is coupled in order to archive a model to change configurations. This model is initialized by experimental kinematics.

Chapter 3: Bio- Inspired Research Platform

This Chapter describes and discusses the primary and secondary research platforms and experiments used for model development and verification.

3.1 Research Platform Details

The primary research platform in this research is the Morpheus Lab custom-built test ornithopter (ML 101) with a solid leading edge spar (Figure 33). This configuration serves as the baseline research platform for the model development.

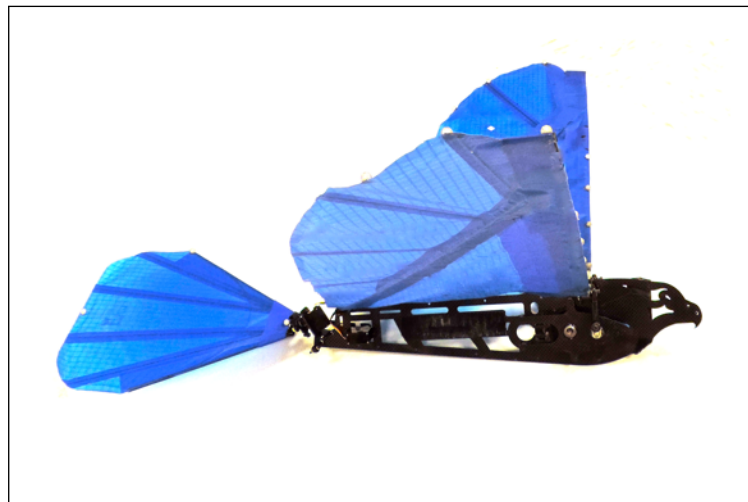


Figure 33: *Primary Research Platform Morpheus Lab Custom-Build test Ornithopter (ML101)*

The secondary research platform is a modified version of a commercially available ornithopter designed by Shawn Kinkade (MSK004)

Figure 34).



Figure 34: *Secondary Research Platform Modified Ornithopter Shawn Kinkade (MSK004)*

The experimental ornithopters have spatially distributed stiffening carbon fiber spars (Figure 36), which are covered by a thin membrane of rip stop material (Figure 35).

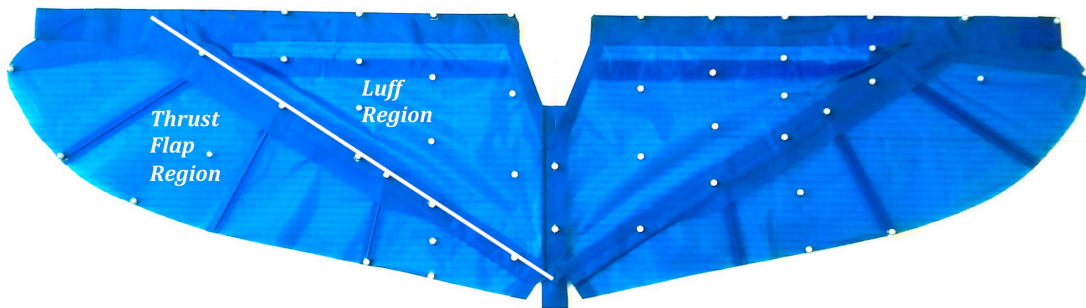


Figure 35: *Wing Structure Bio – inspired Ornithopter Research Platform (ML101)*

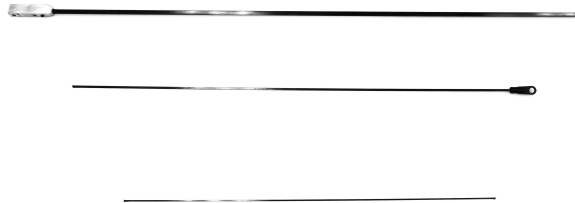


Figure 36: Design Feature Wing Spars (ML101) a) Leading Edge Spar, b) Diagonal Spar c) Finger Spar (ML101)

Stiffening finger spars, spar 1 to 4, a leading edge spar, and a diagonal spar are located on the wing (Figure 37) and provide structural integrity for the wing.

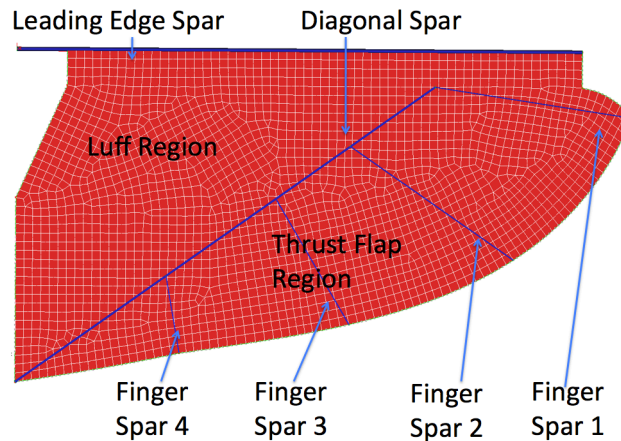


Figure 37: Schematic and Nomenclature Stiffening Carbon Fiber Spar Configuration

Such a structure provides full elastic behavior, while undergoing large deflections such as the flapping motion. The wings of this research platform can be divided into two essential zones, the luff region and the thrust flap region, shown in Figure 35 above. During a wing stroke, the camber of the luff region forms an airfoil shape camber, while the thrust flap region bends out and forms a self-activated flap. These combined characteristics found in birds and bats and are observed in the Bio-inspired research vehicles. The ornithopter research platforms consists of a wing membrane (Figure 35) with stiffening carbon fiber spars, a simplified architecture-like found in bats (Figure 38). In both the vehicle and bats, a camber forms in the wing membrane and forms out during a wing stroke. With camber forming in combination with a complex structure of joint motions, a positive and negative Angle of Attack (AoA)

shapes out during a wing beat. The mechanisms utilized in these bio-inspired research platforms are analogous to bats.



Figure 38: *A bat (Cynopterus brachyotis) in flight Photo from Kampang et. all 2007 (Wei Shyy, 2008)*

Like a bird, the research platform is outfitted with a self-activated flap region; the so-called “Thrust flap region” (Figure 35). According to bird flight, flexible convert feathers (Figure 39) act like self activated flaps similar to the thrust flap region [22].

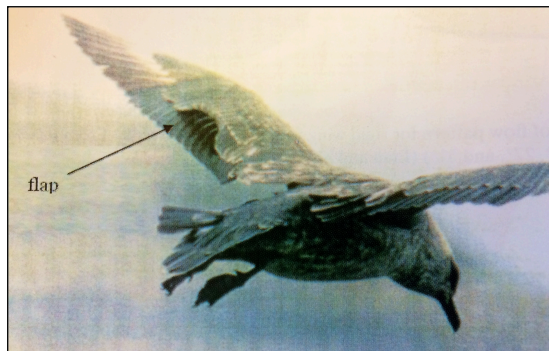


Figure 39: *Upper Wing surface of a Natural Avian Flyer Skua. Photo from Becert et al. 1997 indicating flap region in bird flight*

The primary research platform (Figure 33) features the wing (Figure 35); the tail (Figure 40); the fuselage (Figure 41); and the stiffening carbon fiber spars (Figure

36), which are make up the leading edge spar; the diagonal spar; and, the finger spars.

Table 3 below specifies the material and dimensions of these primary research platform features.



Figure 40: *Design Feature Tail (ML101)*

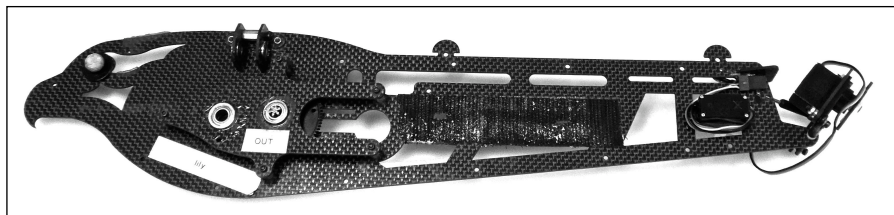


Figure 41: *Design Feature Fuselage (ML101)*

Table 3: *Material and Dimensions of Ornithopter Structures*

Element	Thickness Diameter in [mm]	Material	Density [kg/m ³]
Wing Membrane	0.06	Polyester Ripstop	500
Leading Edge Spar	3.6	Carbon fiber	1750
Diagonal Spar	1.8	Carbon fiber	1750
Finger Spar 1-4	1	Carbon fiber	1750

The research platforms are radio controlled, and the flapping motion is driven by an electric motor through a gear box and a bar linkage. The resulting motion drives the

leading edge spar close to the fuselage where the bar linkage is attached to a shoulder joint provides further details about the research platform [82] [15].

The secondary research platform, MSK004, has a analogous configuration to the primary research platform (ML101), but differs according to aircraft specification found in Table 3 below. The main difference of the secondary research platform (Figure 34) lies in the scale; MSK004 is of larger scale.

Table 4: Aircraft Specifications

Ornithopter Platform	Symbol	ML 101 (Harmon, 2008; Wissa, 2013)	MSK 004 (Harmon, 2008; Grauer, 2011)
Wing span	b_w	1.07 m	1.21 m
Flapping rate	f_r	4 – 6 Hz	2.5-5 Hz
Total Mass	m_t	0.42 kg	0.45 kg
Forward speed	v_f	2.5-8.5 m/s	2.5-8.5 m/s
Wing mean aerodynamic chord	\bar{c}_w	0.22 m	0.29 m
Wing area	S_w	0.23 m ²	0.3 m ²
Wing aspect ratio	AR_w	4.97	4.40
Tail span	b_t		0.20 m
Tail mean aerodynamic chord	\bar{c}_t		0.20 m
Tail area	S_t		0.04 m ²
Tail aspect ratio	AR_t		1.50
Reynolds Number Regime	Re	1.9x10 ⁴ and 23x10 ⁴	1.9x10 ⁴ and 23x10 ⁴

The flapping angle, and the upstroke and downstroke sequence for the research platform are defined next and are used throughout this work.

At maximal negative flapping angle, the flapping angle for an extended wing is 0. The upstroke to downstroke to transition occurs at the maximal positive angle of attack the downstroke to upstroke transition at the minimal negative angle of attack.

Figure 42 shows the Upstroke and Downstroke transition.

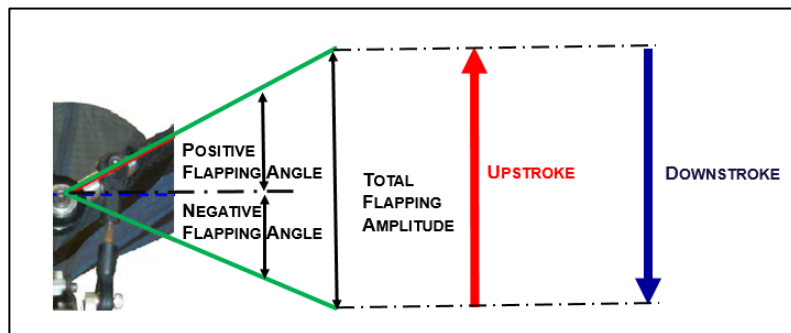


Figure 42: Definition Flapping Angle (FA) and Upstroke and Downstroke on shoulder joint/ bar linkage (ML101)

Figure 11 shows the primary (ML101) scale research platform undergoing a flapping cycle and the upstroke, downstroke sequence.

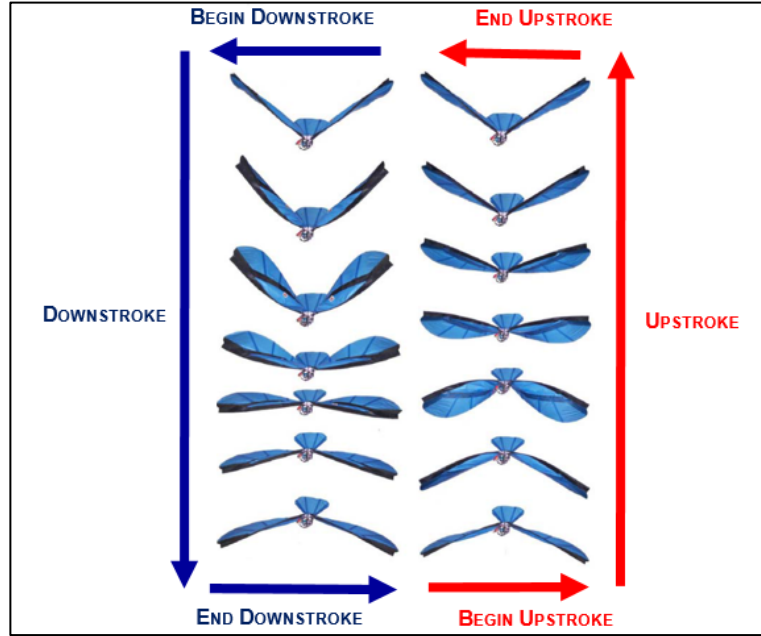


Figure 43: *Upstroke and Down stroke Sequence Ornithopter (ML101) scale; Image credit Harmon [19]*

In summary, this section described the design features and specifications for the primary (ML101) and secondary research platforms (MSK004) used in this work for modeling and verification purposes.

3.2 Experimental Data

In the following sections, the ornithopter experiments utilizing the ML101 and MSK004 research platforms, and resulting data used in this research, are reviewed. First, a brief description regarding the archival ornithopter tests used for verification of this model is provided, in addition, the data extracted that were used in the frame of this work, are presented. Following this is a description of the free flight test and vacuum chamber experiment developed in order to verify and validate the assumptions and constraints of the model. The first archival experiments are named

clamped test E1 and System-ID Experiment E1-I. Further experiments include a free flight experiment, which is denoted as free flight test E2, and the vacuum chamber experiment, which is denoted as E3 in the following work.

3.2.1 Clamped Test Experiment - E1

Experimental flight test data are instrumental in order to model the complex problem given. The University of Maryland has established a unique experimental flight test database of its ornithopter fleet that contains wing surface motions and kinematics as well as force time histories collected using a Vicon ® vision data collection system. Wing kinematics and integrated forces on the ornithopter fuselage, during flapping, were obtained for the ML101 and MSK004 research platforms. Flapping frequencies of 5 Hz and 6.17 Hz were obtained for research platform ML101, and 4.5 Hz for research platform MSK004. In E1, the Vicon Vision ® system uses six high speed cameras at 350 frames/sec to track the 3D position of 3mm reflective markers attached to the wing surface as seen in Figure 44.



Figure 44: *MSK004 wings with tracking markers [19]*

The ornithopter frame was rigidly attached to a ground stand. The vertical propulsive force (VPF) and the horizontal propulsive force (HPF) produced by the flapping motion are measured using a six degree-of-freedom load cell that is mounted to the

ground stand and supports the ornithopter. Harmon (2008) provides additional details [19]. The complete experimental set up is shown in Figure 45.



Figure 45: *MSK004 and Vicon camera system for the measurement of ornithopter wing and configuration motions [19]*

It is noted that the clamped condition provided in load cell testing disturbs the overall system dynamics and kinematics because it interferes with the pitch moments and flight aerodynamics. Constraints are on rotational and translational degrees of freedom of the fuselage body-fixed reference frame as defined in Chapter 4.

Constraint integrated forces and moments measured with the 6 degrees of freedom load cell are used for the verification of overall integrated force production of the model simulated in clamped conditions. Wing kinematics are used for proof-of-concept study of the aerodynamic model development, which is adjusted for the clamped conditions by an adjustment of circulatory effect as described in Chapter 5. Data resulting from E-1 extracted for this work are presented next.

3.2.1.1 Results Experiment- E1

3.2.1.2 Integrated forces- E1

The total measured horizontal and vertical propulsive force measured (HPF/VPF) with the 6-degree of load cell, by Harmon (2008), was used from the Morpheus Lab database, and is utilized for the model verification [19].

HPF and VPF data versus the stroke angle obtained for the ML101 research platform, at flapping frequencies of 5.0 Hz and 6.17 Hz, were extracted and processed from the aforementioned database according to Figure 46 through Figure 49.

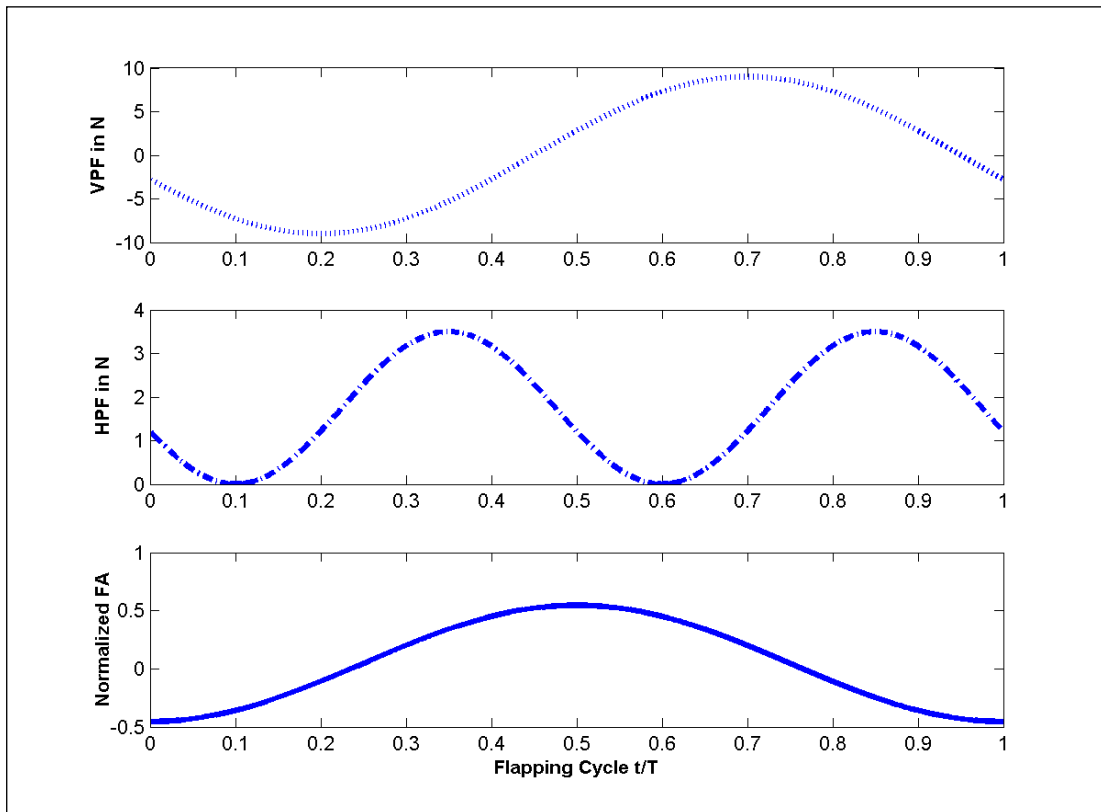


Figure 46: *Harmon Aerodynamic Model Results and Bench Test Results Measured Integrated forces ML 101 at 5 Hz Flapping frequency, over a flapping cycle t/T a) Vertical Propulsive Force VPF b) Horizontal Propulsive Force (HPF) c) Normalized Flapping angle FA*

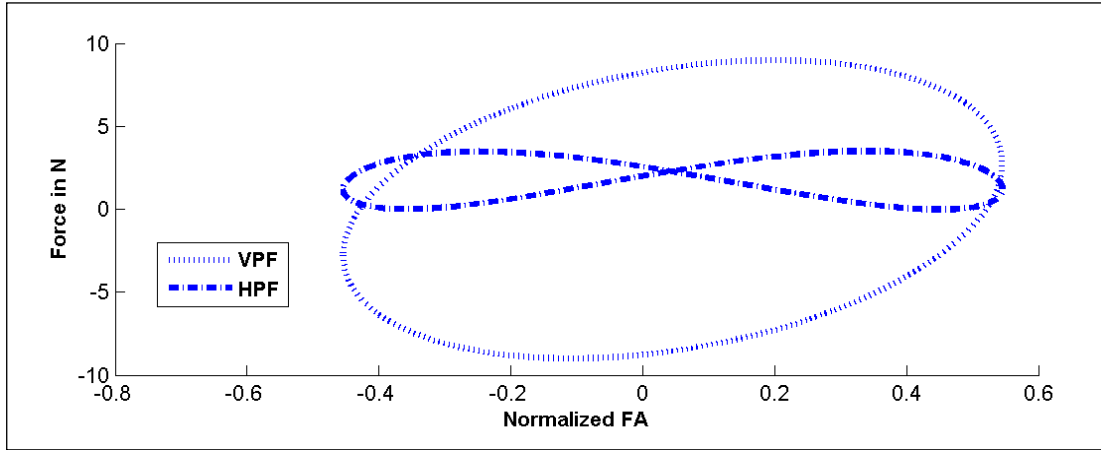


Figure 47: *Harmon Bench Test Results Measured Integrated forces ML 101 at 5 Hz Flapping frequency, over a flapping cycle t/T a) Vertical Propulsive Force VPF b) Horizontal Propulsive Force vs. normalized flapping angle (FA)*

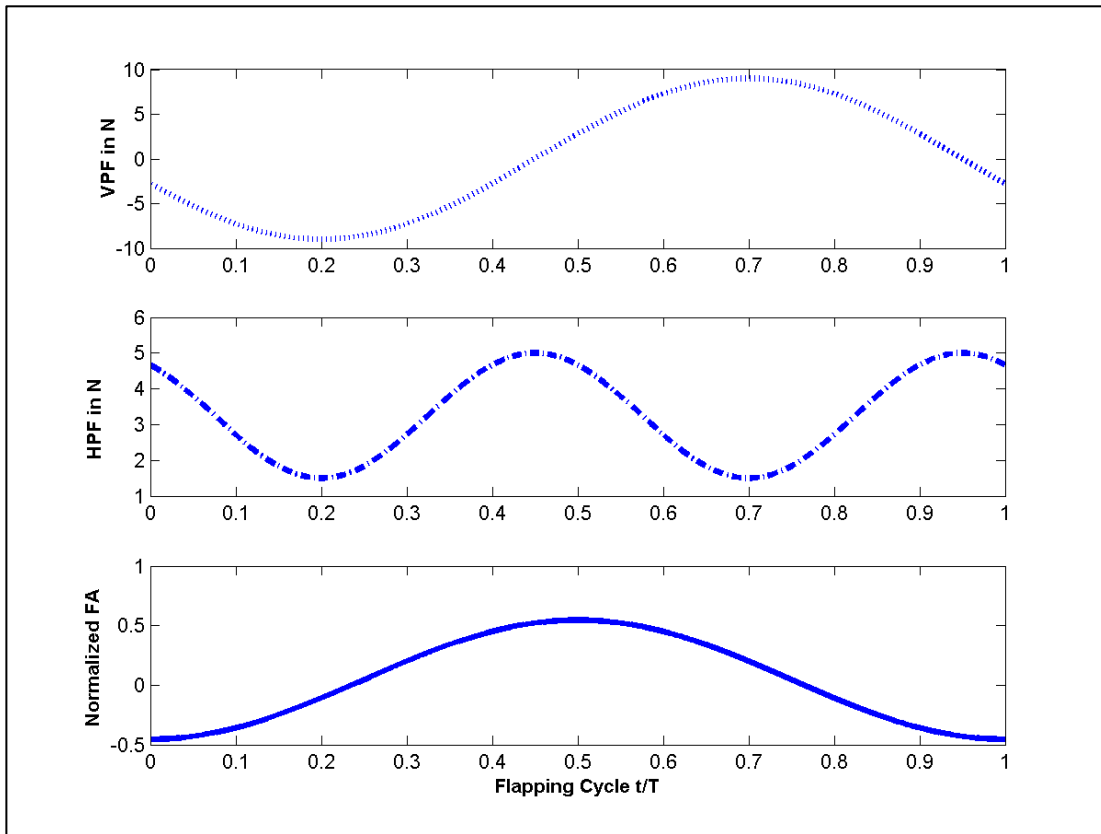


Figure 48: *Harmon Aerodynamic Model Results and Bench Test Results Measured Integrated forces ML 101 at 6.17Hz Flapping frequency, over a flapping cycle t/T a) Vertical Propulsive Force VPF b) Horizontal Propulsive Force (HPF) c) Normalized Flapping angle (FA)*

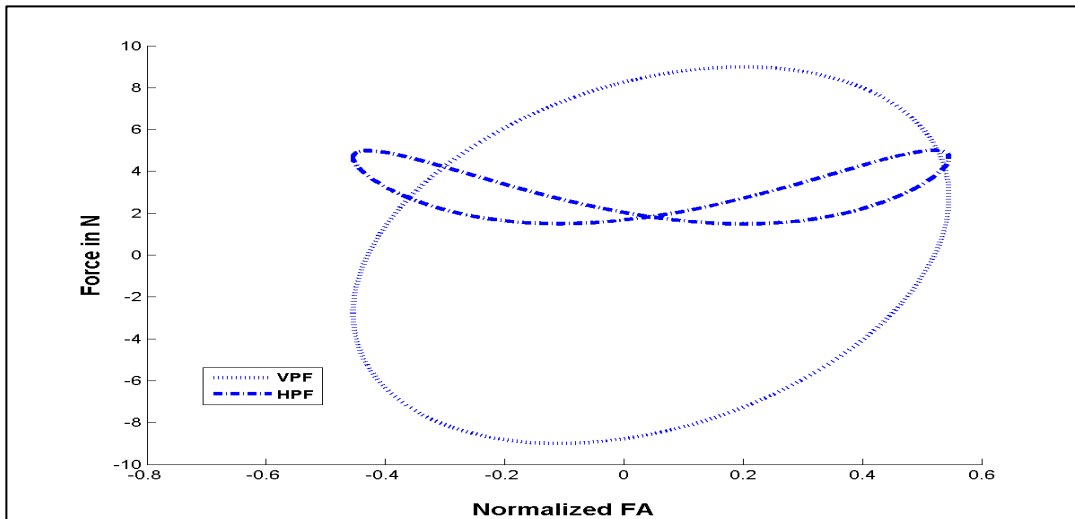


Figure 49: *Harmon Bench Test Results Measured Integrated forces ML 101 at 6.17 Hz Flapping frequency, over a flapping cycle t/T a) Vertical Propulsive Force VPF b) Horizontal Propulsive Force vs. normalized flapping angle (FA)*

Mean Absolute Vertical Propulsive Force (MAVPF) and Mean Horizontal Propulsive Force (MHPF) vs. flapping frequencies were extracted from the E1 experiment database and were used for model verification. Error bars were included according to the properties of load cell and the data measurement system used.

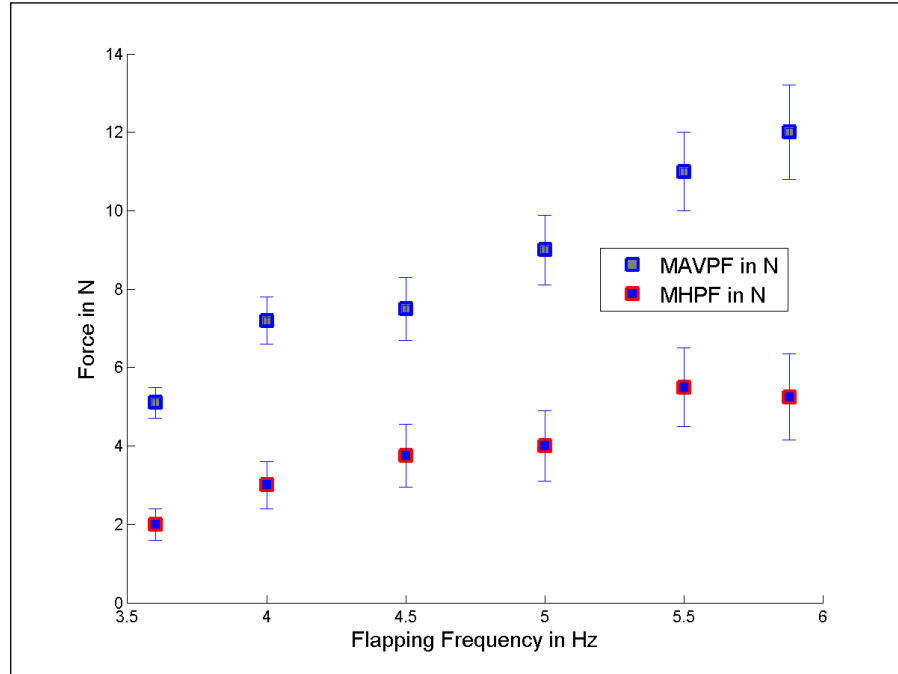


Figure 50: Results and Bench Test Results Measured Integrated forces ML 101 vs. flapping frequency, over a flapping cycle t/T a) Mean Absolute Value Vertical Propulsive Force VPF b) Horizontal Propulsive Force vs. Flapping angle [19]

3.2.1.3 Wing Kinematics - E-1

ML101 wing kinematics obtained in E-1 were used as input for Aerodynamic Model A as described in the Aerodynamic Section below. A data set of 110 tracking markers, at a flapping frequency of 6.17 Hz, was used for kinematic simulation verification and input to Aerodynamic Model A. Data was measured at a resolution of 1-2 millimeters, at a rate of 350 Hz. Data array, for one full flapping cycle of 56 position states for 110 tracking markers, in a fuselage fixed reference frame, was used and extracted from the data base. Three position states of used data are shown in Figure 51.

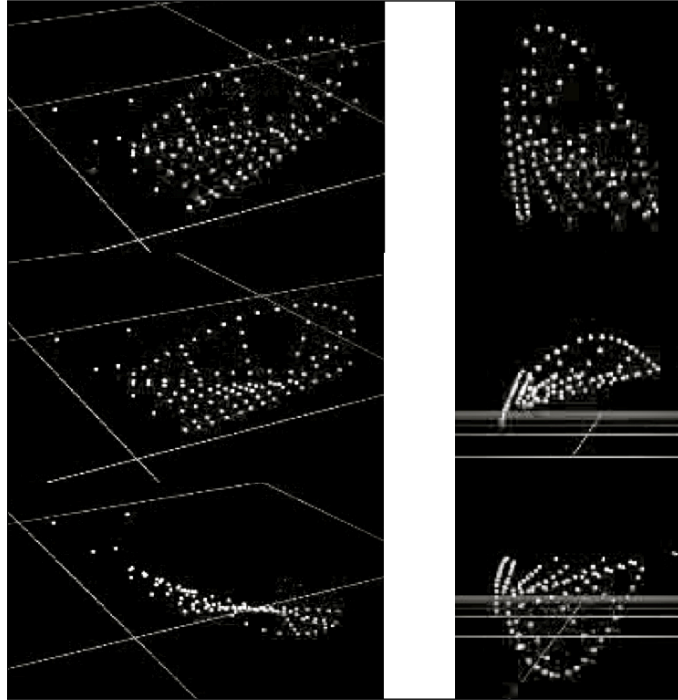


Figure 51: *Vicon Vision ® wing Kinematic sequence – 3 Position State Tracking Markers $i=1$ to 110 a) isometric view b) side view in a fuselage fixed Reference Frame CB0*

3.2.2 System-ID Experiment - E1-I

System identification of the ornithopter wing kinematics and the development of aerodynamics model, using free-flight data, has been done using the MSK004 research platform [9] [16]. Aerodynamic model results obtained from Grauer, 2011 are used to verify the resulting aerodynamics model in this research. In the aforementioned experiments, eight cameras were placed to capture a flight volume of 10 m long by 6 m wide and 5 m tall [9]. At 500 Hz, these cameras recorded the spatial position of the retro reflective markers placed on the ornithopter’s fuselage, wings, and tail (Figure 52); this was done as the ornithopter was flown through the control volume. This method, and the amount of reflective markers, were sufficient to perform a system identification of a 3 body-rigid body dynamics model and

aerodynamics model in straight and level flight. Resulting Aerodynamics model results are based on free flight and provide an appropriate source for verification of free flight Aerodynamics Models B and C (see Chapter Aerodynamics). Aerodynamics model resulting from experiment E1-I by Grauer provides integrated forces acting on the fuselage for MSK004 ornithopter configuration. Model B and C provide spatially distributed aerodynamic forces over the wings, and integrated first in order to be compared to E1-I. Grauer (2010; 2011) provides reference details of the tests and resulting aerodynamics model [9] [16].

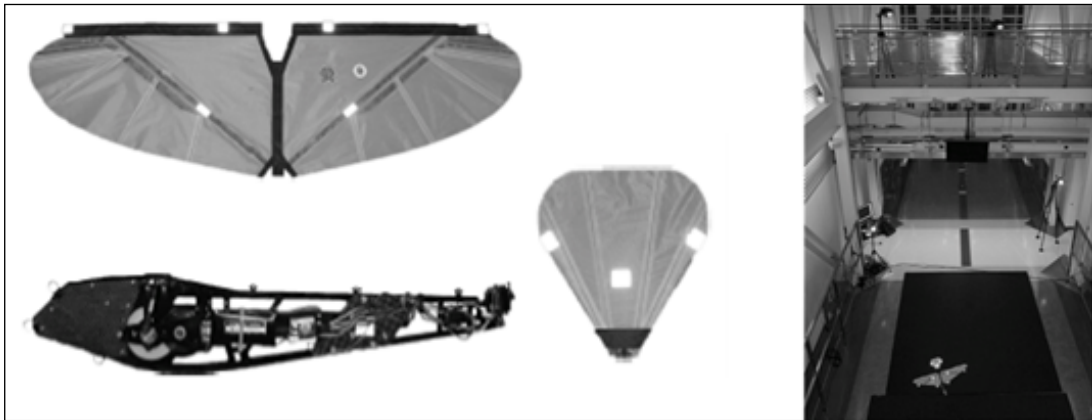


Figure 52: *Vicon ® camera system for the measurement of ornithopter wing and configuration motions [9].*

3.2.2.1 Integrated Aerodynamic Force - E1-I

Following the data from the System ID Aerodynamic Model, which provided integrated forces and moments in free flight for ornithopter configuration MSK004, is used for verification of the aerodynamics model resulting in this research. Vertical and horizontal propulsive forces during a wing stroke were computed using Grauer's model and are plotted in Figure 53. Data serves for verification purposes.

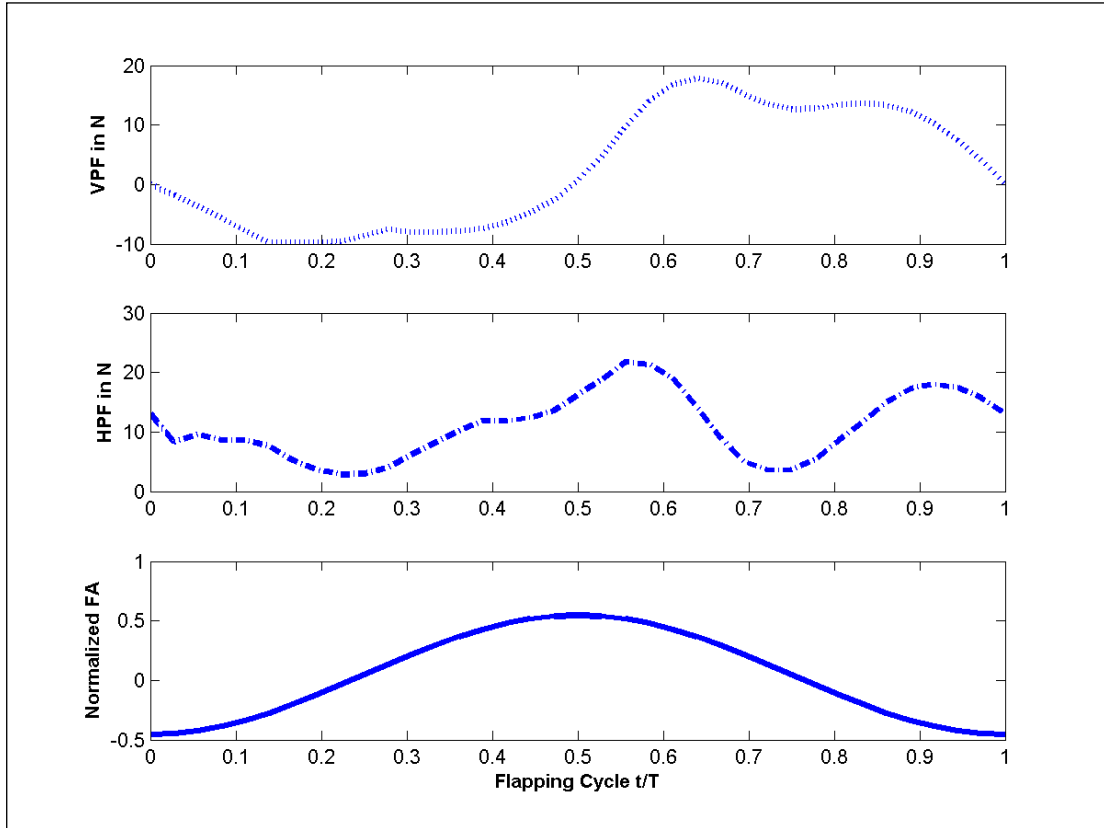


Figure 53: Aerodynamic forces on the wings –Results System ID Model by Grauer [9]

3.2.3 Free Flight Experiment – E2

A free flight test exposing flexible wing kinematics was designed in the framework of this work, and performed by Wissa et. al. [14]. The flight test was conducted with the assumptions and the constraints of this work. The experiment E-2 was designed to capture wing motion profile for verification of the flexible multi-body dynamics model. This resulted in the requirement of a Vicon Vision® software capable of exposing wing flexibility in contrast to the commonly used Vicon Vision systems, which fit rigid body’s in-between reflective markers. This requirement resulted in the flight test to be conducted and facilitated at the Wright Patterson Air

Force Base (WPAFB) in the Air Force Research Lab's (AFRL) indoor small Unmanned Aerial Systems (sUAS) laboratory. The facility hosts the largest Vicon Vision® motion capture system lab in the United States and the test room is fitted with sixty motion cameras tracking retro reflective marker positions with a precision of 1 mm. The following describes the test set up for the experiment, including wing configuration, marker placement, flight test facility, and test set up.

Kinematics of test platform ML101 were measured in free flight in order to verify the flexible multi-body dynamics model. For the test, retro reflective markers were placed on the wing (Figure 35). A diameter of 6.35 mm of the half sphere retro reflective markers was chosen. Chosen marker size lies on the larger spectrum of available markers but ensured the likelihood of full visibility and minimized the likelihood of marker dropout. Precautions were necessary since the desired wing kinematics resulted in the highest marker refinement and the most number of markers flown in the test facility and ensured results. The markers were asymmetrically distributed over both the left and right wings in order to gain high refinement of symmetric wing kinematics of the flight platform, in addition to balancing the weight distribution on both wings. Compared to a symmetric distribution on one wing, this resulted in the feasibility of more tracking points as the distance between the tracking points, for appropriate motion capturing, was provided. Wing tip markers were placed on both wings to test symmetry of wing kinematics during the flight test.



Figure 54: *Asymmetric retro reflective markers on the wing (seen as white dots) and Wing tip Location (Marked in Red)*

Forty-four markers were placed on the wing according to the figure above. Distribution was chosen based on blade element selection for the aerodynamic model. The number of markers on the ML101 test platform were fifty-three in total. In order to determine fuselage kinematics, five markers were placed on the ornithopter fuselage; three were placed on the tail in order to monitor control inputs and one was mounted on the wing root in order to track relative wing displacement. The markers on the flight platform are denoted as $i=1$ to 53 (Figure 55).

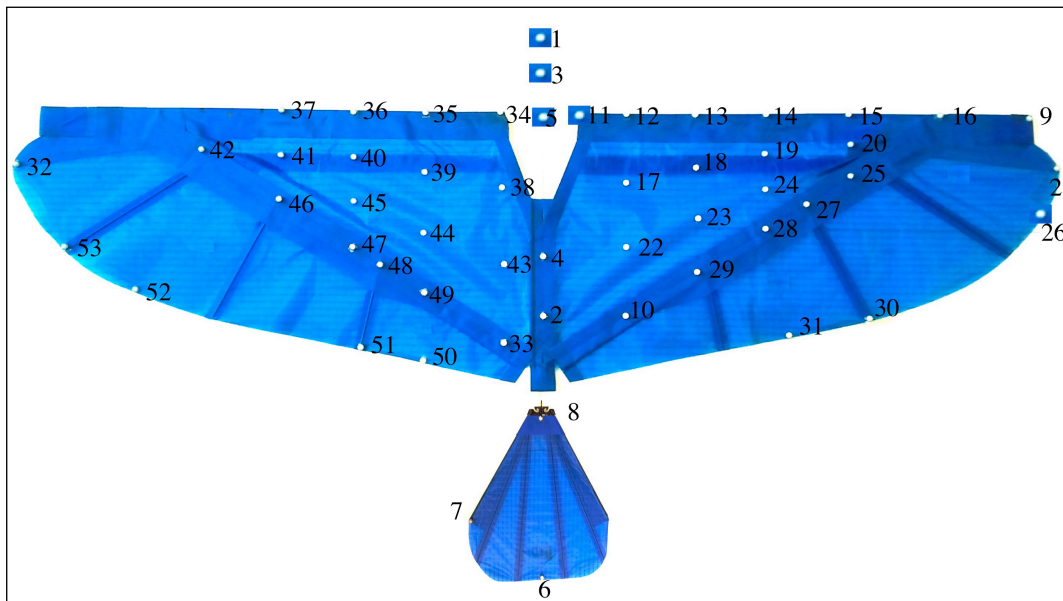


Figure 55: Retro reflective Marker position on the wing measured with Vicon Vision System
 Markers $i = 1$ to 53. Markers $i = 1$ to 5 were mounted on the fuselage.

Data, using the Vicon Vison Nexus® software, was captured at a sampling rate of 200 frames per second (200Hz). The flight test facility was fitted with 60 Vicon Vision cameras (

Figure 56). Figure 57 shows the test set up that was used.

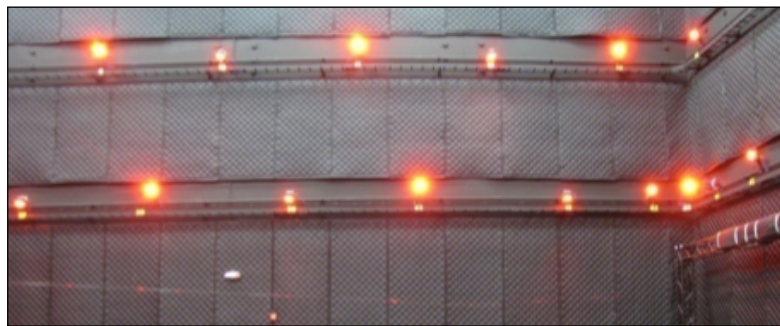


Figure 56: Image SUAS Flight test facility - Vicon ®Vision System Cameras [14]

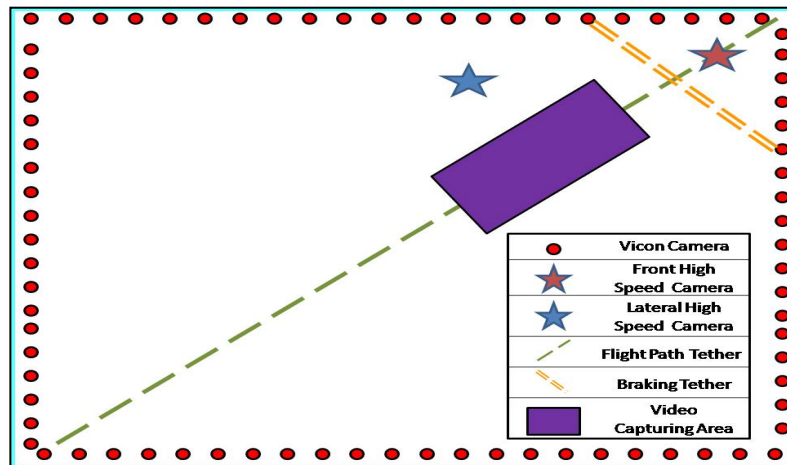


Figure 57: Test Set up Schematic – [Wissa et al., 2012] Test Chamber Dimensions: 70'(W) x 35'(D) x 35'(H) [14]

Additional high speed cameras captured images of the ornthicopter flight; the flight test platform was mounted on a tether to guide flight. Videos were captured using the video capture volume. The test chamber dimensions were 70'(W) x 35'(D) x 35'(H)

[14]. Flight platform ML101 was radio-controlled by a ground pilot and freeflight was ensured in the test volume. Results of the free flight test used for verification of the ornithopter model are described next.

3.2.3.1 Results for Wing Kinematics E-2

A total of fifty-three wing kinematics markers were measured in free flight. Data obtained for the verification was captured in the inertia reference frame CI_0 (Figure 58). Choice of coordinate notation is according to the standard aircraft dynamics; north, east, down (NED) convention. Figure 58 shows the location of the inertia reference frame CI_0 and additional coordinate systems used. For mathematical convenience, the inertia reference frame of the flight test data is rotated 16-degrees into the inertial reference frame CI . The x-axis of CI points in flight direction. R_{IB} is the position vector from the inertial reference frame CI to the body fixed reference frame CB on the fuselage (Figure 58). For verification and modeling purposes, wing position states are rotated and translated in the fuselage fixed reference frame, CB_0 , located on the wing root. The position vector $r_{B B_0}$ is the translation in-between CB and CB_0 .

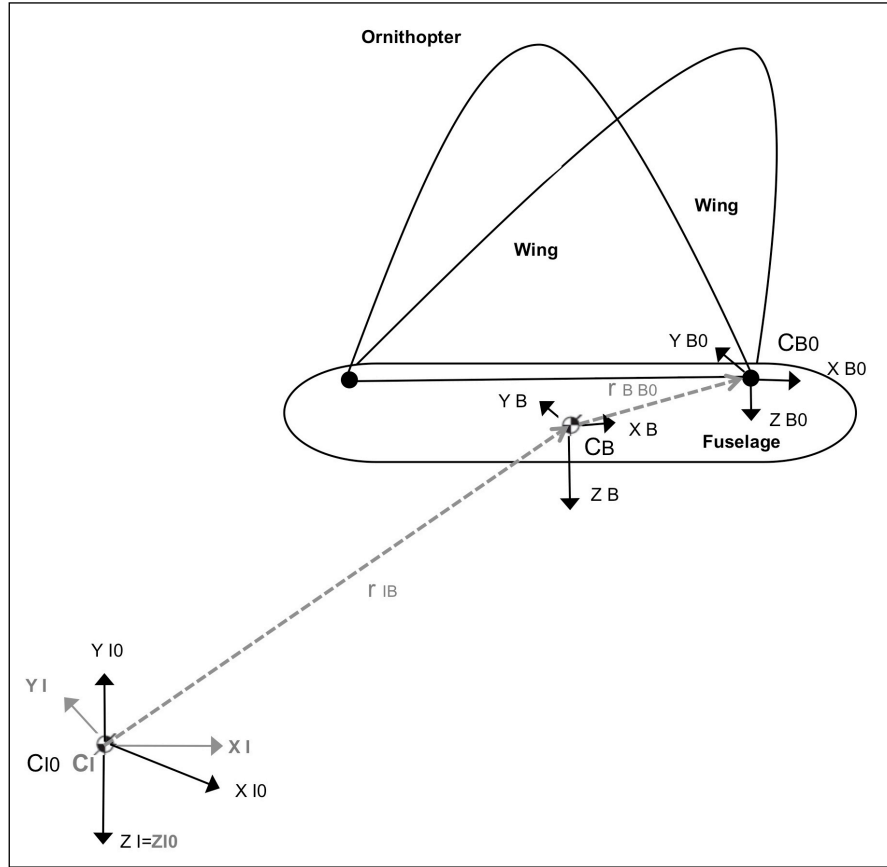


Figure 58: Schematic Ornithopter and Reference Frames used for the processing of free flight test data.

The data matrix used in this work contains 53 Marker locations in 125 position states $X/Y/Z$ and are measured in the inertia frame $CI0$. The data array used for verification and flight test is 34 frames per marker (53), with 3.5 flapping repeatable flapping cycles. Data was captured at a flapping rate of 6.06 Hz, which results in 34 data points per marker, per flapping cycle, hence 125 position states for each marker.

Free flight test data for ML101 flight test platform are shown in Figure 59 to Figure 63. Individual lines in Figure 59 represent the position of markers $i=1$ to 53 during free flight.

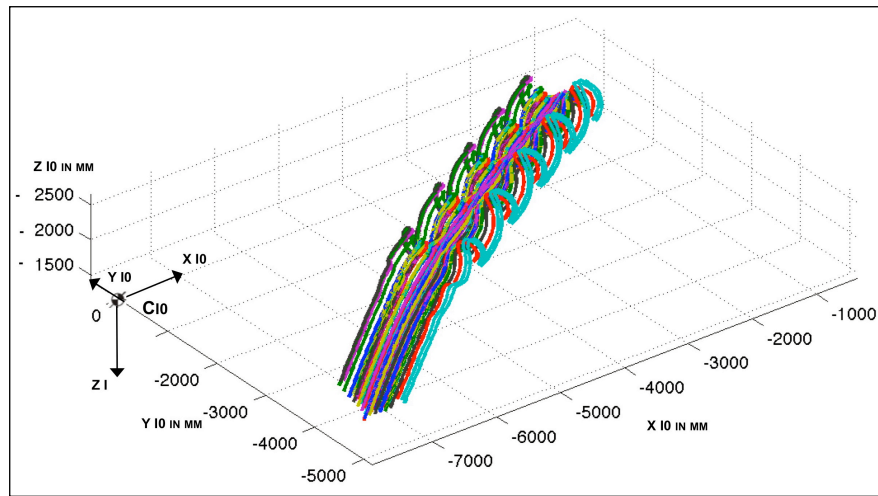


Figure 59: Data Set Marker Position during Free Flight in the inertia reference frame CI_0 .

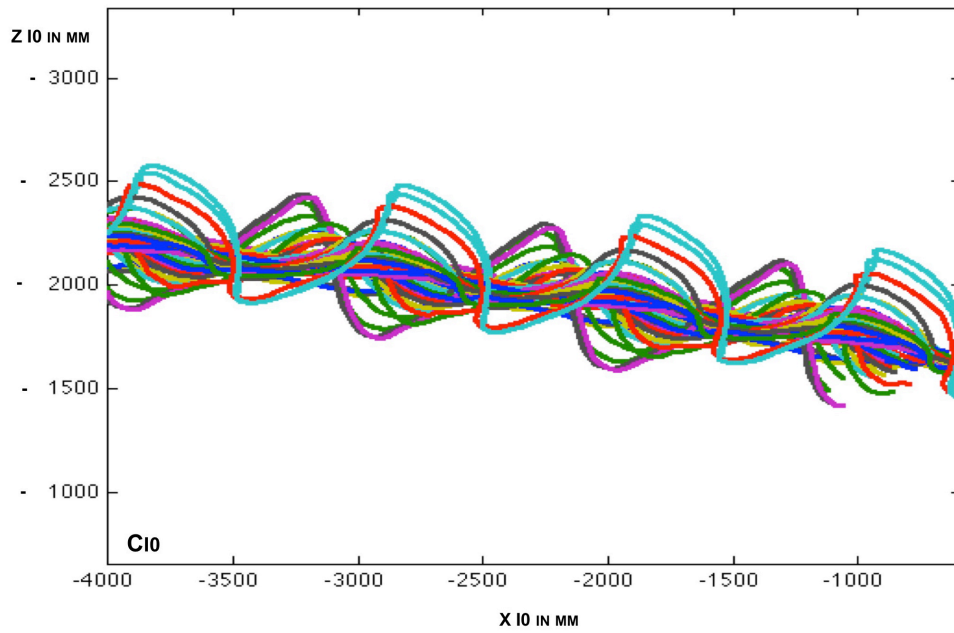


Figure 60: Data Set Marker Position $i=1$ to 53 during Free Flight in the inertia reference frame CI_0 – View ZI_0/ZI_0

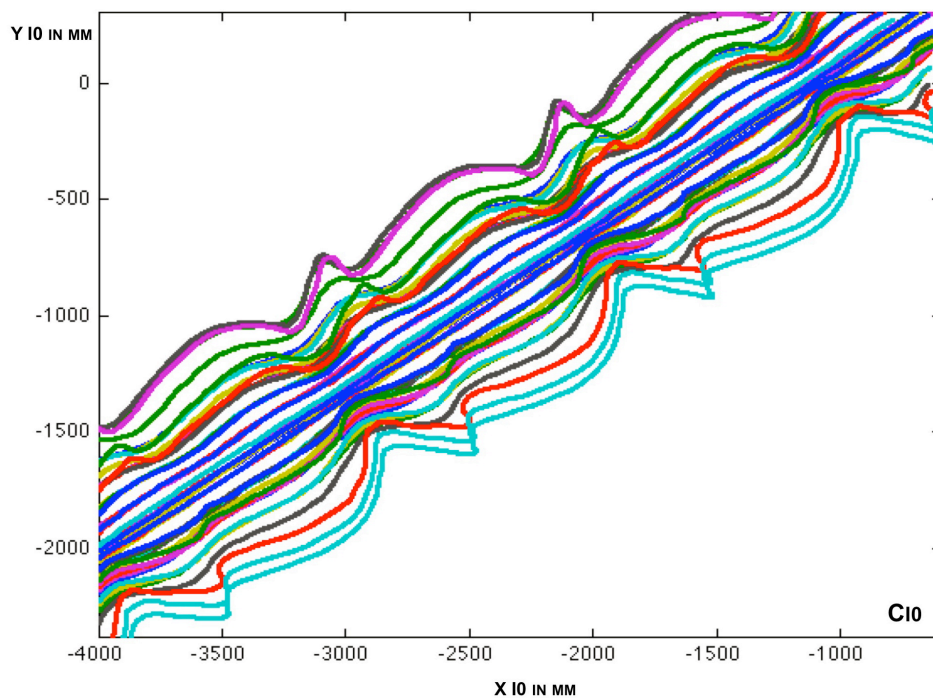


Figure 61: Data Set Marker Position $i=1$ to 53 during Free Flight in the inertia reference frame CI_0 – View YI_0/XI_0

Repeatable free flight flapping cycles were extracted according to the volume shown in Figure 58 and post processed using MATLAB®.

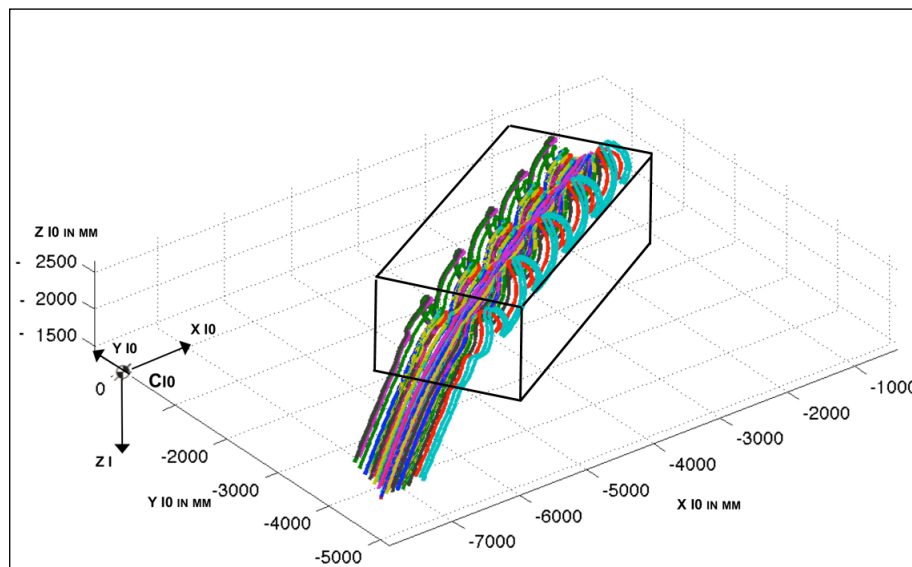


Figure 62: Position States all tracking markers on the wing/ Volume shows test data used for model development- 3.5 Flappingcycles.

For clarification, one position state of all tracking markers, $i=1$ to 53, is illustrated in **Figure 63**. The position state is plotted in the fuselage fixed reference frame CB 0 and is shown in **Figure 58**.

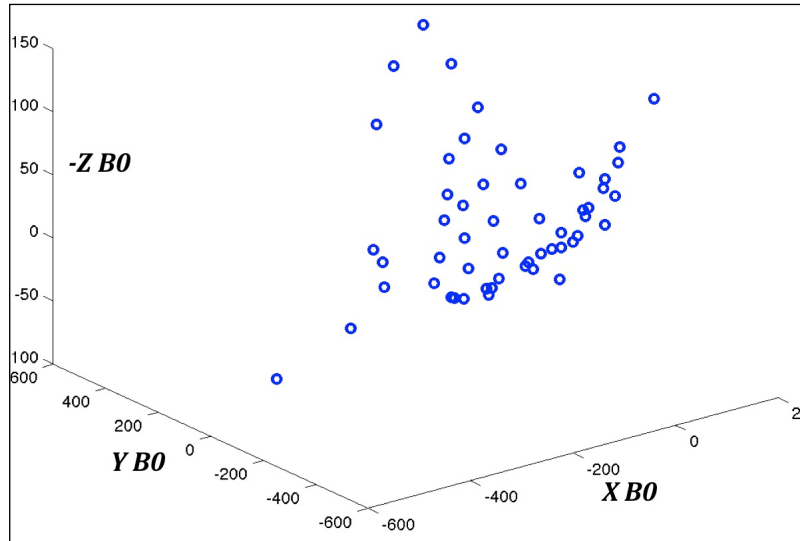


Figure 63: Single position state on Ornithopter shows all tracking markers $i=1$ to 53 in the fuselage fixed reference frame CB0

Wing kinematics data shown in Figure 59 to Figure 63 are used for modeling and verification purposes throughout this work.

3.2.3.2 Total Forces - E2

The total vertical force (VF) was calculated from flight test data at the fuselage center of mass and origin of CB (**Figure 58**). Force is obtained from the total vehicle acceleration calculated from the position state of the fuselage fixed-body reference frame, CB, in the inertial reference frame, CI, and the total vehicle mass of research platform ML101. Following VF and Horizontal Force (HF) (**Figure 64**), results from the flight test data were used to verify model calculations. VF results

from the vehicle acceleration, along the z axis of CI, and HF, along the x axis in CI. In order to determine the state in the flapping cycle, the data was presented in reference to the Flapping Angle (FA).

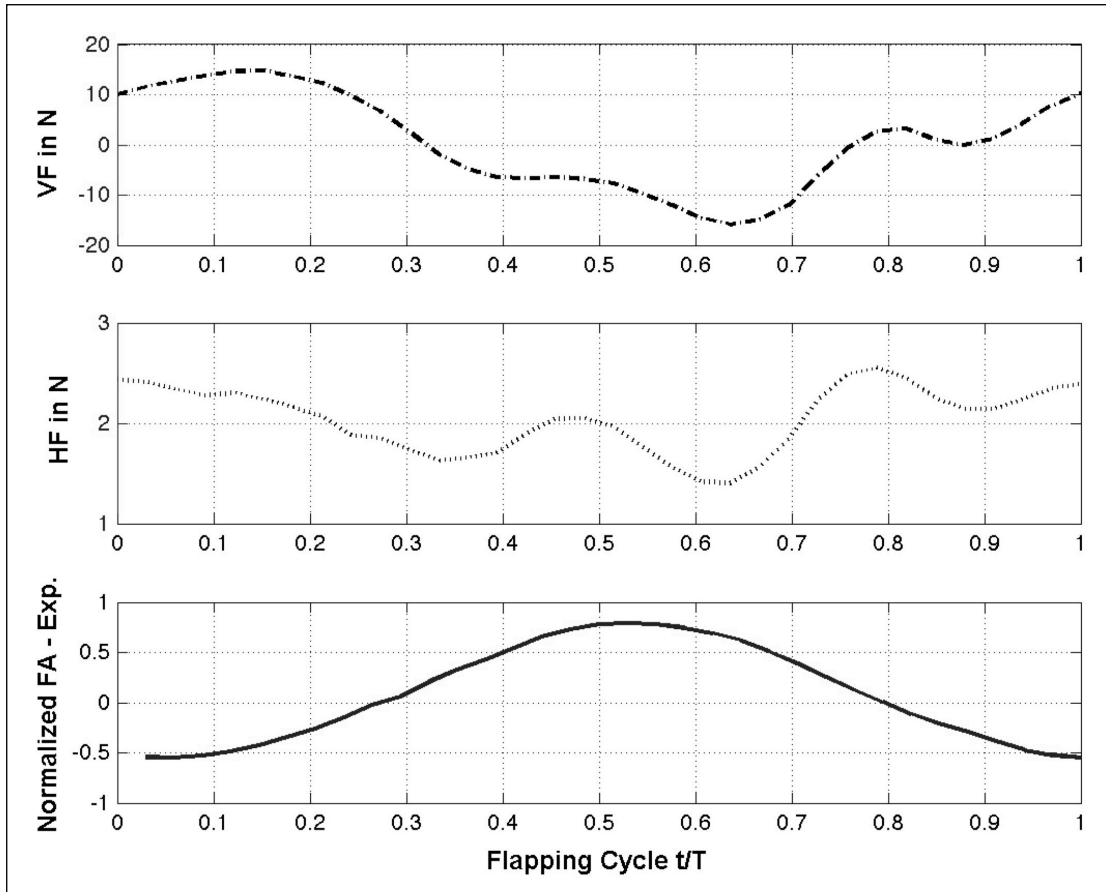


Figure 64: Vertical Propulsive forces acting on the fuselage center of mass – Obtained from Experiment

In summary, free flight verification data obtained and used for the modeling development and verification was presented in this section.

3.2.4 Vacuum Camber Experiment – E3

In order to verify inertial forces without the presence of aerodynamics, the primary research platform was tested in a vacuum. Testing was conducted at NASA Langley Research Center.

The experimental research platform was the primary research platform ML101. It was mounted on a 6-degrees of freedom load cell in a vacuum chamber and integrated forces were measured. Figure 65 shows the experimental set-up reference [91] discusses further details regarding the load test [91].

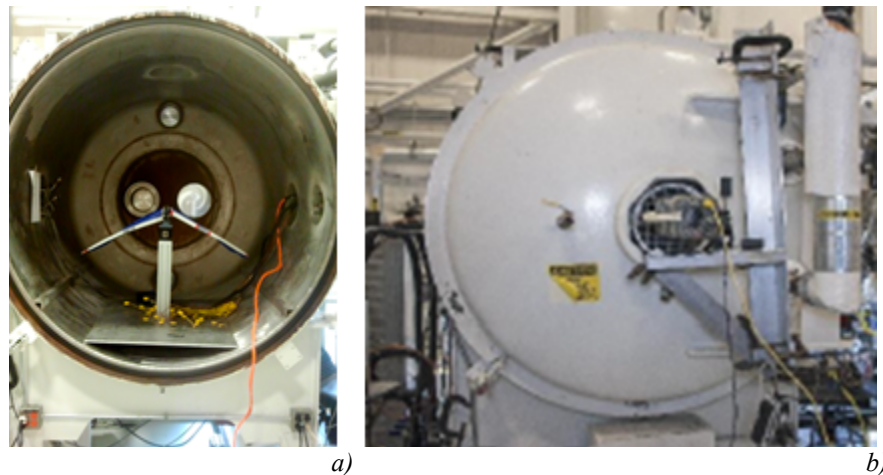


Figure 65: *Vacuum Chamber at NASA Langley Research Center. Left) Research Platform Mounted on 6-degrees of freedom Load Cell, Right) Vacuum Chamber*

An additional wing kinematics test, within the assumptions and constraint of this model, was developed and conducted [82]. Inclusion of wing kinematics data obtained in the vacuum exceeds the framework of this work.

3.2.4.1 Integrated Inertial Forces - E3

Extracted data from the test used for the verification of this model are Inertial Horizontal Propulsive Force (IHPF) and Inertial Vertical Propulsive Force (IVHF),

according to **Figure 66**. Due to the small measured magnitude of the integrated forces and the corresponding low signal to noise ratio mean, integrated forces were used only for verification reference. Pitching moment and verification of integrated forces over the flapping cycle was also excluded for this reason.

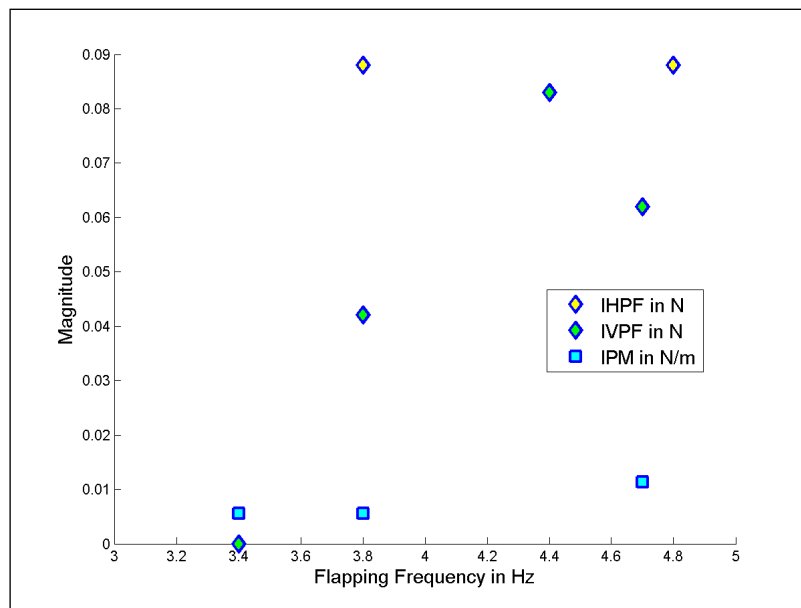


Figure 66: Results Vacuum Chamber test ML 101 Research Platform vs. flapping frequency
a) Inertial Horizontal Propulsive Force IHPF b) Inertial Horizontal Propulsive Force c)
Inertial Pitching Moment vs. Magnitude.

Experimentally measured data used and obtained for this work have been presented in this chapter and experiments E1, E1-I, E2, E3 were discussed briefly. Data was utilized for verification of forces produced by the model, coupled and decoupled, for verification of kinematics simulation, final model initialization, input kinematics for the aerodynamics model, and to check structural and flexible-multi-body dynamics modeling assumptions.

Chapter 4: Flexible Multi-Body Dynamics Model

The topic of flexible-multi- body dynamics itself is an interdisciplinary field that encompasses several other subjects such as rigid body dynamics, continuum mechanics, finite element method, and numerical, matrix and computer methods.

Basic approaches used in Simulation and computer aided calculations for flexible multi-body dynamics and kinematics can be categorized into four different approaches, the floating frame of reference formulation (FFR), the finite element incremental method (FEIM), and the large rotation vector formulations (LRVF) and the absolute nodal coordinate formulation (ANCF). Approaches like the finite segment method (FSM), and the linear theory of elastodynamics (LTED) can be considered derivatives of the first three basic methods mentioned above [52].

The field of flexible multi body dynamics has advanced significantly in the last two decades, however the desired level of maturity in order to apply one numerical method to any flexible-multi body dynamics problem is still lacking, and a deep understanding of the physics of the modeled system is required in order to use appropriate techniques and accomplish reliable calculations.

The field of flexible multi- body dynamics can significantly be furthered if the relationships between different formulations that are established. This allows the assumptions and approximations underlying each method to be clearly defined and research is needed in this area [52]. The potential method for all flexible- multi body

dynamics problems is the absolute nodal coordinate formulation (ANCF) is generally thought of to be able to be used for complex and highly nonlinear systems, but is computationally very expensive due to the high number of DOFs and therefore is a challenge itself to be applicable for complex systems. A wide range of degrees of freedom reduction techniques exist and is a research topic of interest. Earlier attempts used static condensation techniques i.e. Guyan reduction, which rely on master and slave nodes [55] [92]. Reduction only considers stiffness properties often fails to accurately predict, the total mass of the system, center of mass location, moment of inertia and natural frequencies. Research here implements a modal superposition method which accounts for full inertia coupling and relates it to a rigid multi-body assumption of the problem. In the approach a large number of DOFs of a flexible- body are approximated as a linear combination of a smaller number of shape vectors and integrated as such in the global system.

The ornithopter at hand results in a linear elastic multi- body dynamic system in floating reference frame formulation and has following properties which are discussed in this chapter. Development in conjunction with experimental data leads to a linear elastic multi-body system using five bodies. The floating reference frame formulation results in two sets of coordinates to describe the configuration of the individual deformable wing bodies. Herby the elastic deformations are described in local wing fixed reference frames. The wing fixed reference frames are actuated to achieve large global motions i.e. large flapping motion and oscillating body dynamics. The structural deformations are obtained by a linear combination of mode

shapes. The flexible- body constraints and modes are implemented using the Craig-Brampton method. Background, methods used and assumptions and EOM used for the model of ornithopter model are described in this section.

4.1 Linear- Elastic Multibody Systems

Equations of motion for the ornithopter- multi body system were solved using three formulations. A rigid-body formulation and an approach which is coherent with the linear theory of elasto-dynamics by using incremental finite element formulations that is the decoupling of the structural and rigid- body equations of motion. A formulation using full coupling the Equations of Motions (EOM's) through a reduced model compared to an absolute nodal coordinate formulation (ANCF). This is an appropriate floating frame of reference (FFR) formulation. Equations of motions for methods are discussed and investigated in the following in terms of suitability for the flexible multi- body dynamics simulation of ornithopter. The final EOM's used for the ornithopter system is described in the next paragraphs. The approaches are here also reviewed in terms of aerodynamic coupling. Results suggest the inclusion of flexible cross-terms in the time varying mass matrix of the EOM of the system. (See chapter results 6.4.3). Using the appropriate coordinate definition of the linear elastic multi- body system, the problem at hand is adequately modeled using FRR, placement of the coordinate systems facilitates a stiffness matrix that is decoupled from the rigid body equations of motion.

The equations of motion of a deformable body can be described in a general form

according to

$$M^i \ddot{\xi}^i + K^i \xi^i = f_e^i + f_v^i + f_c^i \quad (\text{Eq. 1})$$

Where M is the Mass Matrix, K is the Stiffness Matrix, i denotes the number of bodies, f_e the externally applied forces f_v the Coriolis and Centrifugal Forces, f_c the Constraint forces.

The constraint forces f_c in are in terms of the Jacobien Matrix J and the Lagrange multipliers λ . The Jacobien Matrix J is in terms of the constraint equations the joint constraint and specific motion trajectories (Eq. 2).

$$f_c = -J^{iT} \lambda \quad (\text{Eq. 2})$$

Using the floating reference formulation the, one can partition the generalized coordinate in reference coordinates r and elastic coordinates f according to following:

$$\xi^i = \begin{bmatrix} \xi_r^T & q_f^T \end{bmatrix}^T \quad (\text{Eq. 3})$$

Here ξ^i is the generalized coordinate of the flexible body i . ξ_r is the generalized Coordinate of a rigid body comprised of three translational and three rotational Coordinates (That is the Euler angles) and are thought of to be the reference coordinates. q_f are the elastic coordinates and can be introduced using component mode methods, the finite element method or experimental identification techniques [52]. They are the coordinates of the flexible body in the local reference frame and are described

further in sections below. The elastic coordinates q_f are obtained through the finite element method in this work. They are implemented through a component mode method and compared to experimental identified displacements.

Now the equation of motion (Eq. 1) of the deformable body can be expanded according to following general form.

$$\begin{bmatrix} M_{rr} & M_{rf} \\ M_{fr} & M_{ff} \end{bmatrix} \begin{bmatrix} \ddot{\xi}_r \\ \ddot{q}_f \end{bmatrix} + \begin{bmatrix} 0 & 0 \\ 0 & K_{ff} \end{bmatrix} \begin{bmatrix} \xi_r \\ q_f \end{bmatrix} = \begin{bmatrix} f_{er} \\ f_{ef} \end{bmatrix} + \begin{bmatrix} f_{vr} \\ f_{vf} \end{bmatrix} + \begin{bmatrix} f_{cr} \\ f_{cf} \end{bmatrix} \quad \text{(Eq. 4)}$$

Here the mass matrix is highly nonlinear, inertia coupling between the reference motion and the elastic deformation occurs. The stiffness matrix, is the same as the stiffness matrix used in structural dynamics due to the fact that the elastic coordinates are defined with respect to the local body coordinate system.

One can rewrite the Equation of motion (Eq. 4) in a floating frame of reference formulation (FFR) according to following.

$$M^i_{rr} \ddot{\xi}^i_r + M^i_{rf} \ddot{q}^i_f = (f_e^i)_r + (f_v^i)_r + (f_c^i)_r \quad \text{(Eq. 5)}$$

$$M^i_{fr} \ddot{\xi}^i_r + M^i_{ff} \ddot{q}^i_f + K^i_{ff} q^i_f = (f_e^i)_f + (f_v^i)_f + (f_c^i)_f \quad \text{(Eq. 6)}$$

Assuming the theory of linear elasto- dynamics the cross terms between flexible and rigid-body modes vanish according to (Eq. 7) and (Eq. 8).

$$M^i_{rr} \ddot{\xi}^i_r = (f_e^i)_r \quad (\text{Eq. 7})$$

$$M^i_{ff} \ddot{q}^i_f + K^i_{ff} q^i_f = (f_e^i)_f + (f_v^i)_f - M^i_{fr} \ddot{\xi}^i_r \quad (\text{Eq. 8})$$

It is assumed that the elastic deformation does not have a significant effect on the Rigid-body displacements and the EOM's can be solved independently. It is shown in (Eq. 7) that all terms, including the inertia tensor and forces, are assumed to be independent of the elastic deformations [52].

Aerodynamic loads are introduced in the equations set (Eq. 5)(Eq. 6) and equation set (Eq. 7) (Eq. 8) through external forces f_e . They are dependent on the generalized coordinate of the rigid body ξ_f as well as the modal coordinate q_f of the flexible body $f_e(\xi_f, q_f)$ and couple the equations of motion (EOM).

If the inertial forces due to the elastic deformations are neglected according to (Eq.7) and (Eq. 8) the rigid-body motion and the equations of motion for the elastic deformation are only coupled through the aerodynamics of the system, hence aeroelasticity. One can observe that the (Eq. 7) and (Eq. 8) can be solved independently.

(Eq. 7) can be solved for the reference coordinates, velocities and accelerations as well as the reaction forces using rigid-multi-body computations only. Here the obtained coordinates, velocities, and forces are substituted into (Eq. 8) in order to

determine the deformation of the bodies using standard finite element techniques.

Typically in flight dynamics the nonlinear inertial coupling become significant if one of the following statements are true [71] . The aerodynamic loads are small compared to inertial loads, the elastic frequencies and resulting rotational rates are of the same order, and or the system results in a complex model geometry, such that transverse deflections cause changes in mass distribution [71].

In many of these systems, the inertia coupling between the rigid body motion and the elastic deformation is significant such that the effect of this coupling cannot be neglected in the dynamic simulations [52]. In various applications the elastic modes can also lead to instability of the rigid-body modes [52].

The equations of motion for the flexible multi- body system of the ornithopter were solved using both systems of Equations (Eq.5) and (Eq. 6) and (Eq. 7) and (Eq. 8) respectively. The accuracy of the results obtained using the linear theory of elastodynamics according to (Eq.7) and (Eq.8)) is questionable, particularly, when high speed, light weight mechanical Systems are considered such as the ornithopter system at hand [52].

Equations of motions solved differ in the inclusion of the flexible cross-terms in the time varying mass matrix and are discussed next. Three cases were implemented to solve mentioned EOMs and compared for the in the five body system of the ornithopter. A) Rigid- body motion only B) No inertial coupling between rigid and

flexible body EOMs C) Full coupling.

Continuing the notation the time varying mass matrix for the case *A) Rigid body motion only* becomes

$$M = \begin{bmatrix} M_{rr} & 0 \\ 0 & 0 \end{bmatrix} \quad (\text{Eq. 9})$$

B) Solving the Equations of Motion independently and coupling only occurs through the aerodynamic forces. The flexible body's inertial properties are unaffected by deformation that is, deformation and rigid body motion are uncoupled [93]. The time varying Mass matrix becomes the following

$$M = \begin{bmatrix} M_{rr} & 0 \\ 0 & M_{ff} \end{bmatrix} \quad (\text{Eq. 10})$$

And finally case *C) Full coupling of inertia terms* according to following Mass Matrix

$$M = \begin{bmatrix} M_{rr} & M_{rf} \\ M_{fr} & M_{ff} \end{bmatrix} \quad (\text{Eq. 11})$$

The variation of inertia terms is implemented using the Craig- Brampton method described below in this chapter. With it, the expression for the mass matrix of the generalized coordinate $M(\xi)$ simplifies to an expression in *nine* inertia invariants also further described in the equations of motion below ((Eq. 82)- (Eq. 90)). Herby the

subscripts t denotes translational, o rotational and m modal degrees of freedom. The implemented mass matrix in terms of the generalized coordinate corresponds to the matrix terms introduced above according to following.

For Case A) the time varying mass matrix becomes,

$$M(\xi) = \begin{bmatrix} M_{tt} & M_{to} & 0 \\ M^T_{to} & M_{oo} & 0 \\ 0 & 0 & 0 \end{bmatrix} = \begin{bmatrix} M_{rr} & 0 \\ 0 & 0 \end{bmatrix} \quad (\text{Eq. 12})$$

For Case B) the implemented time varying mass matrix corresponds to following terms

$$M(\xi) = \begin{bmatrix} M_{tt} & M_{to} & 0 \\ M^T_{to} & M_{oo} & 0 \\ 0 & 0 & M_{mm} \end{bmatrix} = \begin{bmatrix} M_{rr} & 0 \\ 0 & M_{ff} \end{bmatrix} \quad (\text{Eq. 13})$$

Finally for the fully coupled Case C) the implemented time varying Mass matrix corresponds to following parts of the flexible and rigid body cross terms,

$$M(\xi) = \begin{bmatrix} M_{tt} & M_{to} & M_{tm} \\ M^T_{to} & M_{oo} & M_{om} \\ M^T_{tm} & M^T_{om} & M_{mm} \end{bmatrix} = \begin{bmatrix} M_{rr} & M_{rf} \\ M_{fr} & M_{ff} \end{bmatrix} \quad (\text{Eq. 14})$$

The floating frame of reference formulation results to a highly nonlinear mass matrix as the because of the inertia coupling between the reference motion and the elastic deformation [52]. Results of the comparison of A) B) C) suggest inclusion of flexible cross-terms in the highly nonlinear mass matrix and are presented in section 6.4.3.

The stiffness matrix now becomes,

$$K(\xi) = \begin{bmatrix} K_{tt} & K_{to} & K_{tm} \\ K_{to}^T & K_{oo} & K_{om} \\ K_{tm}^T & K_{om}^T & K_{mm} \end{bmatrix} = \begin{bmatrix} 0 & 0 \\ 0 & K_{ff} \end{bmatrix} \quad \text{(Eq. 15)}$$

Other than the time varying mass matrix the stiffness matrix is the same as the stiffness matrix used in structural dynamics due to the fact that the elastic coordinates are defined with respect to the body coordinate system and is according to follows [52].

$$K(\xi) = \begin{bmatrix} 0 & 0 & 0 \\ 0 & 0 & 0 \\ 0 & 0 & K_{mm} \end{bmatrix} = \begin{bmatrix} 0 & 0 \\ 0 & K_{ff} \end{bmatrix} \quad \text{(Eq. 16)}$$

4.1.1 Floating Frame of Reference Formulation (FFR)

The floating frame of reference formulation itself is the state of art and most widely used method in computer aided simulations of flexible multi body systems It has been widely established to obtain efficient and accurate solution for Low-order models. Generally finite-element floating frame of reference (FFR) formulation is used, for the most part, in the small deformation analysis of flexible bodies that undergo large reference displacements [94]. This formulation allows for filtering out systematically complex shapes associated with high frequencies that have no significant effect on the solution in the case of small deformations, and therefore the formulation of a linear elastic multi body system such as used in this work [94].

In the floating reference formulations, *two sets of coordinates are used to describe the configuration of the deformable bodies*. One set describes the location and orientation for a selected body coordinate system ξ_r , while the further set describes the deformation of the body with respect to its coordinate system q_f .

The generalized coordinates of the linear elastic- multi body systems are used as follows.

$$\xi = \left[\xi_r^T \ q_f^T \right]^T$$

Model verification concluded that with the appropriate choice of coordinate systems the FFR formulation can be used to describe the ornithopter appropriately [94].

4.2 Five Body Multi Body Dynamics Model

Linear elastic multi-body system of ornithopter and model iteration and verification results in a five -body multi body system dynamics model of the ornithopter according to following **Figure 67**.

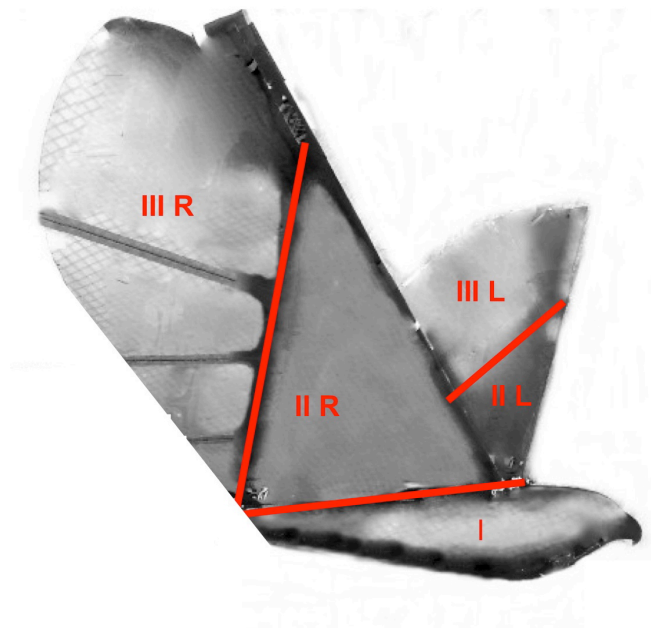


Figure 67: *Schematic Five- Body Dynamics System*

Body I, the ornithopter fuselage body is formulated as using a rigid body formulation, two flexible bodies connected to each other comprise each wing. Label II denotes the luff region body, label III the thrust flap region body. Label R denotes the right wing, Label L the left wing. A flapping motion is super imposed between the Bodies I and Body II its position is the flapping angle beta (β) in the following. A further flapping motion is superimposed between the Bodies II and Body III, its position is denoted the thrust flap angle zeta (ζ) in the following.

Schematic is presented in order to derive equations of motion in this Chapter. Floating Reference frame multi-body dynamics formulation results into following coordinate systems described next.

4.3 Coordinate Systems

Seven coordinate systems are necessary in order to derive the equations of motion of the flexible multi- body ornithopter system, and are used to derive the aerodynamic model as well. Coordinate systems are defined according to Figure 68 and Figure 69 below.

The equations of motion are described in the inertial fixed reference frame CI. CB is a body fixed reference frame at the fuselage center of mass. For convenience in terms of aerodynamic model formulation and verification with experimental data a fuselage body fixed reference frame CB0 is attached to the wing root.

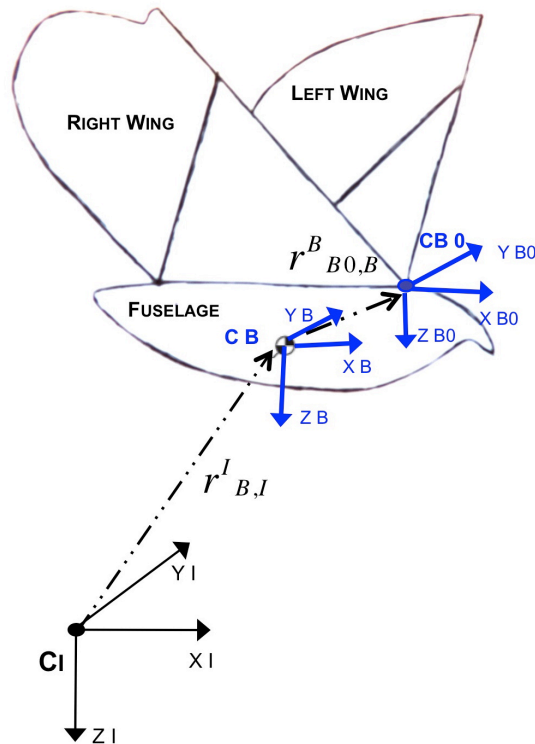


Figure 68: Schematic inertial and Fuselage Body fixed Reference Frames

Local wing fixed reference frames Z_{BW} and Z_{BT} are attached to the wing according to Figure 69. Z_{BW} is attached to the wing root and Z_{BT} to the thrust flap region accordingly. The wing fixed reference frames undergo nonlinear global motions, and the linear elastic deformations are represented in the local wing fixed reference frames.

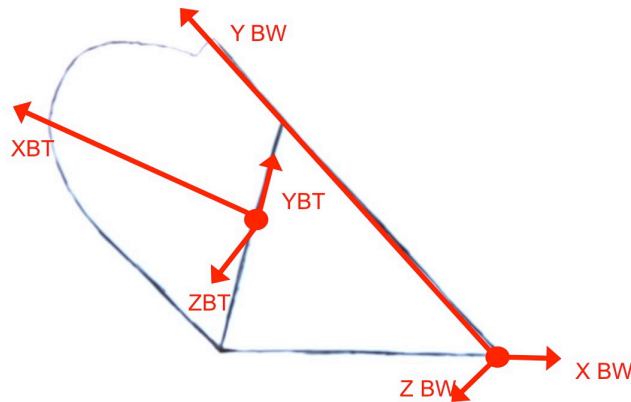


Figure 69: Schematic Wing Fixed Reference Frames

4.4 Underlying Articulated Rigid Body Model

From model iteration resulting underlying rigid motion is described here and extended to the flexible- multi body representation next. In the following the Equations of motion for a rigid body structure of ornithopter are developed.

The choice of rigid body links and connections in **Figure 1** is consistent with the underlying rigid body motions of the Flexible-Multi Body system of an ornithopter at hand but is discussed in a broader sense.

An articulated rigid body system is considered according to Figure 70. It consists of a set of rigid bodies connected through joints in a tree like structure. Exactly one parent joint connects every rigid link [95]. The joint corresponding to the root is distinguished, as it does not connect to any other rigid link. The generalized coordinates are therefore the DOFs of the root link of the tree can represent the global translation and rotation. The joint angles correspond to the admissible joint rotations for all the other joints [95].

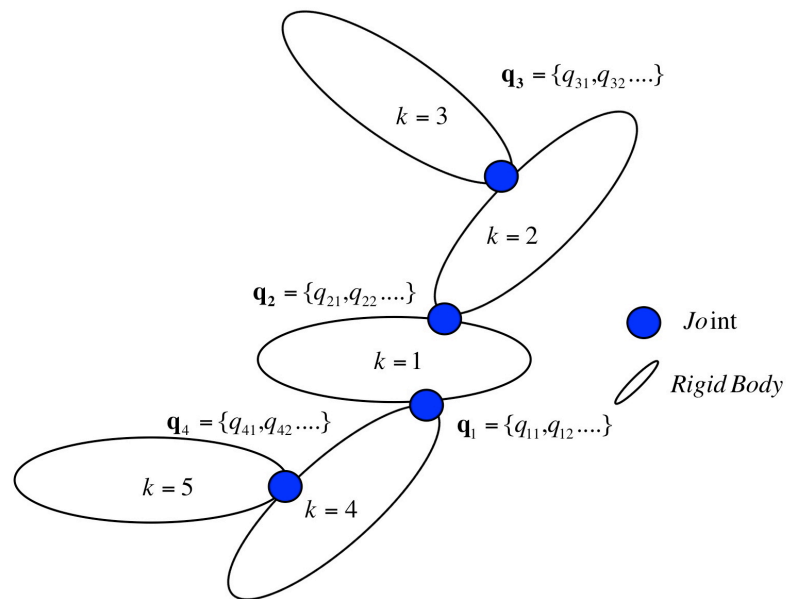


Figure 70: Articulated Multi- Body System representation of the Ornithopter

$k = 1, \dots, m$ and m denotes the number of rigid links. $k=5$ for the ornithopter system at hand hereby $k=1$ is Body I, $k=2$ is Body IIL, $k=3$ is Body IIL, $k=4$ is Body IIR and $k=5$ is Body IIIR according to Figure 67. The state of an articulated rigid body system such as in Figure 70 can be expressed in terms of $(x_k, R_k, v_k, \omega_k)$. Where x_k and R_k are

the position and orientation coordinates, and v_k , and ω_k , are the linear and angular velocity of the center of mass of the rigid link k respectively. They are in viewed in the inertial reference frame.

The articulated rigid body system can also be formulation in terms of generalized coordinates. One defines the generalized state as $(\mathbf{q}, \dot{\mathbf{q}})$, where $\mathbf{q} = (\mathbf{q}_1, \dots, \mathbf{q}_k, \dots, \mathbf{q}_m)$.

Each \mathbf{q}_k is the set of DOFs that connects the joint to the link k to its parent link, i.e for at ball joint three DOF's, a Universal Joint two DOFs and a hinge joint one DOFs [95].

Useful definitions for the following derivations are as follows:

- $p(k)$ returns the index of the parent link k . i.e. $p(5) = 2$ link 5 has 2 parent links, $p(1,k)$ returns the indices of all the links in the chain from the root to the link k . For the rigid-multi body system of the orntihopter **Figure 70** $p(1,1) = \{1\}$, $p(1,2) = \{1,2\}$, $p(1,3) = \{1,2,3\}$, $p(1,4) = \{1,4\}$, $p(1,5) = \{1,4,5\}$ [95].
- $n(k)$ returns the number of DOFs in the joint that connects the link k to the parent link $p(k)$. [58] For example for the orntihopter system in **Figure 70** $n(1) = 6$, $n(2) = 1$, $n(3) = 1$, $n(4) = 1$, $n(5) = 1$. The total number of Degrees of freedom in the system is $n = 10$.

- R_k is the rotation matrix for the link k and depends only on the DOFs R_k^0 is the chain of rotational transformation from the inertial frame to the local frame of the link k. It follows, $R_k^0 = R_{p(k)}^0 R_k$. Since link 1 does not have a parent link and the root link represents the global translation and rotation it follows. $R_{p(1)}^0 = I_3$ [95].

4.4.1 Kinematic Relations

Same derivation of Equations as for a single rigid body for the relation between Cartesian velocities and generalized velocities are applied for the articulated rigid- body system. Here one defines the Jacobean for each rigid link that relate its respective Cartesian velocities to the generalized velocity of the entire system.

4.4.1.1 Angular Velocity

In skew-symmetric matrix form the angular velocity of k can be formulated as is as follows viewed in the inertial frame.

$$\begin{aligned}
 [\omega_k] &= \dot{R}_k^0 R_k^{0T} = \left(R_{p(k)}^0 R_k \right) \left(R_{p(k)}^0 R_k \right)^T & \text{(Eq. 17)} \\
 &= \left(\dot{R}_{p(k)}^0 R_k + R_{p(k)}^0 \dot{R}_k \right) \left(R_k^T R_{p(k)}^0 \right)^T \\
 &= \dot{R}_{p(k)}^0 R_{p(k)}^{oT} + R_{p(k)}^0 \left(\dot{R}_k R_k^T \right) R_{p(k)}^{oT} \\
 &= \left[\omega_{p(k)} \right] + R_{p(k)}^0 \left[\hat{\omega}_k \right] R_{p(k)}^{oT}
 \end{aligned}$$

Herby $\omega_{p(k)}$ denotes the angular velocity of the parent link in the inertial reference frame

$$\omega_{p(k)} = \dot{R}_{p(k)}^0 R_{p(k)}^{oT} \quad \text{(Eq. 18)}$$

and $\hat{\omega}_k$ denotes the angular velocity of the link in the local reference (frame of its parent link $p(k)$).

$$\hat{\omega}_k = \dot{R}_k R_k^T \quad (\text{Eq. 19})$$

Now the angular velocity can be reformulated in terms of the generalized state.

$$\hat{\omega}_k = \hat{J}_{\omega k} \dot{q}_k \quad (\text{Eq. 20})$$

Where $\hat{J}_{\omega k}$ has the dimension of is $3 \times n(k)$ and is the local Jacobian matrix that relates the joint velocity of the link k , its angular velocity in the local reference frame (parent link $p(k)$).

For skew symmetric matrices,

$$[R\omega] = R[\omega]R^T \quad (\text{Eq. 21})$$

One can rewrite the angular velocity in the inertial reference frame according to (Eq. 17) as follows.

$$\omega_k = \omega_{p(k)} + R_{p(k)}^0 \hat{J}_{\omega k} \dot{q}_k \quad (\text{Eq. 22})$$

And by unrolling the recursive definition one obtains:

$$\omega_k = J_{\omega k} \dot{q}_k \quad (\text{Eq. 23})$$

Where the Jacobian $J_{\omega k}$ is:

$$J_{\omega k} = (\hat{J}_{\omega 1} \dots \hat{R}_{p(l)} \hat{J}_{\omega l} \dots 0 \dots) \quad (\text{Eq. 24})$$

The 0 corresponds to the links in the multi body system which are not in the chain.

Also l is defined as $l \in p(1,k)$.

For the articulated rigid-multi body System of the ornithopter in Figure 70 it follows:

$$\omega_1 = \left(\hat{J}_{\omega_1} \ 0 \ 0 \ 0 \ 0 \right) \dot{\mathbf{q}} \quad (\text{Eq. 25})$$

$$\omega_2 = \left(\hat{J}_{\omega_1} \ R_0^1 \hat{J}_{\omega_2} \ 0 \ 0 \ 0 \right) \dot{\mathbf{q}} \quad (\text{Eq. 26})$$

$$\omega_3 = \left(\hat{J}_{\omega_1} \ R_1^0 \hat{J}_{\omega_2} \ R_2^0 \hat{J}_{\omega_3} \ 0 \ 0 \right) \dot{\mathbf{q}} \quad (\text{Eq. 27})$$

$$\omega_4 = \left(\hat{J}_{\omega_1} \ 0 \ 0 \ R_1^0 \hat{J}_{\omega_4} \ 0 \right) \dot{\mathbf{q}} \quad (\text{Eq. 28})$$

$$\omega_5 = \left(\hat{J}_{\omega_1} \ 0 \ 0 \ R_1^0 \hat{J}_{\omega_4} \ R_4^0 \hat{J}_{\omega_5} \right) \dot{\mathbf{q}} \quad (\text{Eq. 29})$$

Angular velocities correspond to the angular velocities of the wing fixed reference frames body I, IIR, IIL, IIIR, IIIL defined in 4.2. Where $\hat{J}_{\omega_1} \in IR^{3 \times 3}$, \hat{J}_{ω_2} to $\hat{J}_{\omega_5} \in IR^{3 \times 1}$.

4.4.1.2 Linear Velocity

Similar to the angular velocity the linear velocity of the center of mass of the link k can be expressed in terms of generalized velocity.

$$v_k = J_{vk} \dot{\mathbf{q}}_k \quad (\text{Eq. 30})$$

Where,

$$J_{vk} = \frac{\partial x_k}{\partial \mathbf{q}} = \frac{\partial W_k^0 c_k}{\partial \mathbf{q}} \quad (\text{Eq. 31})$$

The chain of homogeneous transformations from the inertial frame to the local frame of link k is denoted as W_k^0 . Note that W_k^0 is different from R_k^0 in that W_k^0 includes the translational transformations. c_k is a constant vector that denotes the center of mass of link k in its local frame [95].

Now one can concentrate the Cartesian velocities into a single vector \mathbf{V}_k^0 and denote the relation as:

$$\mathbf{V}_k = J_{vk} \dot{\mathbf{q}}_k \quad (\text{Eq. 32})$$

Where

$$\mathbf{V}_k = \begin{pmatrix} v_k \\ \omega_k \end{pmatrix} \text{ and } J_k = \begin{pmatrix} J_{vk} \\ J_{\omega k} \end{pmatrix} \quad (\text{Eq. 33})$$

4.5 Lagrange Formulation of Equations of Motion

The governing equations of motion for a flexible body is introduced first and derived in the remainder of this section. The final equation of motion originates from Lagrange's equations of the following form [63].

$$\frac{d}{dt} \left(\frac{\partial L}{\partial \dot{\xi}} \right) - \frac{\partial L}{\partial \xi} + \frac{\partial C}{\partial \dot{\xi}} + \left[\frac{\partial \Psi}{\partial \xi} \right]^T \lambda = Q \quad (\text{Eq. 34})$$

T denotes the Kinetic Energy, V the Potential Energy, C is the energy dissipation function, Ψ is the algebraic constraint Equation, λ are the Lagrange

multipliers for the constraint, ξ are the generalized coordinates as defined in (Eq. 45).

Q are the generalized applied forces and represent the applied forces projected on ξ .

Where the algebraic constraint Equation is 0 according to

$$\Psi = 0 \quad (\text{Eq. 35})$$

Herby L is the Lagrange the difference between kinetic energy and potential energy according to Eq.(7)

$$L = T - V \quad (\text{Eq. 36})$$

4.5.1 Kinetic Energy

The kinetic energy in terms of the generalized coordinate ξ becomes

$$T = \frac{1}{2} \dot{\xi} M(\xi) \dot{\xi} \quad (\text{Eq. 37})$$

Where the petitioned mass matrix is according to defined above [93].

$$M(\xi) = \begin{bmatrix} M_{tt} & M_{to} & M_{tm} \\ M_{to}^T & M_{oo} & M_{om} \\ M_{tm}^T & M_{om}^T & M_{mm} \end{bmatrix} \quad (\text{Eq. 38})$$

Terms in the mass matrix in terms of the inertia invariants and the position vector are further described after the derivation of the EOM's in Equations for the five body system in (Eq. 75) to (Eq. 80).

4.5.2 Potential Energy

The potential energy in terms of the generalized coordinate ξ

Becomes,

$$V = V_g(\xi) + \frac{1}{2} \xi^T K \xi \quad (\text{Eq. 39})$$

Recall the generalized stiffness matrix which becomes according to follows,

$$K(\xi) = \begin{bmatrix} K_{tt} & K_{to} & K_{tm} \\ K^T_{to} & K_{oo} & K_{om} \\ K^T_{tm} & K^T_{om} & K_{mm} \end{bmatrix} = \begin{bmatrix} 0 & 0 & 0 \\ 0 & 0 & 0 \\ 0 & 0 & K_{mm} \end{bmatrix} \quad (\text{Eq. 40})$$

It is generally a constant, and only the modal coordinate contributes to the elastic energy [93]. It is not the full structural stiffness matrix of the component. $V_g(\xi)$ is the gravitational potential energy.

The governing differential equation of motion of a multi-body system, in terms of the generalized coordinates, can be derived in the following general form:

$$M(\xi)\ddot{\xi} + \dot{M}(\xi)\dot{\xi} - \frac{1}{2} \left[\frac{\partial M(\xi)}{\partial \xi} \dot{\xi} \right]^T \dot{\xi} + K\xi + f_g + \left[\frac{\partial \Psi}{\partial \xi} \right]^T \lambda = Q(\xi) \quad (\text{Eq. 41})$$

Where M is the time varying Mass Matrix M , K is the generalized Stiffness Matrix.

f_g Is the generalized gravitational force, Ψ are the algebraic constraint equations λ are the Lagrange multipliers for the constraints, ξ is the generalized coordinates of the individual body.

Here the first term denotes the position and time varying inertial forces, the second and third term the Coriolis and centrifugal forces which can be reformulated according to following (Eq. 42).

$$\dot{M}(\xi)\dot{\xi} - \frac{1}{2} \left[\frac{\partial M(\xi)}{\partial \xi} \dot{\xi} \right]^T \dot{\xi} = C(\xi, \dot{\xi}) \quad (\text{Eq. 42})$$

$K\xi$ the forth term in (Eq. 41) is the stiffness matrix times the generalized coordinate and equals zero for a rigid body system.

The sixth term in the Equation of motion (Eq. 41) is the constraint forces and can be formulated according to follows.

$$\left[\frac{\partial \Psi}{\partial \xi} \right]^T \lambda = N(\xi) \quad (\text{Eq. 43})$$

$Q(\xi)$ in (Eq. 41) is the generalized for applied force projected to the generalized coordinate and such as motor torque and aerodynamic forces.

(Eq. 41) can now be reformulated into the following general form

$$M(\xi)\ddot{\xi} + C(\xi, \dot{\xi}) + K\xi + f_g + N(\xi) = Q(\xi) \quad (\text{Eq. 44})$$

The generalized coordinate vector in the equation of motion is comprised of the generalized coordinate of each individual body i . Where i denotes the number of bodies in the multi body system.

$$\xi = \begin{bmatrix} \xi_1 \\ \xi_2 \\ \vdots \\ \xi_i \end{bmatrix}, \quad (\text{Eq. 45})$$

For a rigid body the individual generalized coordinate is comprised of three translational coordinates and three rotational coordinates that is the Euler angles.

$$\xi_i = \begin{bmatrix} x \\ y \\ z \\ \phi \\ \theta \\ \psi \end{bmatrix}_i \quad (\text{Eq. 46})$$

For a flexible body i the generalized coordinate vector is additionally augmented with the modal coordinates, $\mathbf{q}_i = q_{n(n=1\dots N)}$ where N is the number of modes.

$$\xi_i = \begin{bmatrix} x \\ y \\ z \\ \phi \\ \theta \\ \psi \\ q_{n(n=1\dots N)} \end{bmatrix} \quad (\text{Eq. 47})$$

One can observe in (Eq.10) in order to keep the generalized coordinate of a flexible body to a reasonable size modal truncation is necessary, the component mode synthesis via Craig- Brampton method facilitates the semi physical subspace method. Equations of motions of the Multi –body system can be further evaluated looking at the position vector of the system as follows. First the position vector of the rigid body equations of motions for an ornithopter system is presented and extended to a flexible multi body system in order to distinguish the both.

4.5.3 Position Vector – Rigid Body Equations of Motion

Now the position vector for a rigid multi body model of ornithopter is according Figure 71.

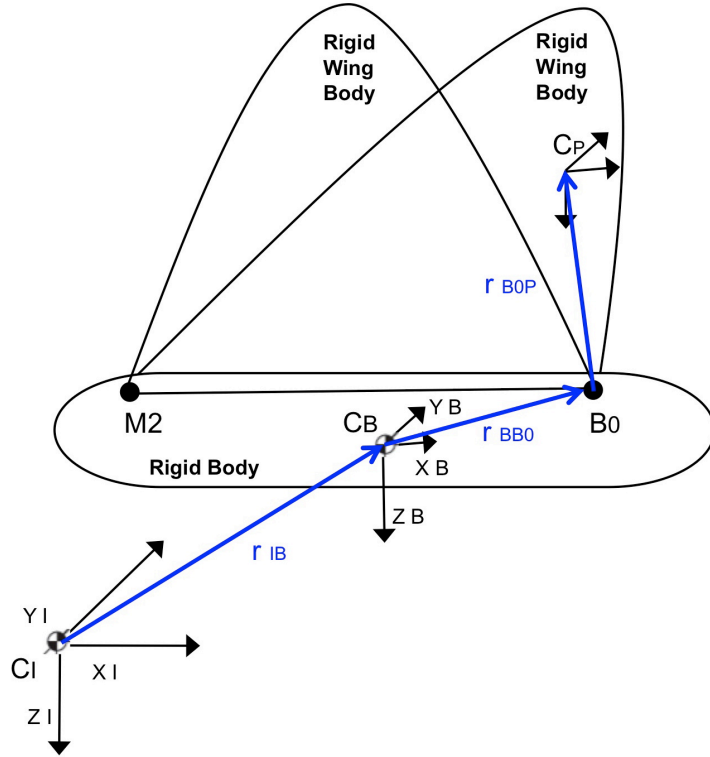


Figure 71: Position Vector of Rigid Multi-Body Model of Ornithopter

Hereby B0 and M2 represent the wing attachment points to the Fuselage. Cp the origin of a local a local wing fixed reference frame where marker Point P is attached.

The instantaneous location of a marker P that is attached to the rigid wing body can be expressed in the inertial reference frame using following.

$$\vec{r}_{IP} = \vec{r}_{IB} + \vec{r}_{BB0} + \vec{r}_{B0P} \quad (\text{Eq. 48})$$

Herby,

\vec{r}_{IP} is the position vector origin of the inertial (ground) reference frame CI to the unreformed location of marker P on the rigid wing body.

\vec{r}_{IB} is the position vector from the origin of the inertial (ground) reference frame to the origin of the local fuselage body fixed reference frame CB.

\vec{r}_{BB0} is the position vector from the fuselage fixed reference frame to CB to the fuselage fixed reference frame CB0.

\vec{r}_{B0P} is the position vector of the unreformed position of point P with respect to the local fuselage body reference frame of Body B0.

4.5.4 Position Vector – Flexible Body Equations of Motion

Now one considers a flexible wing and a Point P' on the flexible wing of the ornithopter according to Figure 72. P denotes a marker point on an undeformed wing body analogous to a rigid wing, P' denotes its deformed position.

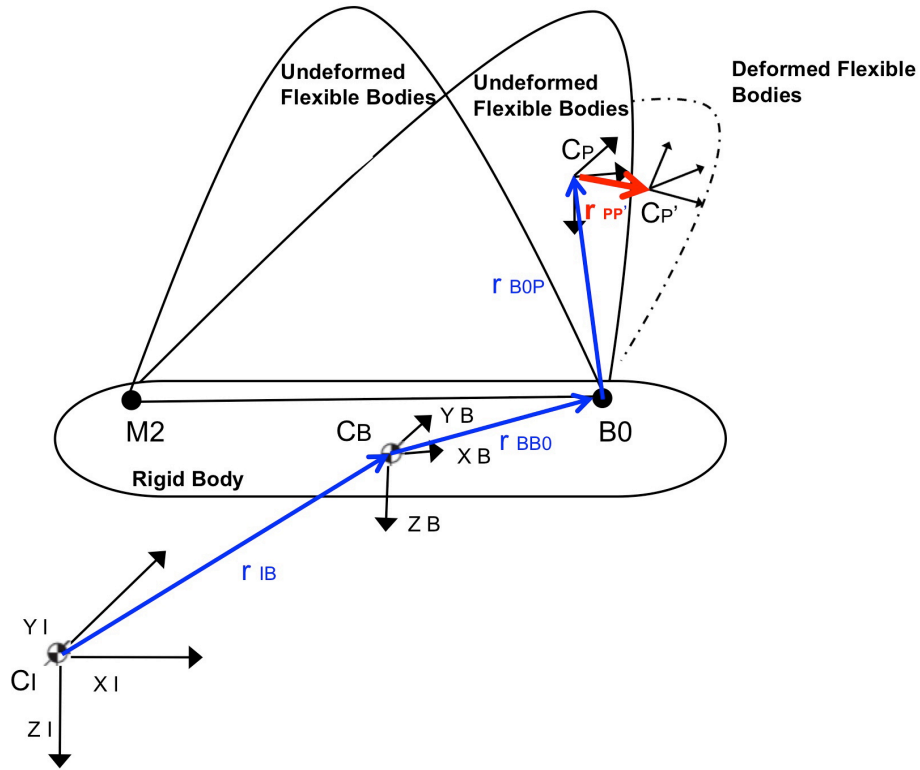


Figure 72: Position Vector of Flexible Multi-Body Model of Ornithopter

The instantaneous location of the deformed point attached to a node on the flexible wing body, becomes.

$$\vec{r}_{IP'} = \vec{r}_{IB} + \vec{r}_{BB0} + \vec{r}_{B0P} + \vec{r}_{PP'} \quad (\text{Eq. 49})$$

$\vec{r}_{PP'}$ is the translational deformation vector of Point P, the position vector from its undeformed to its deformed position P'.

The deformation vector is a modal superposition, for a Point P/ P' on a flexible body i it follows.

$$\vec{r}_{PP'} = \Phi_p q_n \quad (\text{Eq. 50})$$

The modal coordinates q_n are generalized coordinates of the flexible Body according to (Eq. 47). Φ_p is the slice from the modal matrix that corresponds to the translational DOF of node P. The Dimensions of Φ_p matrix is $3 \times n$. Where n is the number of modes.

4.5.5 Modal Superposition

The basic concept of modal superposition is that the deformation behavior of the component with a very large number of DOF such as the flexible wing can be captured with a much smaller number of modal DOF's. Such a reduction of the DOF's is referred to as modal truncation [96].

The discretization of the flexible wing into a finite element model represents a infinite number of Degrees of Freedom (DOF). The linear deformation of the nodes of this finite element model $\mathbf{r}_{PP'}$ can be approximated as a linear combination of a smaller number of shape vectors (or mode shapes), ϕ [96].

$$\mathbf{r}_{PP'} = \sum_{n=1}^N \phi_n q_n \quad (\text{Eq. 51})$$

Where n is the number of mode shapes. Herby (Eq. 51) represents the scale factors or amplitudes, and are the modal coordinates. Equation (Eq. 51) in matrix form becomes.

$$\mathbf{r}_{pp'} = \Phi \mathbf{q} \quad (\text{Eq. 52})$$

Where \mathbf{q} is the vector of modal coordinates and the modes ϕ_n have been deposited in the columns of the modal matrix, Φ . After modal truncation Φ becomes a rectangular matrix. The modal matrix Φ is the transformation for the small set of modal coordinates, \mathbf{q} , to the larger set of physical coordinates, $\mathbf{r}_{pp'}$.

4.6 *Formulation of Five Body Flexible Multi Body Dynamics Model*

The remainder of this sections the derivation of the contributions to the final Equation of Motion of the five-body flexible multi body System Eq. (8) are discussed. They are treated in the following order. 1) Model Generalized Coordinate Vector, 2) Position vector, 3) Velocity, 4) Orientation, and 5) Angular Velocity.

4.6.1 Model Generalized Coordinate Vector

In order to define generalized coordinate vector resulting for the 5 body flexible dynamics model the location of reference systems, body's notation and attachment points schematic of the model can be viewed in **Figure 73** below. Points M1 and T are the interface points between the bodies. M1's are located at the origin of the wing fixed reference frames BW on top of B0, which is attached to the fuselage. Recall Reference frames BW are attached at each wings in the luff Region. T is the located at the origin of the local Body fixed trust flap region reference Frames

BT. Since wings can be treated separately the right and the left wing have their own attachment points denoted R for right and L for left. Location of points T R and M1 R are shown in schematic Figure 73 below.

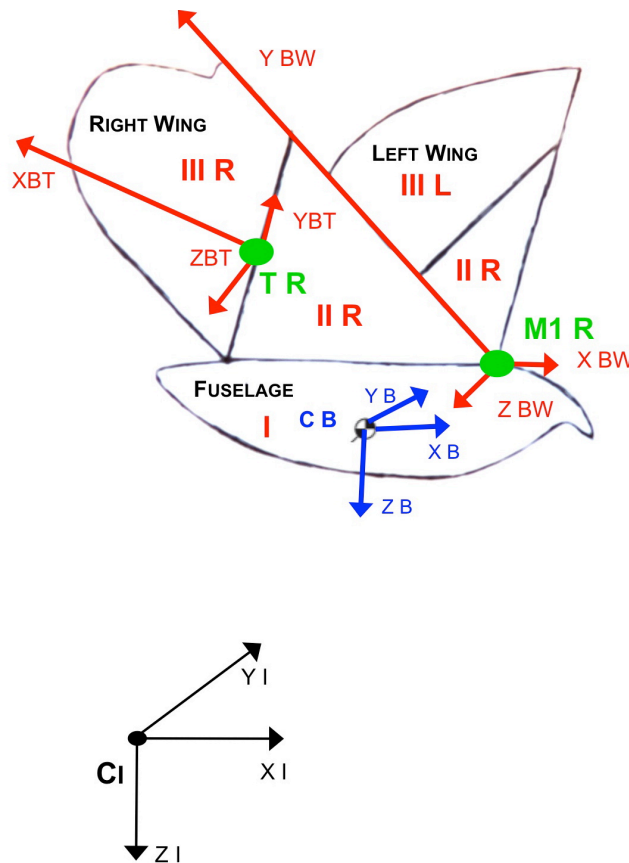


Figure 73: Schematic notation Definition for generalized coordinates of the flexible multi-body system

The generalized coordinate vector of the five- body flexible-multi-body dynamics Systems is augmented as follows, and used in the equations of motion for the flexible multi-body system of ornithopter according to (Eq. 41).

$$\xi = \begin{bmatrix} \xi_I \\ \xi_{IIR} \\ \xi_{IIL} \\ \xi_{IIIR} \\ \xi_{IIIL} \end{bmatrix}, \quad (\text{Eq. 53})$$

Where, the generalized coordinates of the bodies are according to following,

The rigid fuselage body I,

$$\xi_I = \begin{Bmatrix} x_{IB} \\ y_{IB} \\ z_{IB} \\ \psi_{IB} \\ \theta_{IB} \\ \phi_{IB} \end{Bmatrix} \quad (\text{Eq. 54})$$

The flexible luff region wing bodies II (R/L)

$$\xi_{II(R/L)} = \begin{Bmatrix} x_{IM1} \\ y_{IM1} \\ z_{IM1} \\ \psi_{IM1} \\ \theta_{IM1} \\ \phi_{IM1} \\ q_{II} \end{Bmatrix} \quad (\text{Eq. 55})$$

With $q_{II} = q_n (n = 1 \dots N)$.

The flexible luff region wing bodies III (R/L)

$$\xi_{III(R/L)} = \begin{Bmatrix} x_{II} \\ y_{II} \\ z_{II} \\ \psi_{II} \\ \theta_{II} \\ \phi_{II} \\ q_{III} \end{Bmatrix} \quad \text{(Eq. 56)}$$

With $q_{III} = q_n (n = 1 \dots N)$

4.6.2 Position Vector

For the five body dynamics system the instantaneous location of the deformed point attached to a node on the flexible wing body II, and III are presented in the following.

Instantaneous velocity of flexible bodies II (R/L) can be described according in (Eq. 49) Figure 72. An additional vector and therefore coordinate transformation is necessary in order to compute flexible points on the trust flap region. The additional vector in order to reach the local reference frame in which the flexible point is located is shown in Figure 74 below.

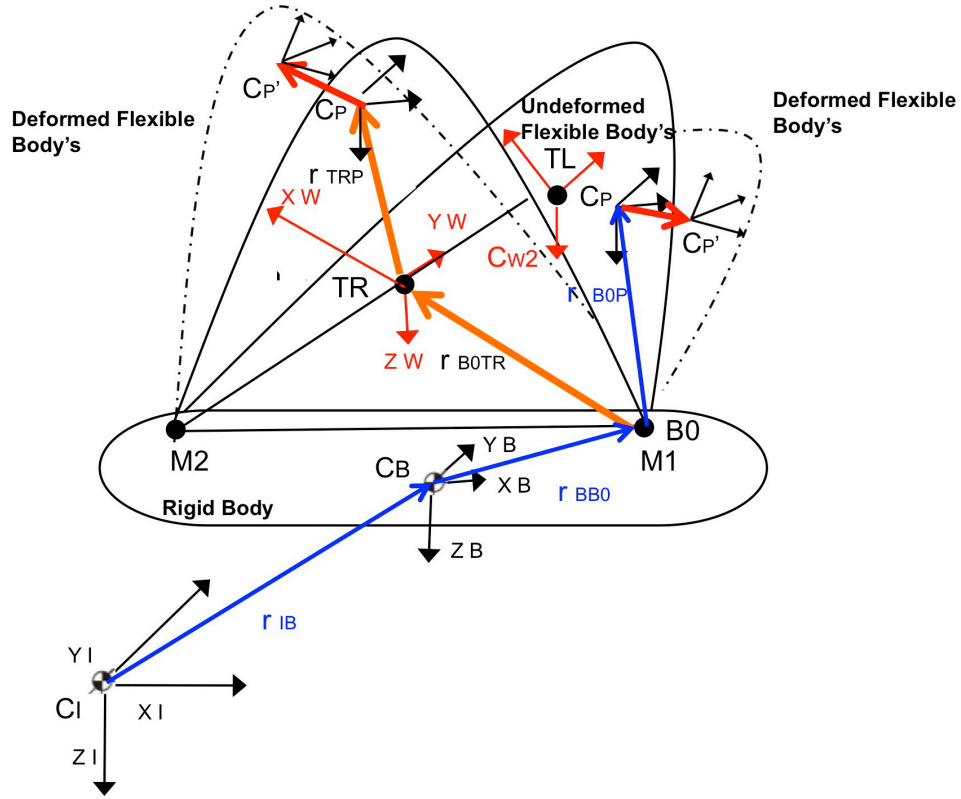


Figure 74: Position Vector of Flexible Multi-Body Model of Ornithopter, luff region (blue and red), thrust flap region (orange and red)

Instantaneous velocity of flexible bodies III (R/L) becomes.

$$\vec{r}_{IP'} = \vec{r}_{IB} + \vec{r}_{BB0} + \vec{r}_{B0TR} + \vec{r}_{TRP} + \vec{r}_{PP'} \quad (\text{Eq. 57})$$

Where the additional vector,

\vec{r}_{B0TR} is the position vector from the fuselage fixed reference frame to B0 to the wing fixed reference frame TR and,

\vec{r}_{TRP} is the position vector of the undeformed position of point P with respect to the wing fixed reference frame of the wing Body II.

The deformed position or nodal point m on the Finite Element Model of the wing luff region (Bodies II (L/R)) can now be expressed in the inertial Coordinate frame according to

$$r_{IP'_m} = r_{IB0} + {}^I A^{B0} \left(\vec{r}_{M_1 P'_m} + \vec{r}_{P'_m P'_m} \right) \quad (\text{Eq. 58})$$

Where ${}^I A^{B0}$ is the transformation matrix from the local body reference frame of B0 (Fuselage Body Fixed) to the inertial reference frame. This matrix can also be described as the direction cosines of the local body reference frame with respect to the ground. In applied Adams solver, the orientation is captured using a body fixed 3-1-3 sets of Euler angles ψ, θ, ϕ . The Euler angles are generalized coordinates of the flexible body [96].

The deformed position, or nodal point m on the Finite Element Model of the trust flap region (Bodies III (L/R)) expressed in the inertial coordinate frame is according to (Eq. 59).

$$\vec{r}_{IP'_m} = \vec{r}_{IB0} + {}^I A^{B0} \left(\vec{r}_{B0 P_m} \right) \quad (\text{Eq. 59})$$

With,

$$\vec{r}_{B0P_m} = \vec{r}_{B0TR} + {}^{B0}A^T \left(\vec{r}_{TP_m} + \vec{r}_{P_mP_m'} \right) \quad (\text{Eq. 60})$$

Where ${}^{B0}A^T$ is the transformation matrix from the local wing body reference frame of ZBW (Luff Region fixed reference frame) to the fuselage body fixed reference frame B0.

4.6.3 Velocity

The instantaneous translational velocity of Point P' is computed by differentiating (Eq. 58) for the luff region (Bodies II (L/R)), and (Eq. 64) for the trust flap region (Bodies III (L/R)) respectively. This is for the purpose for obtaining the kinetic energy of the point [96].

The instantaneous velocity for the luff region now becomes,

$$\vec{v}_{IP'_m} = \dot{\vec{r}}_{IB0} + {}^I\dot{A}^{B0} \left(\vec{r}_{M_1P_m} + \vec{r}_{P_mP_m'} \right) + {}^I A^{B0} \dot{\vec{r}}_{P_mP_m'} \quad (\text{Eq. 61})$$

The instantaneous velocity for the trust flap region becomes according to follows,

$$\vec{v}_{B0P'_m} = \dot{\vec{r}}_{B0TR} + {}^{B0}\dot{A}^T \left(\vec{r}_{TP_m} + \vec{r}_{P_mP_m'} \right) + {}^{B0}A^T \dot{\vec{r}}_{P_mP_m'} \quad (\text{Eq. 62})$$

4.6.4 Orientation

In order to derive the transformation matrix one considers a Point L_{II} on the flexible body II (luff region of the wing). The orientation of Point L relative to the inertial reference frame is represented by the transformation Matrix,

$${}^I A^{LII} = {}^I A^{B B} A^{M1 M1} A^{P P} A^{LII} \quad (\text{Eq. 63})$$

One considers a Point L_{III} on the flexible body III (trust flap region of the wing)
The orientation of Point L relative to the inertial reference frame can be written by the transformation Matrix,

$${}^I A^{LIII} = {}^I A^{B B} A^{M1 M1} A^{T T} A^{P P} A^{LIII} \quad (\text{Eq. 64})$$

In (Eq. 60) the Product of the first two transformation Matrices,

$${}^I A^{M1} = {}^I A^{B B} A^{M1} \quad (\text{Eq. 65})$$

Is the transformation matrix from the local wing fixed reference frame in which the elastic deformation is described, to the inertial reference frame of the system. In the flexible body III (Eq. 63) the additional transformation matrix is added due to the additional global motion of the thrust flap region and the transformation matrix to the local wing fixed reference frame becomes (Eq. 66) here.

$${}^I A^T = {}^I A^{B B} A^{M1 M1} A^T \quad (\text{Eq. 66})$$

${}^I A^{M1}$ Is the transformation matrix from the local body reference frame of BW to the inertial Reference Frame CI and ${}^I A^T$ is the transformation matrix from the local body reference frame of TW to the inertial Reference Frame CI.

The transformation matrices ${}^{M^1}A^P$, ${}^T A^P$ are due to the orientation change due to the deformation of the node P. If one examines ${}^{M^1}A^P$ further which is analogous to ${}^T A^P$ one can expand the matrix according to follows. The direction cosines for a vector of small angles ε are,

$${}^{M^1}A^P = \begin{bmatrix} 1 & -\varepsilon_{pz} & -\varepsilon_{py} \\ \varepsilon_{pz} & 1 & -\varepsilon_{px} \\ \varepsilon_{py} & \varepsilon_{px} & 1 \end{bmatrix} = \mathbf{I} + \tilde{\varepsilon}_p \quad (\text{Eq. 67})$$

Here the tilde denotes the skew operator and \mathbf{I} is the 3x3 Identity Matrix.

The orientation of the Point on a flexible body is instantly evaluated, as the body deforms in order to satisfy angular constraints (Adams, 2008). As the wing deforms, the marker rotates through small angles relative to its reference frames BW (Luff region), BT (Trust flap region respectively). Similar to translational deformations, these angles are obtained through modal superposition according to

$$\varepsilon_p = \Phi_p^* \mathbf{q} \quad (\text{Eq. 68})$$

Hereby Φ_p^* is the slice from the modal matrix that corresponds to the rotational degrees of freedom (DOF) of the node P, and is of 3xN dimension where N is the number of modes [96].

4.6.5 Angular Velocity

Now the angular velocity of a flexible body marker L is the sum of angular velocity of the body and the angular velocity due to deformation.

For flexible Bodies II the angular velocities become and are expressed in the wing body fixed reference frames.

$$\begin{aligned} {}^I\omega_{BW}^{LII} &= {}^I\omega_{BW}^P = {}^I\omega_{BW}^B + {}^B\omega_{BW}^{B0} + {}^{B0}\omega_{BW}^P \\ &= {}^I\omega_{BW}^B + {}^I\omega_{BW}^{B0} + \Phi^* q \end{aligned} \quad (\text{Eq. 69})$$

For flexible Bodies III the angular velocities become and are expressed in the wing body fixed reference frames in the Trust flap Region and become according to follows.

$$\begin{aligned} {}^I\omega_{BT}^{LIII} &= {}^I\omega_{BT}^P = {}^I\omega_{BT}^B + {}^B\omega_{BT}^{B0} + {}^B\omega_{BT}^{BT} + {}^{B0}\omega_{BT}^P \\ &= {}^I\omega_{BT}^B + {}^B\omega_{BT}^{B0} + {}^B\omega_{BT}^{BT} + \Phi^* q \end{aligned} \quad (\text{Eq. 70})$$

Equations (Eq. 69) and (Eq. 70) are the underlying rigid body motion rotations plus the rotation vector due to the elastic deflection.

The angular velocities of the bodies relate to the time derivative of the orientation states according to following.

For Bodies II (L/R) it follows,

$${}^B\omega_{BW}^{B0} = \mathbf{B}_{BW}^* \dot{\psi}_{II(L/R)} \quad (\text{Eq. 71})$$

With $\psi_{II(L/R)}$ is a part of the generalized coordinate,

$$\psi_{II(L/R)} = \left\{ \begin{array}{c} \psi_{IM1} \\ \theta_{IM1} \\ \phi_{IM1} \end{array} \right\}_{II(L/R)} \quad (\text{Eq. 72})$$

For Bodies III (L/R) it follows,

$${}^B \omega_{BT}^{BT} = \mathbf{B}_{BT} * \dot{\psi}_{III(L/R)} \quad (\text{Eq. 73})$$

Where $\psi_{III(L/R)}$ is a part of the generalized coordinate,

$$\psi_{III(L/R)} = \left\{ \begin{array}{c} \psi_{IT} \\ \theta_{IT} \\ \phi_{IT} \end{array} \right\}_{III(L/R)} \quad (\text{Eq. 74})$$

Hereby \mathbf{B}_{BW} and \mathbf{B}_{BT} are the respective transformation matrices.

4.6.6 Inertia Invariants in Mass Matrix

The expression for the mass matrix results in a expression of nine inertia invariants which can now be defined using the position vector. Recall, the Time varying mass matrix,

$$M(\xi) = \begin{bmatrix} M_{tt} & M_{to} & M_{tm} \\ M^T_{to} & M_{oo} & M_{om} \\ M^T_{tm} & M^T_{om} & M_{mm} \end{bmatrix} \quad (\text{Eq. 75})$$

Where the terms in the mass matrix, are dependent on the inertia invariants according to follows,

$$M_{tt} = I^1 \mathbf{I} \quad (\text{Eq. 76})$$

$$M_{to} = -A[I^2 + I_j^3 q_j]B \quad (\text{Eq. 77})$$

$$M_{tm} = AI^3 \quad (\text{Eq. 78})$$

$$M_{oo} = B^T[I^7 - [I_j^8 + I_j^8]q_j - I_{ij}^9 q_i q_j]B \quad (\text{Eq. 79})$$

$$M_{om} = B^T[I^4 - I_j^5 q_j] \quad (\text{Eq. 80})$$

$$M_{mm} = I^6 \quad (\text{Eq. 81})$$

It can be observed that the mass matrix is explicit dependent on the modal coordinates. A and B represent the Transformation Matrixes of the system [93].

The inertia invariants are computed from the nodes N of the finite element model. Inertia variants are based on the node's mass, m_{pp} , its undeformed location \mathbf{v}_p , and its participation in the component modes Φ_p . The discrete form of the inertia invariants are provided in equations below [93].

$$I^1 = N \sum_{p=1}^N m_p \quad (\text{Eq. 82})$$

$$I^2 = \sum_{p=1}^N m_p v_{p(II/III)} \quad (\text{Eq. 83})$$

$$I_j^3 = \sum_{p=1}^N m_p \Phi_p \quad (\text{Eq. 84})$$

$$I_j^4 = \sum_{p=1}^N m_p \tilde{v}_{p(II/III)} \Phi_p + I_P \Phi_p^* \quad (\text{Eq. 85})$$

$$I_j^5 = \sum_{p=1}^N m_p \tilde{\phi}_{pj} \Phi_p + I_p \Phi_p^* \quad (\text{Eq. 86})$$

$$I^6 = \sum_{p=1}^N m_p \Phi_p^T \Phi_p + \Phi_p^{*T} I_p \Phi_p^* \quad (\text{Eq. 87})$$

$$I^7 = \sum_{p=1}^N m_p \tilde{v}_{p(II/III)}^T \tilde{v}_{p(II/III)} + I_p \quad (\text{Eq. 88})$$

$$I_j^8 = \sum_{p=1}^N m_p \tilde{v}_{p(II/III)} \phi_{pj} \quad (\text{Eq. 89})$$

$$I^9 = \sum_{p=1}^N m_p^T \tilde{\phi}_{pj} \tilde{\phi}_{pk} \quad (\text{Eq. 90})$$

With v_p is the position vector from the local body reference frame of B to the point P, expressed in the local body coordinate system, therefore it follows for Body II and Body III it follows, [96].

For Body II (L/R) it follows,

$$v_{PII} = \vec{r}_{BB0} + \vec{r}_{B0P} \quad (\text{Eq. 91})$$

And Body III (L/R):

$$v_{PIII} = \vec{r}_{IP'} = \vec{r}_{BB0} + \vec{r}_{B0TR} + \vec{r}_{TRP} \quad (\text{Eq. 92})$$

4.6.7 Craig-Brampton Method

In order to facilitate the modal superposition in the flexible- multi body system a component mode synthesis method is used which is the Craig- Brampton Method.

Now the goal is to select the mode shape such that the largest possible amount of deformation can be captured with a minimum number of modal coordinates. Therefore the modal basis is optimized.

In previous assumptions it was assumed that eigenvectors would provide a useful modal basis [96]. However this requires an excessive number of modes to capture the effects of attachments on the flexible body [96]. One can observe that the generalized coordinate vector of a flexible body would become unnecessarily long. To prevent unwanted constraints in the system, eigenvectors of the unconstrained system were used. However, these eigenvectors were found to provide an inadequate basis in the system level modeling such as the ornithopter problem at hand.

In order to solve this a Component Mode Synthesis technique is used. The Craig-Brampton Method is adopted here. This method allows to select a subset of DOF which are not to be subjected to modal superposition. They are usually referred to as boundary DOF, attachment DOF or interface DOF. In the context interface DOF will be used.

Interface DOF are preserved exactly in the Craig-Brampton modal basis. There is no loss in resolution of the interface DOF's, when higher order modes are truncated.

Herby the systems DOF are partitioned into two different sets of DOF's interface DOF, u_B , and interior DOF u_I . Two sets of modes shapes, the constraint modes and fixed-boundary normal modes are defined in the following.

Constraint modes are static shapes obtain by giving each boundary DOF a unit displacement while holding all other boundary DOF fixed. The basis of constraint modes completely spans all possible motions of the boundary DOF's, with a one-to-one correspondence between the modal coordinates of the constraint modes and the displacement in the corresponding boundary DOF, $q_C = u_B$.

Fixed- boundary normal modes are obtained by fixing the boundary DOF when computing the Eigen solution. There are as many fixed- boundary normal modes as one desires. These modes define the modal expansion for the interior DOF. The quality of this modal expansion is proportional to the number of modes used for the flexible- multi body.

Now the relationship between the physical DOF and the Craig-Bampton modes and their modal coordinates can be formulated as follows [96].

$$u = \begin{Bmatrix} u_B \\ u_I \end{Bmatrix} = \begin{bmatrix} I & 0 \\ \Phi_{IC} & \Phi_{IN} \end{bmatrix} = \begin{Bmatrix} q_C \\ q_N \end{Bmatrix} \quad (\text{Eq. 93})$$

Where deformation matrix, u is composed of translational deformations \mathbf{r}_{pp} and rotational deformations ϵ_P which are described above and is according to follows.

$$u = \{ \mathbf{r}_{pp} \quad \epsilon_P \} \quad (\text{Eq. 94})$$

In (Eq. 93) u_b , are the boundary DOFs, u_I are the interior DOF's, $I, 0$ are the identity and 0 matrices, respectively. Φ_{IC} are physical displacements of the interior DOF in the constraint modes, Φ_{IN} are physical displacements of the interior DOF in the normal modes, q_C are the modal coordinates of the constraint modes, q_N are the modal coordinates of the flexible-boundary modes.

The generalized stiffness and mass matrices corresponding to the Craig-Bampton modal basis are obtained via a modal transformation. The stiffness transformation is

$$\hat{K} = \Phi^T K \Phi = \begin{bmatrix} I & 0 \\ \Phi_{IC} & \Phi_{IN} \end{bmatrix}^T \begin{bmatrix} K_{BB} & K_{BI} \\ K_{IB} & K_{II} \end{bmatrix} \begin{bmatrix} I & 0 \\ \Phi_{IC} & \Phi_{IN} \end{bmatrix} = \begin{bmatrix} \hat{K}_{CC} & 0 \\ 0 & \hat{K}_{NN} \end{bmatrix} \quad (\text{Eq. 95})$$

,and the mass transformation is according to follows,

$$\hat{M} = \Phi^T M \Phi = \begin{bmatrix} I & 0 \\ \Phi_{IC} & \Phi_{IN} \end{bmatrix}^T \begin{bmatrix} M_{BB} & M_{BI} \\ M_{IB} & M_{II} \end{bmatrix} \begin{bmatrix} I & 0 \\ \Phi_{IC} & \Phi_{IN} \end{bmatrix} = \begin{bmatrix} \hat{M}_{CC} & \hat{M}_{NC} \\ \hat{M}_{NC} & \hat{M}_{NN} \end{bmatrix} \quad (\text{Eq. 96})$$

Here the subscripts B, N, C, and I denote internal DOF, boundary DOF, normal mode and constraint mode, respectively. \hat{M}, \hat{K} Denote the generalized mass and stiffness matrix respectively. The matrices $\hat{M}_{NN}, \hat{K}_{NN}$ are diagonal matrices associated with eigenvectors. \hat{K} is block diagonal, There is no stiffness coupling between the constraint modes and fixed boundary normal modes. \hat{M} is not block diagonal,

because there is inertia coupling between the constraint modes and the fixed-boundary normal modes.

4.6.8 Modal Synthesis Method – Mode Shape Orthonormalization

The Craig- Bampton method tailors the modal basis to capture the desired attachment effects and the desired level of dynamic content. However, further steps make it suitable for direct use in the dynamic system calculation.

This is because in the Craig-Bampton method the constraint modes are six rigid bodies DOF which must be eliminated before the multi- body analysis because here it's own large-motion rigid body DOF is provided [96]. Also the Craig- Bampton constraint modes cannot be eliminated because doing so would be equivalent to applying a constraint on the system [96]. Furthermore with the method the constraint modes are a result of static condensation [96]. Consequently, these modes don not translate the dynamic frequency content that they must contribute to a flexible body. Therefore successful simulation of a non-linear system with unknown frequency content would be unlikely [96].

These issues in the raw formulation of the Craig-Bampton method can be resolved by orthogonalizing the Craig-Bampton modes. The appropriate and verified application in the system results in a stiffness matrix according to (Eq. 16).

The Craig-Bampton modes are not an orthogonal set of modes, as evident by the fact that their generalized mass and stiffness Matrix \hat{M}, \hat{K} in (Eq. 95)(Eq. 96) are not diagonal [96].

By solving the Eigenvalue Problem,

$$\hat{K}q = \lambda \hat{M}q \quad (\text{Eq. 97})$$

We obtain eigenvectors that we arrange in a transformation matrix N , which transforms the Craig-Bampton modal basis to an equivalent, orthogonal basis with modal coordinates.

$$Nq^* = q \quad (\text{Eq. 98})$$

The effect of the superposition formula is:

$$\mathbf{u} = \sum_{n=1}^N \phi_n q_n = \sum_{n=1}^N \phi_n Nq^* = \sum_{n=1}^N \phi_n^* q^* \quad (\text{Eq. 99})$$

Here q^* are the orthogonalized Craig- Bampton modes.

Craig-Bampton orthonormalization yields the modes of the unconstrained system, 6 of which are rigid body modes, which can be disabled after the operation. Following the second Eigen solution, all modes have an associated natural frequency. Problems arising from modes contributing high-frequency content can now be anticipated [96]. Although after the orthonormalization the removal of any mode constrains the body

from adopting that particular shape, the removal of a high-frequency mode prevents the associated boundary node from moving relative to its neighbors. If the constraint mode with unknown frequency contribution would be removed this would only prevent the boundary edge from reaching its degree of waviness [96].

The orthogonalized Craig- Brampton modes are a representation of the system and as such have a natural frequency associated with them [96]. Note that they are not the eigenvectors of the original system and cannot be exactly described physical but have following characteristics.

The in the orthogonalized Craig – Bampton modes and fixed- boundary normal modes are replaced with an approximation of the eigenvectors of the unconstrained body. This is an approximation because it is based only on the Craig-Bampton modes. Out of these modes, 6 are usually the rigid body modes. The constraint modes are replaced with the boundary eigenvector here [96].

4.7 Structural Dynamics Model of the Wings

The finite element model of each wing structure used in the five body vehicle dynamics model (Figure 75) was modeled using Structures workspace in the SimXpert GUI. For the structural solution the geometry of ornithopter is imported and a finite element mesh created. The structural quadratic grid is refined until modal solutions were converged. For the wing structure 1796 plate Elements were used and the bending stiffness was adjusted to fit the physical system. The leading edge spar is

rigidly attached to a shoulder joint and which is pinned to the fuselage at CB0 and undergoes a flapping motion and spatially distributed aerodynamic loads as described in the following aerodynamic section are applied. The aerodynamic loads are introduced as time variant forcing functions on the nodes of corresponding wing structure region. Isotropic material was chosen for the membrane structure according to properties in table below. The CTETRA8/CTRIA6 and the CBEAM elements in SimXpert Structures workspace were applied to the structure made of carbon fiber and Ripstop nylon fabric skin respectively. The beam element used for the Carbon fiber spars has bending, torsion, tension and compression properties and a one-dimensional nonlinear element with 8 nodes. An elastic shell element CQUAD8 is used for the membrane structure. This element is capable of carrying in plane force, bending force, and transverse shear force. An isotropic material is used for the Carbon fiber structural elements and MAT1 and MATT1 solvers are used for the elements. Structural wing model b) is submitted to the solver using MD Nastran (FEM) and simulation is integrated during the multi-body dynamics simulation. In structures workspace of the SimXpert GUI modal solver SOL103 was used to obtain as solution for the wing structure. SOL103 performs a modal analysis and is used to compute the natural frequencies and the associated mode shapes of a structure [82].

Table 5: *Material properties and dimensions of ornithopter structures used for the model [82]*

Element	Thickness Diameter in [mm]	Material	Elastic Modulus [GPa]	Structural Element Type	Poisson Ratio	Density [kg/m ³]
Wing Structure	0.06	Polyester Ripstop	100	Quadratic	0.31	500
Leading Edge Spar	3.6	Carbonfiber	230	Quadratic	0.74	1750
Diagonal Spar	1.8	Carbonfiber	175	Quadratic		1750
Finger Spar 1-4	1	Carbonfiber	175	Quadratic		1750

FEA model schematic of the wing and its components is shown in the following.

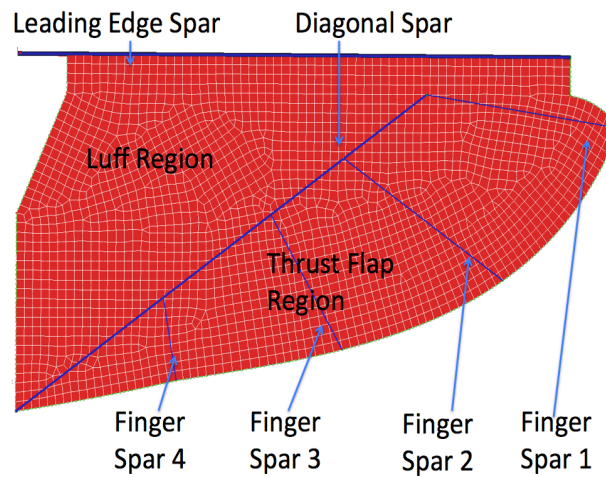


Figure 75: *Schematic FEM Wing Structure Carbon Fiber Spars and Wing*

The wing regions body II (L/R) and wing body III (L/R) are divided by the diagonal spar. Each component such thrust flap region the luff region and the leading edge Spar, the diagonal spar and the finger spar 1-4 are individual flexible elements. For example the mesh and mode shapes for the Thrust flap region are shown in Figure 17 and Figure 18.

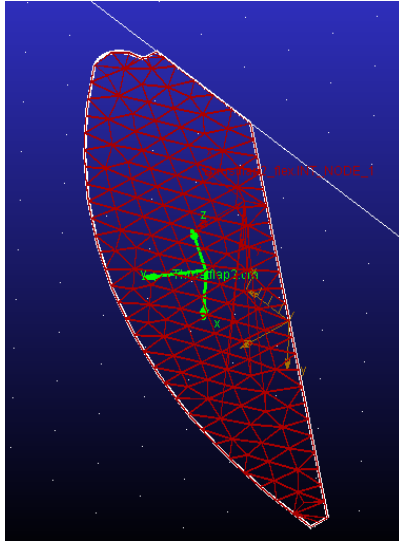


Figure 76: Thrust Flap Region Mesh Nodes=352, Elements=860

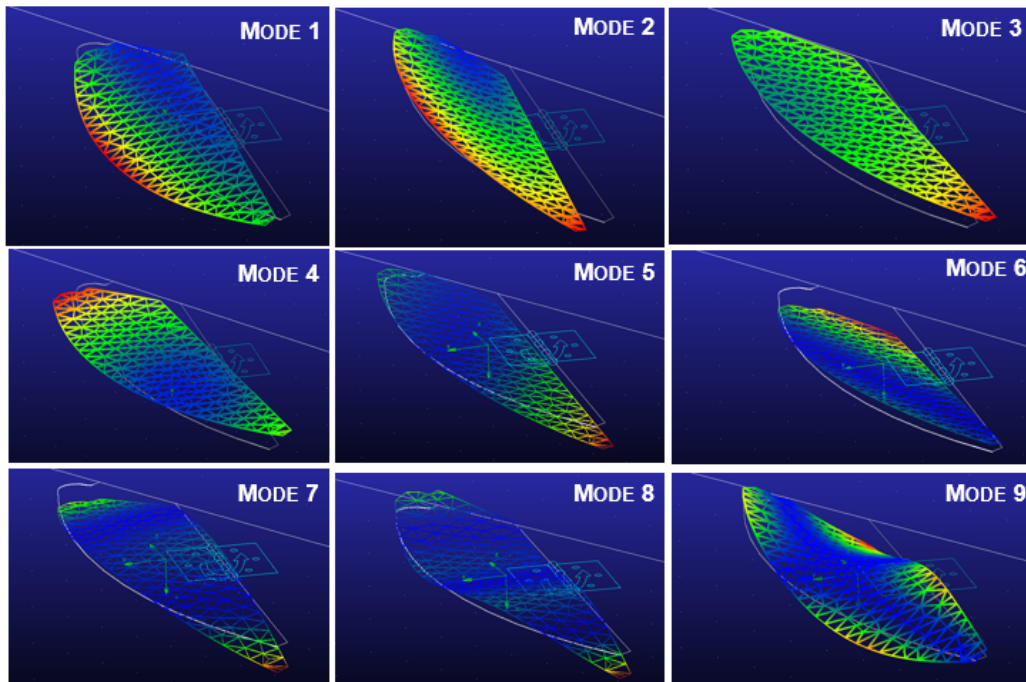


Figure 77: Thrust Flap Region Mode Shapes Couture Plot

Finger spars 1-4 are rigidly attached to the trust flap region and the leading edge spar and diagonal spar are rigidly attached to the luff region. This results in two flexible wing bodies for each wing in the five- body flexible multi- body dynamics

model. Fixed connections of flexile wing components are highlighted by lock image in five body flexible dynamics model image Figure 78.

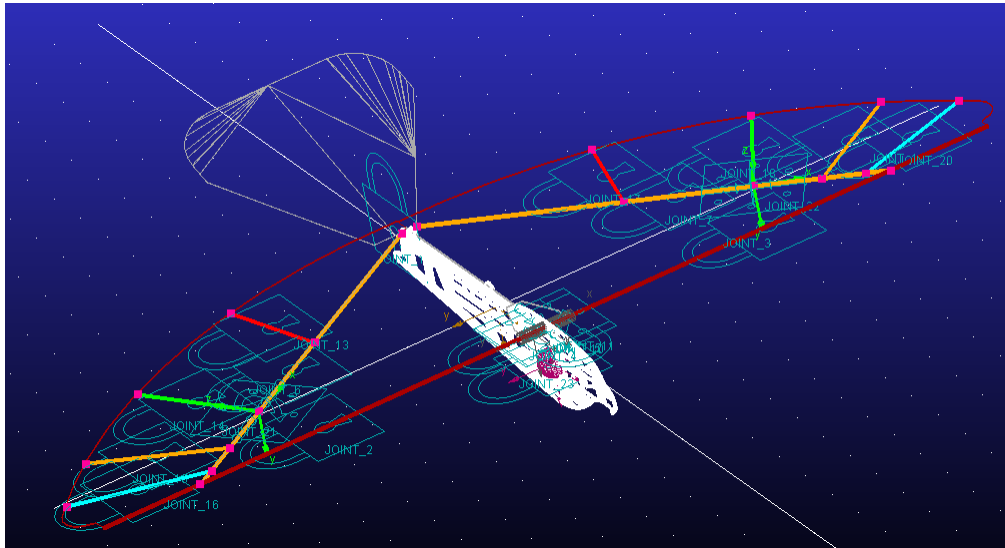


Figure 78: *Model Image Flexible Wing Component Connections*

4.7.1 Implementation - Mode Neutral File

The flexible structural dynamics parts are integrated in the flexible multi body dynamics model via an MNF file. Integration is accomplished through interaction between the Structures and Motion workspaces in the SimXpert (GUI). A modal analysis (SOL 103) is performed in the structures workspace, which generates a Nastran results file and a Modal Neutral File (MNF). In the simulation, displacement and stress data are available for the body in the flexible -multi body dynamics simulation [93].

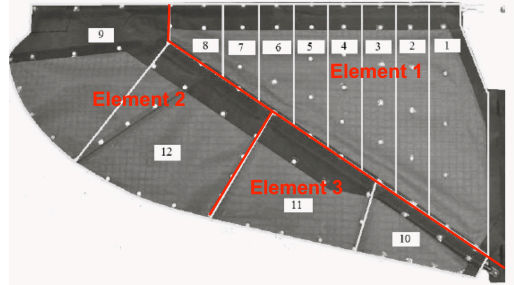
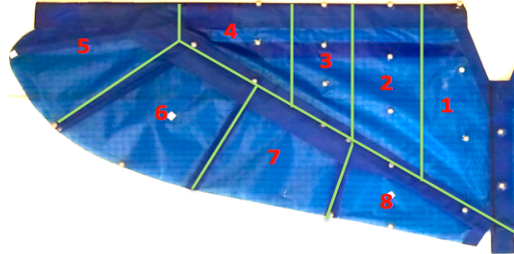
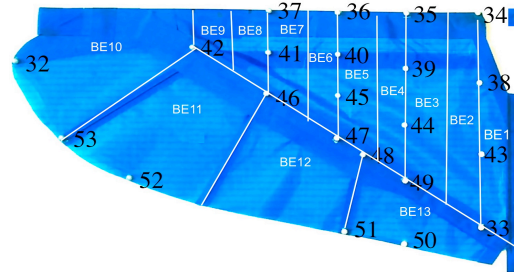
Chapter 5: Aerodynamics

MATLAB ® code was written for the aerodynamic load generation in the five body flexible- multi body dynamics model (FMBD). The final aerodynamic model is a two-fold code where first a MATLAB code was generated to extract time variant aerodynamic load from experimental wing kinematics. This code is called Aero load Experimental Free Flight (AEROLEF) and is the described in the following section. After its iteration and validation second MATLAB code was generated which can be coupled with the FMBD to simulate a different ornithopter configurations. Hereby Experimental data (E-2) serve for initialization and kinematics from the FMBD Model serve as exchange variable. The latter code is called Aero load Initialized Experimental Coupled (AEROIEC) and its formulation is also described in following.

5.1 Aerodynamic Model Versions

Three aerodynamic models (model A, B, and C) have been developed in the course of this study that resulted in AEROLEF and AEROIEC. These aerodynamic models are used as time variant externally applied wing loads, and differ in aerodynamic model assumptions.(e.g. blade element refinement and experimental data source). Differences between model A, B, and C are specified in **Table 6** below. Model C is the updated aerodynamic model with improvements to blade element refinement and aerodynamic modeling assumptions. The codes AEROLEF and AEROIEC use model C assumptions, and are discussed in detail below.

Table 6: Aerodynamic Model Versions Overview

<p>Model Name: Aero-model A</p> <p>Main Assumptions: Blade Element Theory (BET) - Coarse BE Grid, Model assumptions are adjusted for Clamped Conditions</p> <p>Number of Blade Elements: 3</p> <p>Input Kinematics: Vicon Vision ® - E1 bench test (ML 101,MSK004)</p> <p>Model Code: Aero- model A Load Experimental Bench Test (MATLAB®: AEROALEB.m)</p>	 <p>Figure 79: BE Grid Schematic Aero-Model A</p>
<p>Model Name: Aero-model B</p> <p>Assumptions: Blade Element Theory (BET)- Medium Refined BET Grid, Model assumptions are for free flight conditions</p> <p>Number of Blade Elements: 8</p> <p>Input Kinematics: Vicon Vision ® - E2 Flight Test (ML101)</p> <p>Model Code: Aero- model B Load Experimental Free Flight (MATLAB®:AEROBLEF.m)</p>	 <p>Figure 80: BE Grid Schematic Aero-Model B</p>
<p>Model Name: Aero- model C</p> <p>Assumptions: Blade Element Theory (BET)- Refined BET Grid, Model assumptions are for free flight conditions, Input kinematics formulated in terms of generalized coordinates of a 5 body flexible multi-body dynamics model of ornithopter, dynamic stall included</p> <p>Number of Elements: 13</p>	 <p>Figure 81: BE Grid Schematic Aero-</p>

<p>Model Code: Aero- Load Experimental Free Flight (MATLAB®:AEROLEF.m)</p> <p>Input Kinematics: Vicon Vision ® - E2 Flight Test (ML101)</p> <p>Model Code: Aero- load Initialized Experimental Coupled (MATLAB®:AEROIEC.m)</p> <p>Input Kinematics: Output of five- body dynamics model, Initialization is through Vicon Vision ® - E2 flight test (ML101)</p>	<p><i>Model C</i></p>
--	-----------------------

Aero- model A, B, and C generate external aerodynamic forces applied to corresponding nodes in the wing model in the special aperture of a blade element, as seen in Figure 79, Figure 80 and Figure 81. Experimental data (E1-I) was used to correlate and improve model C, which is implemented in AEROLEF. The final and improved model C was further developed to be coupled with the flexible multi-body dynamics model (FMBDM), as described in the next section 5.4. AEROIEC is the code of aero- model C that ties around the five- body vehicle dynamics model.

Aero-model A served mainly for a proof of concept study for the integration with a flexible-multi body dynamics model. It is utilizing wing kinematics data from experiment E1 in clamped conditions for the aerodynamic force generation and doesn't account for circulatory effects. Aero- dynamic model B utilizes wing kinematics data in free flight E2, a refined blade element selection, and accounts for

circulatory and non-circulatory effects. Blade element selection was further refined in Model C, where there was a 35% improvement in correlation of integrated forces to experimental data E2. Like model B final aerodynamic model C also utilizes free flight test kinematics E2 with a further refined blade element selection. Model B was further improved to aerodynamic model C, mainly by the inclusion of dynamic stall assumptions. Implementation of aerodynamic model C is described in detail in this chapter. That is workflow of the model C. Implementation of earlier model iterations model A and B is analogous. For model A, B, and C assumptions used and improvements between the models versions are also discussed in the reminder of this chapter.

5.2 *Aero- Model A*

Blade element theory according to Harmon is used for time variant forces on the wing [19]. Ornithopter research platform used for validation and verification is clamped to a ground stand. Therefore in the iteration of this model, only time variant non-circulatory aerodynamic forces are applied to the wing structural model. It consists of 1475 nodes and aerodynamic loads are applied to the correspondent nodes in the wing region like defined in its blade element selection.. Experimental wing kinematics (E1) of the research ornithopter (ML101) provided local wing deformation during a flapping cycle for the aerodynamic force calculation. Time variant forcing functions are applied to corresponding luff and thrust flap region shown in **Figure 79**.

Due to zero forward velocity at the clamped conditions simulated, it is assumed that only non- circulatory aerodynamic loads are acting on the wing. The non-

circulatory force is the result of the acceleration of a body of air normal to the wing surface as the wing undergoes quasi-steady motion. Local circulatory lift force acts normal to the inflow velocity, and hence produces both vertical and horizontal forces. For a flapping and pitching wing with a non-zero flight speed, the non-circulatory normal force generated by the wing is given by (Eq. 110)[19].

$$dN_{nc} = -\frac{\rho\pi(dc^2)}{4}(\dot{\theta}U + r\ddot{\beta}\cos\theta - ba\ddot{\theta})dr \quad (\text{Eq. 100})$$

This is the normal force value for a wing segment of length dr , where r is the mean span wise position of the segment and dc is the chord length. Herby a is the location of airfoil pitching access form 0.5 cord point, b is the reference span, and c the reference chord respectively. The local angular acceleration of the flapping wing is denoted by $\ddot{\beta}$, and θ is the pitch angle of blade element with respect to flapping axis.

The non-circulatory force acts normal to the wing, and therefore is broken down into vertical and horizontal components as well. Since the local blade element orientation varies along the span, the vertical and horizontal components of each force are computed for the blade element forces. The resulting vertical and horizontal components of the calculated non-circulatory forces are according to (Eq. 111)and (Eq. 112)respectively.

$$dF_{vert_nc} = dN_{nc} \cos(-\theta)\cos(\vartheta + \gamma)\cos\beta \quad (\text{Eq. 101})$$

$$dF_{horiz_nc} = dN_{nc} \sin(-\theta)\cos(\vartheta + \gamma) \quad (\text{Eq. 102})$$

Herby α is the angel between flapping axis and flight velocity, γ the flight path angle of flight velocity with respect to the ground and ϕ is the pitch angle of blade element chord with respect to flapping axis. Kinematic data for the calculations are provided by experimental data. Element forces are summed over each wing region denoted in **Figure 79**. For the simulations, summed time variant forces are applied on the luff and the thrust flap region accordingly. This is assuming uniform special load distribution of the time variant loads at each wing region. Time variant forcing functions resulting from aforementioned Blade Element theory were applied in the form of linear combinations of sign waves. Further details about used aerodynamic modeling methodology can be found in reference [19] Aerodynamic loads and resulting mode shapes of the wing were computed for the flapping frequency of 6.17 Hz and compared to experiment in 6.3.1 in order to asses the quality of the model.

5.3 Aero- Model B/C

For the aerodynamic Model C assumptions according to Lee have been used, which is a improvement of the DeLaurier Model. It accounts for dynamic stall cut off, cord- wise wing flexibility and introduces an attached flow condition a dynamic stall condition and a post stall condition [73]. Improvements in aero- model C compared to Lee include that the model accounts for flexibility in the span and additional flexibility in cord wise direction due to a fore and aft approach of the wing sections. A improved FSI procedure, where aerodynamic forces are formulated as a continuous function and estimated as a superposition of sign waves, which leads to model reduction. This time variant forces in form of the continuous function lead to a more efficient fluid structure interaction procedure. Input kinematics are based on in flight

kinematics (E2) for the model development, and later formed the first set of generalized input coordinates for the coupled model. This lead to an earlier convergence of a solution here, which is based on real in- flight dynamics.

5.3.1.1 Aerodynamic Model

Improvements of aero- model C compared to aero- model B include the inclusion of dynamic stall and a blade element refinement according to Figure 80 and **Figure 81**. The blade element selections and equations for the aerodynamic force calculations for aero-model C are further discussed here. Aero-model B is analogous and excludes dynamic stall cut off, the attached flow condition a dynamic stall condition and a post stall condition compared to aero- model C.

For the free flight aerodynamics models B and C the local airspeed with respect to the vehicle is given by the vector $v(\xi_{IB})$, that is the free speed velocity of the vehicle

$$v(\xi_{IB}) = \sqrt{\dot{x}_{IB}^2 + \dot{y}_{IB}^2 + \dot{z}_{IB}^2} \quad (\text{Eq. 103})$$

Where \dot{x}_{IB} , \dot{y}_{IB} and \dot{z}_{IB} are the translational body- fixed velocity components on CB0. **Figure 68** shows the location of the origin of the wing root fixed reference frame CB0. The flapping axis of the wing is orientated by the pitch angle $\theta = \theta_{IB} + \theta_{IM1}$ to the velocity vector $v(\xi_{IB}) = U$ in the luff region, and $\theta = \theta_{IB} + \theta_{IM1} + \sqrt{\psi_{IT}^2 + \theta_{IT}^2}$ in the thrust flap region.

$$dN_a = \frac{\rho\pi c^2}{4} \ddot{z}_2 dy \quad (\text{Eq. 105})$$

Where y is the coordinate along the semi-span according to defined in **Figure 68**. \ddot{z}_2 is the time rate of change of the mid-cord normal velocity component due to the wings motion. The circulatory normal force used is according to [73],

$$dN_c = 2\pi(\alpha' + \alpha_0 + \bar{\theta}) \cos\gamma \frac{\rho U V_{0.25c}^2}{4} c dy \quad (\text{Eq. 106})$$

Where $V_{0.25c}$ is the resultant velocity at the quarter cord location, γ the relative AOA. $\bar{\theta}$ the total mean pitch angle, α_0 is the zero lift AOA and α' the flow's relative angle of attack at the 0.75 chord location. The leading edge suction force was accounted for using following equation [73],

$$dT_s = \eta_s 2\pi(\alpha' + \bar{\theta} - \frac{1c\dot{\theta}}{4U}) \sin\gamma \frac{\rho U \hat{V}_{0.25c}^2}{4} c dy \quad (\text{Eq. 107})$$

Here η_s is the leading-edge suction efficiency and $\dot{\theta}$ is the pitch velocity of the blade element. The cord-wise force due to the camber was calculated in the model using [73],

$$dD_{camber} = -2\pi\alpha_0(\alpha' + \bar{\theta}) \cos\gamma \frac{\rho U \hat{V}_{0.25c}^2}{2} c dy \quad (\text{Eq. 108})$$

And the cord- friction drag was used as follows [33],

$$dD_f = (C_d) \frac{\rho V_x^2}{2} c dy \quad (\text{Eq. 109})$$

Hereby V_x is the flow speed tangential to the section. And V itself is the flow velocity, which include the downwash as well as the wing's motion relative to U [49]. Vertical velocity V_x at the quarter-cord location is according to Eq. (3) in [28].

The minimum and maximum dynamic stall angles according to Eq.(9-11) in [73] depend on plunging and pitching effects and are included in the model.

Aerodynamic force generation motion variables in equations above were formulated in terms of the generalized coordinates of the five- body flexible dynamics model for the model implementation. This was done in order to couple aero- model C to the five- body flexible model and is described in the next section.

Time variant aerodynamic forces resulting from equations in this section are applied on the nodes of the corresponding blade elements on the wing model. For the special distribution on the blade element section an elliptical shape is assumed. In the remainder of this section the aero -load blade element selection is discussed.

5.3.1.2 Aero- load Blade Element Identification

Due to significant trust flap deflections, which are much larger than the small flap angle, assumption used in the thin airfoil theory a fore and aft blade element approach

was used in this analysis in terms of generalized coordinates of the system. This leads to more accurate results versus covering the entire wing length with blades [19]. The trailing edge flap is a significant portion of the length and therefore also this approach is favorable. For more details please refer to Harmon Reference [19]. Blade element selection for model C was used according to **Table 6** above.

The free flight test analysis showed that only out of plane flexibility is significant (Section 6.1). Wing flexibility and chamber forming leads to insignificant shortening of blade element with dr . Therefore the blade element with dr is assumed to remain constant throughout the computation. Time independent variables y and x used in **Table 7** refer to marker coordinates within its reference frame in PS0 position as discussed in section (6.1.1.1).

The maximal blade element cord length is c_{max} is also computed from the free-flight data where the maximal element length during the flapping cycle was used for the variable (According to PS0). For specifics about blade Element length and with calculation please refer to **Table 7** below. The blade Element identification during a flapping cycle is according to **Figure 83**.

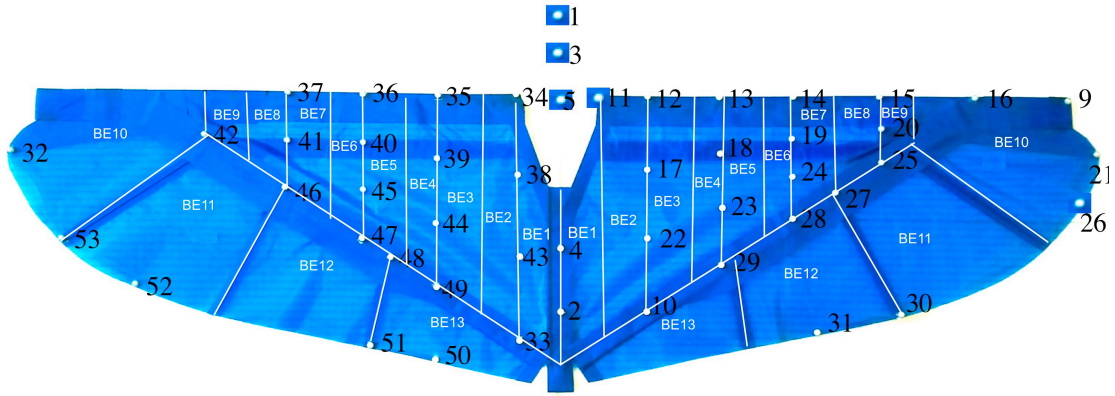


Figure 83: *ML101 Ornthopter Configuration Blade Element Selection*

Table 7: Blade Element Selection ML101 Orntihopter Configuration

Number of Blade Element	Blade Element Cord Length dc_n	Blade Element With dr_n
$n = 1$	$dc_1(t) = (x(t)_{M33}) + sl_d \left(\frac{y_{M33}}{2} \right)$	$dr_1 = y_{M33}$
$n = 2$	$dc_2(t) = (x(t)_{M10}) + sl_d \left(\frac{y_{M10} - y_{M33}}{2} \right)$	$dr_2 = y_{M10} - y_{M33}$
$n = 3$	$dc_3(t) = (x(t)_{M49}) + sl_d \left(\frac{y_{M49} - y_{M10}}{2} \right)$	$dr_3 = y_{M49} - y_{M10}$
$n = 4$	$dc_4(t) = (x(t)_{M29}) + sl_d \left(\frac{y_{M29} - y_{M49}}{2} \right)$	$dr_4 = y_{M29} - y_{M49}$
$n = 5$	$dc_5(t) = (x(t)_{M47}) + sl_d \left(\frac{y_{M47} - y_{M29}}{2} \right)$	$dr_5 = y_{M47} - y_{M29}$
$n = 6$	$dc_6(t) = (x(t)_{M28}) + sl_d \left(\frac{y_{M46} - y_{M47}}{4} \right)$	$dr_6 = \frac{y_{M46} - y_{M47}}{2}$
$n = 7$	$dc_7(t) = (x(t)_{M46}) + sl_d \left(\frac{y_{M46} - y_{M47}}{4} \right)$	$dr_7 = \frac{y_{M46} - y_{M47}}{2}$
$n = 8$	$dc_8(t) = (x(t)_{M25}) + sl_d \left(\frac{y_{M25} - y_{M64}}{2} \right)$	$dr_8 = y_{M25} - y_{M64}$
$n = 9$	$dc_9(t) = (x(t)_{M42}) + sl_d \left(\frac{y_{M42} - y_{M25}}{2} \right)$	$dr_9 = y_{M42} - y_{M25}$
$n = 10$	$dc_{10}(t) = \sqrt{(x(t)_{M53} - x(t)_{M16})^2 \dots \dots + (y_{M53} - y_{M16})^2}$	$dr_{10} = \sqrt{(x_{M42})^2 + (y_{M9} - y_{M42})^2}$
$n = 11$	$dc_{11}(t) = \sqrt{(x(t)_{M52} - x(t)_{M25})^2 \dots \dots + (y_{M55} - y_{M25})^2}$	$dr_{11} = \sqrt{(x_{M27} - x_{M25})^2 + \dots \dots (y_{M25} - y_{M27})^2}$
$n = 12$	$dc_{12}(t) = \sqrt{(x(t)_{M31} - x(t)_{M28})^2 \dots \dots + (y_{M31} - y_{M28})^2}$	$dr_{12} = \sqrt{(x_{M48} - x_{M27})^2 + \dots \dots (y_{M27} - y_{M48})^2}$
$n = 13$	$dc_{13}(t) = \sqrt{(x(t)_{M50} - x(t)_{M10})^2 \dots \dots + (y_{M50} - y_{M10})^2}$	$dr_{13} = \sqrt{((x_{M33} + sl_d (y_{M33} - y_2)) - x_{M48})^2 \dots \dots + (y_{M48})^2 (-x_{M48})^2 + (y_{M48})^2}$

The blade element lengths for elements 1 to 9 are identified with the marker position on their outer edge plus a adjustment for the length in the middle of the Blade Element. These Markers lying between the outer marker points of a blade element identify the local camber. i. e. Blade element 3 according to **Figure 85** above. Markers

12/17/22 and 10 are used to compute the local camber. For blade elements 10 to 13 the Blade Element with is calculated as the diagonal spar distance of markers bordering the Blade Element. i.e. Blade Element 11 Mirrored Marker 42 according to **Figure 83**. Blade Element 10 is of irregular shape and the Blade Element with dr_{10} and length dc_{10} shown in **Figure 84** provide a good approximation. Mainly the blade element with and length are utilized to calculate the surface area.

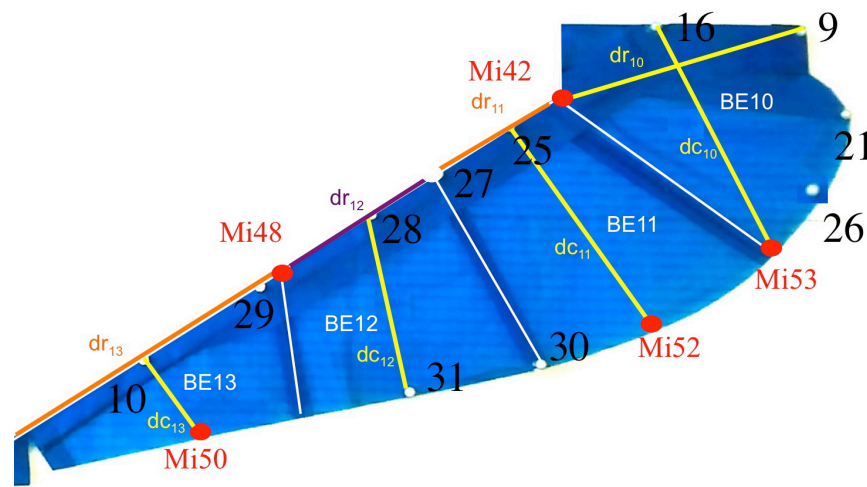


Figure 84: *Blade Element Selection Trust Flap Region ML101 Ornthopter Configuration*

The camber-line (or chord-line) data points are recorded for all blades a set of matrix coordinates representing the blade element to the programs, ‘AEROLEF.m and AEROIEC.m’. This is within the reference frame of their global location and orientation in the body reference frame system.

5.4 Aerodynamic Model Implementation

The workflow of aero- model C is described in the following. Experimental wing kinematics are formulated in terms of the generalized coordinates of the five

body flexible dynamics system, as shown in **Figure 85**. The aerodynamic model is used to compute time variant forces on the wing.

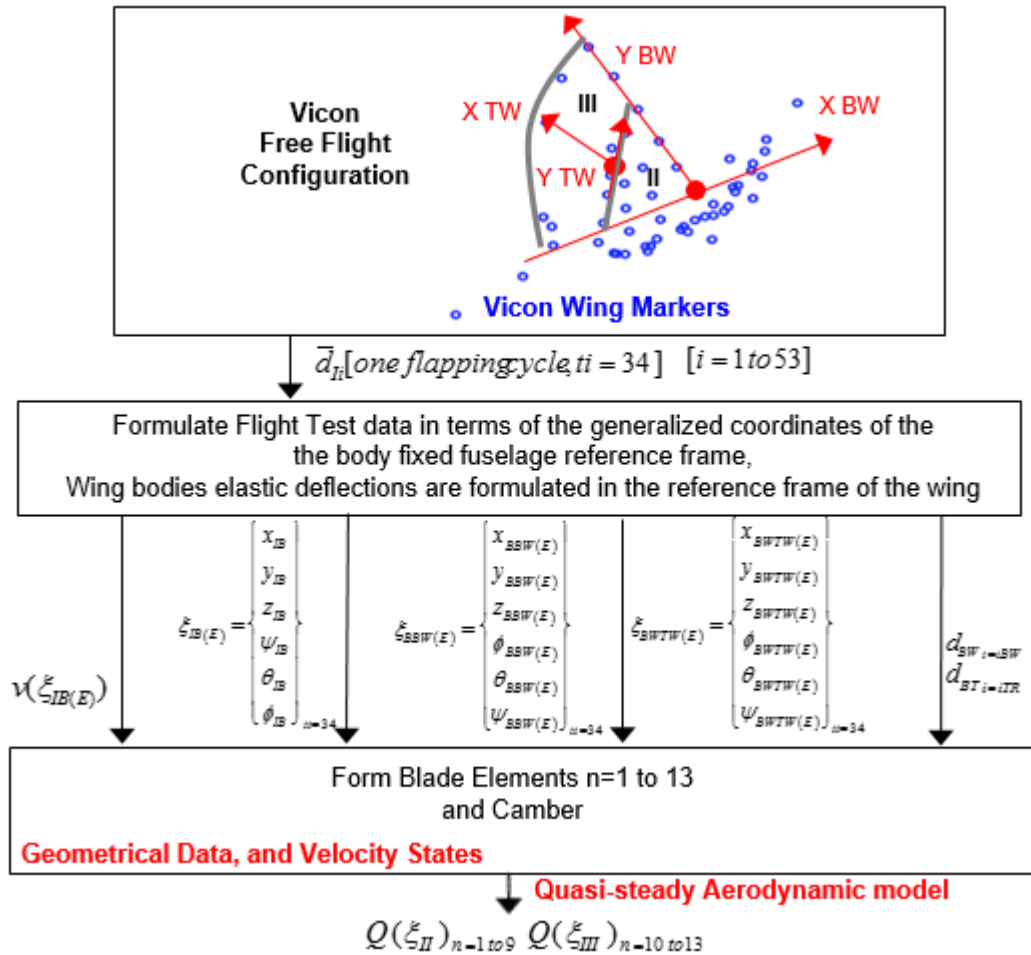


Figure 85: Aerodynamic Loads Model – Workflow

The experimental wing deflections E2 are measured in the inertia reference frame using the Vicon Vision ®, as shown in Figure 85. The experimental data are recorded using 34 time steps (ti=34) over one flapping cycle. Measurements are first transformed into the local body fixed reference frame, CB, then to the wing fixed reference frames, CW and CT. See **Figure 69** for reference frame reference. This removes the underlying reference motion of the five-body dynamics system. The free flight velocity data from the flight test E2 is of the vehicle fuselage fixed reference

frame, $v(\xi_{IB(E)})$, relative to the inertial reference frame. This serves as an input into the aerodynamic model C. The generalized fuselage coordinates are

$$\xi_{IB(E)} = \left. \begin{matrix} x_{IB} \\ y_{IB} \\ z_{IB} \\ \psi_{IB} \\ \theta_{IB} \\ \phi_{IB} \end{matrix} \right\}_{ii=34} \quad \text{(Eq. 110)}$$

See **Figure 72** for nomenclature reference. The generalized coordinates of the thrust flap region

$$\xi_{BBW(E)} = \left. \begin{matrix} x_{BBW(E)} \\ y_{BBW(E)} \\ z_{BBW(E)} \\ \phi_{BBW(E)} \\ \theta_{BBW(E)} \\ \psi_{BBW(E)} \end{matrix} \right\}_{ii=34} \quad \text{(Eq. 111)}$$

The generalized coordinates of the thrust flap region,

$$\xi_{BWTW(E)} = \left. \begin{matrix} x_{BWTW(E)} \\ y_{BWTW(E)} \\ z_{BWTW(E)} \\ \phi_{BWTW(E)} \\ \theta_{BWTW(E)} \\ \psi_{BWTW(E)} \end{matrix} \right\}_{ii=34} \quad \text{(Eq. 112)}$$

(Eq. 100) - (Eq. 120) define the coordinates of the underlying rigid body motion of the wing. The coordinate matrix of the deformation emanating from the underlying rigid-body motion is d_i and is the deformation vector of each marker location on the wing fixed reference frame. In the luff the deformation vector is $d_{BW i=iBW}$ and $d_{BT i=iTR}$ in the thrust flap region respectively. The markers comprising the coordinate matrix over a flapping cycle in the thrust flap region are $iBT = Wing\ Marker\ 9,16,21,26,30,31,32,50\ to\ 53$, and the markers in the wing region are $iBW = Wing\ Marker\ 2,4,5,9\ to\ 53$. The deformation (di) matrix is in timesteps (ti) and described in the generalized coordinates (Eq. 100) - (Eq. 120) of the region. The blade element formation uses the coordinate matrix in this form in order to form blade elements, calculate camber geometry, translational and angular velocities needed for the aerodynamic load calculations on the wing. Aerodynamic load calculation and assumptions were discussed in previous section.

The aerodynamic model load output results in a generalized external force in the multi-body dynamics model EOM's. For each blade element for the two wing bodies (Body II (Blade Elements n=1 to 9) and Body III (Blade Elements n=10 to 13)) the aerodynamic load appears in the generalized loads term $Q(\xi_{II})_{n=1\ to\ 9} Q(\xi_{III})_{n=10\ to\ 13}$ in the EOM of the five-body vehicle dynamics system. $Q(\xi_{II})_{n=1\ to\ 9}$ and $Q(\xi_{III})_{n=10\ to\ 13}$ further discussed in the next section.

d_i is the deformation vector of each marker location on the wing fixed reference frame (experimental data) and are $\mathbf{r}_{PP'}$ (Eq. 52) deformation of the marker in the five-body vehicle dynamics model. Recall $\mathbf{r}_{PP'}$ is the physical coordinate vector from the undeformed position of a marker P on the wing to its deformed position P' and can be obtained from the modal coordinates, \mathbf{q} in the wing reference frame. Experimental kinematics (Subscript E in the following) are interchangeable with five-body flexible vehicle dynamics model coordinates in the aerodynamic model. This is due to the formulation of the aero-model C input data in terms of the generalized coordinates of the five-body vehicle dynamics system.

In AEROIEC generalized coordinates of the free flight test data are replaced by kinematics resulting from the model. (Figure 48)

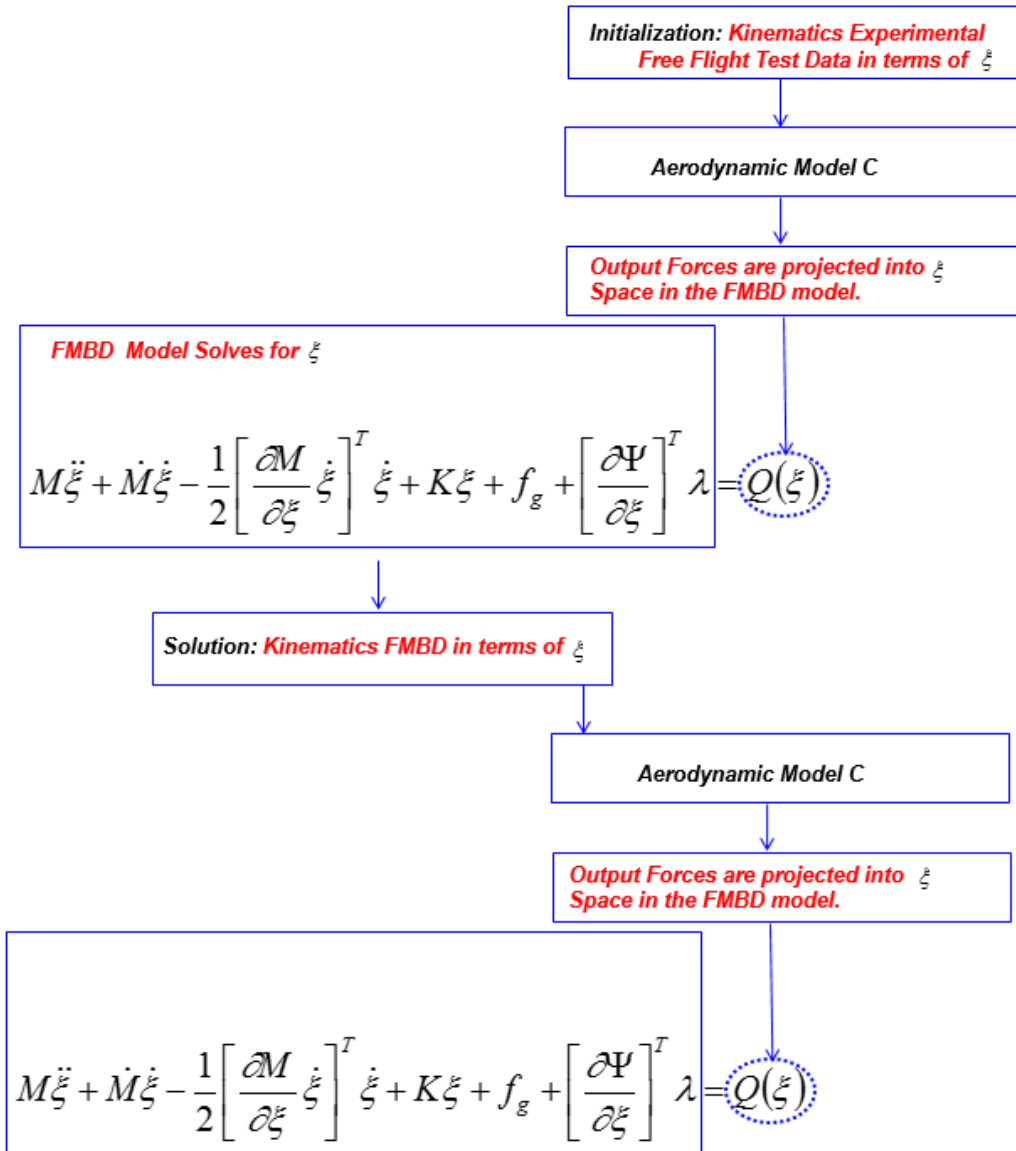


Figure 86: Aerodynamic Loads Model – Workflow AEROIEC

Experimental free flight test data serve as input variable for the aero-model C initialization, in AEROIEC. Output Forces are projected into the generalized coordinate space and applied to the FMBD model. The model solves for the generalized coordinates in the system according to discussed in chapter 4. These position states of the generalized coordinates serve now as input into aero- model C

and result in aerodynamic loads, which serve now as input into FMBD model EOMs. Therefore different configurations in underlying wing motions and wing stiffness's can be run within the integrated FMBDM simulation using AEROIEC and a solution can be correlated.

5.4.1 Distributed Aerodynamic Loads

Distributed aerodynamic loads resulting from aero-model C are introduced to the five- body vehicle dynamics model using an MFORCE element [94]. The distributed load vector is applied to the FEM elements in the model using a half-elliptical special distribution on the blade [93].

For the discussion one examines the physical coordinate from the equations of motion (EOM) in the Finite Element FEM software first

$$M\ddot{x} + Kx = F \quad \text{(Eq. 113)}$$

Here K and M are the Finite Element (FE) mass and stiffness matrices for the flexible component, and x and F are the physical nodal DOF vector and the Load vector respectively [93].

Now one transforms into modal coordinates q using the modal matrix Φ

Therefore

(Eq. 113) becomes,

$$\Phi^T M \Phi \ddot{q} + \Phi^T K \Phi q = \Phi^T F \quad (\text{Eq. 114})$$

Which simplifies to the following EOM.

$$\hat{M} \ddot{q} + \hat{K} q = f \quad (\text{Eq. 115})$$

Where \hat{M} and \hat{K} are the generalized mass and stiffness matrices and f is the modal load vector [93].

The applied aerodynamic force is having a global resultant force and moment. These show up as loads on the rigid- body modes and are treated as point forces and moment on the local reference frame.

The projection of the nodal force vector on the modal coordinates [93]

$$f = \Phi^T F \quad (\text{Eq. 116})$$

is a computationally expensive operation, which poses a problem when F is an arbitrary function of time, and is the case for the time variant aerodynamic force [93].

Now the force is separated in space and time and therefore the load can be viewed as a time varying linear combination of an arbitrary number of static load cases according to following.

$$F(t) = s_1(t)F_1 + \dots + s_n(t)F_n \quad (\text{Eq. 117})$$

The expensive projection of the load to modal coordinates is therefore performed once during the creation of the MNF file according to section 4.7.1. The multi-body dynamics calculation performed by the Adams solver only needs to be aware of the modal form of the load according to follows.

$$f(t) = s_1(t)f_1 + \dots + s_n(t)f_n \quad \text{(Eq. 118)}$$

Where the vectors f_1 to f_n are n different case vectors. Each of the load case vectors contains one entry for each mode in the modal basis [93].

One can reformulate to have an explicit dependency on the system response, where q represents all the states of the system. The modal force of the system can now be described according to (Eq. 119)

$$f(q,t) = s_1(q,t)f_1 + \dots + s_n(q,t)f_n \quad \text{(Eq. 119)}$$

The applied aerodynamic force has a global resultant force and moments. These show up as loads on the rigid body modes and are treated the multi- body dynamics model as point forces and moments on the local wing fixed reference frames.

5.5 Global Resulting Forces and Moments

A point force F and a point moments ME are applied to a marker location on a flexible body must be projected on the generalized coordinates of the flexible-multi body system.

The force and torque are formulated in matrix form, and are expressed in the coordinate system of the marker L in the local reference frames of the wing bodies ZBW and ZBT (Figure 69)

$$F_L = \begin{bmatrix} f_x \\ f_y \\ f_z \end{bmatrix}, \quad ME_L = \begin{bmatrix} me_x \\ me_y \\ me_z \end{bmatrix} \quad (\text{Eq. 120})$$

With the numbers of markers L corresponding to the number of nodal points hence $L=1$ to nl , where nl denotes the number of nodes a force is applied on Bodies II (L/R), and $L=1$ to nm , where nm is the number of nodes on Bodies III (L/R) where a force is applied.

5.5.1 Generalized Forces

The generalized force Q consists of a generalized translational force Q_F , a generalized moments Q_{ME} , which is the generalized force on the Euler angles and a generalized modal force Q_M . Therefore it follows,

$$(\text{Eq. 121})$$

$$Q = \begin{bmatrix} Q_F \\ Q_{ME} \\ Q_M \end{bmatrix}$$

For the EOM in the Inertia Reference Frame (EOM) the generalized translational force is obtained by a coordinate transformation for the Q_F in of Body II and Body III it follows respectively,

$$Q_{FII}^I = {}^I A^{LII} F_{LII} \quad (\text{Eq. 122})$$

$$Q_{FIII}^I = {}^I A^{LIII} F_{LIII} \quad (\text{Eq. 123})$$

The Transformation Matrix ${}^I A^{LII}$ is given in (Eq. 63) and the Transformation Matrix ${}^I A^{LIII}$ in (Eq. 64).

For the total integrated forces in the inertia reference frame due to applied aerodynamics loads it follows is the summation of applied loads on Wing Bodies II (L/R) and Wing Bodies III (L/R).

$$Q_F^I = 2x \left(\sum_I^{nl} Q_{FII}^I + \sum_I^{nm} Q_{FIII}^I \right) \quad (\text{Eq. 124})$$

These applied forces vary per blade element like and are further described in the Aerodynamic section.

For verification the total integrated, translational aerodynamic forces obtained the fuselage fixed reference frame CB according to follows.

$$Q^{CB}_{FIII} = {}^{CB}A^{LII} F_{LII} \quad (\text{Eq. 125})$$

$$Q^{CB}_{FIII} = {}^{CB}A^{LIII} F_{LIII} \quad (\text{Eq. 126})$$

With the transformation Matrices are according to (Eq. 127), and (Eq. 128) respectively.

The coordinate transformation is analogous to describe in section 4.6.4.

$${}^B A^{LIII} = {}^B A^{M1 M1} A^{TT} A^{PP} A^{LIII} \quad (\text{Eq. 127})$$

$${}^B A^{LII} = {}^B A^{M1 M1} A^{PP} A^{LII} \quad (\text{Eq. 128})$$

For the combined forces on the bodies it's the summation of the individual forces over the nodes, and it follows respectively for the combined aerodynamic forces on a wing body

$$Q^{CB}_{FII} = \sum_{n=1}^{nl} Q^{CB}_{FII}{}^n \quad (\text{Eq. 129})$$

$$Q^{CB}_{FIII} = \sum_{n=1}^{nm} Q^{CB}_{FIII}{}^{nm} \quad (\text{Eq. 130})$$

Total Forces and Moments are also computed in the Fuselage Fixed Body Reference Frame CB according to following summation, Q^{CB}_{FI} denotes the generalized translational force applied on the fuselage body.

$$Q^{CB}_{FT} = 2x(Q^{CB}_{FII} + Q^{CB}_{FIII}) + Q^{CB}_{FI} \quad (\text{Eq. 131})$$

The generalized force due to the aerodynamic loads applied on the wings is

$$Q^{CB}_{FT} = 2x(Q^{CB}_{FII} + Q^{CB}_{FIII}) \quad (\text{Eq. 132})$$

5.5.2 Generalized Moments

The generalized moments Q_{ME} on the flexible wings are due to the Force vector F_L and the Moment vector ME_L . It follows for the generalized moments of Bodies II (L/R).

$$Q_{MEII} = \sum_{nl=1}^{nl} ME_{LII} + \sum_{nl=1}^{nl} \vec{p}_{B0A^{nl}} x F_{LII}^{nl} \quad (\text{Eq. 133})$$

Where the vector $\vec{p}_{B0A^{nl}}$ is the position vector from the origin of the local body reference frame CBW (B0) of Bodies II (L/R) to the nodal point nl of force application. For Bodies III (L/R) it follows.

$$Q_{MEIII} = \sum_{nm=1}^{nm} ME_{LIII} + \sum_{nm=1}^{nm} \vec{p}_{TA^{nl}} x F_{LIII}^{nm} \quad (\text{Eq. 134})$$

The vector $\vec{p}_{TA^{mm}}$ is the position vector from the origin of the local body reference frames CBT (T) to the nodal point's nm of force application on Bodies III (L/R).

The total generalized moments Q_{ME} in the fuselage fixed reference frame are computed according to following.

$$Q_{ME} = 2x(Q_{MEII} + Q_{MEIII}) + Q_{MEI} \quad (\text{Eq. 135})$$

5.5.3 Generalized Modal Force

The generalized modal force calculation, on the flexible bodies are described in this section. The forces are transformed in the local wing fixed reference frame of the flexible bodies (II/III - L/R). The generalized modal force results from the multiplication with the corresponding slice of the modal matrix.

The generalized modal force of bodies II (L/R) is according to follows.

$$Q_{MII} = \Phi_P^T Q_{FII}^{CB} + \Phi^*{}^T_P Q_{MEII}^{CB} \quad (\text{Eq. 136})$$

For bodies III (L/R) according to

$$Q_{MIII} = \Phi_P^T Q_{FIII}^{CB} + \Phi^*{}^T_P Q_{MEIII}^{CB} \quad (\text{Eq. 137})$$

Where Φ_P^T and Φ_P^{*T} are the slices of the modal matrix corresponding to the translational and angular DOF according to discussed earlier in this chapter.

The total modal force due to the aerodynamic forces observed in the fuselage body fixed reference frame becomes

$$Q_M = 2*(Q_{MII} + Q_{MIIT}) \quad (\text{Eq. 138})$$

From the Aerodynamic loads resulting generalized translational force Q_F , generalized moments Q_{ME} and a generalized modal force Q_M augment the Generalized force Vector Q (Eq. 121). Torque on the wing root due to motor torque additionally augments $Q(\xi)$ in EOM.

Chapter 6: Results

First in this section the verification of the modeling assumptions and estimation of wing flexibility through flight test data is presented. After which the simulation results are presented, and is followed by a dynamics and kinematics verification of simulation results to flight test data.

6.1 *Modeling Assumptions Verification and Wing Flexibility*

6.1.1 Coordinate Variation

In order to check modeling assumptions and inherent wing flexibility in the experimental flight test data set E2 was first computed and analyzed in the fuselage

body fixed reference Frame CB0 which is located on the wing root. The experimental resulting position states all of the tracking markers $i=1$ to 53 at the verification frequency of 6.06 Hz is shown in **Figure 87** to **Figure 89** below.

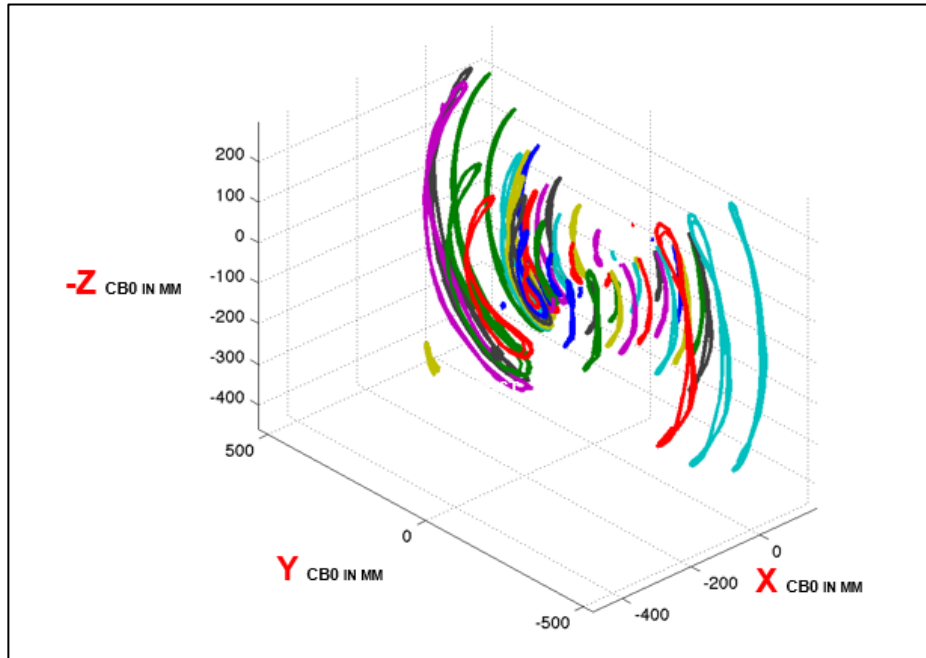


Figure 87: *Isometric View Position States Path all Vicon Markers over one Flapping Cycle at 6.06 Hz*

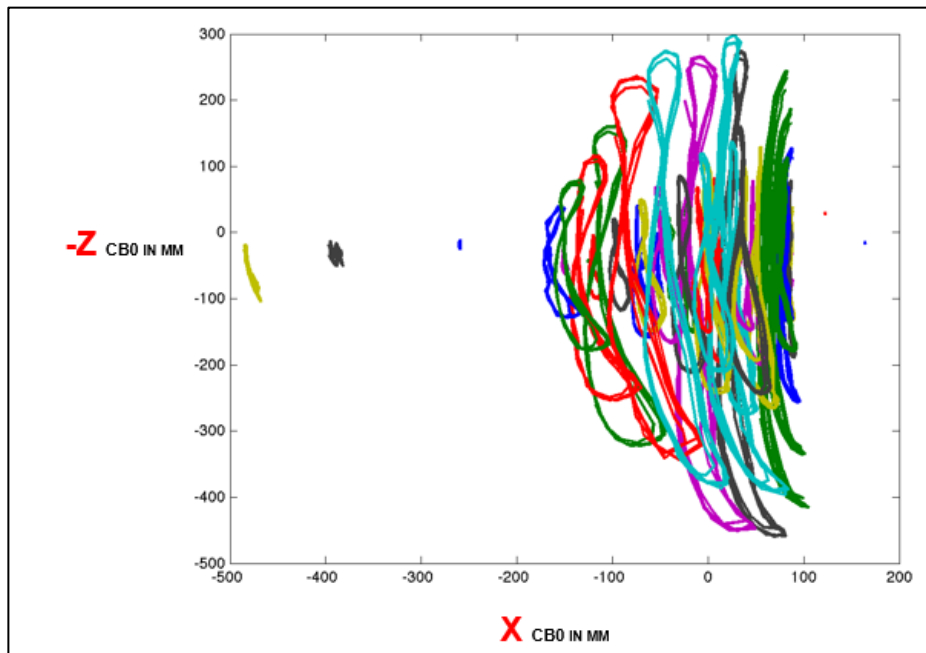


Figure 88: *Side View Position States Path all Vicon Markers over one Flapping Cycle at 6.06 Hz*

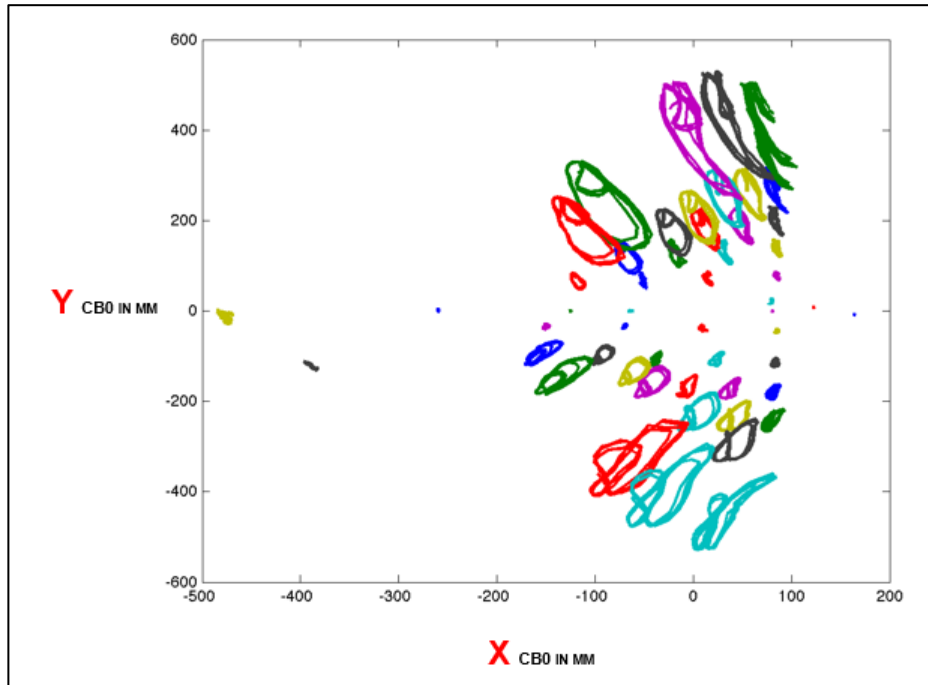


Figure 89: *Top View Position States Path all Vicon Markers over one Flapping Cycle at 6.06 Hz*

6.1.1.1 Zero Deflection Reference Plane

Figure 90 shows the zero deflection reference plane (PS0) of tracking markers in the flight test data which is used for referencing purposes in the following analysis. In the following this position state is named PS0. The zero deflection reference plane is associated with a zero flapping angle (FA) position. These are the wing marker locations in free-flight in extended position that is the maximum norm of the x/y position in CB0 (over a flapping cycle). It represents the x/y plane of the wing fixed reference plane CW defined in the previous chapter (4.6). For PS0 the mean maximum norm of y and mean maximum norm of x of $i=1$ to 53 was computed over 125 position states.

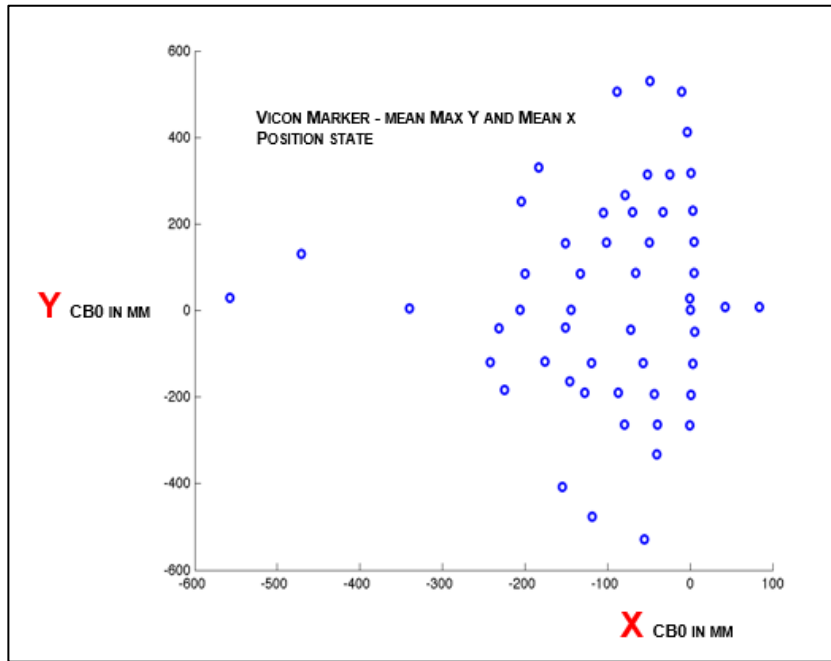


Figure 90: *Top View Ornithopter Markers Position State 0 Deflection Plane*

6.1.1.2 Quantification Wing Flexibility

In order to estimate the wing flexibility in y , maintains the x location constant according to the definition of PS0. PS0 can be thought of as the marker locations of a rigid wing configuration.

Analyzing the flight test data E2 in all position states during the flapping cycle results in a mean standard deviation of 18.054 mm in the y location (y_{CW}) of all marker points on the wing. This indicates the y deflection and therefore flexibility in the wing fixed reference coordinate system CW during the flapping cycle. Sample size hereby is 125 positions states, which represents 3.5 flapping cycles, and is averaged and plotted for one flapping cycle in Figure 91.

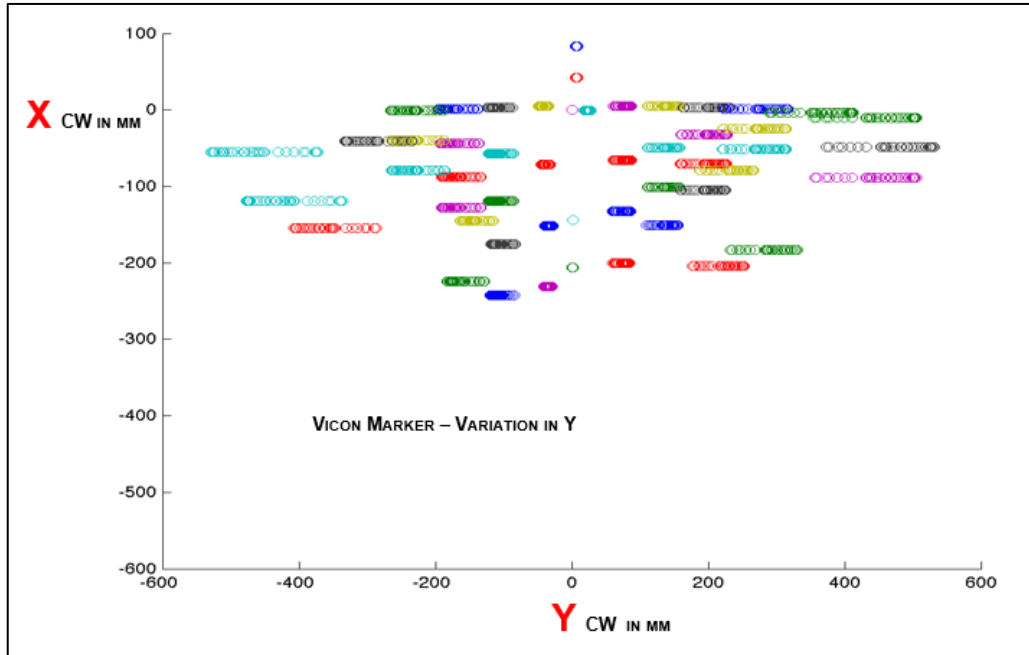


Figure 91: *Top View Y Coordinate Flexibility in the Wing Fixed Reference Plane CW*

The wing flexibility in x is computed analogous to y and results in a mean standard deviation of 7.12 mm in x (xCW) of all marker points and position states during one flapping cycle (Figure 92).

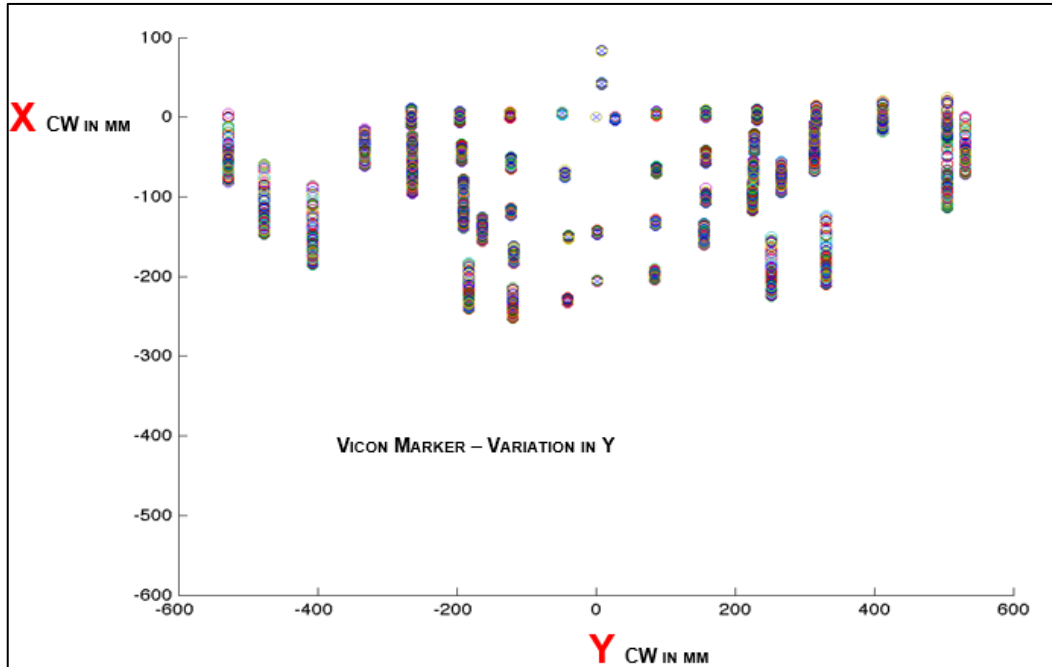


Figure 92: *Top View X Coordinate Flexibility in the Wing Fixed Reference Plane CW*

In summary a mean deformation in x of all tracking markers on the wing of 7.12 mm and a mean deformation in y of 18.05 mm in the wing fixed reference frame CW was found during a flapping cycle and defines the flexibility of the experimental wing ML101 in free flight.

6.1.2 Large Global Deformations

All position states during a flapping cycle of the wing markers of experimental data E2 are mirrored around YCB0 in order to obtain a refinement of wing markers on one wing. By computing a polynomial fit between marker locations in all position states during a flapping cycle the wing surface of the experimental flight platform in free flight is visualized. Large deflections occurring during the free flight can be clearly shown in the fuselage fixed reference frame CB0. **Figure 93**

shows 3 out of 34 example position states of the wings in free flight in the fuselage reference frame CB0.

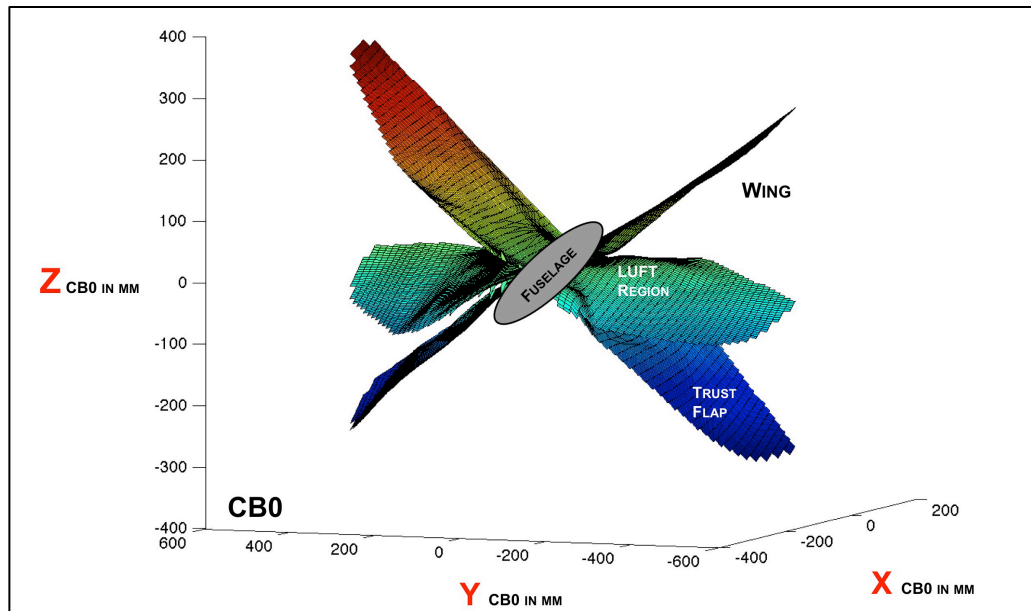


Figure 93: Bio-inspired ornithopter research platform in free flight: *Three Experimental Orientations During a Wing Beat: Viewed in the fuselage Body Fixed Reference Frame CB0*

For orientation the fuselage and the luff and thrust flap region is indicated in the Figure 93 above. The total flapping range and amplitude is 483 mm, which is the total maximal deformation of the wing in the fuselage fixed reference frame CB0. The flapping amplitude in the following normalizes experimental wing deformation emanating of the wing fixed reference frames in order to gain prospective on the magnitudes.

6.1.3 Wing Fixed Reference Frames

Elastic deformations are modeled in local wing fixed reference frames, which are optimally fitted in flight test data E-2 in order to archive small deformations

compliant with linear constitutive material assumptions of the wing components. Modeling assumptions are checked here and experimental deformations emanating from the local reference frames are described. Recall that in the simulation the large global motions are archived through the induced motion of wing reference frames (underlying rigid body motion) and the elastic deformation emanating from the wing fixed reference frames.

Flight test data analysis in the following lead to the five- body model due to remaining large deflections off the wing body fixed reference frames CW in the thrust flap region area. In order to remain accurate in simulation results especially when changing model configuration verification with Flight test data E-2 results in the 5 body approach in order to ensure the validity of linear geometric and material structural dynamic assumptions on the wing.

For the final five body- flexible multi-body dynamics model local wing fixed reference frames are fitted optimally in flight test data E-2 in order to adjust underlying rigid body motion and results in small deformations (<10% of the flapping range) off the wing reference frame. Two reference flapping motions in the flight test data E2 were identified, which can be thought of as underlying rigid body motions. The criteria for optimal fit emanating from wing reference frames were to minimize experimental out of plane deformation.

The local wing fixed reference frames CW attached to wings under zero deflection PS0. For convenience recall definition wing fixed reference frame CW (Figure 94), x is along the axis of the fuselage and y is along the wing span.

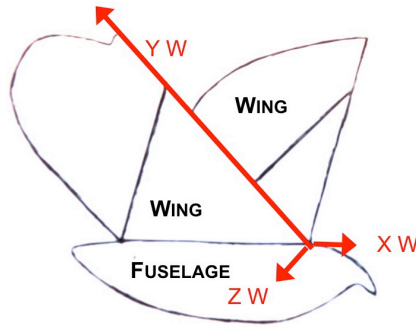


Figure 94: *Wing Fixed Reference Frame CW*

The zw- coordinate describes the deformation off the reference frame which is flapping around x with flapping angle β .

The reference flapping motion of β was optimized such that the smallest deformations off the wing fixed reference plane over the flapping cycle was archived when fitted in the flight test data E2.

Following

Figure 95 shows the computed maximal occurring deformation (for this minimal case) of a wing fixed reference plane. Here the maximum deflection during the flapping cycle of all marker locations in the wing fixed reference frame is computed. Its surface is plotted vs. PS0 reference plane. The maximal elastic deformation occurring during a flapping cycle (mean value over all points) from the wing fixed reference frame in the thrust flap region is 9.54% of the flapping range with a

Standard Deviation (STD) of 5.88%. Here the maximal deflection at a point occurring during a flapping cycle is relatively large and 19.59%.

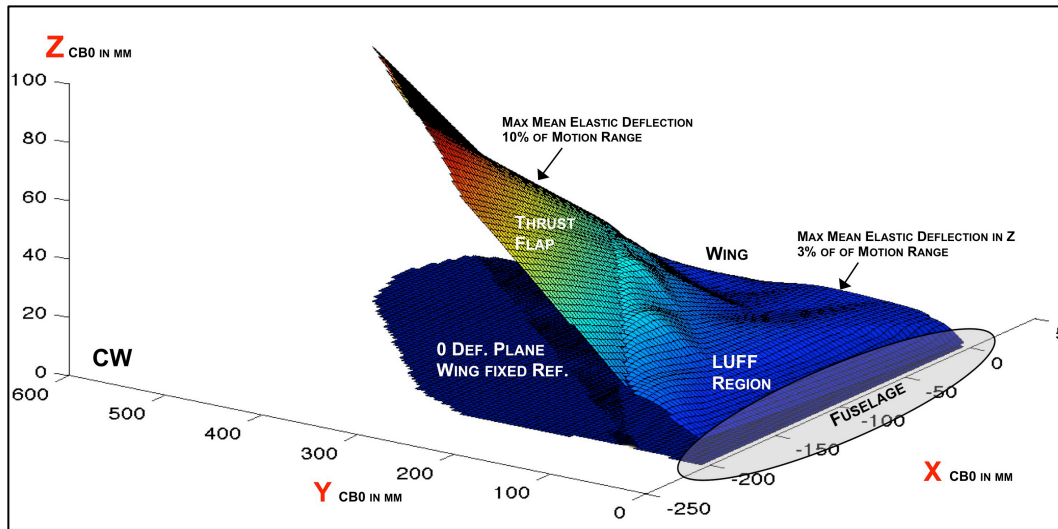


Figure 95: Bio-inspired orntihopter research platform wing in free flight: *Maximal elastic deflections of the wing in the wing fixed reference frame during a wing beat; Viewed in the fuselage fixed reference frame CB0.*

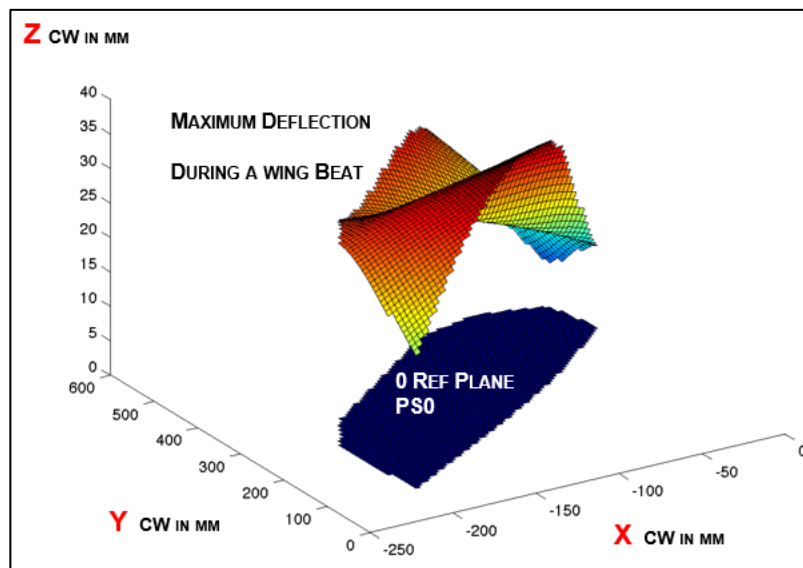


Figure 96: Bio-inspired orntihopter research platform wing in free flight: *Maximal occurring elastic deformation in the thrust flap region of the wing in the wing fixed reference frame CW*

The maximal elastic deflection (mean value over all points) from the wing fixed reference frame in the luff region is relatively small and 3.08% of the flapping range with a standard deviation of 1.96% and shown in Figure 97. The maximal deflection point occurring during a flapping cycle is 7.49% of the flapping amplitude. The maximal deformations are small here and linear elastic material constitutive assumptions are valid.

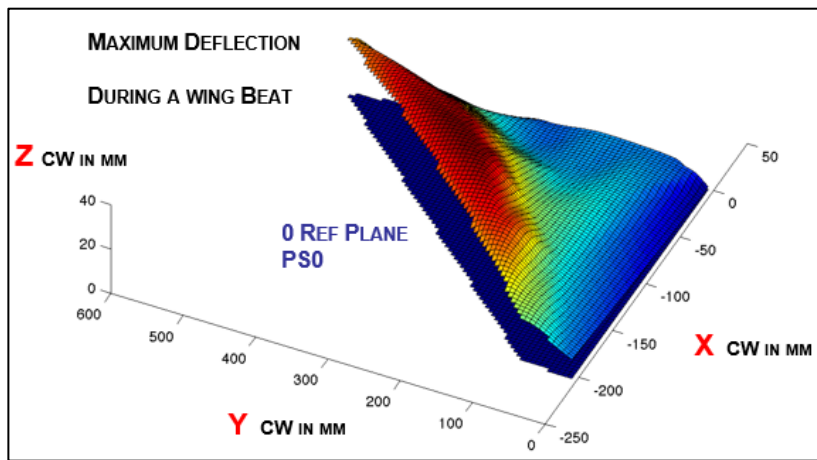


Figure 97: Bio-inspired ornithopter research platform ML 101 wing in free flight: *Maximal occurring elastic deflections luff region in the wing fixed reference frame CW*

Due to the large max. elastic deflection in the thrust flap region shown in Figure 95 to Figure 96 and additional thrust flap region fixed reference plane is required to in order to model the ornithopter system using a linear elastic flexible multi- body dynamics assumptions.

An optimal fit of a thrust flap region reference plane reduced the deformation in the thrust flap region off the wing fixed reference planes significantly. The maximal

mean of all tracking markers elastic deflection of its reference frame reduces from 9.54% of the flapping amplitude to 5.21 % of the flapping amplitude, with a STD of 2.12%. The reductions of mean maximal elastic deformation off the zero reference plane PS0 is shown in Figure 98.

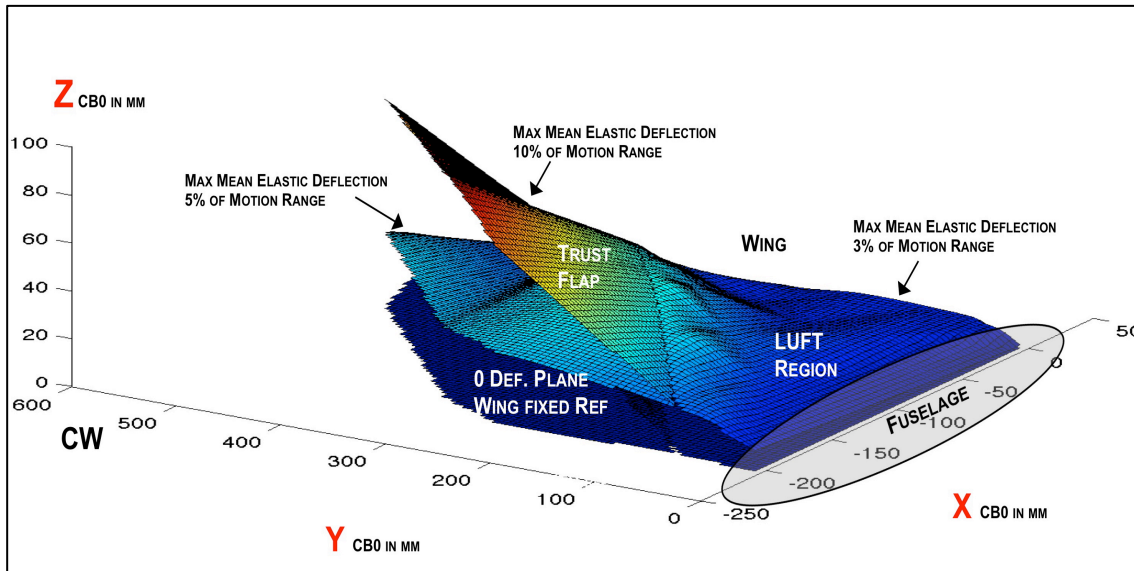


Figure 98: Bio-inspired ornithopter research platform wing in free flight: *Maximal occurring elastic deflections of the wing fixed reference frame during a wing beat; Vied in the fuselage reference frame CB0*

This minimal average deformation off the wing fixed reference frames (which was computed over all position states during a flapping cycle) was archived by an additional thrust flap reference motion. The position states of the x- axis of the thrust flap fixed reference frame CBT at the flapping frequency β of 6.06 Hz are shown in Figure 100 below. For convenience recall the definition of the thrust flap fixed reference frame

Figure 99. The z- location of a marker point are deformations emanating from the thrust flap fixed reference frame.

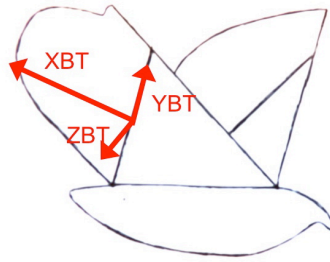


Figure 99: Schematic location Trust flap region Reference frame

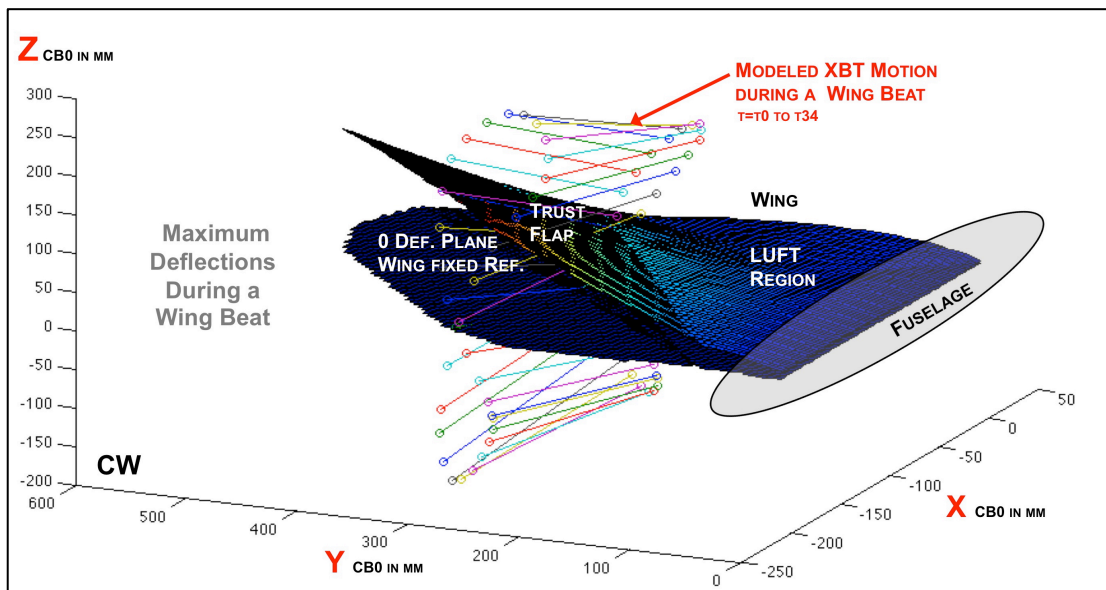


Figure 100: Bio-inspired ornithopter research platform wing in free flight: X- axis of modeled thrust flap region reference frame in 34 position states viewed in the fuselage fixed reference frame CB0.

xBT in Figure 100 is the x- axis of the thrust flap region fixed reference frame plotted in 34 position states and is the underlying rigid body reference motion in five- body flexible dynamics model. Shown location of the xBT is the optimal fit of orientation and location of the rigid reference motion in order to archive the smallest deformations off the wing fixed reference plane PS0. Z and y- axis of CBT remain attached in orientation and location to the wing fixed reference frame CW.

Reference motion and optimal fit (minimal deformation off the wing fixed reference plane in z) was found by fitting the x- axis of CBT between location marker 28 and marker 30 on the wing. The z-axis, and y-axis location of the reference frame CBT in reference frame CW is constant over the flapping cycle and according its PS0 position. The optimal fit of the reference motion (angle zeta ζ) shows the minimal deformation off the thrust flap region reference plane of 5.21 % of the flapping range. Tested underlying rigid body motion combinations were a rigid x- axis fit of CBT between maker locations (42/53, 42/52, 46/53, 46/52, 47/51, 48/51, 49/51, 29/31, 28/31, 27/30, 25/30, 25/26 and 25/9) over the flapping cycle. Therefore the flapping angle (zeta ζ) position states over a flapping cycle results from flight test data according to Figure 100. The position on the wing of the x- axis (reference frame CBT) is shown in **Figure 101** which is a one DOF motion around the y-axis of CBT.

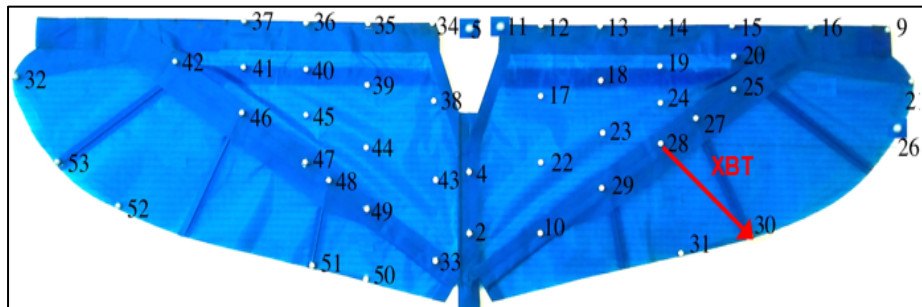


Figure 101: *Bio-inspired ornithopter research platform wing in free flight marker location: XBT- axis location on experimental research platform resulting in minimal deformation off a reference YBT/ZBT reference plane using a 1 degree of freedom flapping motion.*

A one DOF two DOF, and three DOF underlying flapping motion was tested for the aforementioned combinations of marker locations. However additional DOF's showed no significant improvement in the magnitude of deformation emanating from

the reference plane and would unnecessarily complicate the model. Remaining DOF is and θ_{IM1} in flexible- multi body dynamics models generalized coordinate $\xi_{II(R/L)}$ for Bodies II according to preceding nomenclature. Following Figure 102 shows the thrust flap angle zeta location on the wing. For 1 DOF zeta rotates around the y- axis of CBT and is θ_{IM1} in the model.

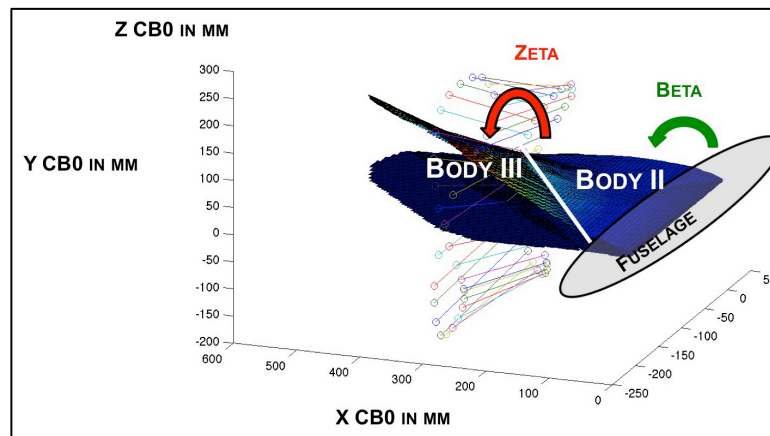


Figure 102: *Flapping Angle Zeta and Beta location on shown in experimental wing test data (maximal deformation of CW, 0 reference plane and XBT Position states)*

Following Figure 103 shows the wing flapping angles of underlying rigid body motion of the five- body flexible dynamics model in comparison to in flight (E2) found wing motions. The mean delta zeta is 1.44% of the flapping angle range with a STD of 8.58 % of the flapping angle range and the mean delta beta is 0.35% of the flapping angle range with a STD of 5.43% of the flapping angle range. The small difference is due to “wobbling” and small flexibility in the x and y plane in CW and CBT respectively found in the flight test data E-2. This x/y plane flexibility is neglected in the underlying rigid body motion of the model according to Figure 103.

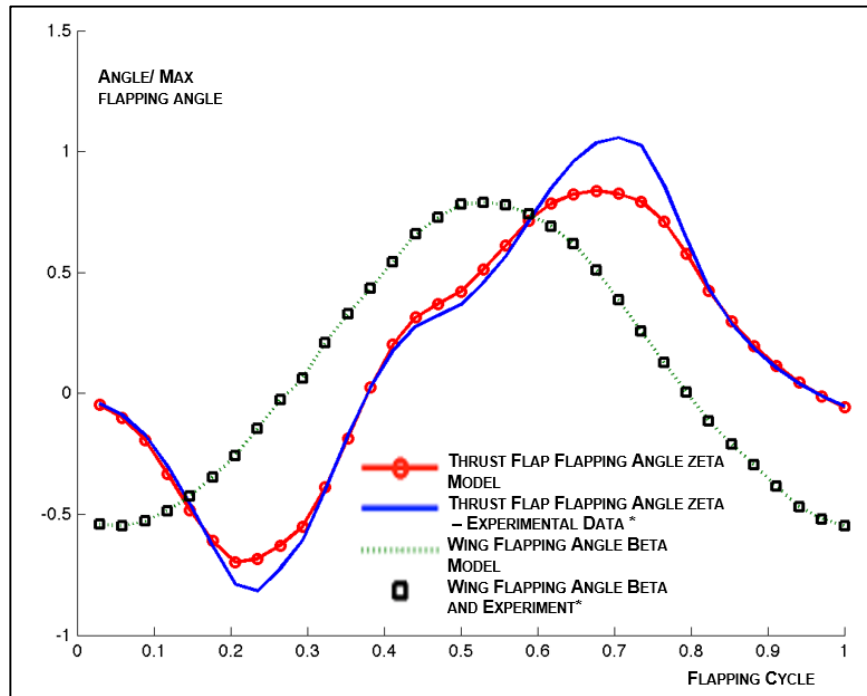


Figure 103: Modeled Flapping Angle Time History based on Flight test data vs. Flapping angle in flight test data E-2

Following Figure 104 shows thrust flap motion zeta in the experimental data in the body fixed reference frame CB0 at 34 position states over the flapping cycle and has the aforementioned three rotational DOFs.

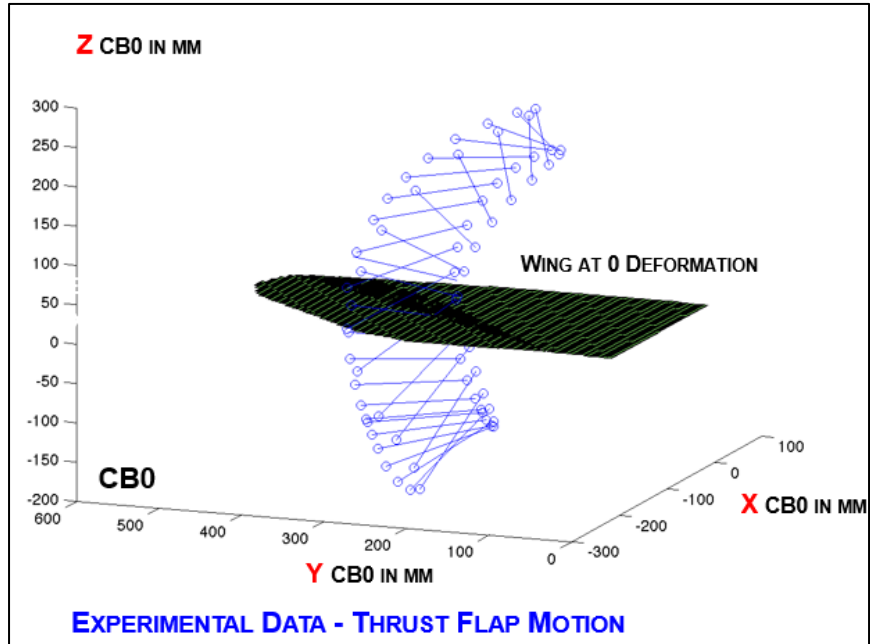


Figure 104: *Experimental Thrust Flap Reference motion in 34 position states in the fuseage fixed reference plane CB0 vs. wing at zero deformation (PS0)*

Modeled thrust flap reference motion according to Figure 105 has one DOF= θ_{IM1} and resembles a figure eight motion.

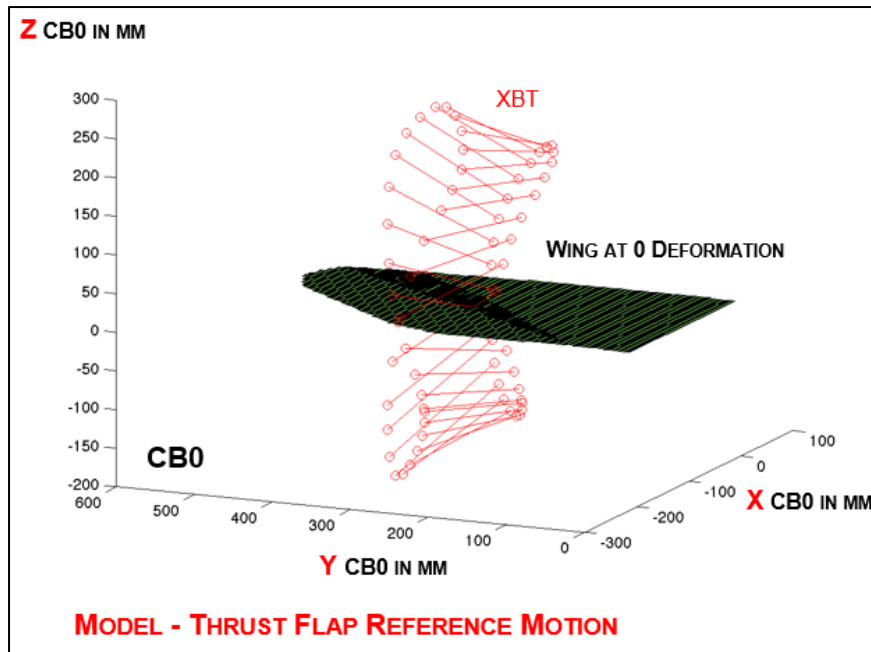


Figure 105: *Modeled thrust flap reference motion in 34 position states in the fuselage fixed reference plane CB0 vs. wing at zero deformation (PS0)*

The mean normalized error over 34 position states of the XCB0 coordinates of the thrust flap region x-axis XBT is 2.64 % with a STD of 1.51% of the range of motion in z.

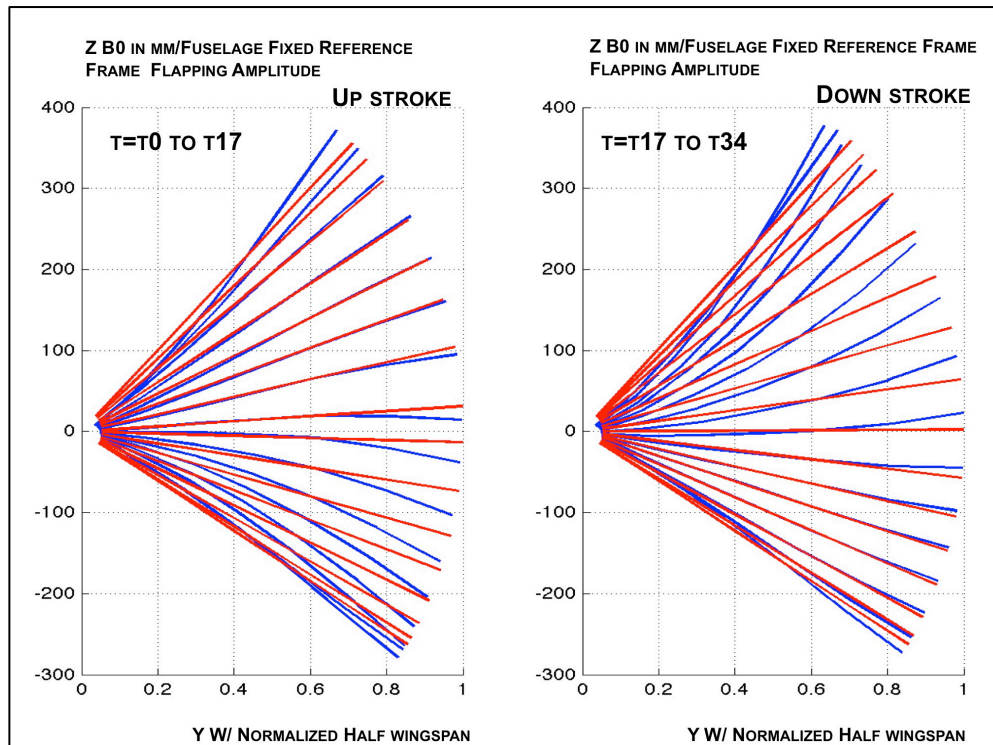
The mean normalized error over 34 position states of the YCB0 coordinates on the thrust flap region x-axis XBT in y is 6.07% with a standard deviation of 3.83% of the range of motion in z.

The small error shows that one rotational DOF θ_{IM1} is significantly dominant in the working ornithopter platform thrust flap region and additional rotational DOFs can be neglected using an optimal thrust flap region reference frame fit. The dominant motion in the thrust flap region of the working ornithopter flight platform can be described accurately by a figure eight motion which represents the underlying rigid body motion of the flexible wing in a five body flexible dynamics model. Recall that superimposed elastic deformation leads to full deformation found in experimental flight test data.

6.1.4 Leading Edge Spar Flexibility

Next, the leading edge spar deformation off the optimal wing fixed reference plane CW is examined. Figure 9 below shows the leading edge spar deformation of ML101 during the up and down strokes and the underlying rigid body motion in the model

that is the x-axis of CW according to Figure 94. X-axis of CW, the underlying rigid body motion of the wing and experimental wing deformation are shown in 34 position states during up and down stroke. Experimental wing deformations are shown, which is a polynomial fit of deformation of leading edge markers 5/11/12/13/14/15/16/9 shown in **Figure 100**. Following Figure 106 shows the modeled and experimental deformation in the fuselage body fixed reference frame CB0 normalized over the wing half span. Modeled reference motion here describes the global large deformation only, which is motion of reference frame CW in the flexible multi-body dynamics model. Experimental kinematics shows the magnitude of the elastic deformation and underlying global large deformations. Comparison is made in order to check validity of the small deformation assumption of the global reference plane in the model and estimate the leading edge spar flexibility.



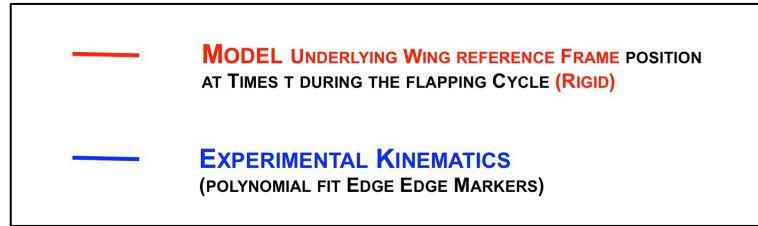


Figure 106: *Experimental elastic deflections in the fuselage fixed reference frame CB0 during a wing beat*

In **Figure 106**, it can be observed that the experimental deformations of the reference plane (model underlying wing reference frame) are small. To examine this closer, one switches to the wing fixed reference frame CW. Figure 107 shows the experimental deformation of the leading edge spar in the wing fixed reference plane during a flapping cycle. The flapping cycle is shown in 34 position states during up and down stroke and the normalized z-coordinate of the experimental data is shown along the wing half span during those position states. In order to get a reference of magnitude, the z-coordinates were normalized by the flapping amplitude. The maximal deformation due to flexion of the leading edge spar is 11% of the flapping amplitude at position state $t=34$.

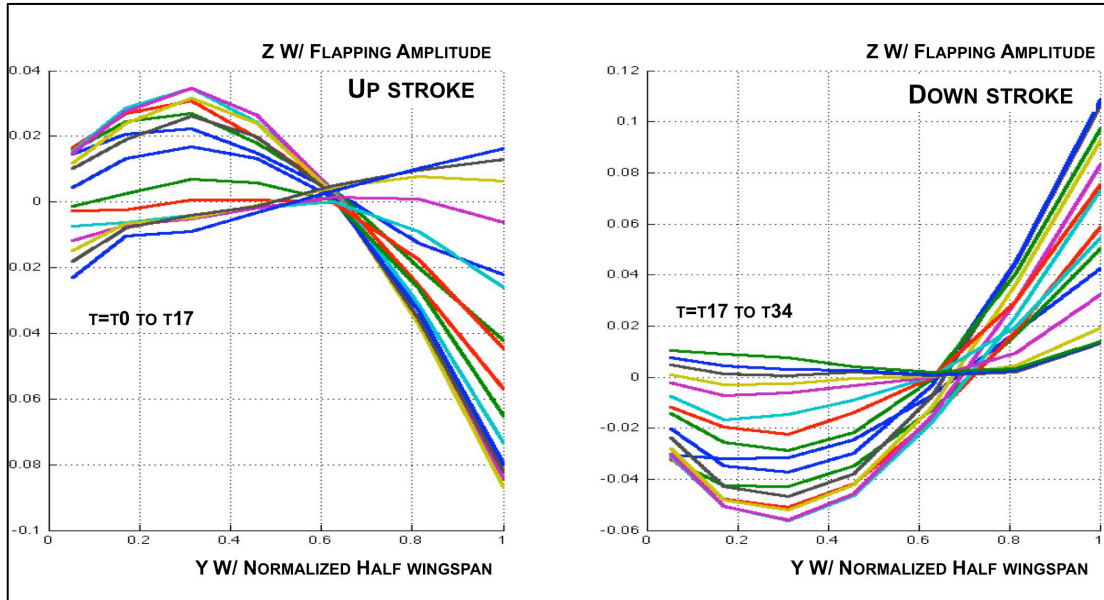


Figure 107: *Experimental elastic deformation in the wing fixed reference frame CW during a wing beat*

This affirms that small deformations of the leading edge spar in free flight of the wing fixed reference frame CW are observed during the flapping cycle and linear material constitutive assumptions are valid for the wing model leading edge spar.

In summary, due to the optimal fit of an additional underlying rigid body motion, small deformations of the wing fixed reference frames are present and linear elastic structural dynamics modeling assumptions for the wing lead to valid results for integration in the flexible multi-body dynamics model. Figure eight motion in the thrust flap region is dominant and inherent in the ornithopter test platform ML101 during free flight.

6.2 Model Results

Model input is the wing motion profile provided by the flapping motion function on the wing root, which results in dependent thrust flap dynamics according to bio-inspired experimental wing kinematics. Further input includes wing stiffness and wing geometry. Model image **Figure 108** is shown in below.

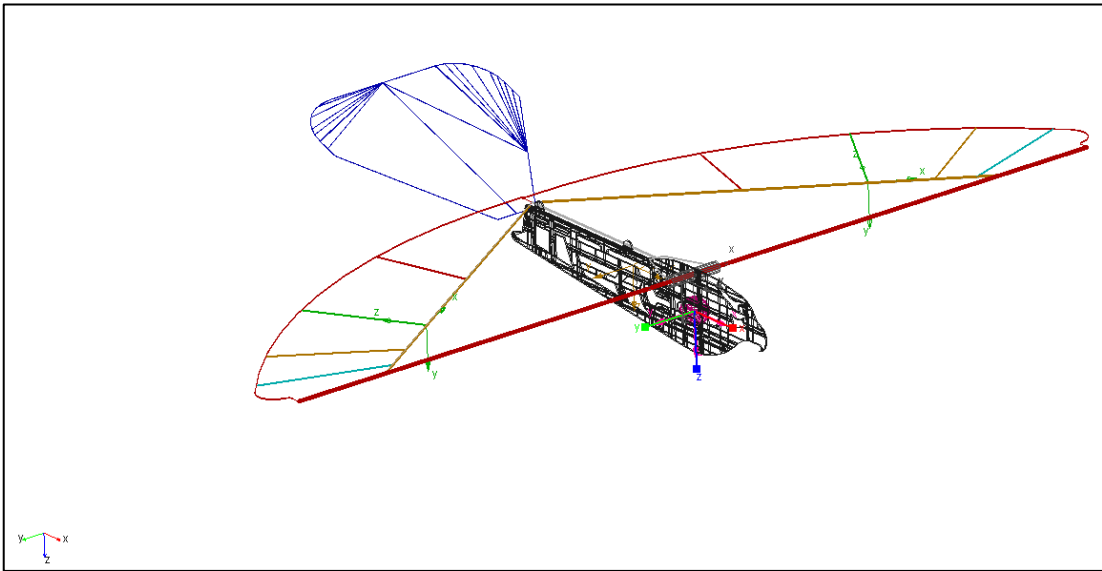


Figure 108: *Model Image SimXpert - ML101 5 body Flexible Multi Body Dynamics Model (Fuselage reference frame CB is highlighted)*

The model output for each body in the system is the kinetic energy magnitude, translational kinetic energy magnitude, angular kinetic energy magnitude, translational momentum (magnitude, x,y,z), angular momentum about CM, potential energy, center of mass (CM) position, CM velocity, CM acceleration, CM angular velocity, and CM angular acceleration (magnitude, x,y,z) for each body in the system. Such bodies are the fuselage, the two wing thrust flap regions (L/R), and the two

wing Luff regions (L/R). For the flexible wing bodies of the system, the mode shapes and strain energy are included in the output.

The model output also includes each body attachment point in the system such as the origin of the wing root reference frames CBW and the origin of the thrust flap region reference frame CBT. Characteristics obtained here are the element force (magnitude, x,y,z), element torque (magnitude x,y,z), translational displacement, projection angles (A_x,A_y,A_z), the translational velocity (magnitude, x,y,z), the translational acceleration (magnitude, x,y,z), the angular velocity (magnitude, $x,y=0,z$), and angular acceleration (magnitude, $x,y=0,z$).

The model outputs for each chosen marker location in the model are translational displacement, projection angles (A_x,A_y,A_z), translational velocity (magnitude, x,y,z), translational acceleration (magnitude, x,y,z), angular velocity (magnitude, $x,y=0,z$), and angular acceleration (magnitude, $x,y=0,z$). These output characteristics can be chosen and obtained for various input characteristics. Input characteristics according to experimental flight platform wing tip kinematics and integrated loads resulting from model simulations are compared to experimental data (E1, E2

Chapter 3: Bio- Inspired Research Platform) in the remainder of this chapter. Loads are obtained in the vehicle dynamics model at the fuselage center of mass CB, which is the highlighted coordinate system in **Figure 108**.

Individual model verification of disciplines comprising and resulting in the final multi-disciplinary model is also presented. These are the final verifications resulting from model iterations of the independent models of the coupled problem. Aerodynamic Model C verification results and FMBD model results without aerodynamic loads are presented in comparison to experimental data in E1-I and E3, respectively

Chapter 3: Bio- Inspired Research Platform. Structural dynamics in FMBD model was evaluated earlier in Chapter 6.1.

6.3 Constraint Model Verification

6.3.1 Integrated Forces

The following shows integrated forces of Aero- model A and inertia forces due to the wings in comparison to Experimental Data E1. That is the constraint configuration of model and experiment.

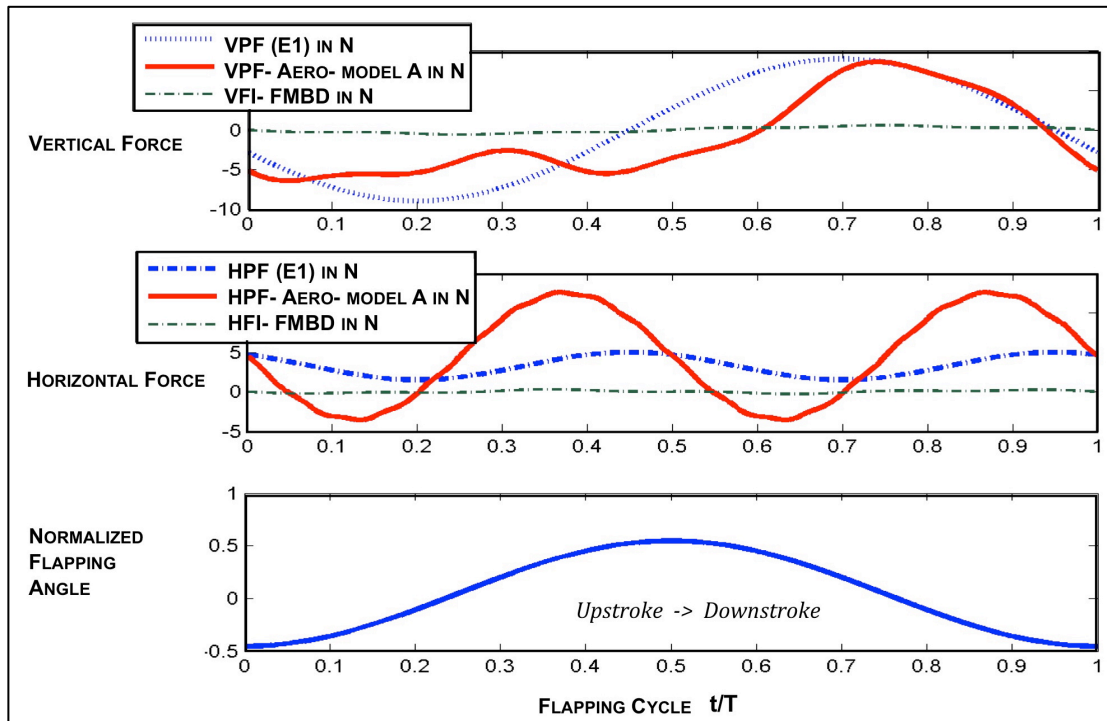


Figure 109: Verification Bench Test – Model 3 A– Scale ML101 (6.17Hz)

The mean absolute error comparing the VPF E1 to Aero model A is 2.9611 N with a mean error of 1.01 N/ STD 3.68 N. The magnitudes of inertia forces due to the wing VFI are comparatively small and the main difference in integrated force results in both (experimental and simulation of constrained vehicles) stems from the aerodynamic modeling assumptions used. Aero- model A uses three blade elements for the proof of concept study of modeling methodology.

The mean absolute error in horizontal direction shows an over prediction due to the circulatory force assumption used according to Harmon. The mean absolute

error in the horizontal direction is 4.59 N with a mean error of 1.25 N and a STD of 5.03 N. The methodology of experimental kinematics based Aero- model A in the FMBDM was proven using that. Using three blade elements only, tracking behavior to experimental data using quasi-steady aerodynamic assumptions works considerably well. Originally, the error was also thought to stem from neglected inertia forces in an aerodynamics model. Inertia forces have been found to be considerably small and main contributions of error stem from aerodynamic assumptions. Model A was used in combination with a FMBDM with only one wing reference frame CW. Three body representation (one wing body each wing) results in the main error in tracking wing kinematics (such as wing tip kinematics) and were discussed earlier in Chapter 6.1.3.

6.3.2 Wing Tip Kinematics

In the previous section, the experimental deformation of the wing was compared to the large global deformation resulting from model simulation, the underlying wing fixed reference plane position. In the following, experimental deformation is compared to the total deformation in the model that is the result of the underlying reference frame motion and the superimposed elastic deformation and model performance is discussed. One chooses the wing tip location in 34 position states in order to compare modeled wing kinematics to experimental wing kinematics. The wing tip position state is determined by the combination of motion of both wing fixed reference frames and the elastic deformation in the model, lies off axis of any reference frames used, and is inherently one of the most extreme deformations on the wing. Therefore, it is a good geometric location for a kinematic verification point on

the wing. The wing tip position is the marker 2 location indicated in **Figure 101** above. Wing tip location is shown in one experimental position state during free flight of the wing during down stroke in Figure 110.

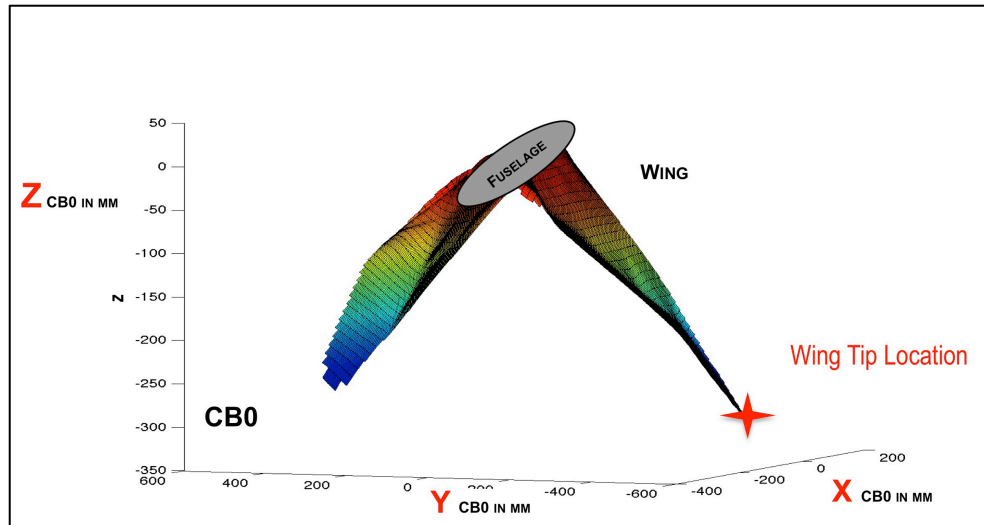


Figure 110: *Wing Tip Location – Viewed at one Experimental Position state (mid Downstroke)*

The blue solid line in **Figure 111** shows the experimentally measured wing tip path (E-2) using 34 position states during one flapping cycle. The red interrupted line shows 34 position states of the five body flexible dynamics model where aerodynamic loads are resulting from final aerodynamic Model C. The wing tip path in free flight and the simulation results in free flight are shown in fuselage body fixed reference frame on the wing root CB0.

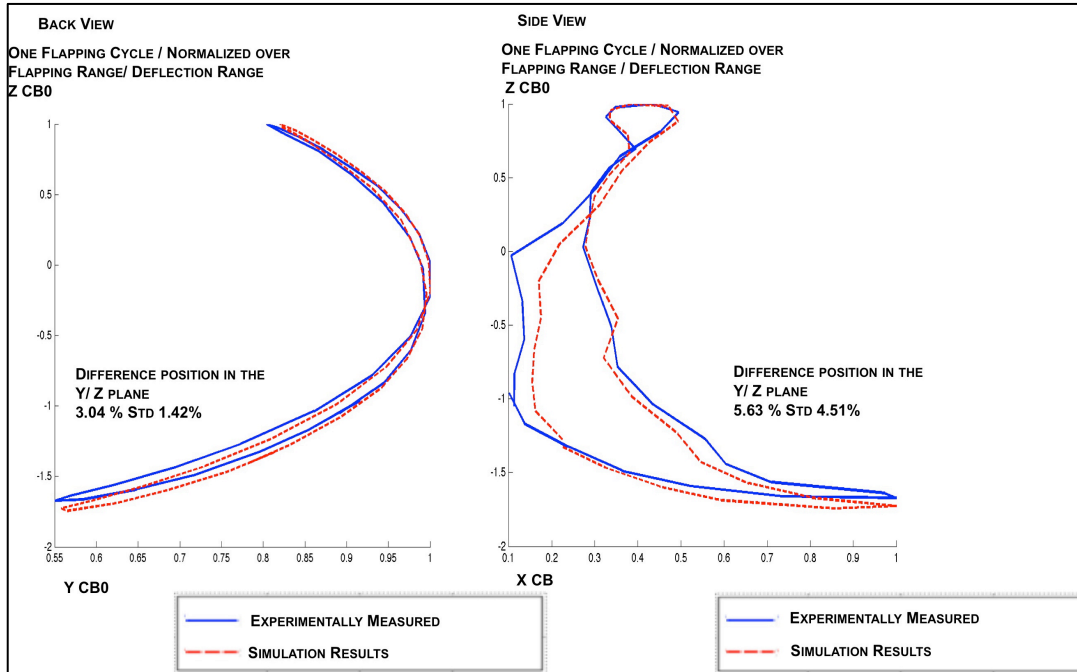


Figure 111: Results Wing Kinematics Model 5 - Experiment: *Flight Test*: a) *Back View* b) *Side View*

The magnitude error of the position state in the y/z plane (Back View) is 3.04% with a STD of 1.42%. The magnitude difference in the position state in the z/x plane (Side View) is 5.43% with a standard deviation of 4.51% over all position states. The data is normalized by its maximal deformation occurring in x, y, and z, respectively. The maximal elastic deformation of the wing tip location during the wing beat off the thrust flap region fixed reference plane is 7.49% of the flapping range.

The magnitude of the error comes from the error in elastic deformation of the wing off the underlying wing reference frames. Due to the kinematics and location of wing fixed reference frames, elastic deformations are mainly directed in ZB0; therefore, only the z/y and z/x plane CB0 is used for verification purposes.

These elastic deformations are the result of geometric and stiffness properties of the wing and aerodynamic load magnitude and distribution.

6.4 *Unconstraint Model Verification*

6.4.1 Integrated Forces

Following addresses the model verification in free flight condition. The fuselage is hereby unconstrained. Vertical and horizontal forces observed at the fuselage center of mass at the origin of CB were observed in free flight test data (E2) and in the unconstrained five- body vehicle dynamics model using aero- model C. Model verification results of are shown in **Figure 112** below. E2 data used are previously discussed in section 3.2.2.2 (**Figure 64**).

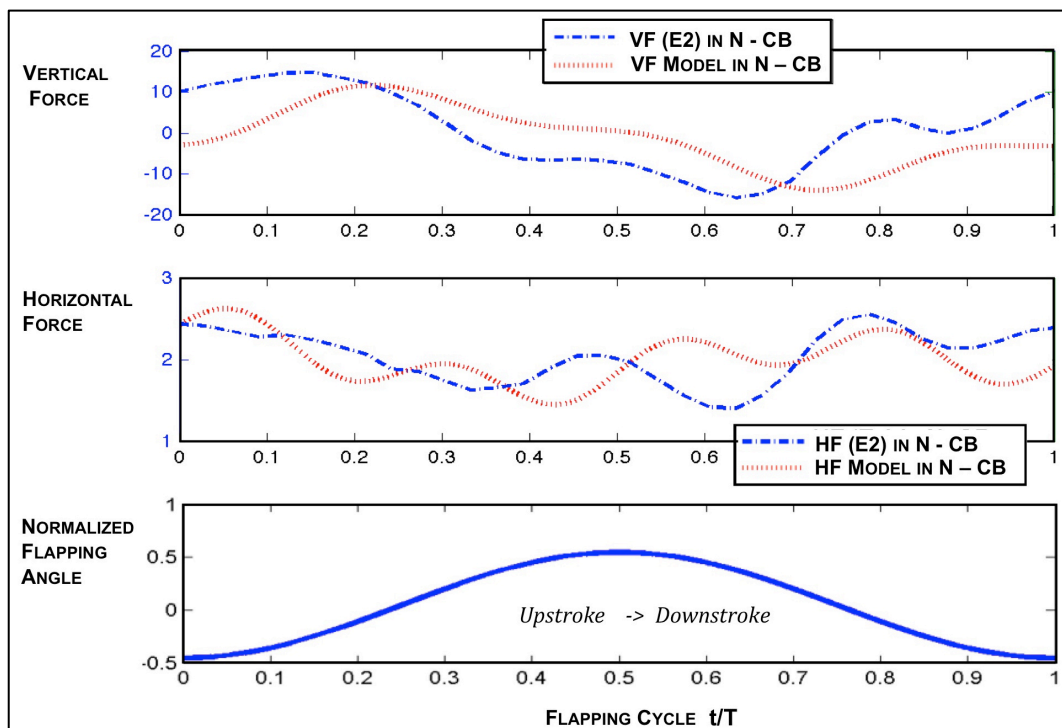


Figure 112: Propulsive forces acting on the fuselage center of mass – Obtained from Experiment (E-2) and Five- Body Vehicle Dynamics Model using Aerodynamic Model C

The mean error in the vertical direction is 2.34N / STD 11.70N (mean absolute error is 9.505N / STD 5.5518N) and observed forces correlate well. A slight under prediction in VF is observed which is assumed to stem from aerodynamic model assumptions. The mean error in the horizontal direction is 3.758N / STD 2.6N (mean absolute error is 2.08N / STD 4.37N). The vehicle is flying with a mean flight velocity and forces observed are due to acceleration in flight direction during the flapping cycle. Vertical forces are observed at the fuselage center of mass due to the present heave motion in the flight platform (ML101) during free flight. Forces on the fuselage center of mass CB give a good estimate about model performance when compared to free flight test data.

6.4.2 Wing Inertia Forces

The total integrated forces acting on the origin of fuselage fixed reference CB are due to the inertia of the wing are discussed next. Two cases are compared: Case 1, with the thrust flap motion zeta turned off (a wing with one flexible body) and Case 2 with the thrust flap motion turned on and two wing bodies according to final five body vehicle dynamics model. Results were computed at a flapping frequency of 6.06

Hz and shown in Figure 113.

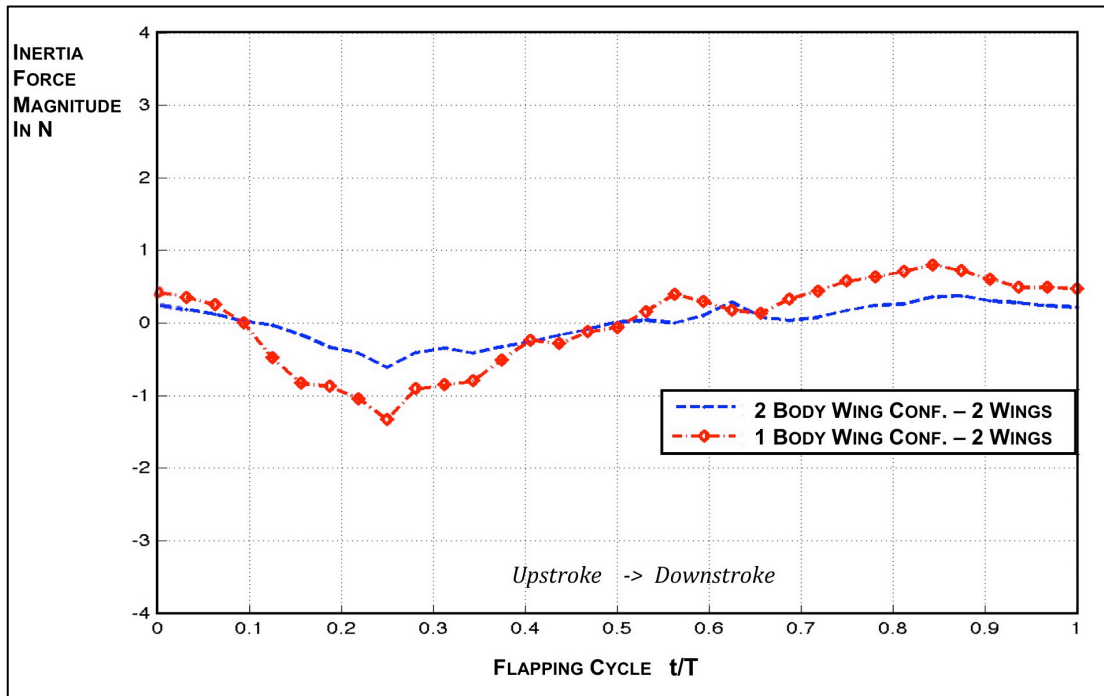


Figure 113: Simulated Inertia forces on Fuselage Center of Mass CB in free flight (IVPF) – Upstroke – Down stroke transition

It can be observed that inertia forces exerted on the fuselage center of mass CB in free flight are smoother using a two body wing simulation, which corresponds to the two section luff and thrust flap region wing vs. a wing using only one body. Inertia forces due to the wing are of small magnitude compared to aerodynamic forces. Besides the aerodynamic advantages, division is advantageous considering inertial forces exerted on the vehicle fuselage only. Using the one wing body model, the mean value of inertia forces is -0.0054N (STD 0.26N) with a mean absolute value of 0.21N (STD 0.13N). For the two- body flexible wing model, the mean of the inertial force is -0.0105N (STD 0.06066N) and the mean absolute value is 0.5108N (STD 0.13N). In summary, the inertial forces are smoother using the two- body flexible wing representation according the five- body flexible multi- body dynamics model.

The magnitude of forces resulting from the five- body dynamics model was compared to the experimental data (E3). It can be observed that the mean absolute value of the simulation lies well within the magnitude of measured inertial vertical propulsive forces (IVPF). A simulation was run at 4.7 Hz flapping frequency of (flapping angle-beta) in order to obtain a comparison operation point for experimental data set E3, and at the baseline flapping frequency used throughout this work, 6.06 Hz. Due to the large measurement error in E3 for this small magnitude of forces, the verification mainly serves to do a magnitude check of the occurring inertia forces in the vertical direction.

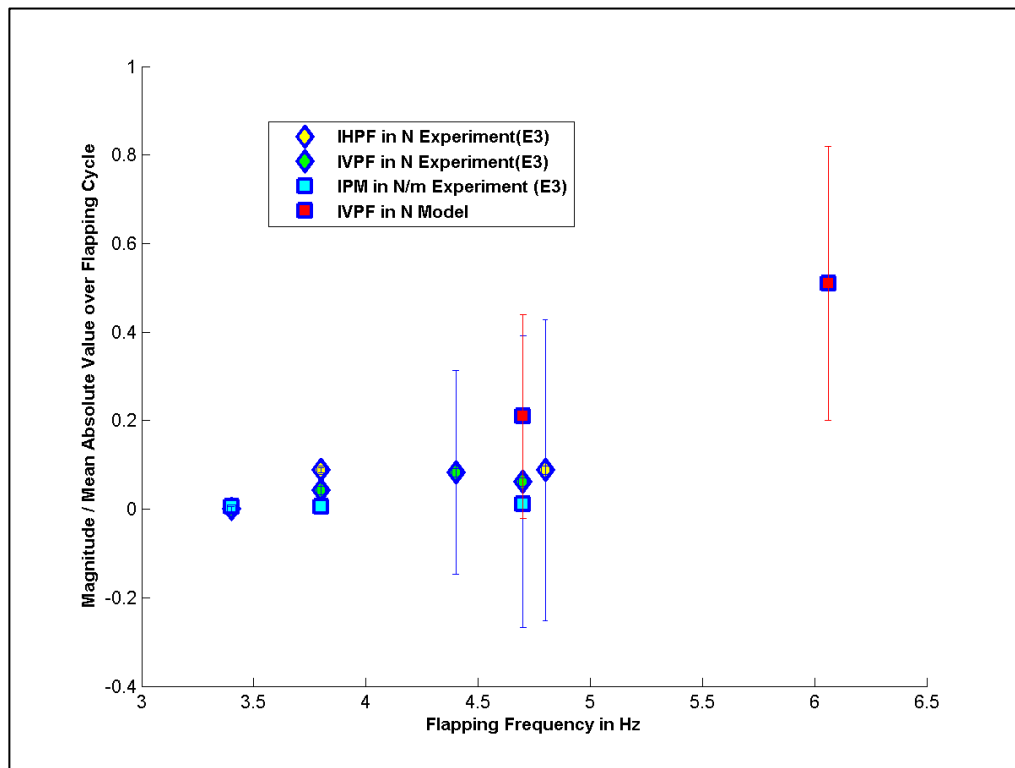


Figure 114: Results Inertia forces (E3) with error bars vs. simulation results with STD a) Inertial Horizontal Propulsive Force IHPF b) Inertial Horizontal Propulsive Force c) Inertial Pitching Moment vs. Magnitude.

Therefore, a further validation of IHPF and IPM adds no additional value to the credibility of the model, but one can observe that measured and simulated forces (averaged over the flapping cycle) are comparable and of same magnitude. It can be concluded that the five- body dynamics model predicts inertia forces accurately. This depends mainly on the masses, mass-distribution, orientation, and acceleration of the model components. Orientation and accelerations are dependent on the flapping frequency (β), dependent thrust flap angle (ζ), and wing reference frames, which are according to flight physics of the research platform. Since the geometry and mass properties of the model components are according to research platform, the mass and mass distributions also lead to accurate results of the flexible multi-body dynamics model. The elastic deformation and therefore the inertia change due to elastic deformation during the flapping cycle without the presence of aerodynamic loads are small. Elastic deformations are mainly caused by the aerodynamic forces which are 45 times larger than occurring inertia forces for ML101 (6.06Hz).

6.4.3 Inertia Invarriants

Recall that the floating frame of reference formulation results to a highly nonlinear mass matrix because of the inertia coupling between the reference motion and the elastic deformation [52]. According to discussed in section 4.1 three cases were implemented to quantify the effect of inertia coupling due to the elastic deformation on the wing. EOMs for the five- body dynamics system of the ornithopter were solved for the cases and also compared to experiment. Here case A) is the rigid body motion only. Case B) includes no inertial coupling between rigid and

flexible body EOMs and case C) where the EOMs are fully coupled.

Case B) leads to a 20.56% (STD 8.64%) difference in the integrated load results compared to case A). This was computed in CB0 for the flapping frequency of angle β of 6.06 Hz and recorded over the flapping cycle. Case B) correlates better to experimental data but is inconclusive and the differences are within the measurement error for the inertia forces due to the wing. Case B) is thought of an improvement over case A) due to its higher fidelity. However this shows that inclusion of wing flexibility using flexible wing structure is not highly significant for the inertial force generation. Wing flexibility is mainly significant for aeroelastic effects in the five body vehicle dynamics model. The effect of the inclusion of a second wing body in the wing model is more significant and results in a 56% (STD 30.81%) difference in inertial forces due to the wings. This was measured in CB0 of the five body rigid vehicle dynamics system vs. CB0 in the three body rigid vehicle dynamics system (for flapping angle β of 6.06 Hz over the flapping cycle.) In the three body system the trust flap regions is rigidly attached to the luff region of the wing.

Including the inertia cross terms (Eq. 82)- (Eq. 90). for the wing bodies according to case C) leads to a 10.56% (STD 5.64%) difference for the inertial loads due to the wings compared to Case B) on CB0 (for flapping angle β of 6.06 Hz over the flapping cycle.). The inclusion of inertia cross terms according to case C) become more significant with higher flapping frequency, increased aspect ratios of the wing, increased mass and increase deformation of the wing of their reference frames. They

are included in the five body vehicle dynamics model to facilitate such a change in configuration.

6.4.4 Aerodynamic Forces

Next, the aerodynamic forces obtained from final aero- model C are compared to aerodynamic forces obtained from system ID through experiment (E1-I). This is the decoupled force verification for aerodynamic forces in free flight conditions according to assumptions and constraints of aerodynamic model C.

To provide comparability to source data, the data (E1-I 3.2.2) is plotted over the wing stroke and normalized over the wing stroke due to the scaling invariance of research platform MSK004 (E1-I) and aero- model C tailored to MSK001.

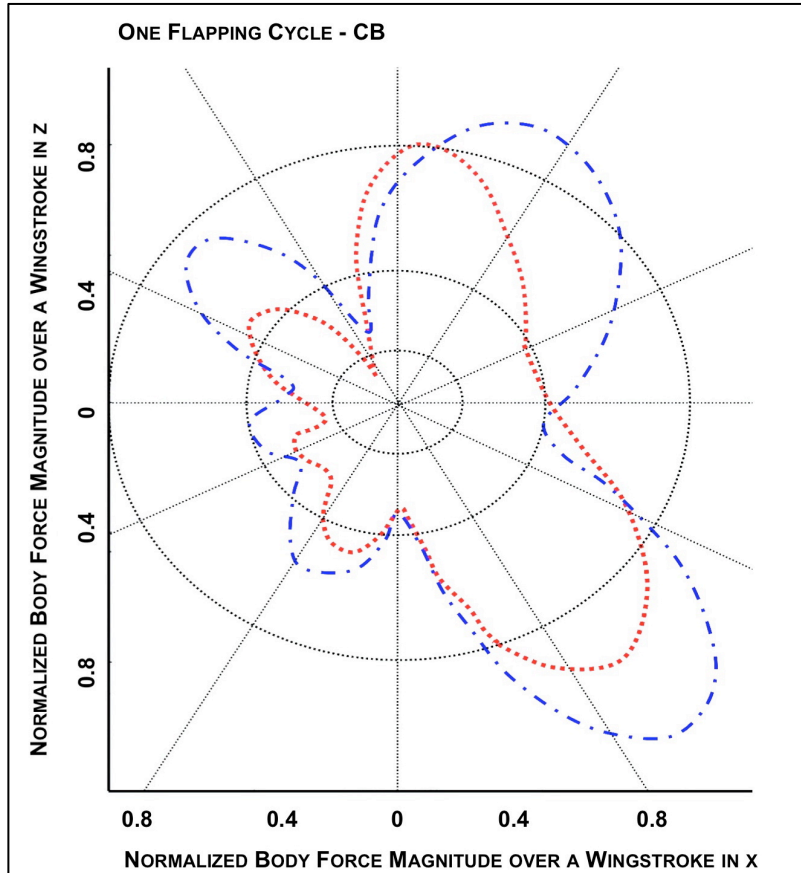


Figure 115: Results: *Body force magnitude System ID Model (MSK 004 E1-I -.-) [9] – Body force magnitude – Aero- model C*

The normalized error (Mean over Wing Stroke/ Normalized By Max Force Sys ID Model) is 10.71% of the max system ID model force with a STD of 9.87%. Good tracking behavior of Aerodynamic model C (based on BET) can be observed to the model obtained by system identification. Difference in magnetite is assumed to mainly stem from differences in wing scale (MSK 004 to ML101).

Note that in workflow Step 2 Validation and Model Iteration (**Figure 27**) The aerodynamic model output is TVSD force. Integrated forces and moments are correlated to integrated forces and moment data obtained by Grauer through systems

identification of free flight test data using the secondary research platform Odyssey MSK 004 [9]. Integrated horizontal and vertical propulsive forces and moments were obtained at the fuselage center of mass through system identification and aero- model C.

Within its limitations the data set by Grauer provides the appropriate and comparable dataset for decoupled aerodynamic forces in free flight. Integrated forces and moments in clamped conditions were also obtained for the primary and secondary research platform by Harmon but are due to numerous factors not suitable for the correlation of the aerodynamic model i.e. Forces and moments contain inertial effects and circulatory effects change the aerodynamics in clamped conditions, as observed in the tests [19].

Correlation of the aerodynamic model output can provide a good estimate of the quality of the aerodynamic model assumptions. However an infinite number of solutions of TVSD forces on the wing can lead to the same horizontal propulsive and vertical lift force. A scaling difference between the research platforms used for the wing kinematic input (primary research platform) and the system identification data (secondary research platform) influences the aerodynamic also. Scaling is still a significant challenge in flapping wing aerodynamics and its influence is not entirely understood [21], leading to magnitude differences between integrated forces of the model and system identification model data by Grauer. Due to the aforementioned infinite number of solutions and a scaling difference, an optimization algorithm for

aerodynamic model improvement was not advantageous and model iterations are performed using an educated model tuning. Aerodynamic model assumption changes were made according to known influence factors significant to flapping wing flight and observed through open literature or empirical knowledge. Model iteration changes entail changes in lift distribution on a blade element, dynamic stall cut off angles, and span-wise lift distribution. The data set by Grauer provides the only available comparison metric in free literature to give a good estimate of the quality of aerodynamic modeling assumption as a stand-alone in the model development process.

Chapter 7: Concluding Remarks

7.1 *Summary of Work*

A novel modeling methodology and a five- body flexible dynamics model considering aeroelasticity has been developed in this work. Structural dynamics and linear elastic modeling assumptions have been verified and compared to in- flight wing kinematics data measured for this work, and an array of arrival experimental data. Model output correlates to experimental test data and the model can be utilized for multi-disciplinary design optimization of a flapping wing ornithopter. This work contributes a nonlinear vehicle dynamics model of an ornithopter using a linear elastic multi-body dynamics representation of an ornithopter with a quasi-steady aerodynamics model (initialized by free- flight kinematics) to consider aeroelasticity of the wings. Linearizing nonlinear structural dynamics of the wings due to its large

deformations during free flight was also explored by investigating free-flight kinematics. A unique modeling methodology was developed to facilitate the model.

Chapter 1 described the background for the areas of interest in this work. That is background in flapping wing, flapping wing aerial vehicles, low Reynolds number unsteady aerodynamics and aerodynamic models for flapping wing, flexible multi-body dynamics, vehicle dynamics and models of ornithopter. Chapter 2 described the modeling methodology developed in this work. Chapter 3 described the experimental research platform, archival data and experiments performed within the assumptions and constraints of the model. Chapter 4 described the flexible multi-body dynamics model developed, and Chapter 5 described the aerodynamics model developed. In Chapters 4 and 5, model integration within the aforementioned modeling methodology was also outlined. Chapter 6 showed and discussed results of verification of modeling assumptions and simulation results.

7.2 Scope and Contributions

The main contribution of this work is the development of an experimentally verified aeroelastic flexible multi-body vehicle dynamics model of a bio-inspired ornithopter using a novel modeling methodology. The multi-disciplinary model results of model iterations in individual disciplines, that involve, aerodynamics, structural dynamics, and multi-body dynamics. The problem of ornithopter was comprised of unsteady aerodynamics in a low Reynolds number flow field, flapping-

wing aerodynamics, fluid structure interaction and nonlinearities in both structural and multi-body dynamics. Experimental data were obtained and analyzed for the understanding of the flight physics and dynamics of avian scale flapping wing flight and aided the model development.

The scope and contributions of this work can be subdivided into the following areas of interest: contributions to flexible multi-body dynamics modeling of an ornithopter; flexible multi-body dynamics modeling; aerodynamics modeling of flapping wing flight; aero elasticity in flexible multi-body dynamics modeling vehicle dynamics modeling; multidisciplinary modeling methodology; and understanding of flight physics and dynamics of flapping wing flight. Novel contributions within this work are highlighted subsequently.

7.2.1 Vehicle Dynamics Model of Ornithopter

In summary, a five-body flexible dynamic model of bio-inspired ornithopter resulted from this research. Hereby, the details of the model are:

- Vehicle dynamics model considered wing flexibility, multi-bodies and FSI in the wings of a bio-inspired ornithopter.
- A floating reference frame formulation was used, where two sets of coordinates described the configuration of a deformable wing body.
- Elastic deformations are described in local wing fixed reference frames.

The local wing fixed reference frames are attached to wings under 0 deformation.

- Wing fixed reference frames are actuated to achieve large global motions (large flapping motion) and oscillating body dynamics.
- Structural deformations are obtained by a linear combination of mode shapes. The flexible body constraints and modes are implemented using the Craig-Bampton method.
- Inertial coupling through elastic deformation of the wing is considered using cross-terms in the inertia matrix. This allows simulation accuracy in changing the ornithopter configurations (mainly if wing mass or flexibility is significantly increased).
- The kinematics obtained in experimental free flight initialize the model.
- The model inputs are: experimental wing kinematics (initialization of aerodynamic loads), wing stiffness, wing geometry, material properties, and the flapping motion at the wing root (that is the flapping angle β). The model outputs are: deformations of the vehicle, kinematics, dynamics and energy. These in addition to modes, stresses and strains on the wings, can be obtained for each component of the system or the system as a whole.
- The in the model utilized structural dynamics, multi-body dynamic and aerodynamic modeling assumptions have been experimentally verified.
- The multi- disciplinary model was implemented using Matlab (Aerodynamics), Patran/Nastran (Structural dynamics) and Adams (Multi-body dynamics) in a SimXpert framework and integrated

simulation was archived.

7.2.2 Aerodynamics Model and Aeroelasticity

In summary, three analytical aerodynamic model iterations (Aerodynamic model A, aerodynamic model B, and aerodynamic model C) using experimental wing kinematic inputs have been developed. The final aerodynamic model C is used for FSI in the five body flexible dynamics model. Final aerodynamic model C is an efficient and practical application for the aerodynamic and aeroelastic analyses of flapping wings. The scope of aerodynamic model C is further discussed next.

- The model is formulated in terms of generalized coordinates of the 5 five body flexible vehicle dynamics system.
- The model considers cord- and span-wise flexibility in the wing, due to camber and orientation in each blade element, and fore and aft approach in wing-cord direction.
- The model used a blade element refinement of 13 blade elements per wing, 4 in the thrust flap region, and 9 in the luff region of the wing. For the model development, experimental wing kinematics over a wing stroke serve as input variables. In the final model, kinematics obtained from the five body flexible dynamics model serve as input variables for aerodynamic load generation. The first set of loads is obtained through experimental kinematics.

- The quasi-steady and analytical aerodynamic model using blade element theory accounts for non-circulatory forces, circulatory forces, leading edge suction, the cord-wise force due to the camber, cordwise friction drag, and dynamic stall.

7.2.3 Modeling Methodology

Contributions and scope of this work in modeling methodology can be summarized according to the following and are novel:

- The individual models are developed in close conjunction with flight based data, due to the shortcoming in state-of-the art understanding of flapping wing flight. Individual models are correlated against experimental data, and integrated into a comprehensive model.
- The wing kinematics, obtained from experimental data serve as input variables for model development, and initialization for fully integrated flexible multi- body dynamics model considering aeroelasticity. The resulting multi-body model is coupled in order to archive the ability to utilize the model for a changed vehicle configuration. This model is initialized by experimental kinematics.
- The novel model initialization with empirical flight test data leads to accuracy throughout the simulation and fast correlation of a new FMBD vehicle configuration when implemented (Wing motion profile, wing stiffness and wing geometry is changed).

- The formulation of aerodynamics in terms of the coordinates of the five body dynamics system in order to fully integrate the model is novel in the modeling- methodology.
- The efficient fluid structure interaction procedure, using superposition of sign waves for the model reduction is novel. The aerodynamic model output is formulated as continuous function which is the exchange variable to the structure. This improves FSI.

7.2.4 Understanding of flight Physics and Dynamics

Summary of novel insight into flight physics and dynamics of efficient bio-inspired ornithopter is as follows:

- The quantification of flight efficient wing motion profiles through flight test data, that is flapping angle β kinematics and associated flapping angle ζ kinematics is a new contribution to the field of flapping wing flight.
- The identification of flight efficient wing flexibility through flight test data is novel and aids the understanding of flapping wing flight physics and dynamics (e.g. flight efficient flexibility of up to 12 % of half-span emanating from the wing fixed reference frames during a flapping cycle).

- The analysis of in-flight test data revealed inherent figure eight motion in thrust flap region and identified efficient wing kinematics in avian scale flapping wing flight.

7.3 *Summary of Novel Contributions*

In the following novel contributions in this work are highlighted. Original contributions of experimentally verified and integrated multi-disciplinary model of an ornithopter were:

- 1) The five-body flexible multi-body dynamics model of an ornithopter itself.
- 2) The five-body vehicle dynamics model of ornithopter considering FSI.
- 3) The flexibility consideration in the wing, here the accurate inclusion of wing flexibility in the multi-body dynamics of an ornithopter is novel as well as that the model accounts for cord and span-wise wing flexibility in both aerodynamics and structural dynamics.
- 4) That the model accounts for dynamic elastic inertial coupling.
- 5) That the aerodynamic model is formulated in terms of generalized coordinates of the five-body flexible dynamics system.
- 6) That the model accounts efficiently for fluid structure interaction through novel model integration and methodology.
- 7) That the model framework is experimentally verified utilizing free-flight test data of ornithopter.

- 8) That the model development is in close conjunction with flight physics and dynamics through empirical observations.
- 9) That the aerodynamic model uses in-flight kinematics as input variables.
- 10) That the quasi-steady BE aerodynamic model provides time-variant loads on the wing as a continuous function. These are specially distributed on the wing. Mentioned is a novel aerodynamic model reduction technique and results in efficient FSI.
- 11) The novel experimental wing kinematics of ornithopter in free flight (E-2), the contribution of this work is the Design of Experiment (DOE) for verification of flexible multi-body dynamics model.
- 12) The verification of individual models comprising the coupled problem of avian scale ornithopter using experimental data, and integration of tools into a fully integrated efficient simulation initialized by free-flight kinematics of flapping wing. That is novel in modeling- methodology.

7.4 Summary of Conclusions

It is concluded that the linear elastic multi-body dynamics model is appropriate for nonlinear elastic vehicle problem with inherent large deformations due to utilization of appropriate underlying rigid body reference motions. Fully integrated model utilizing aerodynamic model C led to accurate multi-body vehicle dynamic predictions. The following summarizes conclusions of this work:

- 1) The model flexibility assumptions are in tune with flexibility and wing deformation kinematics found in working ornithopter platforms in free flight.
- 2) The cord- and span-wise flexibility in the wing is considerable. Camber forming in aerodynamic model has to be done over 2 regions in cord-wise direction. Only out of plane deformations in the z-direction off the wing fixed reference frames are considerable but remain small and under 10% of global deformation amplitude. The x/y flexibility in the wing fixed reference planes are negligible.
- 3) The linear elastic multi-body dynamics model used the Craig-Bampton Method for the integration of the flexible bodies in the multi-body system and lead to accurate predictions for the problem.
- 4) The inertial coupling through elastic deformation of the wing needs to be considered to allow simulation accuracy in changed ornithopter configurations.
- 5) A model that uses in-flight wing kinematics for initialization of aerodynamic loads leads to flight physics based results and fast correlation of flexible multi- body dynamics model considering FSI.
- 6) Five- body underlying rigid-body motions lead to accurate predictions of ornithopter system using linear elastic multi- body dynamics and leads to a considerable model reduction compared to a nonlinear elastic multi-body model.
- 7) Two wing fixed coordinate systems result in small deformations of the

reference frames and therefore diagonalize the stiffness matrix in the EOM of the five body flexible multi-body dynamics system.

7.5 Recommendations

In the following, recommendations are subdivided into modeling recommendations, verification recommendations, and recommendations investigating flight physics and dynamics.

For the model recommended improvements, include a time variant aerodynamic force due to the tail in the flexible multi-body dynamics model of the ornithopter through the coupling of an aerodynamic model. This would allow the tail to be used as a control surface in the vehicle dynamics model (e.g. reduce heave and pitch motions).

Further inclusion of verification of the model using its flight trajectory vs. experiment (E2) flight trajectory is recommended using translational and rotational position states, velocity, and acceleration of fuselage fixed reference frame CB.

At the expense of computational cost, it is recommended to develop a CFD model utilizing in-flight kinematics in order to refine aerodynamic load distribution and aerodynamic load magnitude on the flexible wings in the model.

Furthermore, it is recommended to utilize the model for flight physics and dynamics studies in order to study the variation of the wing motion profiles (that is the flapping angle β) and cord- and span-wise adjustments of wing flexibility (wing stiffness in the model); therefore, improving performance of avian scale ornithopter.

Observing biological flyers and analyzing bio-inspired research platform flight test data, it is believed that underlying figure eight motion in the wing plays an important role in unsteady aerodynamic force generation, and a further investigation of this phenomena in flight physics and dynamics utilizing experiment is recommended.

References

- [1] S. Seeleke, "Robo-Bats May Be Next Remote Control Flyers," 7 July 2009.
- [2] G. Bunget and S. Seeleke, " Smart Structures and Materials & Nondestructive Evaluation and Health Monitoring," 15th International Symposium. pp. 69282F-69282F-12, March 2008.
- [3] F. Bohorquez, D. Pines, and P. Samuel P., "Small rotor design optimization using blade element momentum theory and hover tests," *Journal of Aircraft*, vol. 47, no. 1, pp. 268-283, January 2010.
- [4] R. P. Malhan, "Investigation of Aerodynamics of Flapping Wings for Micro Air Vehicle Applications," *Dissertation* , 2013.
- [5] P. Seshadri, "Experimental investigation of an flapping wing hovering micro air vehicle," *American Helicopter Society Aeromechanics Specialists Conference*, January 2010.
- [6] W. Shyy, "Recent progress in flapping wing aerodynamics and aeroelasticity," *Prog Aerospace Sci*, p. doi:10.1016/j.paerosci.2010.01.001, 2010.
- [7] M. Boyer, "Nano Hummingbird," February 2012. [Online]. Available: <http://www.avinc.com/nano/>.
- [8] Z. Wang, "Flapping Wing Flight Can Save Aerodynamic Power Compared to Steady Flight," *Physical Review letters*, vol. PRL 103, no. 118102 , 2009.
- [9] J. Grauer and J. E. Hubbard, "Modeling and System Identification of an ornithopter flight dynamics model," 2011.
- [10] Usm, "<http://rt.com/news/us-military-instability-afghanistan-891/>," May 2014. [Online].
- [11] Remp, "https://www.rememberpeople.com/articles/target_types/firefighter/," May 2014. [Online].
- [12] Z. Jackowski, "Design and construction of an autonomous ornithopter," *Master's thesis*, 2009.
- [13] J. Grasmeyer, "Development of the black widow and microbat mavs and a vision for the future of mav design," *AIAA International Air and Space Symposium and Exposition Conference*, vol. 2901, July 2003.
- [14] A. Wissa et. al, "Flight Testing of Novel Compliant Spines for Passive Wing Morphing on Ornithopters," *Structural Dynamics, and Materials and Co-located Conferences*, April 2013.
- [15] E. Avadikian, and J.E. Hubbard, "Ornithopter development and optimization guide," *Tech. Rep.*, 2010.
- [16] J. Grauer, and J.E. Hubbard, "Modeling of ornithopter flight dynamics for state estimation and control," *IEEE, American Controls Conference*, June 2010.

- [17] S. Seeleke, "Mechanical properties of bat wing membrane skin," *Journal of Zoology*, vol. 239, pp. 357-378, 1996.
- [18] A. Azuma, "The Biokinetics of Flying and Swimming", Blacksburg, VA: AIAA Education Series, 2005.
- [19] R. Harmon, "Aerodynamic Modeling of a flapping membrane wing using Motion Tracking Experiments," *Masters Thesis*, 2008.
- [20] H. Ben-Gida et. al, "Estimation of Unsteady Aerodynamics in the Wake of a Freely Flying European Starling (*Sturnus vulgaris*)," *Plos one* , 22 November 2013.
- [21] W. Shyy et. al, "Aerodynamics of Low Reynolds Number Flyers," *Cambridge University Press*, 2008.
- [22] W. Shyy et. al, "Aerodynamics of Low Reynolds Number Flyers", New York, NY: Cambridge University Press, 2008.
- [23] D. Floreano et. al, "Flying Insects and Robots", Heidelberg, London New York, NY: Springer, 2009.
- [24] S. Swartz, "Skin and bones: the mechanical properties of bat wing tissue," pp. 109-126, 2010.
- [25] P. Gopalakrishanan, "Unsteady Aerodynamic and Aeroelastic Analysis of Flapping Flight", Dissertation Virginia Polytechnic Institute and State University, 2008.
- [26] M. Waszak, and C. S. Buttrill, "Stability and control properties of an aeroelastic fixed wing micro aerial vehicle", vol. 4005, AIAA Flight Mechanics, pp. A01-37226, Montreal 2001
- [27] J.D. Delaurier, J.D., and T.J.Mueller, "Aerodynamics of small vehicles," Annual Review of Fluid Mechanics, vol. 35, pp. 89-111, 2003.
- [28] M. Waszak, L. Jenkins, and P. Ifju . "Stability and control properties of an aeroelastic fixed wing micro aerial vehicle," *AIAA Atmospheric Flight Mechanics Conference and Exhibit*, Vols. doi: 10.2514/6.2001-4005, August 2001.
- [29] H. Garcia, M. Abdulrahim, M., and Lind R., "Roll control for a micro air vehicle using active wing morphing," *AIAA Paper*, p. 5347, 2003.
- [30] D. Lentink, and M. Gerritsma, "Influence of airfoil shape of performance in insect flight," *Proceeding of 33rd AIAA fluid dynamics conference and exhibit*, Vols. AIAA 2003-3447, 2003.
- [31] J.R. Usherwood and C.P Ellington, "The aerodynamics of revolving wings II. Propeller force coefficients from mayfly to quail.," *Exp Biol*, vol. 2002;205: 1565-76, 2002.
- [32] M.A. Green MA and A.J. Smith, "Effects of three-dimensionality on thrust production by a pitching panel," *Journal of Fluid Mechanics* , vol. 615, p. 211-20, 2008.
- [33] D.L. Althsuler, R.Dudley, and C.P. Ellington, "Aerodynamic forces of revolving hummingbird wings and wing models," *Zool Lond*, vol. 264, p. 327-32, 2004.

- [34] S.A. Ansari, K. Knowles, and R. Zbikowski, "Insectlike flapping wings in the hover. Part 2: Effect of wing geometry," *Journal of Aircraft*, vol. 45, no. 6, p. 1976–90, 2008.
- [35] C. Kang, and H. Aono et al., "Modeling of pitching and plunging airfoils at Reynolds number between 1×10^4 and 6×10^4 ," *Proceeding of 39th AIAA fluid dynamics conference*, Vols. AIAA 2009-4100, 2009.
- [36] S. Katsufumi, Q. Kentaro, et. al, "Scaling of Soaring Seabirds and Implications for Flight Abilities of Giant Pterosaurs," *Plos one*, vol. DOI: 10.1371/journal.pone.0005400, 29 April 2009.
- [37] J. Grauer, and J. E. Hubbard, Modeling and System Identification of an ornithopter flight dynamics model, Dissertation, Ed., Univeristy of Maryland, 2011.
- [38] S. M. Swartz, "Allometric patterning in the limb sceleton of bats: Implications for the mechanics and energies of powered flight," *Journal of Morphology*, vol. 249, pp. 277-94, 1997.
- [39] C. Altenbuchner, "Dynamic Response Characteristics of an Active Morphing Ornithopter Transmission," *ASME 2011 Conference on Smart Materials, Adaptive Structures and Intelligent Systems*., Vols. SMASIS2011-4951, April 2011.
- [40] R. M. Alexander, "Mechanics of bipedal locomotions, in P.S. Davies (Ed.)," *Perspectives in Experimental Biology*, pp. 493-504, 2002.
- [41] N. Moore, and N. Casal, "Birds, bats and insects hold secrets for aerospace engineers," March 2008. [Online]. Available: <http://ns.umich.edu/new/releases/6312-birds-bats-and-insects-hold-secrets-for-aerospace-engineers>. [Accessed 2014].
- [42] N. C. Moore, and N. Casal, "Sensors for bat-inspired spy plane under development," March 2008. [Online]. Available: <http://ns.umich.edu/new/releases/6409-sensors-for-bat-inspired-spy-plane-under-development>. [Accessed 2014].
- [43] J.W.Bahlman, S. M. Swartz, and K. S. Breuer, "Design and characterization of a multi-articulated robotic bat wing," *IOPScience*, Vols. doi:10.1088/1748-3182/8/1/016009, January 2013.
- [44] J. Grauer, and J. E. Hubbard, Modeling and System Identification of an ornithopter flight dynamics model, Dissertation, Ed., Univeristy of Maryland, 2011.
- [45] D.H.Olson, and D.Silin, et. al., "Wind Tunnel Testing and Design of Fixed and Flapping Wing Micro Air Vehicles at the University of Arizona," *Micro Air Vehicle Design Papers*, p. 9, 2005.
- [46] University of Michigan, "COM-BAT: Conzeptualization of Robotic Bat," 2008. [Online]. Available: <http://um3d.dc.umich.edu/2008/09/combat/>. [Accessed 2014].
- [47] Massachusetts Institute of Technology, "MIT Robot Locomotion Group - Agile Flight Project," 2010. [Online]. Available:

<http://groups.csail.mit.edu/locomotion/flight.html>.

- [48] S. Shkarayev, and D.Silin, "Aerodynamics of Flapping-Wing Micro Air Vehicles," *47th AIAA Aerospace Sciences Meeting Including The New Horizons Forum and Aerospace Exposition*, Vols. AIAA 2009-878, January 2009 .
- [49] J. D. DeLaurier, "An Aerodynamic Model for Flapping-Wing Flight," *The Aeronautical Journal*, vol. 97, no. 964, pp. 125-130, April 1993.
- [50] M. Shipman, "Eureka!," 2012. [Online]. Available: <http://www.eureka!ert.org/multimedia/pub/15126.php>. [Accessed June 2014].
- [51] O. Bauchau, *Flexible Multi Body Dynamics*, D. 10.1007/978-94-007-0335-3, Ed., Atlanta, Georgia: Springer, 2010.
- [52] A. A. Shabana, "Flexible Multibody Dynamics: Review of Past and Recent Developments," *Multibody System Dynamics I*, Vols. 189-222, 1997.
- [53] K. Panagoitis, "Model Order Reduction in Structural Mechanics, Coupling the Rigid and Elastic Multi body Dynamics", Dissertation, Institut fuer Bahnfarzeuge und Bahntechnik, Ed., Technische Universitaet Dresden, 2009.
- [54] L. Meirovitch, *Fundamentals of Vibrations*, New York : McGraw-Hill Higher Education , 2001.
- [55] MacNeal-Schwendler Corporation (MSC), *Motion Workspace Guide Introduction - Simxpert*, Newport Beach, CA : MSC , 2011 .
- [56] B. Oliver, "DYMORE: A Finite Element Based Tool for the Analysis of Nonlinear Flexible Multibody Systems," Georgia institute for Technology, Atlanta 2009.
- [57] Johnson Aeronautics CAMRAD II , "COMPREHENSIVE ANALYTICAL MODEL OF ROTORCRAFT AERODYNAMICS AND DYNAMICS," *Analytical Methods, Inc.*, 2010.
- [58] Comsol , "Comsol Multipurpose software platform," 2014. [Online]. Available: www.comsol.com.
- [59] SimXpert, "Integrated Multidisciplinary Enterprise Simulation Solution for the CAE Analyst," February 2012. [Online]. Available: <http://www.mscsoftware.com/Products/CAE-Tools/simxpert.aspx>.
- [60] Dyhr J. P., Noah J., et. al. "Autostabilizing airframe articulation: Animal inspired air vehicle control," *51st IEEE Conference on Decision and Control*, March 2012.
- [61] I. Faruque and J. Humbert, "Dipteran insect flight dynamics: Part i - longitudinal motion about hover," pp. 1-15, 2010.
- [62] G. Taylor, and R. Zbikowski, "Nonlinear time-periodic models of the longitudinal flight dynamics of desert locusts *Schistocerca gregaria*," *Journal of Experimental Biology*, pp. 2803-2829, 2003.
- [63] J.Lee, D.Kim, et. al., "Longitudinal flight dynamics of bioinspired ornithopter considering fluid-structure interaction," *Journal of Guidance, Control, and Dynamics*, vol. 34, no. 3, p. 667, May-June 2011.
- [64] R. C. Nelson, "Flight Stability and Automatic Control", Second Edition ed., WCB McGraw-Hill , 1998.

- [65] K. Sibilski, "Dynamics of micro-air-vehicle with flapping wings," *Acta Polytechnica*, vol. 44, no. 2, pp. 15-22, 2004.
- [66] C. Orłowski, "Flapping Wing Micro Air Vehicles: An Analysis of the Importance of the Mass of the Wings to Flight Dynamics, Stability, and Control", Dissertation, Ed., University of Michigan., 2011.
- [67] X. Deng, L. Schenato et. al., "Flapping- ight for biomimetic robotic insects: Part i - system modeling," *Ieee Transactions on Robotics*., vol. 22, no. 4, pp. 776-788, August 2006.
- [68] X. Deng, L. Schenato et. al., "Flapping- ight for biomimetic robotic insects: Part ii - ight control design," *IEEE Transactions on Robotics*, vol. 22, no. 4, pp. 789-803, August 2006.
- [69] I. Faruque, Control-Oriented Reduced Order Modeling Dipteran Flapping Flight, PhD thesis, University of Maryland , 2011.
- [70] J. Lee, J. Kim, and J. Han, "Cycle-averaged mean and zero-mean time-varying ight dynamics of the ornithopters at trim," 2010.
- [71] M.R. Waszak and C.S. Buttrill, Modeling and Model Simplification of Aeroelastic Vehicles: An Overview," *NASA Technical Memorandum* , vol. 107691, September 1992 .
- [72] J. Dietl, and Garcia E. "Stability in ornithopter longitudinal flight dynamics," *Journal of Guidance, Control, and Dynamics*, vol. 31, no. 4, pp. 1157-1162, August 2008.
- [73] D.K. Kim, J.S. Lee et. al., "Improved aerodynamic model for efficient analysis of flapping-wing flight," *AIAA Journal*, vol. 49, no. 4, pp. 868-872, April 2011.
- [74] M. Bolender, "Rigid multi-body equations-of-motion for flapping wing mavs using kane's equations," *Aiaa, Guidance, Navigation, and Control Conference*., August 2009.
- [75] A.T. Pfeiffer, and Jun-Seong Lee et. al., "Ornithopter Flight Simulation Based on Flexible Multi-Body Dynamics," in *Journal of Bionic Engineering*, 2010.
- [76] J. Grauer and J.E. Hubbard, "Modeling of ornithopter flight dynamics for state estimation and control," *IEEE, American Controls Conference*, June 2010.
- [77] M. Bolender, "Rigid multi-body equations-of-motion for flapping wing mavs using kane's equations," *Guidance, Navigation, and Control Conference*, August 2009.
- [78] T. Rashid, "The flight dynamics of a full-scale ornithopter, Master's thesis," 1995.
- [79] M. Okamoto, and Azuma A., "Experimental Study on Aerodynamic Characteristics of Unsteady Wings at Low Reynolds Number," *AIAA Journal*, vol. 43, no. 12, pp. 2526-2536, 2005.
- [80] W. P. Walker, "Unsteady Aerodynamics of Deformable Thin Airfoils," *Virginia Polytechnic Institute and State University* , 2009 .
- [81] B. Rogot B, and J. Sitaraman, "A Computational Study of Flexible Wing Ornithopter Flight," *26th AIAA Applied Aerodynamics Conference*, 18-21 August 2008.

- [82] C. Altenbuchner, and J.E. Hubbard, "Free Flight Validation of a Flexible-Multi-Body Structural Dynamics Model of a Bioinspired Ornithopter," *51st AIAA Aerospace Sciences Meeting*, January 2013.
- [83] B. K. Stanford, and P.S.Beran, "Analytical Sensitivity Analysis of an Unsteady Vortex-Lattice Method for Flapping-Wing Optimization," *Journal of Aircraft*, vol. 47, no. 2, pp. 647-662, March-April 2010.
- [84] A. Hart and L.Ukeiley,, "Low Reynolds Number Unsteady Aerodynamics over a Pitching-Plunging Flat Plate," *48th AIAA Aerospace Sciences Meeting Including the New Horizons Forum and Aerospace Exposition*, 4-1 January 2010.
- [85] M. R. Visbal, "High-Fidelity Simulation of Transitional Flows past a Plunging Airfoil," *AIAA Journal*, vol. 47, no. 11, pp. 2685- 2697, November 2009.
- [86] W. Yuan,R. Lee et. al., "Numerical and Experimental Simulations of Flapping Wings," *International Journal of Micro Air Vehicles*, pp. 181-209, September 2010.
- [87] I. H. Tuncer, and M.F. Platzer, "Thrust Generation Due to Airfoil Flapping," *AIAA Journal*, vol. 34, pp. 324-331, February 1996.
- [88] I.H. Tuncer, R. Walz, and M.F. Platzer,, "A Computational Study of the Dynamic Stall of a Flapping Airfoil," *AIAA Paper 98-2519*, June 1998.
- [89] M.Yu and J.Z. Wang, "High-Fidelity Flapping-Wing Aerodynamics Simulations with a Dynamic Grid Spectral Difference Method," *ICCFD7 Seventh International Conference on Computational Fluid Dynamics*, 9-13 July 2012.
- [90] D.K. Kim, J.S. Lee et. al."Improved aerodynamic model for efficient analysis of flapping-wing flight," *AIAA Journal*, vol. 49, no. 4, pp. 868-872, April 2011.
- [91] A. Wissa, "Analytical Modeling and Experimental Evaluation of a Passively Morphing Ornithopter Wing," University of Maryland, Department of Aerospace Engineering , 2014.
- [92] MacNeil Schwendler Cooperation (MSC), "Adams flex," MSC, 2011.
- [93] MSC Software , "Adams Flex - Reported in Adams Docs DOC10403," MSC , 2013.
- [94] A. A. Shabana, "Flexible Multibody Dynamics: Review of Past and Recent Developments," *Multibody System Dynamics 1*, Vols. 189-222, 1997.
- [95] C. Jain, and L. Sumit, A Quick Tutorial on Multibody Dynamics, School of Interactive Computing Georgia Institute of Technology, 2010.
- [96] Adams, Appendix - Theoretical Background, 2008.
- [97] C. Altenbuchner, "Free Flight Validation of a Flexible-Multi-Body Structural Dynamics Model of a Bioinspired Ornithopter," *51st Aerospace Sciences Meeting*, January 2013.
- [98] R.R. Craig, and M.C. Bampton,"Coupling of substructures for Dynamic Analyses, vol. 6(7), *AIAA Journal*, 1996, pp. 1313-1319.
- [99] I. Faruque and J. Humbert, "I. Faruque and J. Humbert,," *Journal of Theoretical Biology*, pp. 1-15, 2010.

- [100] I. Faruque ,Control-Oriented Reduced Order Modeling Dipteran Flapping Flight, PhD Thesis, University of Maryland, 2011.
- [101] J. Grauer, and J.E. Hubbard, "System Identification of an Ornithopter Aerodynamics Model," *AIAA Atmospheric Flight Mechanics Conference* , no. 7632, 2-5 August 2010.
- [102] B. Y. Leonard, "Flapping Wing Flight Dynamic Modeling," *Masters Thesis*, August 2011.
- [103] T.J. Mueller, and J.D. DeLaurier, "Aerodynamics of Small Vehicles," *Annual Review of Fluid Mechanics* , vol. 35, pp. 89-111, 2003.
- [104] R. Malhan, M. Benedict, and I. Chopra, "Experimental investigation of a flapping wing concept in hover and forward flight for micro air vehicle applications," *American Helicopter Society*, May 2010.
- [105] RTO, "Unsteady Aerodynamics of Micro Air Vehicles," *RTO Technical Report*, September 2010.
- [106] T. Rashid, "The flight dynamics of a full-scale ornithopter," *Master's thesis*, 1995.
- [107] SimXpert, "Motion Workspace Guide Introduction," Pasadena, CA: MSC Adams , 2011.
- [108] G. Taylor, and R. Zbikowski. "Nonlinear time-periodic models for the longitudinal flight dynamics of desert locusts *schistocerca gregaria*," *Journal of the Royal Society Interface*, vol. 5, pp. 197-221, 2005.
- [109] University of Michigan, "Six-inch Robotic Spy Bat Plane," designworldonline, 2008. [Online]. Available: <http://www.designworldonline.com> [Accessed 2014].
- [110] A. Wissa, and N. Guerreiro et. al., "Flight Testing of Novel Compliant Spines for Passive Wing Morphing on Ornithopters," *Structural Dynamics, and Materials and Co-located Conferences*, April 2013.